UNIVERSITY OF SOUTHAMPTON

Faculty of Engineering and Physical Sciences

Bioengineering Science Research Group

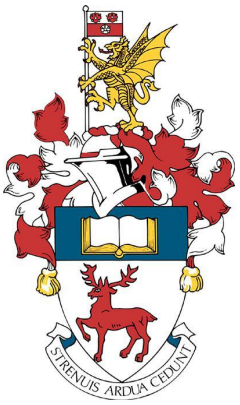

Understanding the Biological and Physical Effects of Sclerotherapy

By

Elisabetta Bottaro,

Thesis for the degree of Doctor of Philosophy

November 2019

November 2019

Abstract

Sclerotherapy is currently employed to effectively treat varicose veins, and relies on the injection of liquid or foamed agents causing endothelial wall damage, vessel shrinkage, and subsequent neovascularization. Pre-clinical *in vitro* studies are conducted to characterize the performance of sclerosing agents; however, they often do not replicate physiologically relevant physical and biological conditions. In this study, three models have been developed in order to gain a more comprehensive understanding of the physical and biological effects of sclerosing agents. These include: (i) 2D *in vitro* models, (ii) *ex vivo* models, and (iii) 3D vein-on-a-chip (VOC).

The 2D *in vitro* model has been employed to quantify the efficacy of sclerosing agents onto a monolayer of endothelial cells. The model allowed investigating the effect of clinically-relevant parameters, including different administration conditions. Moreover, the first systematic comparison of the biological performance of different polidocanol-based sclerosing foam formulations (PEM and physician compounded foams) was carried out, including an attempt to correlate biological effects with foam physical properties. It has been demonstrated that PEM was the most effective foam at disrupting the endothelial layer in a variety of tests and over different timescales of treatment. This was attributed to the slower drainage dynamics of PEM compared to physician compounded foams, and – potentially – to the enhanced polidocanol mobility conferred by its gas formulation.

Subsequently, a quantitative microscopy technique was employed to quantify the level of disruption of cell membranes subject to sclerotherapy. With this method, it was found that exposure to sclerosants causes changes to the lipid packing of cell membranes. Therefore, measurement of the variations in membrane lipid packing was employed to evaluate the bio-physical effects of sclerosing agents. Findings were generally in agreement with the results obtained from *in vitro* efficacy tests. The ability of POL to penetrate and perturb the membrane lipid bilayer was found to be concentration dependent. Similar results were obtained comparing foamed and liquid POL.

Whilst 2D models enabled the investigation of the effect of sclerosants at the cellular level, they did not reproduce the 3D architecture and fluid dynamic environment typical of a varicose vein. Therefore, they were not suitable for investigating the interaction of sclerosing

agents with blood in a biomimetic environment. For this reason, *ex vivo* models have been developed using umbilical cord veins, in order to quantifying sclerosant-induced disruption of the vessel wall using a colorimetric assay. Experiments were carried out using both liquid and foamed sclerosants, in either static or dynamic conditions, and in the presence of blood. When blood was perfused through the umbilical vein, all treatment methods presented similar efficacy.

Afterwards, 3D Vein-on-a-chip (VOCs) models lined with human endothelial cells were developed. Models replicated the architecture of physiological and varicose veins. VOCs were produced in polydimethylsiloxane (PDMS) applying 3D-printing and soft-lithography techniques, and were employed for evaluating the mechanical properties of foams. A protocol was designed to replicate the clinical administration process, using physiologically relevant vein diameter, geometry, and inclination angle (i.e. replicating leg elevation), and reproducing bulk physical properties of blood. The vein-on-a-chip models and experimental methods developed in this study provide a novel technology platform to measure the behaviour of different formulations of sclerosing foams, at physical conditions that resemble their clinical administration.

Despite PDMS-based VOCs provide a useful model to investigate the flow behavior of sclerosing foams and its relation to biological performance, they do not fully replicate the physical properties of both vascular and extra-vascular compartments of a vein. In order to overcome this limitation, the development of hydrogel-based models has been investigated. A method has been developed to manufacture channel geometries inside a hydrogel-based scaffold.

Overall, these technological developments and research findings can form the basis for a novel technological pipeline to accelerate clinical translation and innovation of sclerosing agents.

Table of Contents

List of Tables

List of Equations

Equation 1:

$$GP = \frac{I_B - I_R}{I_B + I_R}$$

Equation 2:

$$\Delta GP_m = GP_{mt} - GP_{m0}$$

Equation 3:

$$\Delta EB_e = EB_{dn+5} - Eb_{dn}$$

Equation 4:

$$Re = \frac{\rho v D}{\mu}$$

Equation 5:

$$E = \frac{FL}{A\Delta L}$$

List of Figures

The experiment was repeated four times. One asterisk (*) indicates p-value ≤ 0.05, two asterisks (**) indicate p-value ≤ 0.01, three asterisks (***) indicate p ≤ 0.001, and four asterisks (****) indicate p-value ≤ 0.0001.

Figure 25. *In vitro evaluation of the effect of foam exposure time on HUVECs, using different types of foam. Methods of foam production investigated included PEM (blue), DSS (red), and TSS (green). 1 mL of foam was injected in these experiments, using a 16G needle. Cell monolayers were exposed to each foam for 15, 30, 60 and 120 seconds. Data are reported (Tukey's box plot) as percentage of attached cells after treatment (compared to untreated cells), determined via methylene blue method. The effect of treatment time (for each foam production method) is illustrated in (A), while a comparison between foam production methods (for each treatment time) is illustrated in (B). The experiment was repeated ten times. One asterisk (*) indicates p-value ≤ 0.05, two asterisks (**) indicate p-value ≤ 0.01, three asterisks (***) indicate p-value ≤ 0.001, and four asterisks (****) indicate p-value ≤ 0.0001.*

Figure 26. *In vitro evaluation of the effect of PEM gas formulation on HUVECs. 1 mL of PEM foam was injected in these experiments, using a 16G needle. Cell monolayers were exposed to each foam type for 15 seconds. Foams tested were PEM containing either room air, 100% O_2, and 35:65 CO_2:O_2. Data are reported (Tukey's box plot) as percentage of attached cells after treatment (compared to untreated cells), determined via methylene blue method. The experiment was repeated twenty times. Four asterisks (****) indicate p-value ≤ 0.0001.*

Figure 27. *Histopathologic observation of HUVECs upon treatment with sclerosing foams. Microscope images (4x magnification) illustrate HUVECs monolayers treated for 15 seconds using PEM (A), DSS (B), Tessari (C) foams, and untreated (D). Scale bars are 200 µm.*

Figure 28. *Representative schematics of a surfactant molecule and a micelle. (A) Surfactants are amphiphilic molecules composed by a hydrophilic head and a hydrophobic tail. (B) Surfactant monomers at a certain concentration (known as CMC) aggregate to generate (C) micelles.*

Figure 29. *Schematic representation of the main component of the cellular membrane. The cellular membrane is a bilayer composed of phospholipids (amphiphilic molecules), which present a polar head and two hydrophobic tails. The most abundant phospholipids are phosphatidylcholines.*

Figure 30. *Chemical structure of common polarity-sensitive fluorescent probes, namely Laurdan, Di-4-AN(F)EPPTEA and Di-4-ANEPPDHQ.*

Figure 31. *Schematic representation of the lipid bilayer in its two phases: liquid (disordered) and gel (ordered). Lipid bilayers exist in either the liquid or gel phase, at a broad range of temperatures. The GP value varies from -1 to +1, which indicates the disordered and ordered phases, respectively.*

Figure 32. *Spectral GP imaging of live HUH7 cells. (A, C, E, G and I) HUH7 cells image stacks (grey scale images converted into LUT file). (B, D, F, H and J) Pseudo-colored GP maps (40 µm x 40 µm) of the equatorial plane of live HUH7 cells using the environment-sensitive membrane dye Di-4-AN(F)EPPTEA between 560 nm and 650 nm wavelength emission (scale bar 50 µm).*

Figure 33. *Control HUH7 membrane GP measurements. (A) Histograms of GP values following Gaussian fitting indicating the variation of membrane GP up to 40s. (B) Average GP value up to 40s (blue line). Time point measurements were performed every 5 seconds. The experiment was repeated six times, and results are reported as mean value ± standard deviation.*

Figure 34. *Average membrane GP value in live HUH7, for 12 different independent samples (blue dots). The GP value was measured three times for each sample, and results are reported as mean value ± standard deviation.*

Figure 35. *Average membrane GP value in live HUH7 and PTK2. (A) Average membrane GP value in live PTK2, for 12 different independent samples (red dots). The GP_m value was measured three times for each sample, and results are reported as mean value ± standard deviation. (B) Comparison between physiological GP_m values of HUH7 and PTK2. The GP value was measured 12 times for each cell line using different samples, and results are reported as mean value ± standard deviation. Two asterisks (**) indicate that differences between mean values are very statistically significant (p-value < 0.01).*

Figure 36. *Spectral GP imaging of live HUH7 cells treated with 0.06% liquid POL. GP maps (40 µm x 40 µm) of the equatorial plane of live HUH7 cells using the environment-sensitive membrane dye Di-4-AN(F)EPPTEA between 560 nm and 650 nm wavelength emission. Images correspond to different time points: (A) before POL injection (t_0), (B) 5s (t_{10}), (C) 15s (t_{20}) and (D) 35s (t_{40}) of exposure time with 0.06% POL (scale bar 50 µm).*

Figure 37. *GP_m measurement of HUH7 treated with 0.06% POL. (A) Histograms of GP_m values following Gaussian fitting indicating the variation of membrane GP over 40s. (B) Average GP_m value of HUH7 treated with 0.06% (blue line) compared to the control (red line) over time, up to 40s. Time point measurements were performed every 5 seconds. The experiment was repeated six times, and results are reported as mean value ± standard deviation.*

Figure 38. *Spectral GP imaging of live HUH7 cells treated with 0.06% liquid POL for 55s. GP maps (40 µm x 40 µm) of the equatorial plane of live HUH7 cells using the environment-sensitive membrane dye Di-4-AN(F)EPPTEA between 560 nm and 650 nm wavelength emission (scale bar 50 µm).*

Figure 39. *GP measurement of PtK2 treated with 0.06%. (A) Histograms of GP values following Gaussian fitting indicating the variation of membrane GP over 40s. (B) Average GP value of PTK2 treated with 0.06% POL (blue line) compared to the control (red line) over time, up to 40s. Time point measurements were carried out every 5 seconds. The experiment was repeated six times, and results are reported as mean value ± standard deviation.*

Figure 40. *PtK2 seeded at different density treated with 0.06% POL. Average GP value of PTK2 treated with 0.06% at confluence >10% (blue line) or <10% (red line) over time, up to 40s. At $t_{6,}$ all the lipids moved into the intracellular space and the GP measurable is only the intracellular GP (GP_i). Time point measurements were carried out every 5 seconds. The experiment was repeated six times, and results are reported as mean value ± standard deviation.*

Figure 41. *Spectral GP imaging of live PtK2 cells treated with 0.06% liquid POL. GP maps (40 µm x 40 µm) of the equatorial plane of live PTK2 cells using the environment-sensitive membrane dye Di-4-AN(F)EPPTEA between 560 nm and 650 nm wavelength emission. Images correspond to different time points: (A, B) before injection (t_0), (C, D) after 15s of treatment time (t_{20}). Scale bar 50 µm).*

Figure 42. *Spectral GP imaging of single PtK2 cells treated with 0.06% liquid POL. GP maps (40 µm x 40 µm) of the equatorial plane of live PTK2 cells using the environment-sensitive*

membrane dye Di-4-AN(F)EPPTEA between 560 nm and 650 nm wavelength emission. Images correspond to different time points: before POL injection (t_5) and 1s (t_6), 2s (t_7), 3s (t_8), 4s (t_9) and 5s (t_{10}) of exposure time with 0.06% POL. The yellow arrows indicate the intracellular movement of the lipids (scale bar 50 µm).

Figure 43. *Comparison membrane GP measurement of PTK2 and HUH7 treated with 0.06%. Average GP value of HUH7 (red line) compared to PTK2 (blue line) over time, up to 40s. Time point measurements were performed every 5 seconds. The experiment was repeated six times, and results are reported as mean value ± standard deviation.*

Figure 44. *GP measurement of live HUH7 treated with five different dilutions of liquid POL, namely (A) 1.00%, (B) 0.50%, (C) 0.06%, (D) 0.03%, and (E) 0.01%. Histograms of GP values following Gaussian fitting indicating the variation of GP distribution over time, up to 40s. Time point measurements were performed every 5 seconds.*

Figure 45. *Average GP_m measurement of live HUH7 treated with five different dilutions of liquid POL, namely 1.00% (blue line), 0.50% (red line), 0.06% (green line), 0.03% (purple line) and 0.01% (orange line). Average GP_m values were measured over time, up to 40s. Time point measurements were performed every 5 seconds. The experiment was repeated six times, and results are reported as mean value ± standard deviation.*

Figure 46. *Spectral GP imaging of live HUH7 treated with five different dilutions of liquid POL, namely 1.0%, 0.50%, 0.06%, 0.03% and 0.01%. HUH7 GP images (40 µm x 40 µm) of the equatorial plane of live cells using the environment-sensitive membrane dye DDi-4-AN(F)EPPTEA at t_0 (before injection) and after 10, 20, 30 and 40 s. Images were acquired between 560 nm and 650 nm wavelength emission (scale bar: 50 µm).*

Figure 47*. Spectral GP imaging of live HUH7 cells treated with 0.06% liquid POL. (A, B, and C) HUH7 cells image stacks (grey scale images converted into LUT file). (D, E and F) HUH7 GP images (40 µm x 40 µm) of the equatorial plane of live cells using the environment-sensitive membrane dye Di-4-ANEPPDHQ at t_{40}. Images were acquired between 560 nm and 650 nm wavelength emission (scale bar 50 µm).*

Figure 48. *Spectral GP imaging of live HUH7 cells treated with 0.06% liquid POL. HUH7 GP images (40 µm x 40 µm) of the equatorial plane of live cells using the environment-sensitive membrane dye Di-4-ANEPPDHQ at t_0 (A, D), t40 (B, E) and t100 (C, F). The purple arrows indicate segments of membrane not in contact with other cells, whereas the red arrows indicate segments of membrane between two or more cells. Images were acquired between 560 nm and 650 nm wavelength emission and zoomed in at 150% in ImageJ (scale bar 50 µm).*

Figure 49. *Spectral GP imaging of live HUH7 cells treated with 0.03% liquid POL. HUH7 GP images (40 µm x 40 µm) of the equatorial plane of live cells using the environment-sensitive membrane dye Di-4-ANEPPDHQ at t_0 (A, D), t_{40} (B, E) and t_{100} (C, F). The purple arrows indicate segments of membrane not in contact with other cells, whereas the red arrows indicate segments of membrane between two or more cells. Images were acquired between 560 nm and 650 nm wavelength emission and zoomed in at 150% in ImageJ (scale bar 50 µm).*

Figure 50*. GP measurement of live HUH7 treated with TSS (A-B), DSS (C-D) and PEM (E-F). Experiments involved the injection of the foam directly onto the cells, referred to as dry-test (A, C, E), or onto a monolayer of cells covered by 500 µL of PBS, referred to as wet-test (B, D, F).*

Figure 59. *Evaluation of the effect of PEM, PCFs and liquid POL treatment on umbilical cord vein in static condition, in the presence of blood. (A) Evaluation of the effect of PEM, PCFs and liquid POL treatment on umbilical cord vein at d_0, d_5 and d_{10}. The vein was left filled with whole human blood, and subject to 1 minute of treatment. Data are reported as mg of EB per grams of tissue, determined via Evans Blue method. The experiment was repeated six times. (B) Evaluation of the effect of PEM, PCFs and liquid POL treatment on umbilical cord vein (10 cm). The vein wall was exposed to the sclerosing agents for 1 minute. Data are reported as average of mg of EB per grams of tissue, determined via Evans Blue method. One asterisk (*) indicates p-value ≤ 0.05.*

Figure 60. *Ex vivo evaluation of the effect of liquid/foamed POL in the presence (SB) or absence (S) of blood in static conditions. The vein was either prewashed (S) or filled with whole human blood (SB), and subject to 1 minute of treatment. Data are reported as mg of EB per grams of tissue, determined via Evans Blue method. The experiment was repeated six times.*

Figure 61*. Ex vivo evaluation of the performance of liquid and foamed POL, under dynamic flow conditions. (A) Evaluation of the effect of PEM, PCFs and liquid POL treatment on the umbilical cord vein at d_0, d_5 and d_{10}. A steady flow of PBS (62.5 mL/h) was injected through the vein, which was subsequently treated with liquid/foamed POL for 1 minute. Data are reported as mg of EB per grams of tissue, determined via Evans Blue method. The experiment was repeated six times. (B) Evaluation of the effect of PEM, PCFs and liquid POL treatment on umbilical cord vein (10 cm). Data are reported as the average mg of EB per grams of tissue, determined via Evans Blue method. One asterisk (*) indicates p-value ≤ 0.05.*

Figure 62. *Ex vivo evaluation of the effect of liquid/foamed sclerosant under static or dynamic conditions. The vein model in either static or dynamic (62.5 mL/h) conditions was exposed to 1 minute of treatment. Data are reported as mg of EB per grams of tissue, determined via Evans Blue method. The experiment was repeated six times.*

Figure 63*. Ex vivo evaluation of the effect of liquid/foamed POL in dynamic conditions in the presence of blood. (A) Evaluation of the effect of PEM, PCFs and liquid POL treatment on umbilical cord vein at d_0, d_5 and d_{10}. The vein walls, exposed to a steady flow of whole human blood (62.5 mL/h), were subject to 1 minute of treatment. Data are reported as mg of EB per grams of tissue, determined via Evans Blue method. The experiment was repeated six times. (B) Evaluation of the effect of PEM, PCFs and liquid POL treatment on umbilical cord vein (10 cm). Data are reported as average of mg of EB per grams of tissue, determined via Evans Blue method.*

Figure 64. *Ex vivo evaluation of the performance of liquid/foamed sclerosants in dynamic and static conditions, in the presence of blood. A steady flow of blood (BD) or absence of flow (SB) were applied to the system. The vein was subject to 1 minute of treatment. Data are reported as mg of EB per grams of tissue, determined via Evans Blue method. The experiment was repeated six times.*

Figure 65. *Ex vivo evaluation of the effect of liquid/foamed sclerosants in dynamic conditions, in the presence/absence of blood. A steady flow of PBS (D) or blood (BD) was injected through the vein model. The vein was subject to 1 minute of treatment. Data are reported as mg of EB per grams of tissue, determined via Evans Blue method. The experiment was repeated six times.*

Figure 66. *Photographs showing representative umbilical cord anatomies. Umbilical cord showing (A) left twist, (B) single or (C) multiple pseudo knots. In the presence of pseudo knot, the umbilical vein is dilated and visible through the Wharton jelly (scale bar 2 cm).*

Figure 67. *Evaluation of the impact of umbilical cord anatomy. Umbilical cords presenting pseudo knots have been analysed. (A) Umbilical cord with two pseudo-knots in the position d_4 and d_{10} (4 cm and 10 cm from the injection point). (B) Umbilical cord with two pseudo-knots in the position d_0 and d_{10} (0 cm and 10 cm from the injection point). The veins were pre-washed and subject to 1 minute of treatment. Data are reported as mg of EB per grams of tissue, determined via Evans Blue method. The measurements are an average of three repeats.*

Figure 68. *Assembled VOCs representing simplified physiological (A) and varicose (B) vein models, and demonstration of perfusion using a red dye. These models were employed to test the flow behavior of foams. The main channel was punctured with a needle (21 G), in order to mimic the clinical process of injection more closely (scale bar 8mm).*

Figure 69. *Schematic of VOCs production via replica molding. Firstly, (A) a CAD design of positive molds was generated and 3D printed. Secondly, (B) two PDMS layers were produced from the molds, aligned together, and permanently bonded via oxygen plasma treatment to obtain a fully circular channel cross-section (C). Finally, the main channel was punctured with a 21G needle (D).*

Figure 70. *Schematic illustrating the set-up for evaluating the flow behaviour of foams in the VOC model. A steady flow is imposed using a syringe pump (A), and a pressure transducer (B) is positioned in line with the inlet tubing and prior to the VOC (C). The foam is injected through the 16G needle into the main channel (D). The pressure transducer is connected to a National Instruments I/O module. The NI-DAQ system supports analog and digital inputs, and communicates with the NI-DAQ software. A Matlab code is employed to store pressure data in an automated fashion (E).*

Figure 71. *Representative pressure vs. time curve obtained by the CfAS. The plots were divided into three phases: (i) an increase of the pressure due to the expansion of the foam inside the channel, (ii) a decrease of the pressure caused by the degradation of the foam, and (iii) an initial peak due to the injection.*

Figure 72. *Pressure plots obtained from the CfAS while injecting DSS (A,C) and TSS (B,D) foams. The upper panels show the recordings obtained using the straight channel geometry, whereas the lower panels show the recording obtained using the serpentine-like channel geometry. As a control test (E), the pressure was measured without injecting foam, at a background constant flow rate (72 mL/h). The pressure inside the vein models was also measured while injecting the foam in the absence of a blood-surrogate flow (F).*

Figure 73. *Expansion rate values at the different flow rates investigated, and different foam production methods (TSS blue bars, DSS red bars). Measurements were obtained from the straight (A) and curved (B) channel geometry. Data represent the average of 6 measurements ± SD. An asterisk (*) indicates that differences between mean values are statistically significant (p-value < 0.05). The experiment was repeated six times, and results are reported as mean value ± standard deviation.*

Figure 74. *Expansion time values at the different flow rates investigated, and different foam production methods (TSS blue bars, DSS red bars). Measurements were obtained from the straight (A) and curved (B) channel geometry. Two asterisks (**) indicate that differences between mean values are very statistically significant (p-value < 0.01). The experiment was repeated six times, and*

results are reported as mean value ± standard deviation.

Figure 75. *Degradation rate values at the different flow rates investigated, and different foam production methods (TSS blue bars, DSS red bars). The measurements were obtained from the straight (A) and curved (B) channel geometry. An asterisk (*) indicates that differences between mean values are statistically significant (p-value < 0.05). The experiment was repeated six times, and results are reported as mean value ± standard deviation.*

Figure 76. *Degradation time values at the different flow rates investigated, and different foam production methods (TSS blue bars, DSS red bars). The measurements were obtained from the straight (A) and curved (B) channel geometry. An asterisk (*) indicates that differences between mean values are statistically significant (p-value < 0.05) and two asterisks (**) indicate that differences between mean values are very statistically significant (p-value < 0.01). The experiment was repeated six times, and results are reported as mean value ± standard deviation.*

Figure 77. *Agarose polymeric unit:1,3 linked β-d-galactose residue; 1,4 linked 3,6-anhydro-α-l-galactose residue (source: https://en.wikipedia.org/wiki/Agarose#/media/File:Agarose_polymere.svg).*

Figure 78. *Chemical structure of alginate: G-blocks and M-blocks. An ionic cross-linking occurs in the presence of divalent cations (Ca^{2+}), with the hydrogel formation characterized by the presence of the typical egg-box structure (source: Kühbeck, D., Mayr, J., Häring, M., Hofmann, M., Quignard, F., and Díaz Díaz, D. (2015). Evaluation of the nitroaldol reaction in the presence of metal ion-crosslinked alginates. New J. Chem. 39, 2306–2315).*

Figure 79*. CAD drawings of VOC models (1mm diameter, 50 mm long) representing physiological veins. The devices were characterized by one inlet/one outlet, two inlets/two outlets, or two inlets/one outlet.*

Figure 80*. Images of VOC models (1mm diameter, 50 mm length) representing physiological veins. The devices are characterized by (A) one inlet and one outlet, (B) two inlets and two outlets, or (C) two inlets one outlet. Channels were perfused with red food dye (scale bar 4 mm).*

Figure 81*. CAD drawings of the VOC models (1mm in diameter, 50 mm long) representing physiological and varicose vein (1-3 mm in diameter, 70 mm long). Devices are characterized by two inlets and one outlet.*

Figure 82. *Images of VOC models (1mm in diameter, 50 mm long) representing physiological and varicose veins (1-3 mm in diameter, 70 mm long). Devices are characterized by two inlets and one outlet. Channels were perfused with red food dye (scale bar 4 mm).*

Figure 83*. Arterioles-on-a-chip models (A) of smaller arterioles tree network (200 μm* in *diameter, 50 mm length) and (B) larger arterioles network (1-2 mm in diameter, 50 mm length). The channels were perfused with blue food dye. Scale bar 2mm.*

Figure 84. *CAD drawings of 3D printed agarose mold templates in different perspective views. Molds comprised of (A) 6 cylinders (5mm in width, 5 mm in height), with edge length of 5 mm, (B) 6 cubes, 5mm in width and depth, and (C) 6 disks, 15 mm in width and 2 mm in height.*

Figure 85. *Schematic of alginate scaffold production. (A) A 3D printed template was employed*

for generating negative patterns onto the agarose gel. (B) 1% agarose/1.5% $CaCl_2$ was heated in a microwave and was poured into a petri dish. The 3D printed mold was gently positioned on surface of the mixture and allowed to solidify for 30 minutes. (C-D) Once the agarose-$CaCl_2$ mold was solidified the 3D printed mold was gently removed and the chosen volume of alginate was poured into the wells. After 30 minutes, the scaffolds were extracted and left soaking 20 minutes into 0.15 5% $CaCl_2$ solution.

Figure 86. *Schematic drawing of the PDMS template employed for the fabrication of the gelatin mold. In this study a microfluidic hydrodynamic focusing geometry has been employed, characterized by three inlets and one outlet (depth: 1 mm, width: 1mm, length of main channel: 50 mm).*

Figure 87. *CAD drawings of 3D printed agarose mold in different perspective views. The mold employed was a parallelepiped (50 mm long, 30 mm high, and 10 mm deep), which allows producing a negative chamber into the agarose gel.*

Figure 88. *Schematic of the production of an alginate scaffold containing microfluidic channels. (A) 3D printed parallelepiped (50 mm long, 30 mm high, and 10 mm deep) template was employed for generating a negative chamber onto the agarose gel. (B) 1% agarose/1.5% $CaCl_2$ was heated in a microwave, poured into a petri dish, and the 3D printed mold was gently positioned on the surface of the mixture and allowed to solidify for 30 minutes. (C) Once the agarose-$CaCl_2$ mold was solidified, the 3D printed mold was gently removed. (D) In parallel, the gelatin sacrificial mold was generated by replica molding. (E) The agarose chamber was filled with 2 mL s of alginate in order to make a thin layer of gel, and the gelatin sacrificial mold was then positioned into the middle of the chamber, which was then completely filled with alginate solution. A flat sheet of 1% agarose/1.5% $CaCl_2$ can be used as a lid to allow the gelation process to occur from all boundaries. After gelation, the alginate scaffold was removed using a spatula.*

Figure 89. *Surface modification of well plates and PDMS using collagen. HUVECs exhibit similar adhesion and morphology on either substrate. On the left, the photographs (4X magnification) show HUVECs attached on the plastic coated with collagen after 48 hours, whereas on the right HUVECs were let to attach on PDMS coated with collagen after 48 hours. In either substrate, cells exhibited good attachment with typical elongated shape, although the monolayers attached onto PDMS show areas without cells. Scale bars are 200 µm.*

Figure 90. *Surface modification of well plates and PDMS using fibronectin. HUVECs exhibit similar adhesion and morphology on either substrate. On the left, the photographs (4x magnification) show HUVECs attached on the plastic coated with fibronectin after 48 hours, whereas on the right the photographs (4X magnification) show HUVECs attached on the PDMS coated with fibronectin after 48 hours. In either substrate, the cells exhibited good attachment with a typical long shape. Scale bars are 200 µm.*

Figure 91. *Surface modification of well plates and PDMS using Geltrex™. HUVECs cells exhibit similar adhesion and morphology on either substrate. On the left the photographs (4X magnification) show HUVECs attached on the plastic coated with Geltrex™ after 48 hours, whereas on the right the photographs (4x magnification) show HUVECs attached on the PDMS coated with Geltrex™ after 48 hours (scale bars are 200 µm).*

Figure 92. *Comparison between surface modification of PDMS with collagen (A), fibronectin*

(B), Geltrex™ (higher concentration) (C), and PDMS uncoated (D) as control. HUVECs exhibit similar adhesion and morphology whene fibronectin and collagen coating are performed, whereas they exhibit a lower growth rate with Geltrex™. In the untreated PDMS, no cells adhered. Images (4X magnification) were taken after 48 hours from seeding (scale bars are 200 µm).

Figure 93. *HUVECs cultured in fully circular channels after 24 hours. Images on the left show the lower channel wall coated with collagen (A) and fibronectin (C), respectively. Photographs on the right show the upper channel wall coated with collagen (B) and fibronectin (D), respectively. Images (4X magnification) were taken after 24 hours (scale bars are 200 µm).*

Figure 94. *HUVECs cultured in fully circular channels after 48 hours. Images on the left show the lower channel wall coated with collagen (A) and fibronectin (C), respectively. Photographs on the right show the upper channel wall coated with collagen (B) and fibronectin (D), respectively. Images (4X magnification) were taken after 48 hours (scale bars are 200 µm).*

Figure 95. *Fluorescence images of HUVECs culture into a 24-well-plates. After 48h, cell nuclei were labeled with Acridine Orange (green) and imaged with fluorescence microscopy. (A) 4X and (B) 10x, (scale bar 200 µm).*

Figure 96*. Fluorescence images of HUVECs into the VOCs (1 mm in diameter) in the inlet (A) and in the outlet (B) regions along the channel. HUVECs were cultured in a PDMS channel and allowed to cover all surfaces. After 48h, cell nuclei were labeled (green) and imaged with fluorescence microscopy (scale bar 200 µm).*

Figure 97. *Fluorescence images of HUVECs into the VOCs (1 mm in diameter) in the outlet region injected only from the inlet (A) or from the inlet/outlet (B) along the channel. HUVECs were cultured in a PDMS channel and allowed to cover all surfaces. After 48h, cell nuclei were labeled (green) and imaged with fluorescence microscopy (scale bar 200 µm).*

Figure 98. *ECs covering of the microfluidic channel wall. Fluorescence images of HUVECs into the VOCs (1 mm in diameter) in different regions along the channel. HUVECs were cultured in a PDMS channel and allowed to cover all surfaces. After 48h, cell nuclei were labeled (green) and imaged with fluorescence microscopy.*

Figure 99. *ECs covering of the microfluidic channel wall. Fluorescence images of HUVECs within an arterioles-on-a-chip (0.2 mm diameter) at different regions along the channel network. HUVECs were cultured in the PDMS microfluidic device and allowed to cover the inner surfaces. After 48h, cell nuclei were labeled (green) and imaged with fluorescence microscopy.*

Figure 100. *Fluorescence images of HUVECs in the same vascular segment of a arterioles-on-a-chip device (0.2 mm diameter) after 24 h (A) and 48 h (B), and corresponding cell edges analysis images obtained through the analyze particles tools of ImageJ employed for cell counting (A_1 and B_1). HUVECs were cultured in the PDMS microfluidic channels and allowed to cover all inner surfaces. After 24 and 48h cells nuclei were labeled (green) and imaged with fluorescence microscopy. Scale bars are 200 µm.*

Figure 101. *Fluorescence images of HUVECs in the same vascular segment of a arterioles-on-a-chip device (0.2 mm diameter) after 24 h (A) and 48 h (B), and corresponding cell edges analysis images obtained through the analyze particles tools of ImageJ employed for cell counting (A_1 and B_1). HUVECs were cultured in the PDMS microfluidic channels and allowed to cover all inner*

surfaces. After 24 and 48h cells nuclei were labeled (green) and imaged with fluorescence microscopy. Scale bars are 200 µm.

Figure 102. *Evaluation of cell attachment on agarose and alginate gels with (B, F) and without (A, E) collagen coating (2% w/v). At the top, photographs (4x magnification) show HUVECs seeded on the agarose gel after 48 hours, whereas the photographs at the bottom (4x magnification) show HUVECs seeded on alginate gel after 48 hours. Both substrates were compared to the control (C, G), where cells were seeded onto a plastic well. Scale bar 200 µm.*

Figure 103. *Photographs of the alginate scaffold production process, using different types of 3D printed molds, such as (A_1) cylindrical, (B_1) cubic, and (C_1) discoid. For each type of mold the agarose mold obtained is shown (A_2-B_2-C_2). The obtained (A_3) cylinder, (B_3) cube, and (C_3) disk of alginate are also shown.*

Figure 104. *Microscope images of two alginate cylinders fabricated by the agarose molding technique. Images were taken when the scaffold was stored into 0.15% $CaCl_2$ (A), or into at open air (B) for 30 minutes. (1X magnification, scale bars are 1000 µm).*

Figure 105. *Evaluation of the effect of alginate gelation time. Microscope images of alginate cylinders fabricated by agarose molding after 1-110 minutes from the beginning of the gelation process (1X magnification). The cylinder are completed gelified after 30 minutes. The ideal gelation time is between 30-70 minutes, after which dehydration occurs, causing shrinkage of the gel (scale bars are 1000 µm).*

Figure 106. *Photographs of an alginate scaffold containing microfluidic channels, and illustration of the production process. (A) The 3D printed parallelepiped template was employed for generating a chamber into the agarose gel. (B) 1% agarose/1.5% $CaCl_2$ was heated in the microwave and poured into a petri dish. The 3D printed mold was gently positioned on the surface of the mixture and allowed to solidify for 30 minutes. (C) Once the agarose-$CaCl_2$ mold was solidified, the 3D printed mold was gently removed. (D) In parallel, the gelatin sacrificial mold was generated by replica molding. (E) The agarose chamber was filled with few microliters of alginate in order to make a thin layer of gel, and the gelatin sacrificial mold was positioned into the middle of the chamber, which was then completely filled with the alginate solution. A flat sheet of 1% agarose/1.5% $CaCl_2$ can be used as a lid to allow the gelation process to happen from all the boundaries. After gelation, the alginate scaffold was removed using a spatula.*

Figure 107. *Photographs of an alginate scaffold containing vascular channels, and illustration of some steps of the production process. (A) The gelatin vessel structure was placed onto the agarose chamber, which was filled with few milliliters of alginate. (C) After gelation, the alginate scaffold was removed using a spatula and the gelatin was removed by melting, in order to obtain an empty channel (D).*

Figure 108. *Evaluation of HUVECs attachment on the surfaces of the channels. Microscope photographs show HUVECs attached on the alginate channel lumen, (A-C) taken at 4X magnification and (B-D) at 10X magnification, after 48 hours. Scale bars are 200 µm.*

Declaration of Authorship

I, Elisabetta Bottaro, declare that this thesis and the work presented in it is my own and has been generated by me as the result of my own original research. I confirm that:

1. This work was done wholly or mainly while in candidature for a research degree at this University;
2. Where any part of this thesis has previously been submitted for a degree or any other qualification at this University or any other institution, this has been clearly stated;
3. Where I have consulted the published work of others, this is always clearly attributed;
4. Where I have quoted from the work of others, the source is always given. With the exception of such quotations, this thesis is entirely my own work;
5. I have acknowledged all main sources of help;
6. Where the thesis is based on work done by myself jointly with others, I have made clear exactly what was done by others and what I have contributed myself;
7. Parts of this work have been published as:

Journal Articles:

1. Physical Vein Models to Quantify the Flow Performance of Sclerosing Foams.

E Bottaro, J Paterson, X Zhang, M Hill, V. A. Patel, S. A. Jones, A. L. Lewis, T. M. Millar & D. Carugo.Frontiers in bioengineering and biotechnology 7, 109, 2019.

Included in Chapter 7.

2. In vitro and ex vivo evaluation of the biological performance of sclerosing foams.

E Bottaro, J Paterson, L. Quercia, X Zhang, M Hill, V. A. Patel, S. A. Jones, A. L. Lewis, T. M. Millar & D. Carugo Scientific reports 9 (1), 9880, 2019.

Included in Chapter 4.

Conferences:

Vein-on-a-chip: an investigational tool for innovating sclerotherapy.

E. Bottaro, J. Paterson, X. Zhang, M. Hill, A. L. Lewis, T. Millar, D. Carugo, 2017.

Conference: The 21st International Conference on Miniaturized Systems for Chemistry and

Life Sciences (MicroTAS 2017).

Future publications from the material in this thesis:

The material in Chapter 5 will be submitted as a journal paper describing the effect of sclerosants onto the cell membrane.

The material in Chapter 6 will be submitted as a journal paper describing the sclerosing performance in a more realistic biological *ex vivo* model.

The material in Chapter 8 will be submitted as a journal paper describing a new method for creating complex channel structures within alginate scaffolds.

Not included in this thesis:

1. Suramin inhibits chikungunya virus replication through multiple mechanisms.

I. C. Albulescu, M. V. Hoolwerff, L. A. Wolters, E. Bottaro, C. Nastruzzi, S. C. Yang, S. Tsay, J. R. H., E. J. S., M. J. Van Hemert.

Antiviral research 121, 39-46, 2015.

2. Liposome production by microfluidics: potential and limiting factors.

D. Carugo, E. Bottaro, J. Owen, E. Stride, C. Nastruzzi.

Scientific reports 6, 25876, 2016.

3. Fabrication of Multifunctional Material for Cells Trabsplantation by Microfluidic.

S. Mazzitelli, E. Bottaro, C. Nastruzzi

Smart Materials for Tissue Engineering, 566-609, 2016.

4. "Off-the-shelf" microfluidic devices for the production of liposomes for drug delivery.

E. Bottaro, C. Nastruzzi.

Materials Science and Engineering: C 64, 29-33, 2016.

5. Analysis of the Diffusion Process by pH Indicator in Microfluidic Chips

for Liposome Production.

E. Bottaro, A. Mosayyebi, D. Carugo, C. Nastruzzi.

Micromachines 8 (7), 209, 2017.

Signature: Date:

Definitions and Abbreviations

AOC	Arteriole-on-a-chip
AVA	Arteriovenous Anastomoses
BAECs	Bovine Aorta Endothelial Cells
BEC	Blood Endothelial Cell
CAS	Computational Analysis System
CMC	Critical Micellar Concentration
CVI	Chronic Venous Insufficiency
DAF-FM	4-Amino-5-methylamino-2',7'-difluorofluorescein
DAPI	4',6-diamidin-2-fenilindolo
DR	Degradation Rate
DSS	Double-Syringe System
DVT	Deep Vein Thrombosis
EB	Evans Blue
EC	Endothelial Cell
ECM	Extra Cellular Matrix
ER	Expansion Rate
EVLA	Endovenous Laser Therapy
FDT	Foam Drainage Time
FHT	Foam Half Time
FLUO4/ AM	2,2'-((2-(2-(2-(bis(carboxymethyl)amino)-5-(2,7-difluoro-6-hydroxy-3-oxo-3H-xanthen-9-yl)phenoxy)ethoxy)-4-methylphenyl)azanediyl)diacetic acid acetoxymethyl ester
GP	Generalized Polarization
GSV	Great Saphenous Vein
HBSS	HEPES Buffered Saline Solution
H & E	Hematoxylin and eosin stain
HLMVEC	Human Lung Microvascular Endothelial Cell

HM	HUVEC Medium
HUH7	Human Hepatoma Cell Line
HUVEC	Human Umbilical Vein Endothelial Cell
IC_{50}	Half Maximal Inhibitory Concentration
ICAM-1	Intercellular Adhesion Molecule 1
iPSC	Induced Pluripotent Stem Cell
LEC	Lymphatic Endothelial Cell
LAT	Light Transmission Aggregometry
MB	Methylene Blue
MPFF	Micronized Purified Flavonoid Fraction
MTT	MTT 3-(4,5-dimethylthiazol-2-yl)-2,5-diphenyltetrazolium bromide
NO	Nitric Oxide
PCF	Physician Compounded Foams
PDMS	Polydimethylsiloxane
PEG	Polyethyleneglycole
PIN	Perforation-Invagination
POL	Polidocanol
POMaC	Poly(Octamethylene Maleate (Anhydride) Citrate)
PtK2	Long-nosed potoroo (Potorous tridactylis) epithelial kidney cells
QOL	Quality Of Life
RA	Room Air
RBC	Red Blood Cell
RFA	Radiofrequency Ablation
SGS	Short Saphenous Vein
STS	Sodium Tetradecyl Sulphate
TNF-α	Tumor Necrosis Factor Alpha
TSS	Tessari
VEGF	Vascular Endothelial Growth Factor
VOC	Vein-on-a-chip
WSS	Wall Shear Stress

Chapter 1: Thesis Overview

Chapter 1 introduces the importance of the work.

1.1 Background and significance

Varicose veins are a common venous disorder of the lower extremities, affecting approximately 25% of Western adults (Baliyan et al., 2016). Varicose veins (also called varix, varices, and varicosities) can occur in the main axial superficial vein, in the great saphenous vein, in the small saphenous vein, or in any other superficial vein (Campbell, 2006). Although the mechanisms behind its pathogenesis are not fully understood, the condition is most often associated with structural failures such as valve weakening and wall dilatation of the great saphenous vein, resulting in venous retrograde flow and venous hypertension (Goldman et al., 2017).

Varicose veins are generally treated in order to prevent venous stasis, reflux, hypertension and ulcers (Murad et al., 2011). The most common varicose vein treatment procedures include: (i) medical treatment; (ii) compression therapy, (iii) surgery; (iv) radiofrequency, (v) laser ablation and (vi) sclerotherapy.

Sclerotherapy has been employed to treat varicose veins for decades. This technique involves injection of a sclerosing agent, commonly into the vein lumen to cause inflammatory reaction, leading to venous shrinkage and to the development of new veins (Dietzek, 2007). Sclerosing agents are administered in either liquid or foamed form. The use of foam offers many benefits in the treatment of larger varicose veins. When the foam is injected into the vessel, it doesn't readily mix with blood; thus, foamed sclerosants are diluted less rapidly when compared to liquid sclerosants. This property allows a longer contact time between the sclerosing agent and the vessel wall, resulting in greater therapeutic efficacy (Goldman et al., 2017).

Since the first reports on foam sclerotherapy, multiple studies have been conducted to determine the physical properties and behavior of foams, but relatively little is known about their biological effects on the endothelial cells lining the vessel wall. This is often due to the lack of appropriate models and methods to quantitatively assess the biological and physical effects of sclerosing agents.

The most commonly used *in vitro* model is a monolayer of cells on a rigid substrate, which has been used in recent studies to investigate the microscopic effects of sclerosants. Most of these studies involve culturing of endothelial cells (ECs) over a plate, exposing cells to sclerosants, followed by staining with dyes to evaluate cell membrane lysis or cell death. Cell models typically used in these experiments are BAECs (bovine aortic endothelial cells) (Kobayashi et al., 2006), HUVECs (human umbilical vein endothelial cells) (Mol et al., 2007), and HMEC-1 (human microvascular endothelial cell line) (Parsi et al., 2008).

The use of *ex vivo* models has also been reported; in these studies, segments of vein are treated with sclerosing agents, and stained afterwards with dyes to evaluate damage to the vessel wall. *Ex vivo* models can thus be a reliable means to quantify and compare different treatments at the macroscopical level, within a physiologically relevant environment (Erkin et al., 2012; Orsini and Brotto, 2007; Kendler et al., 2013)

1.2 Organization of the thesis

Chapter 1 introduces the importance of the work and the thesis overview.

Chapter 2 is a literature review presenting an overview of the anatomy and structure of physiological veins in the lower limb. Afterwards, varicose vein pathophysiology is described, followed by methods of diagnosis and treatment. Among the different treatment methods, this Chapter specifically focuses on sclerotherapy. Finally, pre-clinical models of varicose veins are described and current limitations reviewed.

Chapter 3 outlines specific objectives of the study.

Chapter 4 describes the development of a 2D *in vitro* model to evaluate the therapeutic efficacy of liquid and foamed sclerosants. The model provides a 2D environment to investigate the effectiveness of liquid and foamed sclerosants. Part of this chapter has been published in:

In vitro and ex vivo evaluation of the biological performance of sclerosing foams.

E Bottaro, J Paterson, L. Quercia, X Zhang, M Hill, V. A. Patel, S. A. Jones, A. L. Lewis, T. M. Millar & D. Carugo Scientific reports 9 (1), 9880, 2019.

Chapter 5 describes the use of a quantitative fluorescence microscopy technique (i.e. spectral imaging) to measure changes in the physical properties of cell membrane interacting with liquid and foamed sclerosants.

Chapter 6 describes the development of *ex vivo* vein models to quantify sclerosant-induced disruption of the endothelial layer, through quantification of the extravasation of a probe molecule. Part of this chapter has been published in:

In vitro and ex vivo evaluation of the biological performance of sclerosing foams.

E Bottaro, J Paterson, L. Quercia, X Zhang, M Hill, V. A. Patel, S. A. Jones, A. L. Lewis, T. M. Millar & D. Carugo Scientific reports 9 (1), 9880, 2019.

Chapter 7 covers the development of more complex *in vitro* models, referred to as vein-on-a-chip. The chapter describes device manufacturing, followed by the design of an experimental set-up to quantify and compare the flow behaviour of different sclerosing foams. The method was employed to evaluate physical prosperities of foams, which were correlated to their biological performance. Part of this chapter has been published in:

Physical Vein Models to Quantify the Flow Performance of Sclerosing Foams.

E Bottaro, J Paterson, X Zhang, M Hill, V. A. Patel, S. A. Jones, A. L. Lewis, T. M. Millar & D. Carugo.Frontiers in bioengineering and biotechnology 7, 109, 2019.

Chapter 8 describes the development of a method to create channel networks within an hydrogel matrix in a facile, rapid and reproducible way, and using only natural hydrogels. The method was used for the production of both scaffold (i.e. extra-vascular compartment) and perfusable channel networks. Particular attention was devoted to the use of replica or sacrificial molding techniques to generate the scaffold.

Chapter 9 summarizes the final conclusions from the study, its limitations, and avenues for future research.

Appendix I reports the Python script employed for evaluating foam drainage time (refer to Chapter 4).

Appendix II reports the Python script employed for extracting the spectral stacks from the image sequences recorded during spectral imaging (refer to Chapter 5).

Appendix III reports the MATLAB® code employed for storing pressure data obtained from the pressure Transducer Harvard apparatus (refer to Chapter 7).

Chapter 2: Literature Review

Chapter 2 is a literature review presenting an overview of the anatomy and structure of physiological veins in the lower limb. Afterwards, varicose vein pathophysiology is described, followed by methods of diagnosis and treatment. Among the different treatment methods, this Chapter specifically focuses on sclerotherapy. Finally, pre-clinical models of varicose veins are described and current limitations reviewed.

2.1 Anatomy and structure of physiological veins

The venous system includes the network of blood vessels that work to deliver deoxygenated blood back to the heart. The anatomical classification of veins includes venules and veins. A venule is a small blood vessel in the microcirculation that allows deoxygenated blood to return from the capillary beds to the veins. Venules' diameter can range from 7 μm to 1 mm. Veins are blood vessels that carry blood from peripheral tissues and organs back to the heart (Genovese, 2002).

The vein's wall consists of concentric layers called *intima*, *media* and *adventitia* (from the innermost to the outermost). The vein diameter ranges in size from 1 mm to 1-1.5 cm (the average is 5 mm), and the average wall thickness is 0.5 mm (Goldman et al., 2017).

The *adventitia* is the outermost layer of the vascular wall, mostly containing collagen fibers, which has the function to anchor the blood vessel to the surrounding tissues. The *tunica media* is made of smooth muscle cells and elastic tissue. The *intima* is a thin monolayer of endothelial cells at the luminal surface, which lies on an *elastic lamina* located at the boundary with the tunica media (Mazurek et al., 2017). This layer sometimes contains bi-leaflet one-way valves. The luminal monolayer of endothelial cells acts as an interface between blood and nearby tissues (Figure 1).

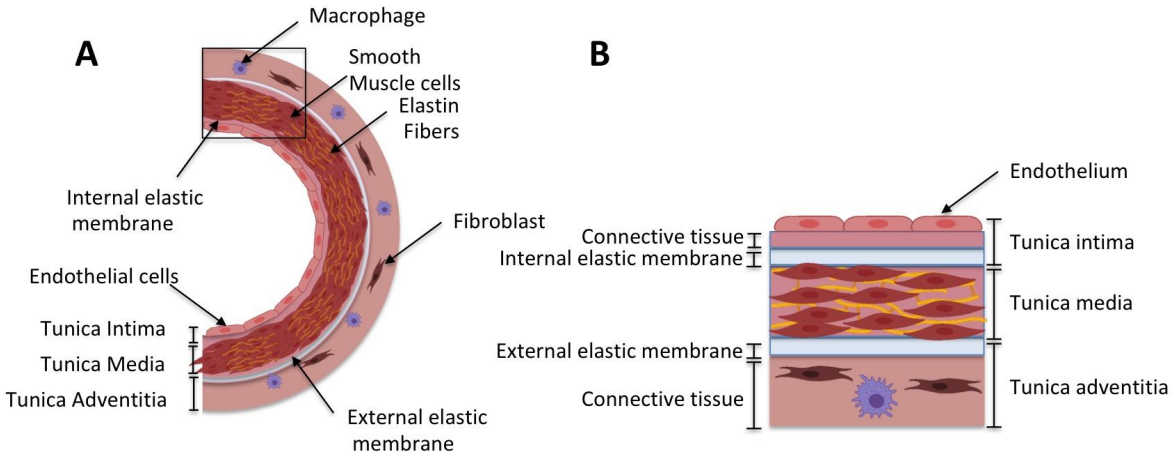

Figure 1. *Schematic showing the different layers composing the vein wall. (A) The vein wall is composed of three layers: tunica intima (endothelial cells), tunica media (vascular smooth muscle cells and elastin fibers), and tunica adventitia (fibroblast cells and macrophages). (B) Cross-sectional schematic section of the vein wall. The tunica adventitia includes connective tissue and external elastic membrane and the tunica intima includes the connective tissue, the internal elastic membrane and the endothelium.*

Vascular endothelial cells regulate important physiological properties and functions such as vascular permeability, angiogenesis (i.e. formation of new blood vessels), endothelial cell

migration, proliferation, and apoptosis, and pathological processes such as inflammation, thrombosis, and metastasis. ECs are exposed to various mechanical forces associated with blood flow, which include fluid shear, tensile and normal stress (Sumpio et al., 2002).

It is well know that these fluid forces induce changes in cell morphology, organization, migration and gene expression. The venous system of the lower limb comprises superficial, deep, and perforating veins (Genovese, 2002) (Figure 2).

Figure available from the following source: MP Goldman, JJ Guex, and RA Weiss, Sclerotherapy: treatment of varicose and telangiectatic leg veins, 5th edition, pp. 6. Copyright 2011).

Figure 2. *Cross-sectional schematic diagram of the venous anatomy of the leg, including the cutaneous/subcutaneous, superficial (saphenous), perforating, and deep venous systems. (source: MP Goldman, JJ Guex, and RA Weiss, Sclerotherapy: treatment of varicose and telangiectatic leg veins, 5th edition, pp. 6. Copyright 2011).*

The superficial venous system is further classified in thin-walled collecting veins (tributary veins) and thick-walled truncal veins, such as the great saphenous vein (GSV) and short saphenous vein (SSV). The GSV usually has at least 6 valves and the SSV has an average of 7 to 10 valves. The deep venous system includes the plantar vein, the paired peroneal, anterior and posterior tibial veins. The perforating veins connect the superficial and deep venous systems (Kendler et al., 2013) (Figure 3).

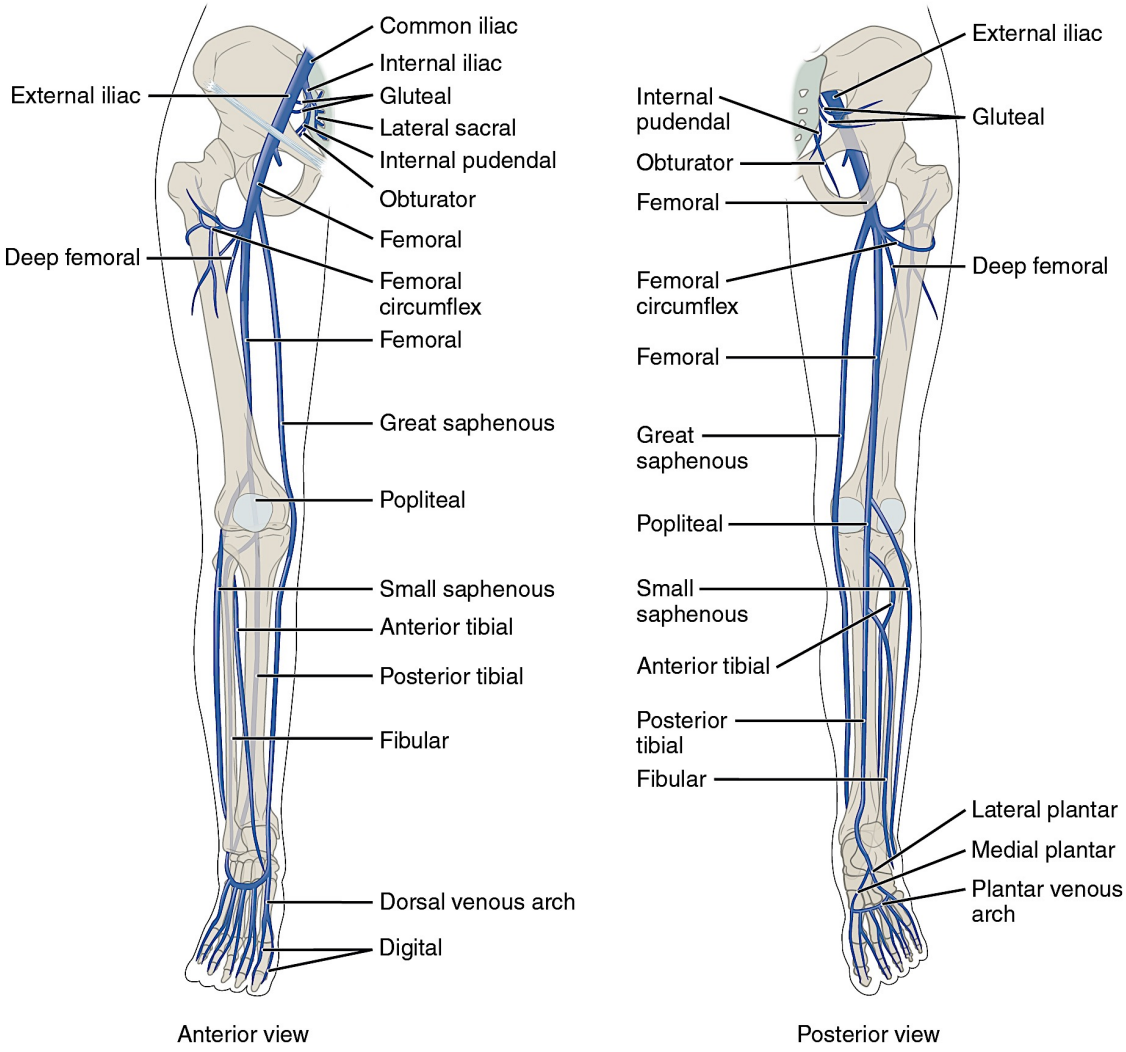

***Figure 3**. Anterior and posterior views of the venous system of the lower limb. The superficial venous system comprises the great saphenous vein (GSV) and saphenous vein (SV) (source: https://opentextbc.ca/anatomyandphysiology/chapter/20-5-circulatory-pathways/).*

The primary venous function is to carry blood towards the right heart, taking advantage of its volume capacity. Other primary important functions are tissue drainage, thermal regulation, and blood storage. Blood flow in the lower extremity is controlled by the calf muscle pump, the venous valves and the perforating veins. Venous bicuspid valves play a critical role in the prevention of pathological blood reflux (Baliyan et al., 2016) (Figure 4).

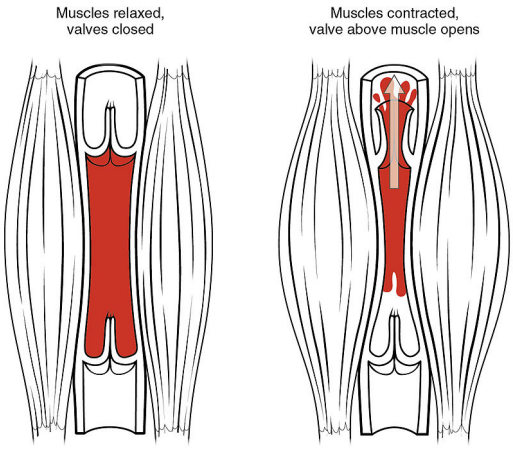

Figure 4. *Mechanism of action of the vein valve. The return of blood to the heart is assisted by the action of the muscle pump; notably, the vein valve opens upstream the contracting muscle and it closes downstream the contracting muscle (source: https://en.wikipedia.org/wiki/Skeletal-muscle_pump#/media/File:2114_Skeletal_Muscle_Vein_Pump.jpg).*

They are composed of a thin layer of collagen and a variable amount of smooth muscle, covered by endothelium. The muscle and collagen fibers are present in the base, whereas elastic fibers extend along the whole length of the cusp and close to the endothelium.

The valve cusp changes with age becoming thicker and less flexible; these changes may cause abnormal blood flow and eventually lead to valvular incompetence. The vein wall composition varies with the type and location of the vein. Depending on their location, veins may have different functions, and this is reflected in the muscular content of the vein wall. Being at the same time blood pumps and reservoirs, the vein walls need to withstand variations in gravitational and intravascular pressure. The percentage of smooth muscle increases in the veins with distal locations; notably, veins in the lower extremities are composed of more than 40% of smooth muscle (Goldman et al., 2017).

The function of collagen in the vein wall is to prevent over-distention, whereas elastin governs elastic recoil. With advancing age, multiple changes may occur in the vessel wall; the intima thickens, the elastic fibers increase in number and become more disoriented, and the adventitia becomes increasingly fibrous. These changes may increase the susceptibility of the vein walls to pressure-induced distention.

2.2 Lower extremity venous disorders and varicose veins

Lower extremity venous diseases are a worldwide health problem, with a significant cost for healthcare providers. Venous incompetence in the lower limb is a common disease. Changes

in hemodynamic forces such as shear stress and static pressure may cause remodelling of the vein wall and venous valves, leading to various venous pathologies, including telangiectasias (i.e spider veins), reticular veins, and varicose veins (Chiu and Chien, 2011).

Varicose veins are a common venous disorder of the lower extremities, affecting approximately 25% of Western adults (Krijnen et al., 1997). Varicose veins (also called varix, varices, and varicosities) can occur in the main axial superficial vein, in the great saphenous vein, in the small saphenous vein, or in any other superficial vein tributaries of the lower limbs. Varicose veins appear tortuous and swollen and are often easily detectable (Figure 5). Unilateral swelling of a leg with big varicose veins is the most typical presentation (Meissner, 2005).

Figure available from the following source: MP Goldman, JJ Guex, and RA Weiss, Sclerotherapy: treatment of varicose and telangiectatic leg veins, 5th edition, pp. 6. Copyright 2011).

Figure 5. *Example of varicose vein appearance. (A) Lateral aspect of varicose veins and (B) posterior aspect of varicose veins before treatment (source: Goldman, M.P., Weiss, R.A., and Guex, J.-J. (2017). Sclerotherapy: treatment of varicose and telangiectatic leg veins).*

Varicose veins have long been considered a cosmetic problem but frequently, if untreated, they may lead to more advanced form of chronic venous dysfunction such as chronic venous insufficiency (CVI). They may cause discomfort, pain, disability, and an overall reduction of a patient's quality of life (QOL). Although the mechanisms behind its pathogenesis are not fully understood, the condition is most often associated with structural failures such as valve weakening and wall dilatation of the great saphenous vein, resulting in venous retrograde flow and venous hypertension (Figure 6).

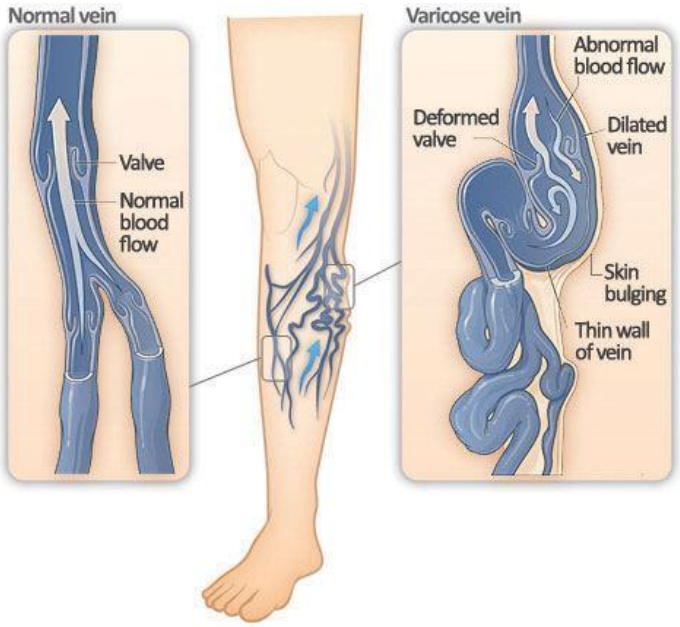

Figure 6. *Schematic representation of a physiological and varicose vein. In varicose veins the valve is deformed and incompetent, causing an abnormal retrograde blood flow. Generally, varicose vein appear swollen and enlarged (source: https://en.wikipedia.org/wiki/Varicose_veins).*

Most varicose veins are mainly caused by primary venous disease although the etiology can also be multifactorial. Varicosities can also develop as a result of secondary causes, such as untreated deep vein thrombosis (DVT), deep venous obstruction, superficial thrombophlebitis, or arteriovenous fistula. Epidemiological studies have shown that varicose veins have hereditary nature. In addition, various risk factors are also involved such as prolonged standing, obesity, and pregnancy (Surendran et al., 2016).

Varicose vein symptoms commonly present as heaviness, swelling, aching, restless legs, cramps, itching, and tingling (Bradbury et al., 1999). The diagnosis of varicosities is carried out *via* clinical examination of the lower limbs, which consists of an inspection and palpation of the visible varicose veins. In addition, ankle mobility is examined, because patients with severe venous disorder frequently experience reduced mobility in the ankle joints. Afterwards, duplex ultrasound scanning of the deep and superficial veins is performed. This diagnostic test allows the visualization and measurement of the vein compressibility, venous flow and duration.

2.3 Pathophysiology of varicose veins

Approximately 60% of the body's total blood volume is contained within the peripheral venous system. Venous blood pressure is determined by numerous factors such as the pressure generated by the heart, the hydrostatic gravitational forces, the blood volume, the vein wall

composition/mechanics and venous valve's efficiency (Campbell, 2006).

Chronic venous hypertension in the lower limb causes an expansion of the venous diameter. This may lead to valvular insufficiency, which usually causes a backward blood flow. Pathologic development of varicose veins can be divided into four main categories: (i) increased deep venous pressure, (ii) primary valvular incompetence, (iii) secondary valvular incompetence, and (iv) hereditary factors. All of these categories coexist and are influenced by temperature, alcohol consumption, hormonal and other vasodilatory stimuli (Goldman et al., 2017).

An increase in deep venous pressure may be of proximal or distal origin. Proximal causes include pelvic obstruction, saphenofemoral incompetence, and intraluminal venous obstruction. Distal causes include perforating vein valvular incompetence, arteriovenous anastomosis, and intraluminal venous obstruction.

Pelvic obstruction is an uncommon cause of varicose veins. Saphenofemoral junction (SFJ) incompetence is generally caused by pathological damage in the valves. Incompetence of the SFJ clearly produces distal retrograde flow into the GSV, and thus causes distal venous hypertension. The GSV then expands, causing further distal valvular incompetence and retrograde flow (Cooper et al., 2003). This causes hypertrophy and dilation of the superficial veins.

Generally, perforating vein valvular incompetence is caused by direct valve destruction after venous thrombosis. Another important factor that may lead to increased venous pressure in cutaneous veins is the opening of arteriovenous communications, also known as arteriovenous anastomoses (AVAs). Opening of the AVA may occur through abnormalities of vasa vasorum (i.e a network of small blood vessels of the venous wall) or it may occur due to proximal venous hypertension, which causes the rapture of the capillary barrier. However, whether AVAs are the direct cause of varicose veins is still not clear (Gius, 1960).

Primary and secondary valvular incompetence are serious contributor factors of varicose veins. Primary valvular incompetence might be caused by a pre-existing weakness of the vessel wall or valve leaflet, while secondary valvular incompetence might be caused by direct damage (e.g., as result of DVT).

Other predisposing factors might increase the risk of development of varicose veins such as gender, age, hereditary factors, obesity, and lifestyle (Chiu and Chien, 2011).

2.4 Diagnosis

Before treatment is performed, clinicians must investigate the patient's history and perform a

physical examination of the patient, including vein inspection and palpation, followed by a confirmatory diagnostic test.

The CEAP classification for chronic venous disease was introduced in 1994 at the American Venous Forum. A table for classifying the clinical levels of venous insufficiency has been proposed, which includes four categories and descriptors such as: clinical manifestations (C), etiology (E), anatomy (A) and underlying pathophysiology (P). The CEAP classification has been endorsed worldwide, despite its acknowledged deficiencies (Table 1). It has been adopted as the standard in many clinics in Europe, Asia, South America and the United States for categorizing chronic venous disorders, guiding treatment decisions, and predicting prognosis. It was revised in 2004 and is now referred to as *advanced CEAP* (Eklöf et al., 2004).

Table 1. CEAP classification

Clinical Manifestations (C)	Etiology (E)	Anatomy (A)	Pathophysiology (P)
C0: No visible or palpable signs of venous disease.	**Ec:**congenital (usually present at birth).	**As:**Superficial veins.	**Pr:** Reflux.
C1: Telangiectatic and reticular veins.	**Ep:**primary (degenerative, typically varicose veins)	**Ap:**Perforator veins	**Po:** Obstruction
C2: Varicose veins	**Es:**secondary (as in post thrombotic syndrome).		**Pr,o:** Reflux and obstruction.
C3: Edema	**En**:no venous etiology identified.		**Pn:** No venous pathophysiology identifiable.
C4a: Pigmentation and/or eczema. C4b: Lipodermatosclerosis and/or atrophie blanche.			
C5: Healed ulcer.			
C6: Active ulcer.			

2.5 Varicose vein treatment

Varicose veins are generally treated in order to prevent venous stasis, reflux, hypertension and ulcers (Murad et al., 2011). There are different varicose vein treatment procedures, including: (i) pharmaceutical treatment, (ii) compression therapy, (iii) surgery, (iv) radiofrequency, (v) laser ablation and (vi) sclerotherapy (Gloviczki et al., 2011; Brittenden et al., 2014; Piazza, 2014).

2.5.1 Pharmaceutical therapy

Venoactive drugs have been proposed for the treatment of varicosities. The most commonly employed are saponins (aescin), gamma-benzopyrenes (rutosides, diosmin, and hesperidin), and the micronized purified flavonoid fraction (MPFF). The active mechanism of these compounds is the improvement of the venous tone and capillary permeability, although the precise mechanism of action is mostly unknown. Generally, in addition to these drugs, compression therapy is suggested (Gloviczki et al., 2011).

2.5.2 Compression therapy

Compression therapy is a clinically effective means to improve venous hemodynamics and reduce edema in patients with chronic venous disease, and it is recommended as the first therapeutic modality. It is also used as adjuvant treatment to superficial vein ablation and sclerotherapy to prevent ulcer recurrence (Sell et al., 2014). Compression therapy involves the use of elastic compression stockings, paste gauze boots, multilayer elastic wraps, dressings, elastic and non-elastic bandages, and non-elastic garments (Huang et al., 2013).

2.5.3 Surgery

Open surgical treatment of varicose veins has been employed as a standard treatment for decades (Ombrellino and Kabnick, 2005). The traditional procedure consisted of an incision at the level of the deep fascia, followed by ligation of the saphenous junction, and a more or less extensive resection of the saphenous vein and of diseased tributaries. The original method of stripping (removal of a long vein segment) has been changed over time, by using different devices and developing alternative techniques. Generally, open surgical treatment consists of saphenofemoral ligation of the GSV at its confluence with the common femoral vein, and stripping of the long saphenous vein carried out under anesthesia (Kendler et al., 2012). In recent years, this technique has been improved becoming less invasive and is performed under local tumescent anesthesia in many cases, such as in the perforation-invagination (PIN) strippers' technique (Kent et al., 1999).

Afterwards, in order to reduce formation of hematoma, pain and swelling, it is recommended that postoperative compression therapy is maintained for at least 1 week (Goldman et al., 2017).

2.5.4 Radiofrequency and laser ablation

Recently, endovenous thermal ablation (i.e., in the form of laser and radiofrequency ablation) has been introduced as an alternative to surgical approaches. Both techniques involve the insertion of a catheter or fiber into the lumen of the saphenous vein (from knee level to the groin) under ultrasound guidance, followed by ablation of the vein in sections.

With respect to laser ablation, a laser generator emits monochromatic light, which is transmitted to the tip of the fiber and is converted into thermal energy (Liu et al., 2016); whereas in the case of radiofrequency ablation a generator produces an electrical current that is delivered at the tip of a catheter (Poder et al., 2018). These techniques present several benefits compared to surgery, such as reduction of bruising and discomfort, and a quicker recovery. The outcome results are variable and some studies reported less neovascularisation compared to the surgical approach.

2.5.5 Sclerotherapy

Sclerotherapy has been employed to treat varicose veins for decades. In the 1968 Hobbs was the first to demonstrate the effectiveness of sclerotherapy compared with surgery (Smith, 2009).

This technique involves injection of a sclerosing agent, commonly into the vein lumen to cause inflammatory reaction, leading to venous shrinkage and to the development of new veins (Dietzek, 2007). Liquid sclerotherapy has been widely used for obliteration of spider veins or telangiectasia until the 1995, when Cabrera and colleagues for the first time produced foam by mixing a gas with the detergent polidocanol. Both liquid and foam sclerotherapy are currently widely used throughout the world.

The aim of the current study is to investigate the mechanisms of action and effectiveness of sclerotherapy; therefore, among the several techniques currently employed for the treatment of varicose veins, this thesis will focus primarily on sclerotherapy from herein.

2.6 Liquid and Foam Sclerotherapy

Sclerosing agents are administered in either liquid or foamed form. Prior to administration, the sclerosing agent is usually diluted in order to obtain the desired concentration, based on the size of the vein that should be treated. Generally, the recommended volumetric concentrations of sodium tetradecyl sulphate STS and polidocanol (POL) are 0.5-3% and 1-3%, respectively, for the treatment of larger veins (from 3 to 8 mm in diameter). Liquid

sclerotherapy is performed by injecting the sclerosing solution using a small syringe, and a 30 or 25 Gauge needle (Gloviczki et al., 2011). The number of injections performed in a clinical session typically does not exceed 10-20. The standard procedure includes the following steps: (i) placing of gauze pads on the injection sites, (ii) positioning the patient supine with the leg elevated, (iii) injection of the sclerosant and (iii) performing compression therapy after treatment (Smith, 2009).

Foam sclerotherapy is a modification of liquid sclerotherapy, in which the liquid sclerosant is converted into foam by mixing it with air or other gases, such as oxygen and carbon dioxide (or mixtures of the two). Many studies demonstrated that foam sclerotherapy increases the effectiveness of sclerosants because of foam's ability to distribute widely through the vein, displacing the blood aside, thus prolonging the time of contact between the sclerosing agent and the vessel wall (Figure 7).

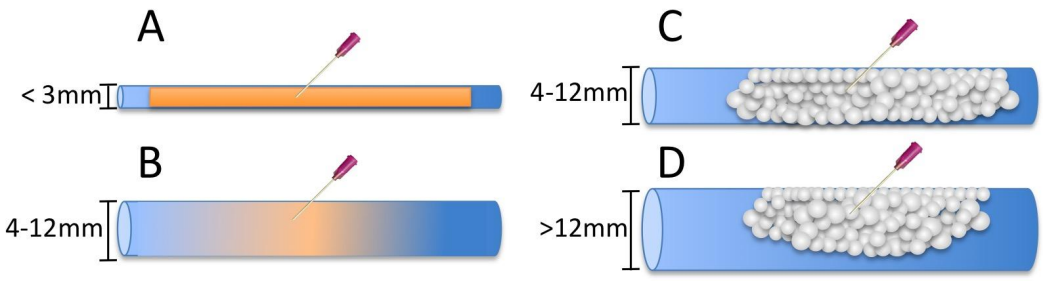

Figure 7. *Theoretical modeling of dilution of liquid or foamed sclerosing agents. (A) In veins with a diameter smaller than 3 mm, after injection, liquid sclerosants do not mix with blood. (B) In veins with a diameter between 4 mm to 12 mm, liquid sclerosant is diluted with blood and the endothelium disruption occurs only near the injection site. (C) In veins with a diameter between 4 mm to 12 mm, foamed sclerosants fills up the vein and the endothelium disruption occurs homogeneously. (D) In larger veins (>12mm), foam floats so its action is limited to the superficial wall.*

Foam sclerotherapy is an effective, safe, and minimally invasive endovenous treatment for varicose veins with a low rate of complications reported. In addition, foam based treatments require a lower concentration of sclerosant, which is beneficial for reducing side effects (Goldman et al., 2017). For these reasons, foam sclerotherapy is gaining more popularity among both patients and clinicians, becoming one of the most common treatments for varicose veins.

The most commonly used technique for generating sclerosing foams was developed by Tessari *et al.* using a three-way stopcock connecting two syringes (Tessari et al., 2001). The liquid-to-

gas ratio employed has a remarkable role in the chemical–physical properties of the foam; indeed, a 1:6 ratio produces dry foams, whereas a 1:3 ratio produces wet foams (Cavezzi and Tessari, 2009). However, the optimum liquid-to-gas ratio, in terms of foam stability is 1:4, as reported in recent publications (Wollmann, 2010). The foam is formed by rapidly mixing the gas with the liquid sclerosant from one syringe into the other (i.e., repeating the process from 10 to 20 times). The double syringe system (DSS) method was later introduced, which involves passing the sclerosant liquid and gas between two syringes joined by a simple straight connector (Rao and Goldman, 2005). Foams produced using these two methods are also referred to as physician compounded foams (PCFs). Recently, an automated method for polidocanol foam production has also been introduced (and approved by the FDA); this is referred to as polidocanol endovenous microfoam (PEM) or Varithena®. The automatic system contains the liquid agent (1% polidocanol) and a gas mixture of oxygen:carbon dioxide (65:35 ratio, respectively) with a low-nitrogen content (<0.8%) (Eckmann, 2009). The foam produced is cohesive with a uniform median bubble diameter of <100 μm, and no bubbles with a diameter >500 μm (Carugo et al., 2016).

Foam sclerotherapy is performed by injecting the foam (maximum 20 mL per session) into the vein, using a small syringe and a 30 or 25 gauge needle or a cannula (Cavezzi and Tessari, 2009). The foam is thus administered following the same procedure reported for liquid sclerosants.

The incidence of severe complications after foam sclerotherapy, such as anaphylactic reaction, pulmonary emboli, stroke, thromboembolism and large areas of skin necrosis, are very rare (<0.01% of cases). Visual disturbances have been reported, particularly in individuals with migraine. In 2010, a stroke after injection of an unusually large volume of foam has been observed (DeLaney et al., 2010). The most common side effects reported are matting, pigmentation, pain, allergy, and skin urticarial, which are also correlated with the dosage of the sclerosing agent (Gloviczki et al., 2011).

Duplex ultrasonography is used to guide the injection in a selected vessel, and to monitor the distribution of sclerosant through the veins.

The mechanisms of action are disruption of the endothelium, exposure of sub-endothelial collagen fibers, and formation of a fibrotic obstruction. Sclerosing agents can be classified in (i) osmotic agents, (ii) detergents and (iii) alcohol-based agents (Goldman et al., 2017).

2.6.1 Osmotic agents

Osmotic agents are employed to treat small varicose veins. The mechanism of action is dehydration of endothelial cells through osmosis that causes cell death. The most common osmotic agent employed is sodium chloride at the concentration of 23.4%, but there are other commercial forms available. In these treatments, patients may experience burning during injection, and skin ulcers and tissue necrosis may occur (Worthington-Kirsch, 2005).

2.6.2 Detergents

Detergents are employed for the treatment of all varicosities. The mechanism of action is destruction of the endothelium by lysis of cell membrane proteins. The most used detergents are sodium tetradecyl sulphate (STS) and polidocanol (POL) (Figure 8).

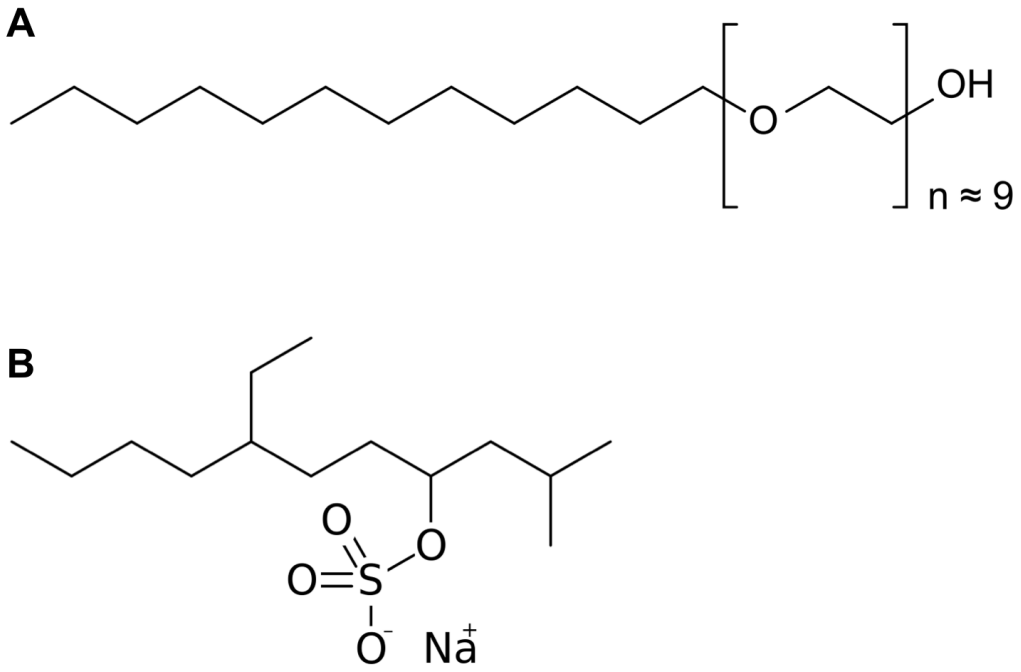

Figure 8. *Chemical structure of polidocanol (A) and STS (B).*

STS is a long-chain fatty alcohol. A critical micellar concentration (i.e. concentration of surfactants above which micelles form) is required in order to destroy the endothelial cells, and repeated treatments are frequently necessary. The injection is safe and painless, but higher concentrations may cause extravasation of the sclerosant, resulting in tissue necrosis (Yiannakopoulou, 2016). Other side effects reported are hyperpigmentation, matting, and

allergic reactions. This detergent is used also in a foamed form, which allows reducing the therapeutic concentration required and achieves longer contact time between the bioactive detergent and the endothelium (Gillet et al., 2009).

Polidocanol is a synthetic long-chain fatty alcohol and is the most commonly used detergent in Sclerotherapy, to treat varicose veins in the lower limbs (Alòs et al., 2006). The injection is safe and painless with low risk of tissue necrosis when used at low concentration. Side effects include hyperpigmentation, with only very few cases of allergic or anaphylactic reaction (Gillet et al., 2009).

Sodium morrhuate is a detergent obtained by the mixture of saturated and unsaturated fatty acids. It is used less frequently compared to other detergents, because it can cause extensive cutaneous necrosis upon extravasation, and higher risk of anaphylactic reaction has been observed (Albanese and Kondo, 2010).

2.6.3 Alcohol agents

Alcohol agents are weak sclerosants used for the treatment of small varicosities or telangiectasia. The most commonly used is glycerin, a chemical able to bind to the endothelium surface, causing endothelial cell death. The alcohol solution most frequently employed contains chromated glycerin, benzyl alcohol and sterile water mixed with 1% lidocaine and epinephrine. It is safe and rarely leads to tissue necrosis, hyperpigmentation, or allergy, although it may cause hematuria when used at higher concentration (Goldman et al., 2017).

2.7 Pre-clinical models of varicose veins

The main purpose of pre-clinical studies is to select drug candidates with potential therapeutic activity, ensuring that they satisfy all the safety and therapeutic regulatory requirements prior to human clinical trials. Preclinical testing involves *in vitro* analyses using appropriate cell line models, as well as *in vivo* studies in relevant animal models with the aim of determining toxicity, pharmacokinetics, and pharmacological effects. Indeed, the pre-clinical study of a single compound can take many years to be completed and the overall process may cost billions of pounds, considering man-hours, ethics licensing, facilities, and equipment (Raven, 2012). For these reasons, the success rate of new drug candidates is relatively low (DiMasi et al., 2010).

In the last decades, review and refinement of standard methods for animal testing has been investigated by industries and academic researcher (Michael Balls, 2010)(Denayer et al., 2014), nevertheless animal models remain a regulatory requirement, even if they often don't accurately mimic the complexities of human physiology or diseases (Mak et al., 2014).

With respect to venous diseases, various animal models have been researched, with murine models being the most commonly used in pre-clinical studies (Diaz Jose A. et al., 2019). Mice provide a unique biological environment to study disease progression and treatment in a highly controlled manner, with the added availability of genetically manipulated strains to uncover molecular pathways. The advantages of *in vivo* models are the presence of surrounding anatomical strictures, blood flow and pressure. Additionally, the evaluation can be carried out at different time points and adverse reactions can been evaluated (Denayer et al., 2014).

In recent studies, several models have been proposed for venous disease, which can be categorized into four main groups, utilizing (i) vessel occlusion/obstruction, (ii) valvular incompetence, (iii) augmented hemodymamics, or (iv) a combination of these models (Dalsing et al., 1998; Pascarella et al., 2005). However, all the reported cases are not able to fully reproduce superficial varicose veins.

Superficial varicose veins do not form spontaneously in lower animals and this might represent a considerable barrier in the development of varicose vein treatments. Jones *et al.* developed a method to induce superficial varicose veins in pigs; the resulting varicose vein presented similar characteristics to the human varicose vein such as intimal thickening, fibrosis, and chronic valvular degeneration (Jones et al., 2009).

On the other hand, in addition to the ethical concerns, animal models present several disadvantages, such as the need for skilled personnel, time-consuming protocols, and high associated costs (Doke and Dhawale, 2015). It is therefore necessary to improve *in vitro* cell-based models for a more accurate prediction of sclerosing agents' efficacy and toxicity. In recent years, several alternatives to animal model testing have been proposed such as 2D and 3D in vitro models (Figure 9).

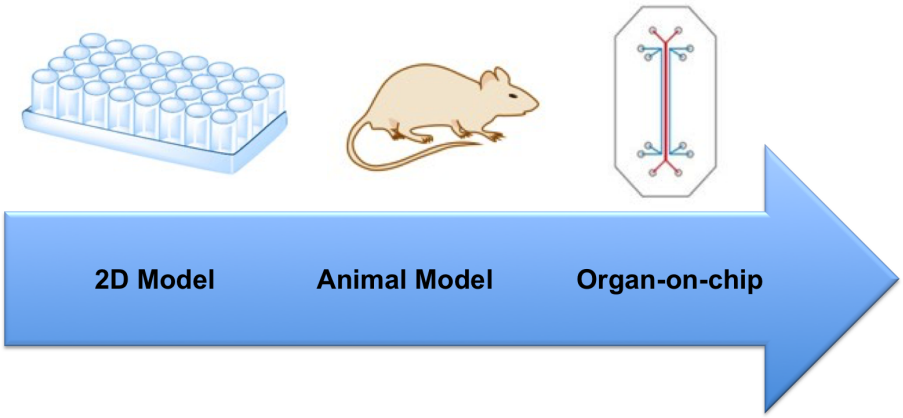

Figure 9. *Examples of models for drug testing, including 2D in vitro models, animal models and the recently developed organ-on-chip devices (the representative device reported here has been developed at Harvard University).*

Besides the major advantage of a reduction in animal use, these methods provide additional benefits, such as time efficiency, tight control in experimental conditions and standardization, requirement of less manpower, and lower costs (Doke and Dhawale, 2015).

The most commonly used *in vitro* model is a monolayer of cells on a rigid substrate. In recent studies, few *in vitro* models have been proposed to investigate the microscopic effects of sclerosants. Most of these studies involve culturing of ECs over a plate, exposing cells to sclerosants, followed by staining with dyes to evaluate cell membrane lysis or cell death. Generally, the cells employed are BAECs (bovine aortic endothelial cells)(Kobayashi et al., 2006), HUVECs (human umbilical vein endothelial cells) (Mol et al., 2007) and HMEC-1 (human microvascular endothelial cell line) (Parsi et al., 2008).

In pre-clinical research, although two-dimensional (2D) models have made significant contributions to biological and pharmacological research, they also present well-known limitations, which have led to the development of three-dimensional (3D) models. Compared to 2D models, 3D models can provide a cellular microenvironment that more closely mimics native tissues. For instance, they can reproduce (i) intercellular signals (Ohkubo et al., 2018), (ii) the presence of soluble factors in the interstitial fluid, (iii) cell-cell or cell-extracellular matrix (ECM) adhesion (Baker et al., 2013), and (iv) mechanical stimuli (Polacheck et al., 2013). These factors have a great influence on cell morphology motility, proliferation, differentiation (Rangamani et al., 2013), and apoptosis (Elmore, 2007). 2D models do not include these fundamental factors, and this may lead to the selection of drug candidates that are not effective *in vivo*.

The most commonly employed 3D model in sclerotherapy research is the *ex vivo* vein model

(Erkin et al., 2012; Orsini and Brotto, 2007; Whiteley et al., 2017)
In most studies, segments of vein are treated with sclerosing agents, and stained afterwards with dyes to evaluate damage to the vessel wall. *Ex vivo* models can thus be a reliable means to quantify and compare different treatments at the macroscopical level, within a physiologically relevant environment. The major limitation of earlier *ex vivo* studies is the limited investigation of the physico-chemical effects of blood on sclerosant's efficacy. Additionally, from the removal of the vein segment to the test, ischemic or hypoxic events may occur.

Nonetheless, both techniques present limitations: (i) cells are not exposed to physiological mechanical cues, including fluid shear stress, tension and compression, and (ii) the absence of complex interactions between different types of cells, which are mediated by various gradients of soluble and insoluble factors such as cytokines, nutrients, growth factors, and hormones (Billiet et al., 2012).

Advances in tissue engineering have enabled rapid development of *in vitro* 3D models for mimicking physiological tissues and organs (Kimlin et al., 2013) (i.e., liver, breast, cardiovascular, muscles, bone) and pathological conditions (i.e., tumours) (Bhadriraju and Chen, 2002). In general, there are two types of 3D culture methods: scaffold (Hutmacher and Cool, 2007) and scaffold-free techniques (Norotte et al., 2009; Napolitano et al., 2007). The first refers to the use of exogenous biocompatible structures, in which cells can be seeded to resemble native tissues with structural and physiological properties (Deligkaris et al., 2010). The second refers to any platform that does not require cell seeding or adherence within an exogenous, three-dimensional material (DuRaine et al., 2015).

In the recent years, researchers have developed 3D micro-engineered cell culture models, often referred to as 'Organs-on-a-Chip' (Esch et al., 2015). These miniaturised devices contain perfusable channels and chambers lined with different types of cells, recapitulating the complex microenvironment and physiological functionality of living human organs (Huh et al., 2011).

Organs-on-a-chip provide a new model to study human physiology in an organ-specific context, and to develop specialized *in vitro* disease models, overcoming the technical, economic and ethical issues associated with other approaches. Hence, microfluidics can be

employed to co-culture different cells in 3D-structures, generate different forms of mechanical stress, and create growth factor gradients in a continuous-flow environment. Culture conditions, cell seeding, and microchannel geometry can be optimized for creating robust, predictive tools for drug discovery and development (Gómez-Sjöberg et al., 2007).

These devices are usually fabricated using traditional microfabrication techniques, providing a high level of precision and control in the fabrication process. Typically, replica molding based on soft lithography is used to produce the microfluidic devices (Qin et al., 2010; Anderson et al., 2000) (Figure 10). The most common material employed is polydimethylsiloxane (PDMS), a silicone-based polymer that is biocompatible, oxygen-permeable, and optically transparent (Mata et al., 2005).

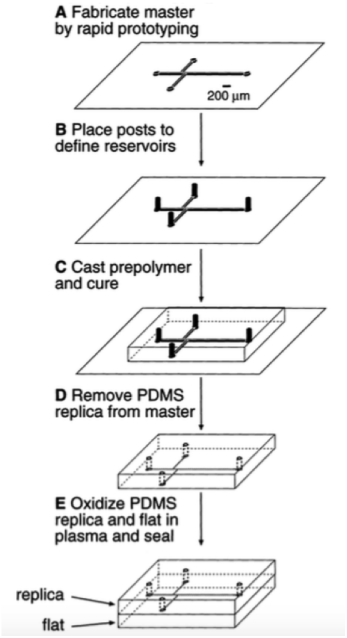

***Figure 10**. Scheme describing the replica molding process based on soft lithography technique. The device reported was made of PDMS. (a) The high-resolution master containing the design of the channels was used as the mask in photolithography to produce a positive relief of photoresist on a silicon wafer (b) Posts were placed on the wafer in order to make reservoirs for the reagents. (c) The PDMS was poured onto the silicon wafer and let to cure at 65 °C for 1 h. (d) The PDMS negative mold was peeled off from the silicon wafer. (E) Plasma oxidation treatment was employed to permanently bond the PDMS mold and a flat slab of PDMS (source: Anderson, J. R., Chiu, D. T., Wu, H., Schueller, O. J. & Whitesides, G. M. Fabrication of microfluidic systems in poly (dimethylsiloxane). Electrophoresis 21, 27–40, 2000).*

Thus organ-on-a-chip devices have significant advantages over other 2D models: (i) greater flexibility in the design, and superior standardization of the fabrication process; (ii) precise control over the experimental conditions; (iii) *in situ* monitoring of biological processes *via* coupling with microscopes, and (iv) reduction of the amount chemicals/reagents employed.

Although animal models can emulate the physiological complexity of whole organisms, they have demonstrated a poor predictive correlation between animal and human outcomes when employed to model human diseases, due to substantial interspecies differences.

Nowadays, this emerging technology has gained significant interest among researchers and some organ-on-a-chip platforms such liver (Bhise et al., 2016), lung (Jain et al., 2018) and gut (Maschmeyer et al., 2015) have been developed (Figure 11). The research in this thesis specifically focuses on the use of microfluidic techniques to produce vascular models, which have unquestionable biomedical relevance because of their involvement in the progression of major diseases.

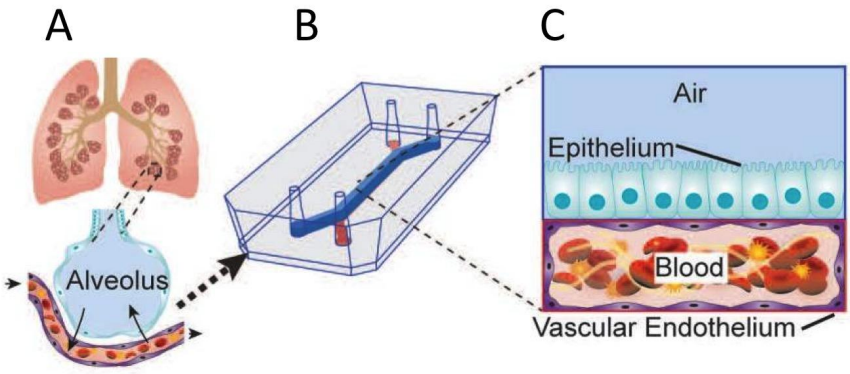

Figure 11*. Schematic of lung alveolus-on-a-chip. (A) Schematic of the human lung showing that the alveoli interact with the neighboring blood vessels during hemostasis or pulmonary dysfunction. (B) Drawing of the PDMS microfluidic device containing two compartments separated by a thin porous membrane that replicates the microarchitecture of the alveolar-capillary interface. (C) Schematic illustration showing the top compartment (1 mm wide and 1 mm tall) cultured with human primary alveolar epithelial cells, and the entire bottom chamber (1 mm wide and 250 μm tall) lined with human endothelial cells. Whole blood is perfused through the bottom chamber and thrombus formation is visualized using fluorescence microscopy from the bottom (figure adapted from the source: Jain et al., 2018. Primary Human Lung Alveolus-on-a-chip Model of Intravascular Thrombosis for Assessment of Therapeutics. Clin. Pharmacol. Ther. 103, 332–340).*

The major challenge in *in vitro* modeling is mimicking the complex multi-scaled branching structure of a functional vascular network. Microfabrication techniques allow the construction of biomimetic vasculature channels, which cannot be recapitulated using current *in vitro* systems. Microfabrication techniques include soft- and photo-lithography (Qin et al., 2010), laser ablation (Gómez-Sjöberg et al., 2007) and more recently new methods such as bioprinting (Murphy and Atala, 2014), needle-casting (Buchanan et al., 2013) and sacrificial

templating (Wang et al., 2009) approaches. With respect to the first two methods, microdevices are commonly made from plastic or silicon-based (i.e., PDMS) materials (Choi et al., 2013); whereas in the last three methods they are made from hydrogels (Li et al., 2012). Although PDMS-based microdevices have allowed significant progress in the development of physiologically relevant models of the vascular system, the material and surface properties of PDMS do not represent the ones of native ECM. Therefore, hydrogel-based microfluidics is gaining interest as an alternative method for producing models that more closely mimic the *in vivo* microenvironment.

Nonetheless, being a relatively recent technology, further efforts need to be put in place in order to be able to (i) fabricate capillary-sized channels (i.e., due to the resolution of current bio-printers); (ii) standardize the fabrication techniques; and (iii) produce complex vascular networks. Therefore, hydrogel-based microdevices often present simpler architectures and the production process is frequently more complex in comparison to PDMS-based methods. For these reasons, PDMS microdevices are commonly employed to characterize the effects of mechanical stimuli on ECs (Booth et al., 2014; Hattori et al., 2014) whereas hydrogel-based devices are the preferred option for performing permeability assays (Yang et al., 2016). A more effective integration between microfabrication techniques and tissue engineering methods is therefore needed in order to obtain more realistic vascular models, where physiologically relevant geometrical/mechanical characteristics are combined with biochemical/biophysical properties.

Vasculature-on-a-chip devices have greatly advanced our knowledge about vascular system functions under both physiological and pathological conditions. Microdevices typically consist of microchannels lined with endothelial cells, recapitulating key vascular properties such as dimensional scale, the 3D structure, and physiologically relevant haemodynamic parameters. Areas of application for these devices include the study of (i) morphogenesis of ECs and the regulation of angiogenesis (Song and Munn, 2011); (ii) haemodynamics and the effect of shear stress on EC morphology and function (Song et al., 2012); (iii) regulation of vascular permeability (Zanotelli et al., 2016); (iv) pathological conditions such as tumor vasculature and thrombosis (Chrobak et al., 2006); and (v) the production of vascular systems for tissue engineering and organ-on-chip constructs (Westein et al., 2013).

Vascular models found in the literature are mainly recreating smaller vessel (50 and 400 μm) (Chrobak et al., 2006; Westein et al., 2013) and no vein models have been proposed yet. The

advantages of this technology could be applied for evaluating venous diseases, where the blood flow and vessel architecture are relevant factors that influence therapeutic effectiveness. Additionally, the technology allows creating complex vascular geometries and therefore might be employed for modeling venous abnormalities, particularly those present in varicose veins.

Chapter 3: Aim and Objectives

Chapter 3 outlines specific objectives of the study.

3.1 Research Gaps and scope of the work

The work in this thesis concerns the development of robust per-clinical models to quantify the effects of sclerotherapy, compare different treatment methods, and to obtain a greater understanding of the underlying mechanisms of actions. After a review of the literature, the following major limitations and gaps were identified:

1. Need for a more pervasive understanding of the mechanisms of action of sclerosing agents.
2. Identification of the correlation between physical properties of foamed sclerosants and the resulting biological effects.
3. Lack of a pre-clinical model having the following characteristics: (i) a biomimetic vein architecture, (ii) a three-dimensional (3D) endothelial layer, and (iii) blood flow.
4. A comparison between different formulations and types of sclerotherapy treatments.

Therefore, the main aim of the present study is to understand the physical and biological effects of sclerosing agents for the treatment of varicose veins. In order to address this aim, three models have been developed to pre-clinically screen the therapeutic effectiveness of sclerotherapy from the cellular level to the whole vessel structure. These include: (i) 2D *in vitro* models, (ii) *ex vivo* models, and (iii) 3D vein-on-a-chip (VOC) (Figure 12).

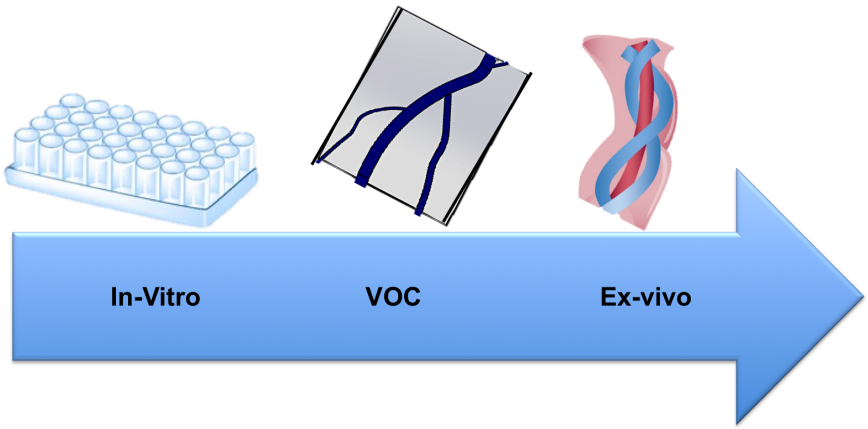

Figure 12. *Sclerotherapy models: 2D (monolayers of HUVECs), 3D (vein-on-a- chip) and ex vivo (human umbilical cord).*

3.2 Objectives of the study

1. Design a 2D *in vitro* model for understanding the effect of sclerosing agents on the endothelium, and develop a quantitative method to assess treatment efficacy and compare different treatment methods.

2. Quantify the physical properties of foamed sclerosants, and correlated them with biological effects.

3. Identify a suitable technique to evaluate the interaction between sclerosant molecules and cell membranes.

4. Design an *ex vivo* model to investigate the biological performance of sclerosing foams in physiologically relevant conditions, and develop a quantitative method to evaluate and compare different sclerosing agents.

5. Design an artificial vein model with the following characteristics: (i) a biomimetic vein architecture, (ii) a three-dimensional (3D) endothelial coating layer, and (iii) perfusion with blood flow.

3.3 Project Milestones

The specific milestones achieved in this study are outlined in the following paragraphs.

Milestone 1 – *In vitro* evaluation of the biological performance of sclerosing foams

The first objective of the study was the development of a 2D *in vitro* model for evaluating the therapeutic efficacy of liquid and foamed sclerosants. The model consisted of a monolayer of isolated vein endothelial cells, which have been exposed to liquid and foamed sclerosants. A quantitative method was developed in order to quantify and compare the efficacy of different treatments. Treatments included manual techniques (DSS and Tessari) and an automated technique (Polidocanol Endovenous Microfoam, PEM). The model allowed evaluating different clinical parameters, which might be employed by clinician as guidelines.

The tasks achieved in Chapter 4 are summarized in Table 2.

Table 2. Development of a 2D *in vitro* model.

Milestone 1
Development of a robust 2D *in vitro* model.
Development of a quantitative assay for evaluating the effect of sclerosants on cells.
Evaluation of the effect of liquid/foamed sclerosants on endothelial cells.
Investigation of different clinical parameters (exposure time, volume injected, needle diameter, etc.).
Evaluation of the correlation between physical and mechanical properties.

Milestone 2 – Evaluation of the sclerotherapy effect at the membrane level measuring the variation of lipid packing

Sclerosants produce endothelial damage interfering with cell surface lipids. The surfactants are absorbed by the cell membrane and they disrupt the normal architecture of the lipid bilayer reducing its surface tension. In the present milestone a quantitative fluorescence microscopy technique was employed to measure changes in the physical properties of cell membranes interacting with liquid and foamed sclerosants. The results were employed to (i) understand the mechanism of action of polidocanol at the membrane level and (ii) quantify and compare the effectiveness of liquid/foamed sclerotherapy.

The tasks achieved in Chapter 5 are summarized in Table 3.

Table 3. Evaluation of sclerosants' effect at the membrane level.

Milestone 2
Evaluation of cell membrane lipid-packing in different cell lines
Evaluation of cell membrane lipid-packing of live cells treated with liquid polidocanol
Evaluation of cell membrane lipid-packing of live cell treated with foamed polidocanol

Milestone 3 – *Ex vivo* evaluation of the biological performance of sclerosing agents

In order to investigate the sclerosing performance in a more realistic biological model, *ex vivo* models from umbilical cord veins were established to quantify sclerosant-induced disruption of the endothelial layer from extravasation of a probe molecule.

Ex vivo models may help understanding the biological effects of sclerosants on a real vascular tissue, and were employed in either static and dynamic conditions, to replicate stagnant and physiological blood flow. The tasks achieved in Chapter 6 are summarized in Table 4.

Table 4. Development of an *ex vivo* model for quantifying sclerosant-induced disruption of the endothelial layer.

Milestone 3
Development of a robust *ex vivo* model
Development of a quantitative assay for evaluating the effect of sclerosants
Evaluation of liquid sclerosant effect on endothelial cells in static conditions.
Investigation of different clinical parameters (exposure time, volume injected, needle employed, etc.).
Evaluation of liquid sclerosant effect on endothelial cells in the presence of whole blood.
Evaluation of liquid sclerosant effect on endothelial cells in dynamic conditions.

Milestone 4 – Vein-on-a-Chip models for evaluating the mechanical properties of sclerosing foams

In this objective of the study, more complex *in vitro* models (referred to as vein-on-a-chip models) were developed. Devices were constructed to replicate the physiological and pathological (varicose) structure of great and small saphenous veins. A novel experimental method to quantify and compare the flow behavior of sclerosing foams was developed. The method was employed to evaluate physical prosperities of the foams, which are correlated to the biological performance. The tasks achieved in Chapter 7 are summarized in Table 5.

Table 5. Development of VOC models for evaluating the mechanical and biological performance of sclerosants.

Milestones 4
Development of a robust VOC production method
Evaluation of mechanical properties of sclerosing foams in VOC models

Milestones 5 – Development of 3D vascular *in vitro* models

In order to more faithfully mimic the physiological environment of the vessel, endothelial cells were cultured inside the VOC channels, recreating an endothelial layer. Afterwards, hydrogels were utilized to replicate the extracellular matrix (ECM), or as a bulk material for the whole device. A method to create channel networks within a hydrogel matrix in a simple, rapid and reproducible way, and using only natural hydrogels, were investigated.

The method allowed the production of both a scaffold (extra-vascular compartment) and a perfusable channel network. Particular attention was devoted to the use of replica or sacrificial molding techniques to generate the scaffold.

The tasks achieved in Chapter 8 are summarized in Table 6.

Table 6. Development of 3D vascular *in vitro* models.

Milestones 5
Generation of an endothelial layer inside VOCs
Development of a new a method for fabricating vascularized hydrogels
Generation of an endothelial layer inside vascularized hydrogels

3.4 Novelty

Different elements of novelty are demonstrated in this study:

1. A quantitative method has been employed in a 2D biological model for evaluating the efficacy of sclerosants in both liquid and foamed form. Several parameters have been investigated in order to assess the role of different treatment-related variables (such as exposure time, volume injected, gas composition, etc.).

2. The present study represents the first systematic comparison of the biological performance of different sclerosing foam formulations, and a first attempt to correlate biological performance with foam physical properties. In particular, a qualitative correlation between foam drainage dynamics, gas composition, and the resulting biological effects was postulated for the first time.

3. This is the first study where spectral microscopy has been employed to assess membrane fluidity in live cells for evaluating the effect of surfactant molecules. It has been demonstrated that sclerosants affect the lipid-packing of cell membranes.

4. For the first time an *ex vivo* model was employed in dynamic conditions to replicate a clinical procedure. A new assay was developed for quantifying sclerosant-induced vessel wall disruption. Moreover, the effect of liquid/foamed sclerosants on the vessel wall was evaluated in both static and dynamic conditions, in the presence of blood.

5. In this study for the first time has been described the development of vein-on-a-chip models replicating the qualitative architecture of physiological and varicose veins, and their utility as model platforms to screen the flow behavior of sclerosing foams, upon different formulation

and administration conditions.

A simple method to manufacture vein models was developed, which aimed at generating channels with circular section and with a geometry that recapitulates some characteristics of the varicose vein. An experimental protocol was also established to investigate the flow performance of foams at conditions relevant to their clinical administration.

It has been demonstrated that the vein-on-a-chip models and experimental methods developed in this study provide a novel technology platform to measure the behaviour of different formulations of sclerosing foams, at physical conditions that resemble their clinical administration.

6. A novel pre-clinical model for sclerotherapy has been developed, which has the following characteristics: (i) a biomimetic vein architecture, (ii) a three-dimensional (3D) endothelial layer, and (iii) the presence of blood flow.

7. A new method for creating simple or complex channel geometries inside a hydrogel-based scaffold has been proposed. The results showed great potential for application in various bioengineering applications.

Chapter 4: In vitro evaluation of the biological performance of sclerosing foams

Chapter 4 describes the development of a 2D *in vitro* model to evaluate the therapeutic efficacy of liquid and foamed sclerosants. The model provides a 2D environment to investigate the effectiveness of liquid and foamed sclerosants.

Abstract

Since the first reports on foam sclerotherapy, multiple studies have been conducted to determine the physical properties and behavior of foams, but relatively little is known about their biological effects on the endothelial cells lining the vessel wall. Moreover, a systematic comparison of the biological performance of foams produced with different methods has not been carried out yet. Herein, a 2D *in vitro* method was developed to compare efficacy of commercially available polidocanol injectable foam (PEM, Varithena) and physician-compounded foams (PCFs). Endothelial cell attachment upon treatment with foam was quantified as an indicator of therapeutic efficacy, and was correlated with foam physical characteristics and administration conditions. In a series of comparisons, PEM presented a greater overall efficacy compared to PCFs, across the different biological models, which was attributed to its drainage dynamics and gas formulation. This is consistent with earlier studies that indicated superior physical cohesiveness of PEM compared to PCFs.

4.1 Introduction

Chronic venous insufficiency (CVI) is the global term to describe failure of venous drainage. CVI can occur in the superficial venous system, the deep venous system (veins within the muscle compartment of the leg), or both. Superficial venous incompetence of the leg may involve any of the veins of the superficial venous system, which includes the great saphenous vein (GSV), small saphenous vein (SSV), and their tributaries. The outward manifestation of superficial venous incompetence is often referred to as varicose veins (Spiridon and Corduneanu, 2017; Gloviczki et al., 2011). Sclerotherapy has been employed (along with surgery, radiofrequency and laser ablation) to treat all types and sizes of varicosities by damaging the endothelial lining of the vein wall, causing shrinkage of the treated vessel and leading to the development of new veins.

Sclerosing agents in the form of liquid surfactant solutions have been largely used in the clinic (Rasmussen et al., 2011). Since the first reports of the ability to create stable foams from detergent-type sclerosants, foam sclerotherapy has however become widely adopted by clinicians, largely replacing the traditional injection of liquid sclerosants (Bountouroglou et al., 2006). This change in clinical practice is due to several advantages of foamed sclerosing agents when compared to their liquid counterparts (Hamel-Desnos et al., 2003). When a liquid sclerosant is injected into a vein, it is rapidly diluted by the circulating blood volume. It has been demonstrated that the interaction with blood decreases the efficacy of sclerosants, due to binding with plasma proteins that ultimately reduces the number of active molecules (Parsi et al., 2007; Parsi et al., 2008). A foamed sclerosant on the other hand, is able to displace blood rather than mixing with it, increasing the contact time of a higher concentration of active agent with the vein wall and thus resulting in greater efficacy. For these reasons, in foam sclerotherapy, lower concentrations of sclerosant are required to obtain the same therapeutic effect as in their liquid counterpart, reducing the prevalence of side effects associated with higher concentrations (Jia et al., 2007).

Over the last 60 years, different foam production methods have been proposed. The two most common techniques that clinicians employ to generate physician-compounded foams (PCFs), are the double syringe system (DSS) and the Tessari method (TSS) (Cavezzi and Tessari, 2009). DSS involves passing the sclerosant liquid and a gas between two syringes joined by a straight connector, whereas in the Tessari method the connector is replaced with a three-way valve. Recently, automated production methods have been introduced, such as polidocanol injectable foam (PEM) (Varithena, Provensis Ltd, a BTG International group company),

which is designed with a foam generating device for producing a 1% polidocanol O_2:CO_2 (65:35) based foam (1:7 liquid:gas ratio), which is virtually nitrogen-free (<0.8%).

The most clinically employed sclerosants are liquid polidocanol (POL) and sodium tetradecyl sulfate (STS) at concentrations of 0.5% to 3% by volume. PCFs are typically produced with carbon dioxide (CO_2) or room air (RA) at different liquid:gas volume ratios (1:4, 1:3 and 1:7) by phlebologists (Cavezzi and Tessari, 2009). CO_2 foam presents a shorter half-life compared to RA foam (Peterson and Goldman, 2012), but the latter is associated with higher incidence of side effects including visual disturbances, chest tightness, cough, and dizziness (Peterson and Goldman, 2011). In addition, RA foam has a high nitrogen content (>70%), which increases the risk of microembolism because of greater bubble persistence due to the low solubility of nitrogen in blood (Ceulen et al., 2008).

The ideal sclerosing foam should offer desirable physical and biological performance. From a physical perspective, it should be sufficiently cohesive to completely fill the vein lumen upon injection, acting as a piston to displace blood rather than mixing with it (Carugo et al., 2015). Moreover, it should be sufficiently stable to maintain maximal activity from preparation to administration, but short-lived enough to cause limited side effects (Nastasa et al., 2015). Previous studies have shown that these properties strongly depend on the foam manufacturing method, the gas formulation, the gas-to-liquid volume ratio, the type and concentration of surfactant (Goldman et al., 2017). From a biological perspective, the ideal foam should damage all endothelial cells in the treated area, with negligible off-target and systemic effects (Goldman et al., 2017). Greater endothelial damage is preferable as the smooth muscle layer of the vein wall can theoretically regenerate a partially compromised endothelium, and endothelial cells can migrate long distances to re-establish a functional conduit (Valenzuela et al., 2013).

It has been previously postulated that biological effects of sclerosing foams may depend on their physical characteristics (Wong et al., 2015; Carugo et al., 2016). However, whilst numerous studies have been conducted to determine the physical and mechanical properties of foams (i.e., foam dwell time, drainage time, bubble size distribution, etc.) (McAree et al., 2012; Hamel-Desnos et al., 2003; Carugo et al., 2016), relatively little is known about their biological effects on the endothelial cells lining the vessel wall. It is widely accepted that sclerosants disrupt the cell membrane causing (i) endothelial cell (EC) death microscopically, and (ii) macroscopic vein wall damage, such as disruption of the *subintima* (i.e. the elastic tissue located underneath the endothelium) and mild alterations of the smooth muscle layer

(Whiteley et al., 2016; Connor et al., 2015).

Limited *in vitro* studies have been performed to investigate the microscopic effects of sclerosants (Kobayashi et al., 2006; Mol et al., 2007; Parsi et al., 2008).

Most of these studies involve culturing of ECs over a plate, exposing cells to sclerosants, followed by staining with dyes to evaluate cell membrane lysis or cell death (see Table 7).

Table 7. Summary of *in vitro* studies performed to investigate the microscopic effects of sclerosants.

Author	Kobayashi	Mol	Parsi
Cell type	BAECs Bovine aortic endothelial cells	HUVECs Human umbilical vein endothelial cells	HMEC-1 Human microvascular endothelial cell line
Treatment	Liquid 3% POL or 1% STS (and further dilutions)	Liquid POL (1.5%, and further dilutions)	Liquid STS (3%) and POL (3%, and further dilutions)
Treatment Time	0-1 hr	5 s	15 min
Method of Administration	Injection	Injection	Injection
Analysis/Outcome	Fluorescent dye measurement/cell death	Dye measurement /cell death	Dye measurement/cell lysis
Quantification method	Fluo4/AM and DAF-FM/DAPI	MTT/Trypan blue/DiI/ICAM	Leishman's stain

Kobayashi *et al.* determined an inverse correlation between sclerosant concentration and the minimum contact time required to cause-endothelial cell death (Kobayashi et al., 2006). They found that upon exposure to 1.5% POL liquid solution, cell death occurred after 15 seconds, while a 0.3% POL solution required 15 minutes to achieve the same effect. At very low concentrations of POL (0.003%) cell death did not occur, even after 1 hour of exposure. In a similar study by Mol *et al.,* it was found that almost all cells died after 5 seconds of exposure to 0.025% POL, whereas at lower concentrations (<0.0125%) cell death occurred within 2 minutes (Mol et al., 2007). Both studies demonstrated that treatment time is dependent on POL concentration, although there were some significant differences in the time required to

cause endothelial cell death *in vitro*.

Parsi *et al.* investigated the deactivating effect of circulating blood cells on the lytic activity of detergent sclerosants (Parsi et al., 2008). ECs were exposed for 15 minutes to different mixtures of sclerosants with blood, and subsequently labeled with a Leishman's stain. Results showed that the number of non-lysed cells was concentration-dependent, and that POL had a lower lytic action compared to STS.

Notably, these earlier *in vitro* studies only focused on liquid sclerosants; thus, a systematic comparison of the biological effects induced by foamed sclerosants has not been performed yet. These studies also reported that therapeutic effects were largely dependent on treatment time and sclerosant concentration, although treatment timescales differed between investigations. This could be due to differences in the physical properties of the sclerosing agent used and the experimental conditions. To the best of my knowledge, there is no comparative quantitative analysis between different foam production or administration methods, or attempt to correlate physical with biological performance of sclerosing foams. This is also reflected in the lack of clinical studies comparing efficacy and safety of different foam production methods.

Herein, a new method for quantifying sclerosant-induced disruption of the endothelial layer is proposed. Using the *in vitro* model, the therapeutic efficacy of different polidocanol-based sclerosing agents was investigated, and correlated with their physical characteristics and administration protocols. Results from this study can provide clinicians with some fundamental understanding of how different foam formulations may perform in the body.

4.2 Materials and Methods

4.2.1 Foam production methods

In this study, the commercially available Varithena 1% varicose vein treatment (referred to as polidocanol injectable foam or PEM) was employed, and its performance compared with physician compounded foams (PCFs) made using different foam generation methods (Figure 13).

With respect to PCFs, POL (Croda, Goole, UK) at a concentration of 1% (v/v in buffered saline) was employed as a surfactant agent. Foams were produced by mixing liquid and room air (at a volume ratio of 1:4, respectively) as this is the most widely used formulation adopted in clinical practice. Two methods of PCF production were investigated: (i) DSS and (ii) Tessari. In the DSS method, foam was produced by passing the POL solution from a 5 mL

syringe, ten times into and out of a 10 mL syringe. Silicon-free syringes (BD Biosciences, USA) were connected *via* a Combidyn adapter (B. Braun Melsungen, Germany).

In the Tessari method, the straight connector was replaced with a three-way valve that was set at a 30° off-set. Polidocanol endovenous microfoam (PEM) Varithena is a commercially available microfoam combination produced by Provensis Ltd (a BTG International group company, London, UK) consisting of a proprietary 35:65 CO_2:O_2 gas mixture with ultralow nitrogen content (<0.8%) and 1% POL solution. The foam is contained within a pressurized canister combined with a transfer unit, which can be connected to a 10 mL silicone-free syringe. Once connected, the syringe is filled with 5 mL of foam. Experiments were conducted at room temperature (23 °C), after foam production, and foams were produced by the same operator.

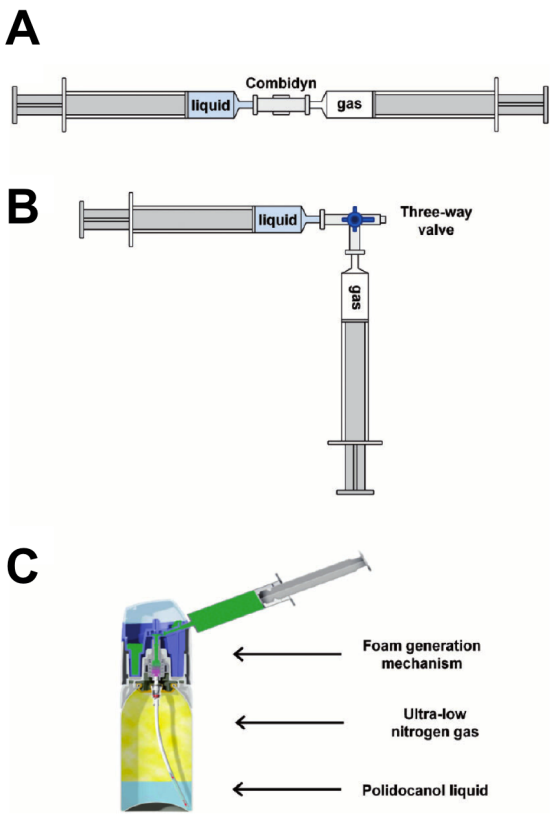

Figure 13. *Methods for producing PCFs and PEM. In the DSS method, syringes are connected by a Combidyn™ adapter (A), while in the Tessari method; a three-way valve connects them (B). In either technique, the foam was produced by passing the polidocanol solution (liquid phase) from one syringe, 10 times into and out of the other syringe initially containing room air. The proprietary canister system for generating PEM (Varithena®) is shown in (C) (source: Carugo, D. et al. Benefits of polidocanol endovenous microfoam (Varithena®) compared with physician-compounded foams. Phlebology 31, 283–295, 2016).*

4.2.2 In vitro test method to evaluate performance of sclerosants

A method was designed to test the efficacy of sclerosants, in both their liquid and foamed form. A monolayer of human umbilical vein endothelial cells (HUVECs) was cultured until confluence into 24 well-plates (Sigma-Aldrich Co. LLC., USA). The following steps were designed to mimic different phases of sclerosant's injection: (i) the HUVECs media (HM) (Thermo Fisher Scientific Inc., USA) was removed from the wells, in order to achieve direct contact between cells and sclerosants; (ii) the cell monolayer was exposed to various sclerosing agents during a fixed time of approximately 15 seconds, reproducing the injection process; (iii) sclerosants were removed using a pipette, and cells were washed once using a HBSS buffer (Hanks Buffered Saline Solution, Sigma-Aldrich Co. LLC., USA) mimicking the sclerosant's displacement and dilution caused by blood flow; and (iv) fresh medium was added. Sclerosants' injection was performed manually using a 5 mL syringe (BD Biosciences, USA), with and without a needle. The syringe was kept perpendicular to the bottom plane of the well, and the sclerosing agent was injected from the centre of the well. The standard procedure was carried out under these conditions: 1 mL of liquid/foamed sclerosant, 15 seconds of exposure time, and a 16G needle employed for injection. Following treatment, the medium was removed and cells were washed gently in warm HBSS, which was subsequently removed by aspiration.

Cells were subsequently fixed with the addition of 0.7 mL of a 10% formyl saline solution (Sigma-Aldrich Co. LLC., USA). Fixative was then removed by aspiration, and a methylene blue solution (MB) 1 % (w/v methylene blue in 0.01 M-borate buffer pH 8.5) (Sigma-Aldrich Co. LLC., USA) was added to each well.

The MB solution was then transferred to a 96 well flat-bottomed plate (Sigma-Aldrich Co. LLC., USA), with 0.1 mL being added in duplicate wells. A control set of untreated cells was used to generate a standard curve of MB equivalent to serial dilutions of 100% cells. MB absorbance was then measured using a plate reading spectrophotometer, at a wavelength of 650 nm. Absorbance values of treated cells were then converted into a percentage of attached cells, using a calibration function. The number of cells attached is a measure of the number of live cells upon treatment. The latter was derived from linear regression of experimental data points (Figure 14), using Prism software (GraphPad Software, Inc., USA).

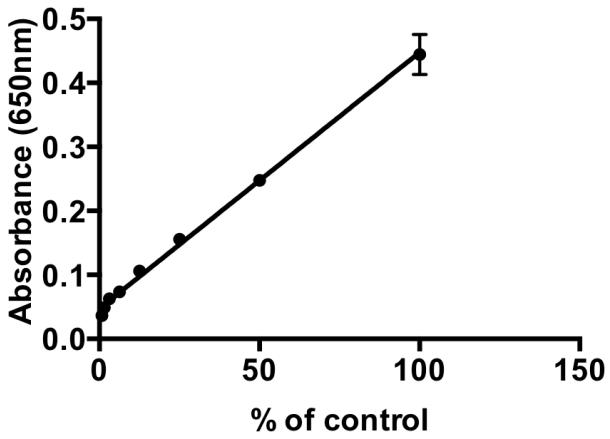

Figure 14. *Standard curve showing the absorbance (at 650 nm) at different concentration of methylene blue, which is proportional to cell number. The interpolating linear function can then be used to calculate numbers of experimental cell samples.*

During the study different parameters were varied, such as (i) volume injected, (ii) exposure time, (iii) needle bore size, and (iv) gas formulation. The volumes of injected sclerosant investigated were 0.5, 1, and 2 mL, whilst the exposure times investigated were 15, 30, 60 and 120 seconds. The needles employed were selected based on the common clinical practice, and had an inner diameter of 30G, 25G and 21G, corresponding to 0.16, 0.26 and 0.51 mm, respectively (BD Biosciences, USA). In order to investigate the effect of the gas formulation, PEM foam was produced using different gas constituents (in addition to the commercial formulation), including 100% O_2 and room air.

4.2.3 Measurement of foam drainage dynamics

A transparent glass vial (outer diameter: 10.9 mm) was placed within a custom-built photographic chamber with a black background. A charge-coupled device (CCD) camera (Canon EOS06) was positioned in front of the vial. The foam was produced and injected (2 mL) inside the vial, using different types of needle (16G, 25G, and 30G) and different foam production techniques (PCFs and PEM). The experiment was repeated five times, for each condition investigated.

The time between foam injection and the beginning of the video recording was approximately 23 seconds. Videos were recorded for 5 minutes (25 frames per second), and subsequently analysed using a Phyton script developed in-house (Figure 15). The script loads the video and extracts its individual frames. It then performs the following steps in a semi-automated fashion:

(i) User selection of a region of interest for analysis.

(ii) Calibrating the image dimensions, by converting pixels into physical units. This is carried out by user selection of a feature of known length (for instance, the diameter of the vial).

(iii) Converting the image into a black and white binary format, where black corresponds to the liquid phase and white corresponds to foam.

(iv) The centerline of the selected region of interest is determined, and a rectangular window for analysis is defined. The width of this window extends 5 pixels away from the centerline, at both sides. It was decided to analyse foam drainage within an interrogation window (as opposed to a line), as data would be less sensitive to experimental noise.

(v) Automated counting of the number of black pixels along the height of the interrogation window. An average height was determined, which corresponded to the height of liquid POL in the vial (upon dimensional calibration).

(vi) Steps (iii)-(v) were performed automatically on each image frame, and a plot of the liquid height (in mm) *vs*. time was generated. This provided a quantitative measure of foam drainage dynamics.

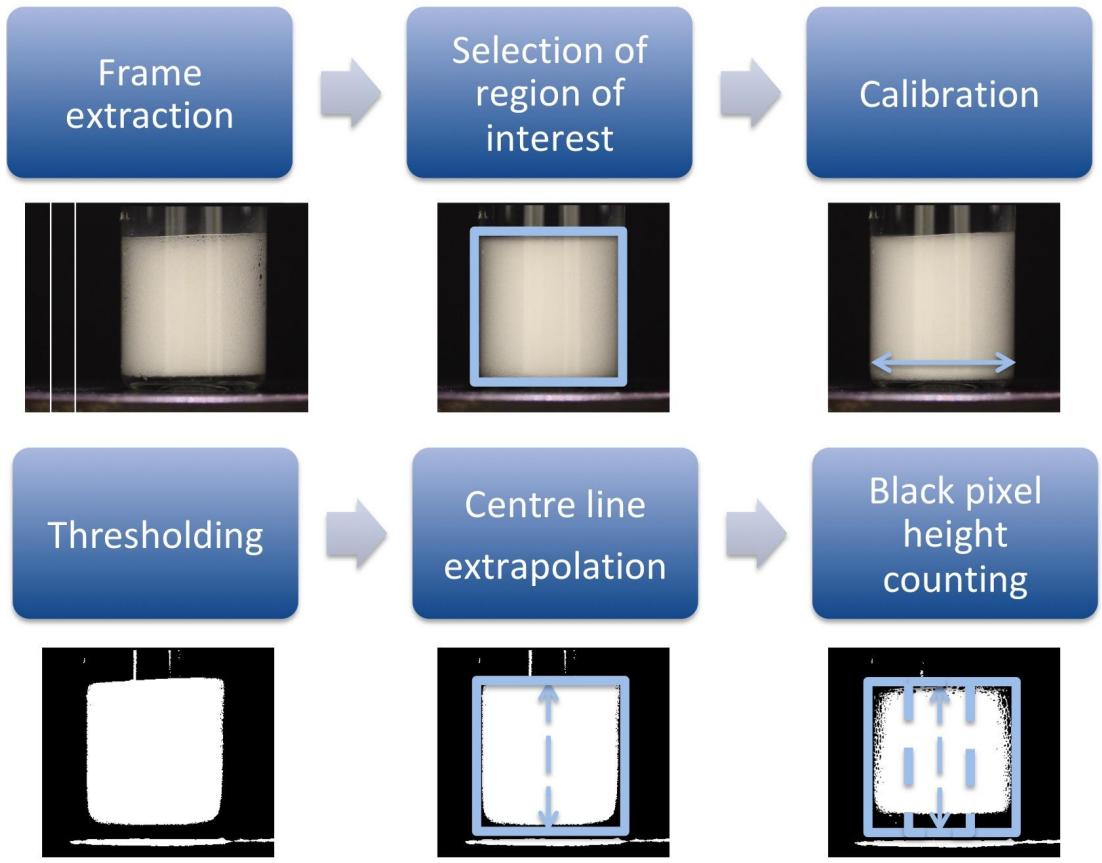

Figure 15. *Schematic representation of the python code video processing analysis. The code proceeds the analysis following several steps: (i) Frame extraction (25 frames per second) (ii) Selection of region of interest, (iii) calibration, (iv) thresholding, (v) center line extrapolation) and (vi) black pixel height measurement.*

4.2.4 Measurement of bubble size distribution

The bubble size distribution was measured using an in-house glass-plate method, as described in previous study (Carugo et al., 2016). Briefly, an aliquot of freshly generated foam (volume: 49 µL) was placed on a glass plate and immediately covered by another. The plates were thick enough not to bend, and were separated by a 32 µm thick gap.

A flattened foam monolayer was thus created, which comprised 32 µm high, flat cylindrical bubbles. A light microscope and camera (AxioCam ICc 1, Carl Zeiss Microscopy, Cambridge, UK), with lighting adjusted to create sharp images of circular boundaries, were employed to capture sequential image fields. A built-in software was used to "stitch" fields together. Each individual bubble was identified and the bubble diameter measured using the image analysis (AxioVision, Zeiss) programme, with bespoke BubbleSizerMeasure macro. Approximately 2000-3000 bubbles per sample were measured using this procedure. The experiment was repeated five times, for each condition investigated.

4.2.5 Microscope imaging of treated cells

Bright field images of HUVECs were acquired with an optical microscope (Olympus, CKX41, Japan). Images were taken of live samples immediately after treatment, with phase contrast microscopy (objective magnification 4X).

4.2.6 Statistical analysis

The comparisons between treatments were performed using unpaired Student's t-test with Welch's correction. Statistical significance was assumed for p-value < 0.05. All statistical tests were performed with Prism software. Data were reported either as the mean ± standard deviation, or in the form of a Tukey's box plot (comprising 25th percentile, median, and 75th percentile).

4.3 Results

4.3.1 Evaluation of the reproducibility of the *in vitro* test method

In the first step of the study, a method replicating the clinical treatment procedure was designed in order to investigate the biological effects of sclerosants on a two-dimensional (2D) endothelial model (see Methods section for additional details). The mechanism of action of sclerosing agents relies on endothelial damage; therefore, endothelial cell attachment was employed as a metrics for therapeutic efficacy. Since detached endothelial cells are known to undergo apoptosis, cell attachment was considered as an indicator of cell viability (Goldman et al., 2017). Therefore, a lower percentage of attached cells upon treatment indicated a more effective sclerosing agent.

Firstly, the repeatability of the method was assessed by fixing the injection and treatment parameters (PEM foam, 15 seconds of treatment time, and 1 mL of foam injected without needle) and repeating the experiment six times. Results showed consistency of foam performance across multiple independent repeats (Figure 16).

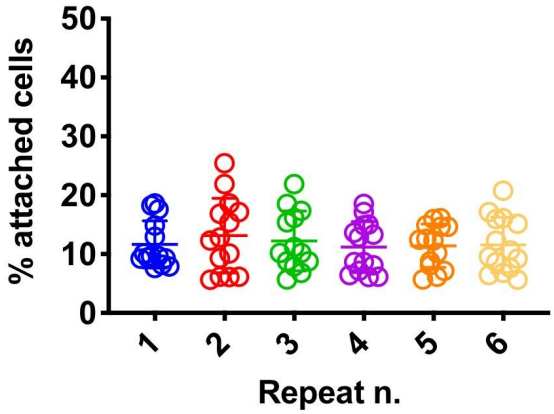

Figure 16. *Evaluation of the reproducibility of the in vitro test method. 1 mL of PEM was injected onto the ECs monolayer, using a 16G needle. The exposure time to the sclerosing foam was set to 15s. The experiment was repeated six times.*

4.3.2 *In vitro* evaluation of the effect of liquid polidocanol concentration on HUVECs

Subsequently, the sclerosing efficacy of liquid POL was investigated. A 1% POL solution was serially diluted in PBS in order to identify the minimum effective and 50% inhibitory concentrations (15 seconds treatment duration, and 1 mL of sclerosant injection without needle). Figure 17 shows that POL 1% is still effective even after five serial dilutions (0.03% final volumetric concentration), removing >50% of cells in a well. Concentrations of liquid below 0.02% rendered the treatment ineffective (85 ± 10% of attached cells). A 50% inhibitory concentration of 0.024% was determined from these experiments.

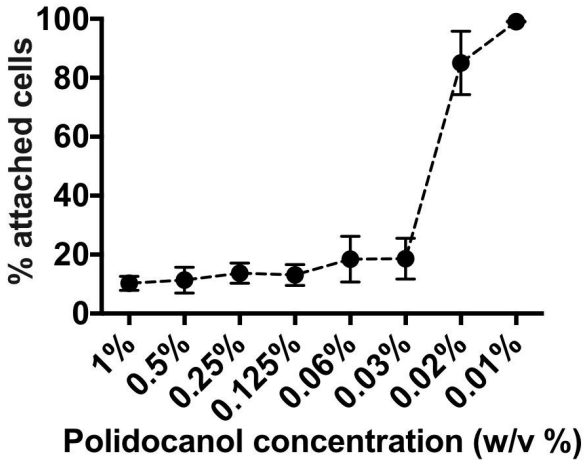

Figure 17. *In vitro evaluation of the effect of liquid polidocanol concentration on HUVECs. 1% polidocanol (in PBS) was serially diluted seven times using PBS. HUVECs were treated with 1 mL polidocanol solutions for 15 seconds. Data are reported as percentage of attached cells (compared to untreated cells), determined via methylene blue method. The experiment was repeated six times, and results are reported as mean value ± standard deviation.*

4.3.3 Assessment of polidocanol depletion *in vitro*

An additional experiment was designed to investigate the extent of polidocanol 'depletion', potentially due to the interaction with cell medium constituents or intercalation within cell membrane fragments. In these experiments, 1 mL of liquid POL was injected into one well and left for 15 seconds. The solution was then transferred into a neighbouring well, and the process was repeated in order to treat five wells in series. As shown in Figure 18, the 1% polidocanol solution maintained the same efficacy after five serial injections (only 17.5 ± 4.0% of cells remained attached after the 5th injection). The experiment was repeated using a lower POL concentration of 0.03%. Results demonstrated that depletion of active POL occurred, as the percentage of attached cells after treatment increased from 29.3 ± 2.0% (3rd injection) to 49.82 ± 11.8% (4th injection) and 57.7 ± 19.6% (5th injection). Reducing the POL concentration further (to 0.02%) resulted in a similar trend, although the change in percentage of attached cells was less significant because of the reduced effectiveness of the sclerosing solution (coherently with the results shown in Figure 17).

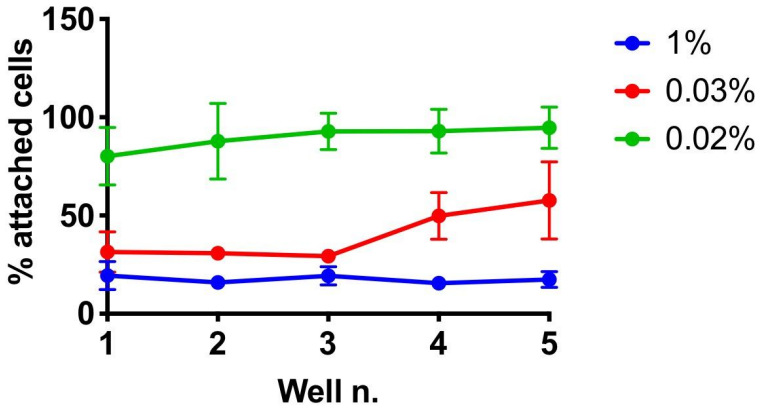

Figure 18. *Assessment of polidocanol depletion in vitro. POL solutions at different volumetric concentrations (1%, 0.03% and 0.02%, in PBS) were injected into one well and left for 15s to interact with HUVECs. They were then removed and injected in a neighbouring well. The process was repeated to treat five wells serially, in order to investigate potential depletion of active polidocanol. Data are reported as % of attached cells, determined via methylene blue assay. The experiment was repeated six times, and results are reported as mean value ± standard deviation.*

4.3.4 *In vitro* evaluation of the effect of a needle during foam injection

The usage of injection needles with different bore size was also investigated, because of their potential effect on foam size and stability. Cells were exposed to 1 mL of PEM foam for 15 seconds, either with or without a needle. Firstly, a needle with the greatest bore size in the range investigated was employed (16G). Figure 19 shows that the presence of a 16G needle

had a negative impact on foam treatment efficacy (i.e., the percentage of attached cells upon treatment increased from 10.12 ± 2.2% to 16.26 ± 3.0%; p-value < 0.001).

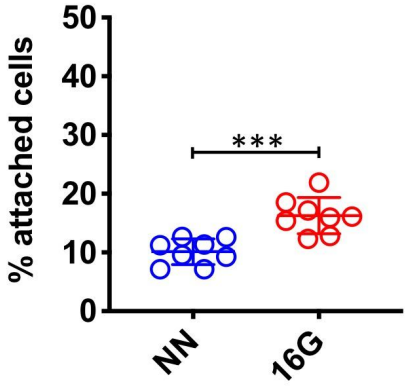

Figure 19. *In vitro evaluation of the effect of a needle during foam injection. PEM (15 s exposure time, 1 mL) was injected without (NN, filled circles) and with a 16 G needle (filled squares). Data are reported as % of attached cells (compared to untreated cells), determined via methylene blue method. The experiment was repeated eight times. (***) Asterisks indicate that the difference between mean values is statistically significant (p-value < 0.001).*

Therefore, in order to investigate this effect further, additional needle bore sizes were tested, corresponding to 25G and 30G. These are the types of needle most frequently employed in clinical practice, allowing us to reproduce more faithfully a clinical injection procedure. Overall, decreasing the needle diameter from 16G to 30G resulted in lower cell death. In the case of PEM, there was statistically significant difference in foam efficacy between 16G and 30G needles (p = 0.03) (Figure 20A). Comparing the different foam production methods, statistical difference was found only when using the largest needle (16G), with PEM associated with statistically greater treatment efficacy (% attached cells: 11.8 ± 4.6 %) compared to both DSS (% attached cells: 19.5 ± 8.9 %) and TSS (% attached cells: 20.0 ± 11.3 %) foams (Figure 20B).

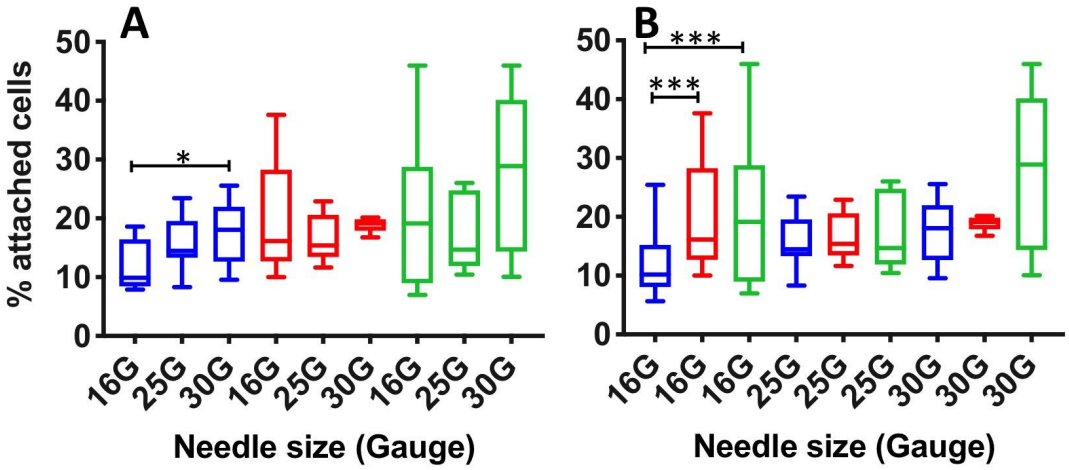

Figure 20. *In vitro evaluation of the effect of needle bore size on HUVECs, using different types of foam. Treatment efficacy was evaluated at varying injection needle diameters (30G, 25G and 16G) and foam production methods [PEM (blue), DSS (red), and TSS (green)]. Experiments were performed with a 15 seconds exposure time and 1 mL of injected foam. Data are reported (Tukey's box plot) as % of cells attached after treatment (compared to untreated cells), determined via methylene blue method. The effect of needle bore size (for each foam production method) is illustrated in (A), while a comparison between foam production methods (for each needle bore size) is illustrated in (B). The experiment was repeated six times. One asterisk (*) indicates p-value ≤ 0.05, three asterisks (***) indicate p-value ≤ 0.001.*

4.3.5 Bubble size and drainage time measurements

In order to determine the effect of needles on foam physical properties, bubble size measurements were carried out using the glass-plate method. Figure 21 shows the bubble size distribution of PEM and PCF foams, injected through different needle sizes.

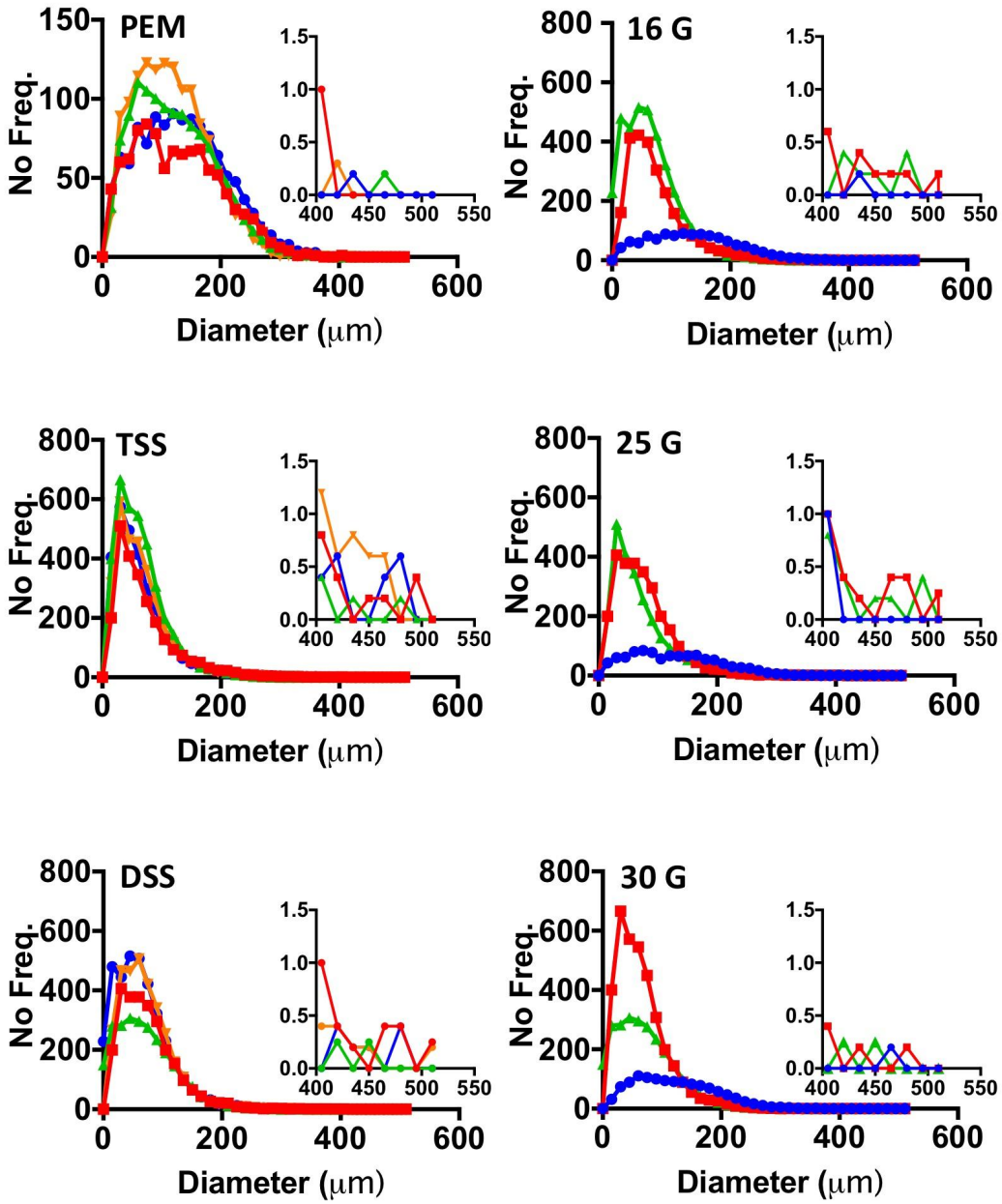

Figure 21. *Quantification of the effect of needle bore size on bubble size distribution, for both PCFs and PEM. Bubble size distribution was measured using the glass-plate method, and is reported in the form of a frequency plot. The comparison between different needle inner diameters, for a fixed foam production method, is reported on the left column [30G (green), 25G (red), 16G (blue), no needle (orange)]. The comparison between different foam production methods, for a fixed needle inner diameter, is instead reported on the right column [PEM (blue), TSS (red), and DSS (green)]. Each experimental condition was repeated five times.*

Results show that injection through a needle did not significantly impact on the bubble size distribution of all types of foam. Comparing the different foam types, room air PCFs had a narrower bubble size distribution than PEM (in the bubble size range 0-400 μm) for all needle inner diameters investigated. However, PCFs had a greater number of bubbles in the size range 400-510 μm compared to PEM. Despite there was no significant change in bubble size

distribution, foam injection through a needle caused visible phase separation between the liquid and gaseous phases. Therefore, an experiment was developed to quantify foam drainage dynamics within a vial, upon foam injection through needles of different bore size. The vial inner diameter was comparable to the one of well plates used for *in vitro* biological testing. Figure 22 shows the time evolution of the height of liquid POL solution at the bottom of the vial, which was employed as a metrics for drainage.

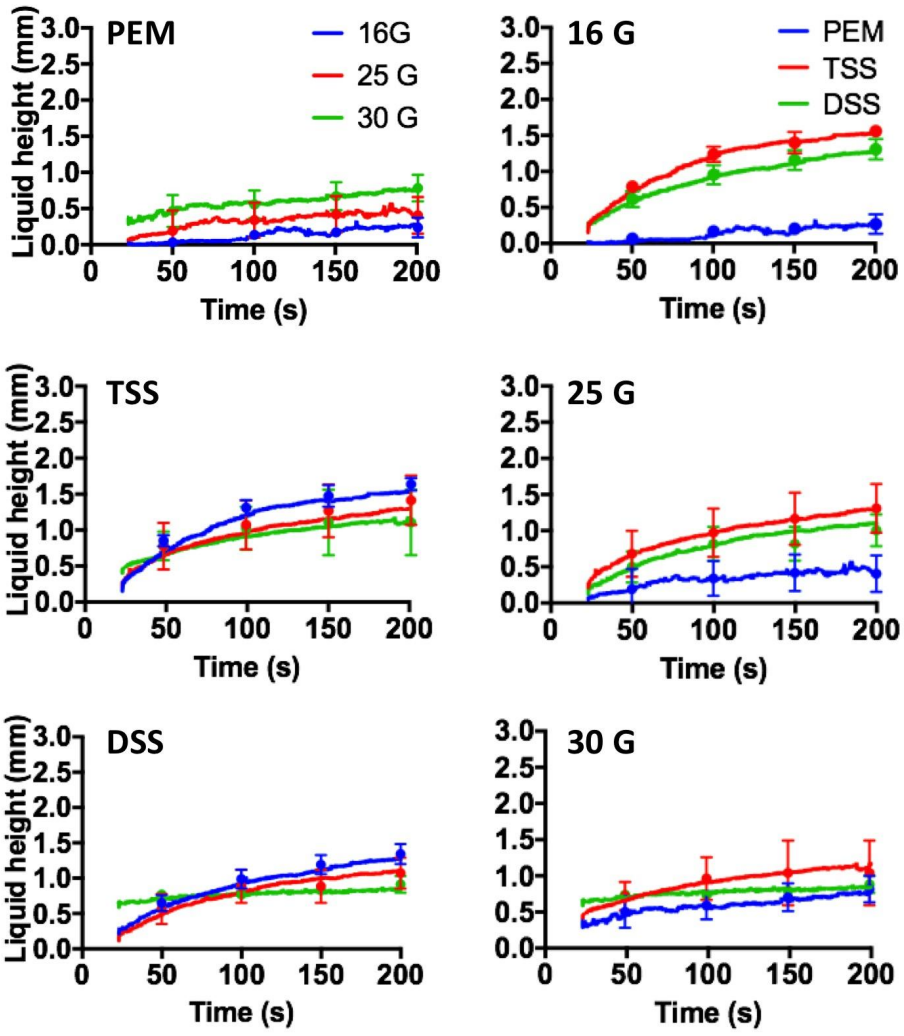

***Figure 22**. Quantification of the effect of needle bore size on foam drainage dynamics. The height of liquid POL solution at the bottom of the vial was quantified over time (up to 200 seconds; representative time points are shown at 50, 100, 150 and 200s), using a custom-built Phyton script. On the left column, results are reported to illustrate the comparison between needle diameters for a fixed foam production method [30G (green), 25G (red), and 16G (blue)]. On the right column, results are reported to illustrate the comparison between foam production methods, for a fixed needle diameter [PEM (blue), TSS (red), and DSS (green)]. The experiment was repeated five times, for each condition investigated.*

When injected using the narrowest needle diameter (30G), all foams presented a higher liquid fraction at the beginning of the experiment [liquid height was 0.45 mm (PEM), 0.66 mm (TSS), and 0.67 mm (DSS)], followed by a relatively slow drainage dynamics. After 200s, the liquid height was 0.77 mm for PEM, 1.67 mm for TSS, and 0.84 mm for DSS. Differences between foams were more evident at the larger needle diameters; with PEM foam undergoing a significantly slower drainage compared to DSS and TSS foams. The largest difference between foam types was observed when using the 16G needle; after 200s, the liquid height was equal to 0.23 mm (PEM), 1.52 mm (TSS), and 1.26 mm (DSS) (Figure 23).

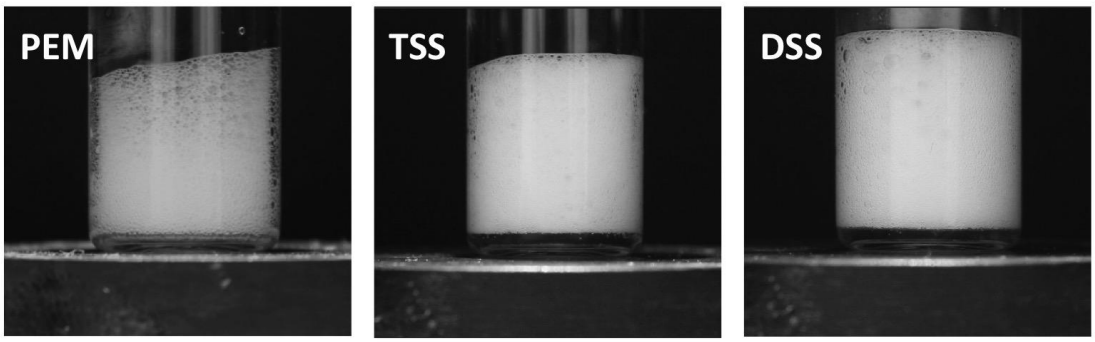

Figure 23. *Evaluation of foam drainage dynamics. A transparent glass vial was placed within a custom-built photographic chamber with a black background. The foam was produced and injected (using a 16 G needle) inside the vial, employing different foam production techniques (PCFs and PEM). The foam behavior was recorded for 5 minutes using a charge-coupled device (CCD) camera (Canon EOS06). The images show a sample of foam, 73s after injection.*

4.3.6 *In vitro* evaluation of the effect of foam volume on HUVECs

The biological effect of changing the foam volume was also investigated, by injecting either 0.5 mL, 1.0 mL, or 2.0 mL (which are comparable to clinically injected volumes, if normalised to the surface area) (Goldman et al., 2017).

In these experiments, the treatment time was fixed to 15 seconds. Results showed a significant reduction in the percentage of attached cells with increasing the volume of foam from 0.5 mL to 2.0 mL (Figure 24). Moreover, PEM had significantly greater efficacy compared to PCFs when using 0.5 and 1.0 mL of foam. Increasing the foam volume further (2.0 mL) resulted in comparable percentage of attached cells between PEM and PCFs (<10% in all cases).

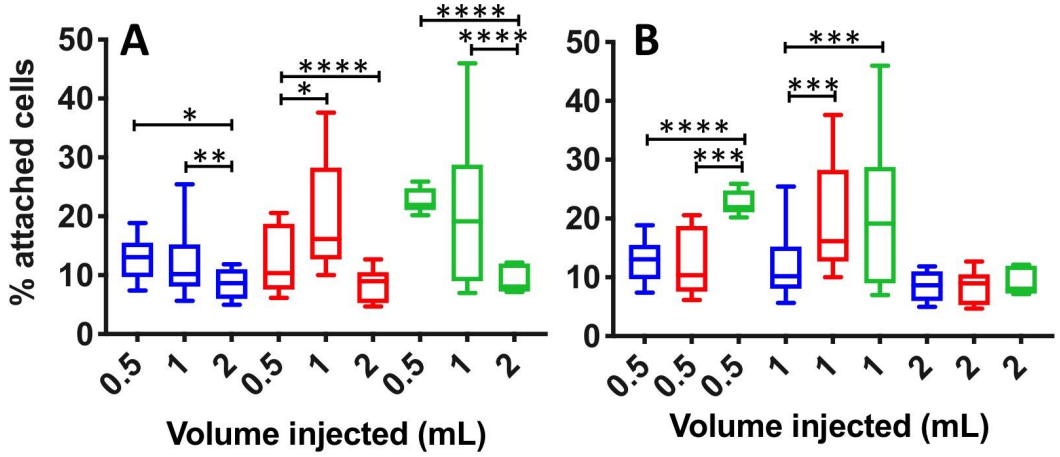

Figure 24. *In vitro evaluation of the effect of foam volume on HUVECs, using different types of foam. Different foam production methods were investigated, including PEM (blue), DSS (red), and TSS (green). The volume injected was 0.5 mL, 1 mL, or 2 mL, for each type of foam. Data are reported (Tukey's box plot) as % of cells attached after treatment (compared to untreated cells), determined via methylene blue method. The effect of injected foam volume (for each foam production method) is illustrated in (A), while a comparison between foam production methods (for each foam volume) is illustrated in (B). The experiment was repeated four times. One asterisk (*) indicates p-value ≤ 0.05, two asterisks (**) indicate p-value ≤ 0.01, three asterisks (***) indicate p ≤ 0.001, and four asterisks (****) indicate p-value ≤ 0.0001.*

4.3.7 *In vitro* evaluation of the effect of foam exposure time on HUVECs

The effect of varying the exposure time of HUVECs monolayers to sclerosing agents was investigated. Earlier *in vitro* and *ex vivo* studies have reported on treatment times in the range 5 s – 1 h, whilst it is usually recognized to be in the order of a few seconds *in vivo* (Yamaki et al., 2004). In this study, the treatment time was varied in the range 15 – 120 s, which is consistent with previous determinations of foam plug persistence within an artificial vein model (Carugo et al., 2015). As shown in Figure 25 the efficacy of a 120s long treatment (PEM = 6.5 ± 0.9%, DSS = 10.5 ± 2.6%, DSS = 9.7 ± 2.3%) was significantly higher compared to shorter treatments. Overall, PEM was statistically more effective than both DSS and TSS, at all treatment times investigated.

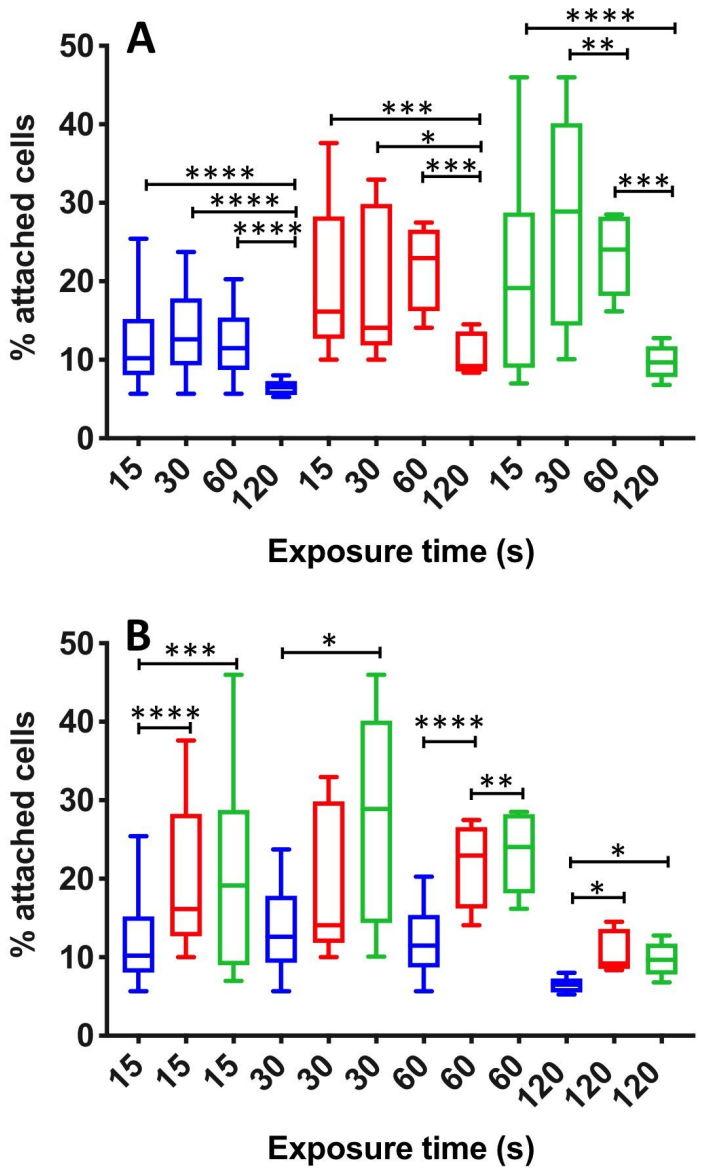

Figure 25. *In vitro evaluation of the effect of foam exposure time on HUVECs, using different types of foam. Methods of foam production investigated included PEM (blue), DSS (red), and TSS (green). 1 mL of foam was injected in these experiments, using a 16G needle. Cell monolayers were exposed to each foam for 15, 30, 60 and 120 seconds. Data are reported (Tukey's box plot) as percentage of attached cells after treatment (compared to untreated cells), determined via methylene blue method. The effect of treatment time (for each foam production method) is illustrated in (A), while a comparison between foam production methods (for each treatment time) is illustrated in (B). The experiment was repeated ten times. One asterisk (*) indicates p-value ≤ 0.05, two asterisks (**) indicate p-value ≤ 0.01, three asterisks (***) indicate p-value ≤ 0.001, and four asterisks (****) indicate p-value ≤ 0.0001.*

4.3.8 *In vitro* evaluation of the effect of PEM gas formulation on HUVECs

In a final series of experiments, the effect of the gas formulation was investigated by comparing the efficacy of PEM foams containing either 35:65 CO_2:O_2 (conventional PEM formulation), RA, and 100% O_2. The 35:65 CO_2:O_2 PEM had significantly greater efficacy (11.8 ± 4.6% of

cells attached) compared to RA (21.8 ± 0.9%) and 100% O_2 (20.5 ± 2.9%) PEM formulations (Figure 26).

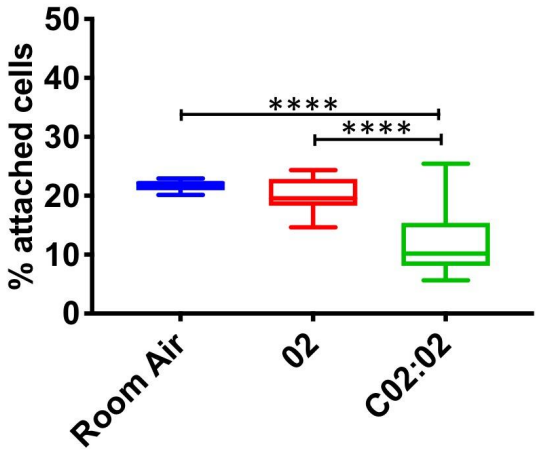

Figure 26. *In vitro evaluation of the effect of PEM gas formulation on HUVECs. 1 mL of PEM foam was injected in these experiments, using a 16G needle. Cell monolayers were exposed to each foam type for 15 seconds. Foams tested were PEM containing either room air, 100% O_2, and 35:65 CO_2:O_2. Data are reported (Tukey's box plot) as percentage of attached cells after treatment (compared to untreated cells), determined via methylene blue method. The experiment was repeated twenty times. Four asterisks (****) indicate p-value ≤ 0.0001.*

4.3.9 Histopathologic observation of HUVECs upon treatment with sclerosing foams

In addition to the above quantitative assays, histopathologic observations of treated HUVECs were performed. Images of cell monolayers exposed to various sclerosing agents were captured, using an optical microscope with phase contrast. The untreated (control) cells displayed a normal EC morphology for confluent monolayers, and were adherent to the substrate (Figure 27D). Following treatment, cell morphology changed to a more rounded appearance; the monolayer became disrupted, where a large number of cells detached from the substrate and, in some cases, only fragments of cells were present. Figure 27 A-C show images of cells after exposure to foam generated using different production methods (15 seconds treatment duration, and 1 mL of foam injected without needle). It is evident that PEM (Figure 27A) and DSS RA (Figure 27B) foams caused greater cell detachment compared to TSS foam (Figure 27C), which is coherent with the quantitative determinations.

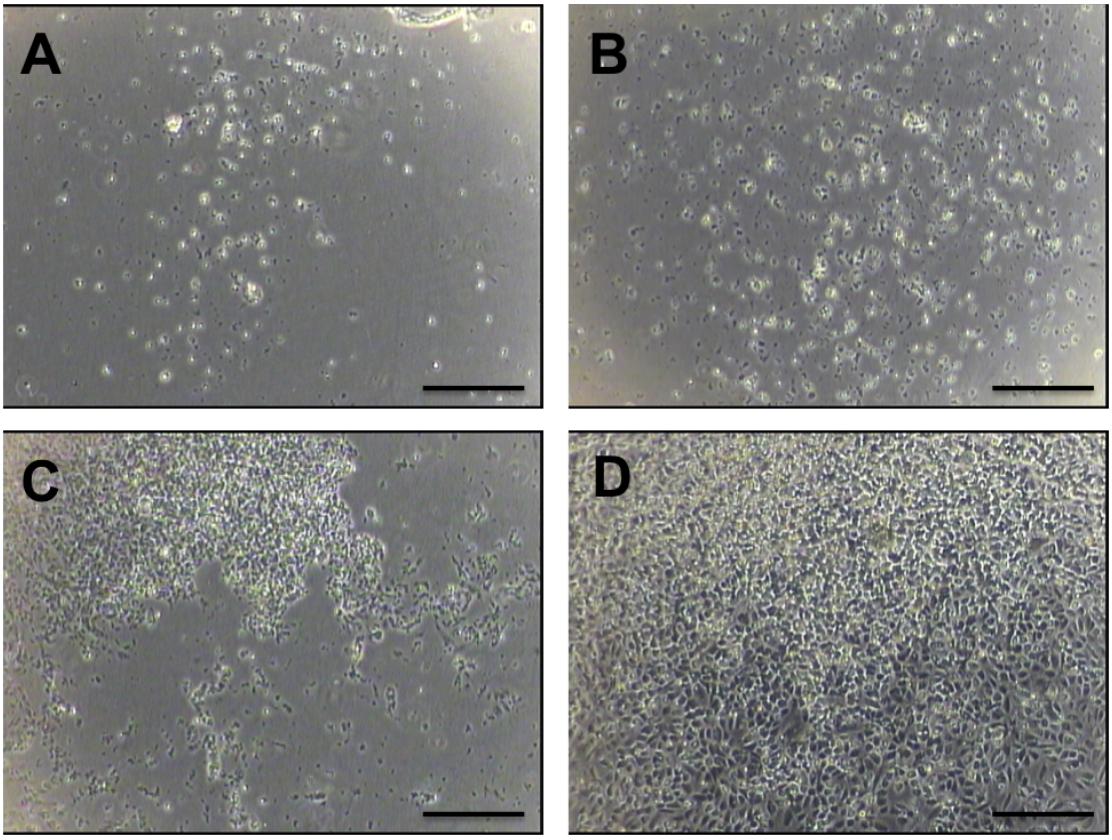

Figure 27. *Histopathologic observation of HUVECs upon treatment with sclerosing foams. Microscope images (4x magnification) illustrate HUVECs monolayers treated for 15 seconds using PEM (A), DSS (B), Tessari (C) foams, and untreated (D). Scale bars are 200 µm.*

4.4 Discussion

Since the introduction of foam sclerotherapy as a treatment method against varicose veins, numerous studies have been conducted in order to further the understanding of the physical properties and behavior of foams (McAree et al., 2012).

However, a relatively limited body of work has focused on the biological effects of sclerosants on endothelial cells and the vessel wall (Parsi et al., 2008).

Earlier studies have revealed that sclerosing efficacy is directly correlated to treatment time and sclerosant concentration (Erkin et al., 2012). However, the lack of quantitative analyses and the difference between the physical properties of sclerosing agents investigated have both hindered the ability to draw generalized conclusions about the efficacy of different foam production and administration methods.

In this study, a simple quantitative method were employed to compare the microscopic effect of different foam production techniques on the endothelium. Therefore, an *in vitro* model that allows the quantification of sclerosant-induced endothelial disruption has been proposed, by determining the number of cells attached to a substrate after treatment. In this method, monolayers of endothelial cells provide a simplified replica of a small segment of vascular

endothelium. The experimental protocol has been designed to mimic the different treatment phases occurring *in vivo,* i.e. (i) injection of the foam and its contact with the endothelium, and (ii) washing out of the foam due to blood flow. Being a biological model within a static fluidic environment, foam-induced blood displacement occurring *in vivo* is reproduced by an active washing phase. With this model, clinically relevant procedural parameters have been investigated, such as volume of foam injected, treatment time, and usage of different types of needle.

The repeatability of the method was initially evaluated, showing significant consistency across multiple independent repeats (Figure 16). In a first step of the study, the model was utilised to investigate the sclerosing efficacy of liquid POL. Only at volumetric concentrations <0.02% the surfactant was rendered ineffective, confirming the potency of this detergent at disrupting the endothelial cell membrane and inducing cell death (Kobayashi et al., 2006)(Figure 17). Serial treatments using the same POL solution were performed to assess whether polidocanol deactivation occurred. Reducing the number of active molecules (i.e., by lowering the POL concentration) caused reduced efficacy after a certain number of treatments, which was dependent upon the POL concentration (see Figure 18). Depletion of active polidocanol over consecutive treatments was likely due to its intercalation within lysed membrane fragments. However, the 1% POL solution (employed to manufacture both PCF and PEM foams) maintained its potency across multiple treatments, and its *in vitro* biological performance was not affected by polidocanol depletion.

Upon verification of polidocanol efficacy *in vitro*, the effect of administering sclerosing foams with needles of different bore diameter was investigated. The needle bore size is typically selected based on the vein to be treated, with smaller veins often requiring the smaller 25-30G needles (Goldman et al., 2017).

The performance of different sclerosing foams was statistically different only when using the larger needle (16G) (Figure 20). Employing narrower needles (i.e., 25G and 30G), foam efficacy reduced and differences between foam types were not statistically significant. This observation may be due to changes in the physical properties of foams when they were conveyed through a needle. Bubble size measurements however revealed that the bubble size distribution of all types of foam was virtually unaffected by the needle inner diameter (Figure 21). Previous studies have shown that as foam flows through a pipe, the change in bubble

diameter is dependent on the pressure drop across the pipe. It can therefore be inferred that the pressure drop required to administer foams manually through clinical needles – and the resultant shear rate – were not sufficient to cause a significant change in the bubble size of PEM and PCF foams. Thus, the observed changes in foam therapeutic efficacy could not be directly related to the foam bubble size distribution. For this reason, additional experiments were performed to quantify the effect of needle injection on foam drainage dynamics, where drainage describes the flow of liquid through a foam (Bikerman, 1973). During free drainage, the liquid volume fraction increases monotonically from the top to the bottom of a foam column. This bottom liquid layer is depleted of surfactant molecules, as the surfactant preferentially stabilises the gas-liquid interface of bubbles located in the upper foam layer. The liquid then continues to drain downward over time, until the liquid height reaches a steady state (Koehler et al., 2000)(as shown in Figure 22). Given that drainage is strongly affected by the size and shape of the foam container, a vial with inner diameter comparable to the well plate used in biological tests was employed. By injecting foams through the narrowest needle (30G) caused visible separation of the liquid and gaseous phases upon injection; thus, the ejected foam experienced only limited drainage. Phase separation may occur because of the liquid POL travelling at a different velocity compared to the gas bubbles, as observed for other multi-phase systems delivered through needles, such as pastes and cements (O'Neill et al., 2017).

The extent of phase separation reduced with increasing the needle inner diameter (corresponding to lower injection velocity), and was almost absent when foams were administered using the largest 16G needle. When foam separation occurred (i.e., using the 25G and 30G needles), the biological efficacy of foams was dominated by their 'static' liquid fraction, and differences between foam types were not statistically significant (Figure 20). Conversely, when phase separation was significantly reduced (as in the 16G needle experiments), the ejected foams displayed distinct drainage dynamics that in turn led to differences in their biological efficacy. Notably, the slower drainage of PEM foam resulted in statistically greater therapeutic efficacy compared to PCF foams (Figure 20), which instead presented a faster initial drainage dynamics. The more rapid drainage of room air PCF foams could be attributed to: (i) the greater liquid:gas volume ratio compared to PEM foam (Carugo et al., 2016), with previous studies reporting on a direct correlation between foam drainage velocity and liquid fraction (Saint-Jalmes, 2006). (ii) The lower average bubble diameter combined with the presence of a greater proportion of bubbles with diameter >400 μm (see

Fig. 20). Notably, higher pressure within the smaller bubbles drives diffusive gas exchange towards the larger bubbles, and the resulting coarsening of the foam accelerates its initial drainage dynamics (Cohen-Addad et al., 2013).

The mechanism, for which the slower foam drainage of PEM leads to greater therapeutic efficacy *in vitro*, is not fully understood yet. However, it could be attributed to the persistence of gas bubbles in the vicinity of the cell membrane, with higher concentration of active polidocanol located at the gas-liquid interface. Conversely, when fast-draining foam is employed, cells are exposed to the liquid phase that has been depleted of polidocanol, particularly in the shorter term. Depletion is greater in N_2-containing foams, given to the lower 'mobility' of surfactant molecules in these foams (Sun et al., 2016)

The effect of the injected foam volume was also investigated, as it represents a parameter that is varied in the clinical practice. Generally, the volume injected is dependent on the diameter and length of the vein to be treated (Dietzek, 2007). There was a significant difference between foam production methods when injecting 0.5 and 1 mL of foam, whereas all treatments had very similar biological performance and became more effective when injecting a greater volume of foam (2 mL) (see Figure 24). Earlier studies have reported that the dependence of drainage time on the foam liquid fraction reduces with increasing the height of a foam column (Saint-Jalmes et al., 1999), which may explain the comparable efficacy of PEM (liquid fraction: 12.5%) and PCFs (liquid fraction: 20%) at 2 mL. The positive correlation between the injected volume and treatment efficacy may be attributed to increased gravitational effects at the higher foam heights[43], which favors downward motion of active polidocanol towards the cell monolayer. It should be noted that a foam volume ≤1 mL is more representative of a clinical injection procedure, considering the volume of foam normalised to the area of the treated endothelial layer. At these lower volumes, drainage dynamics is governed by both capillarity and gravitational effects.

The effect of varying the treatment time was also investigated. The exposure time was defined based on the predicted persistence of a foam plug *in vivo* (Carugo et al., 2015) and values investigated were 15, 30, 60 and 120 seconds (Figure 25). Overall, there was significant difference in biological efficacy between 15, 30, and 60 seconds of exposure. However, for all types of foam, efficacy significantly increased at 120 seconds of exposure. Notably, bubble collapse in the longer term causes a release of active polidocanol, and biological effects thus become dependent on the liquid POL solution. Further investigations are required to fully

elucidate the interplay between foam drainage and the temporal dynamics of membrane disruption upon exposure to the surfactant agent. Overall, PEM maintained superior performance across the all range of exposure times investigated and was more effective over longer term exposures, likely due to its sustained drainage dynamics compared to PCFs.

Considering the potency of the 1% POL solution over multiple treatments *in vitro* the greater therapeutic efficacy of PEM compared to PCFs may not be solely attributed to differences in foam stability and drainage dynamics. Previous studies have demonstrated that the diffusion velocity (or mobility) of water-soluble surfactants in foams is affected by the gas formulation, and that it is greatest in CO_2 foams, followed by O_2 foams and N2 foams (Sun et al., 2016). Experiments were thus conducted using PEM manufactured using different gas formulations (Figure 26), to assess whether changes in surfactant mobility may influence its therapeutic efficacy. Coherently with these previous findings, the commercial PEM formulation (35:65 CO_2:O_2) had greater efficacy than both 100% O_2 PEM and N_2-containing (RA) PEM. These results suggest that polidocanol is more readily available for interaction with cell membranes, when N_2-free foams are employed.

4.5 Conclusion

The present study represents the first systematic comparison of the biological performance of different sclerosing foam formulations, and a first attempt to correlate biological performance with foam physical properties.

Overall, PEM was the most effective foam for disrupting the endothelial layer in a variety of tests and over different timescales of treatment. This was attributed to the slower drainage dynamics of PEM compared to PCFs, and – potentially – to the enhanced polidocanol mobility conferred by its gas formulation. It was also shown that reducing the injection needle diameter, increasing the volume of injected foam, and increasing the treatment time, all contributed towards increasing treatment efficacy (for all types of foam).

It should also be highlighted that PCFs made from room air have associated risks, with persistent nitrogen bubbles in the circulation, whereas PEM, made with a low-nitrogen CO_2:O_2 gas mixture, is not associated with the risks of high-nitrogen content.

In conclusion, in this study a simple 2D *in vitro* method to quantify the efficacy of foam sclerotherapy has been developed. The method allows for the investigation of different clinical parameters such as exposure time, injected volume, concentration of sclerosant, and needle

bore size amongst others. However, the model does not fully reflect the clinical setting for foam sclerotherapy, because it is employed in static conditions and thus does not replicate foam-induced blood displacement, and also does not provide a faithful replication of the varicose vein architecture.

Therefore, a more realistic biological model, i.e. a three-dimensional *ex vivo* vein model, could be utilized as a further method of evaluation to understand the effect of sclerosants on the endothelial layer of the veins.

Chapter 5: Evaluation of the membrane effects of sclerosants by measuring the variation of lipid packing.

Chapter 5 describes the use of a quantitative fluorescence microscopy technique (i.e. spectral imaging) to measure changes in the physical properties of cell membranes interacting with liquid and foamed sclerosants.

Abstract

Polidocanol is a surfactant agent commonly used for the treatment of varicose veins. Although the mechanism of action has not been clearly identified, it has been postulated that POL interferes with cell membranes upon administration. The surfactant molecules are absorbed by the cell membrane, disrupting the normal architecture of the lipid bilayer.

In the present study, a quantitative fluorescence microscopy technique has been employed to measure changes in the physical properties of cell membrane interacting with liquid and foamed POL. A polarity-sensitive fluorescent probe (Di-4-AN(F)EPPTEA) has been used to quantify cell membrane lipid packing. This probe detects changes in membrane hydration thanks to its sensitivity to the polarity of the surrounding micro-environment. More tightly packed (ordered) lipid environments accommodate a lower number of water molecules and are therefore relatively less polar than disordered environments. Variations in membrane water content cause shifts in the probe emission spectrum, which are quantified by calculating the generalized polarization (GP) ratiometric parameter. Herein, membrane fluidity changes in two cell lines have been investigated. Variations in cell membrane fluidity caused by POL-based agents have been studied by spectral imaging using laser scanning microscopy, in order to gain a greater understanding of their mechanisms of action.

5.1 Introduction

Surfactant sclerosing solutions are commonly used for the treatment of varicose veins, as they cause endothelial damage by interfering with cell surface lipids (Jia et al., 2007). Surfactants are absorbed by the cell membrane and disrupt the normal architecture of the lipid bilayer, reducing the surface tension. The outcome of this interaction is dependent upon the concentration of surfactant (Parsi, 2015). Above certain concentration levels, surfactants solubilize cell membranes resulting in cell lysis (Goldman et al., 2017).

Surfactant compounds are characterized by having hydrophilic and hydrophobic moieties in their chemical structure (Hua and Rosen, 1991). The amphiphilic nature of these compounds is responsible for their surface activity. Notably, surfactants can decrease the surface tension between two fluids, i.e. between a gas and a liquid, or between a liquid and a solid, by adsorbing at the interface between the two fluid phases (Phan, 2018). Surface tension is a measure of the contracting power of the surface (measured in N/m; i.e. force per unit length). When surfactant molecules are solubilized into an aqueous solution, they orientate themselves at the surface in order to remove the hydrophobic group from the aqueous phase and hence achieve a minimum free energy state. Increasing the surfactant concentration causes the surface tension of a surfactant solution to progressively decrease, due to the higher number of molecules entering the interface layer between liquid and gas. At a certain critical concentration, this layer becomes saturated of surfactants molecules, which start to aggregate generating micelles, an aggregate of molecules that arrange themselves in a spherical form (Gu and Sjöblom, 1992) (Figure 28).

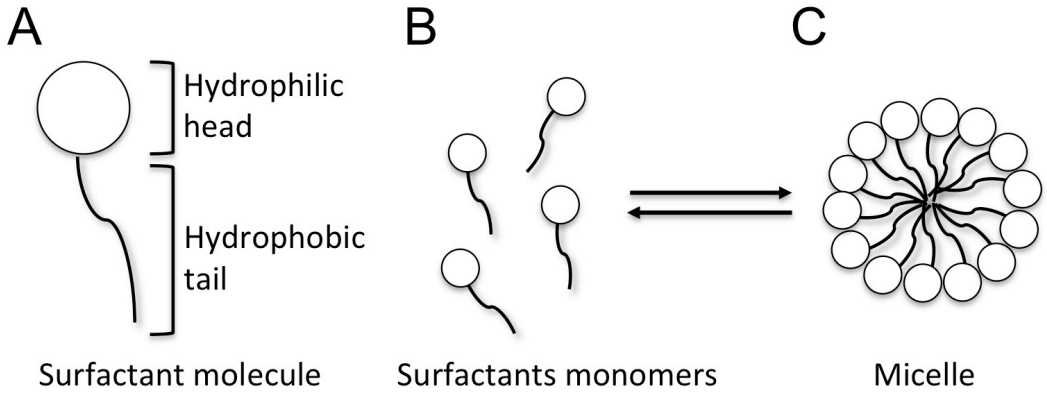

Figure 28. *Representative schematics of a surfactant molecule and a micelle. (A) Surfactants are amphiphilic molecules composed by a hydrophilic head and a hydrophobic tail. (B) Surfactant monomers at a certain concentration (known as CMC) aggregate to generate (C) micelles.*

The concentration at which micelles begin to form is termed *critical micelle concentration* or CMC. Above the CMC, monomers of surfactant molecules and micelles exist in dynamic equilibrium. The CMC value is dependent on the size, charge and length of the surfactant molecule and varies with the buffer/salt used (Kuni et al., 2004).

Surfactants have a striking similarity to the phospholipid molecules that constitute the lipid bilayer of cell membranes.

The cellular membrane has been theorized as a fluid mosaic model, as proposed by Singer and Nicholson in 1972 (Singer and Nicolson, 1972). The cellular membrane is mainly composed by lipids such as phosphatidylethanolamine and phosphatidylcholine, and by a less abundant quantity of glycolipids, cholesterol and proteins (van Meer et al., 2008) (Figure 29).

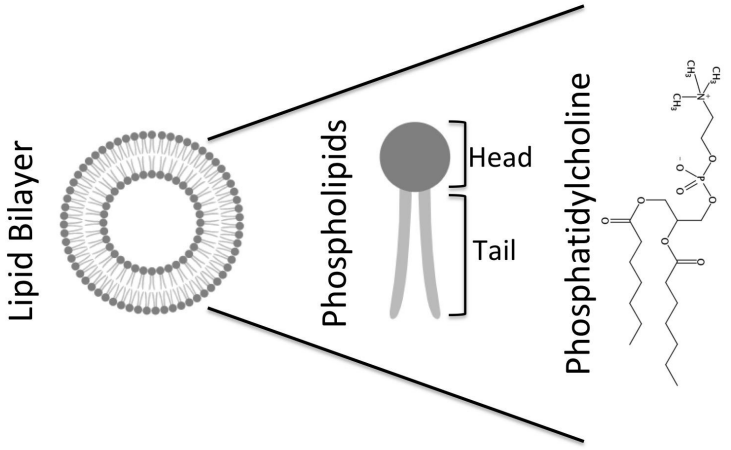

***Figure 29**. Schematic representation of the main component of the cellular membrane. The cellular membrane is a bilayer composed of phospholipids (amphiphilic molecules), which present a polar head and two hydrophobic tails. The most abundant phospholipids are phosphatidylcholines.*

The whole cell membrane is held together by non-covalent interaction between the hydrophobic tails of the lipids, which are freely to move on the membrane surface. Membrane phospholipids are also amphiphilic molecules, and usually contain two hydrocarbon chains forming the tail group (while surfactants may have one or two such chains) (Watson, 2015).

The lipid bilayer is a thermodynamic system that shifts from the relatively disordered liquid phase to the relatively ordered gel or solid-phase depending on the temperature in the system. In the gel phase, the lipid bilayer goes through a fundamental molecular reorganization characterized by an increase in order, a loss of lateral mobility along with change in acyl chain configuration within a single lipid molecule, and a change in the topology of the membrane

(Alvares et al., 2017). In the gel phase, individual lipids within the lipid bilayer lose lateral mobility, associated with a further increase in order. The lipid head groups become more tightly packed and dehydrated, and the lipid acyl chain tails become fully extended and more tightly packed with increased Van der Waals interactions.

The large compositional heterogeneity of phospholipids in the cellular membranes can generate heterogeneous physical properties in the physiological temperature range, namely the coexistence of the gel and the liquid phases.

Different lipid-packing states are related directly to the water concentration of the system. The hydration increases in the following order: liquid phase (lipid disordered) > gel (lipid ordered) (Quinn and Wolf, 2009).

In biochemistry, surfactants are generally employed to solubilise membrane proteins and lipids (Heerklotz, 2008; Partearroyo et al., 1990; Pang et al., 2006). The solubilisation process includes four phases determined by the surfactant concentration:

(i) Non-co-operative interaction. At low concentration, surfactant monomers inserts into the outer membrane leaflet. The process is usually fast (50-500ms). Secondly, the surfactant has to equilibrate between the outer and inner leaflet of the cell membrane. Therefore, its polar head has to cross the hydrophobic core by flip-flop or another mechanism of penetration (within milliseconds to some tens of seconds). The surfactant leaving the outer leaflet by flipping to the inner leaflet is partially replaced by further uptake from the aqueous phase.

(ii) Co-operative interaction and saturation. Above a certain 'critical saturation concentration (C_{sat}), surfactant monomers aggregate within the membrane to generate small domains, which are capped at the edges by toroidal (doughnut-shaped) complexes of surfactant monomers.

(iii) Solubilisation. As the surfactant to lipid ratio increases to reach the 'critical solubilisation concentration' (CSC), the bilayer is disrupted and mixed surfactant-lipid micelles and small membrane sheets are generated.

Ultimately, only mixed lipid-surfactant micelles and surfactant-covered membrane fragments are present. Surfactants also interact with the hydrophobic portions of membrane proteins.

Therefore, when the surfactant to lipid ratio increases, the lipid bilayer is progressively penetrated, fragmented and eventually solubilised. The level of cell membrane disruption is

influenced by the physical and chemical characteristics of the surfactant molecule, such as its CMC, electrostatic charge and length if the hydrocarbon chain.

Surfactants with a neutral and large head group and longer hydrocarbon chains (such as POL) have milder solubilisation potential compared to ionic detergents (such as sodium dodecyl sulfate - SDS), since non-ionic detergents break lipid-lipid and lipid-protein, but not protein-protein interactions (Heerklotz, 2008; Jones, 1992; Parsi, 2015).

POL molecules, having a non-ionic head and hydrophilic-hydrophobic properties of the polyoxyethylene tails are able to rapidly re-orientate from one leaflet of the membrane bilayer to the other (flip-flop), whereas detergents with strongly hydrophilic heads - such as SDS - flip at a low velocity, resulting in delayed solubilisation (Parsi, 2015).

The insertion of the surfactant molecules into the bilayer leads to an imbalance in area requirement between the two coupled lipid leaflets, resulting in a local bend and/or the development of a bilayer curvature strain, which causes reduction in the lipid packing. In turn, the membrane becomes thinner and more flexible. Chain disordering is accompanied by changes in the interfacial and head group region of the membrane. Therefore surfactants tend to shift crystalline state of the cellular membrane from gel to liquid (Groot and Rabone, 2001).

Additionally, surfactants can increase the membrane permeability due to the induced bilayer curvature strain and the formation of toroidal membrane pores, where the hydrophobic edges of the pores are covered by surfactants molecules. The size of the pores depends on the concentration of the surfactant and the spontaneous curvature of the molecules.

At higher concentration, surfactants may disrupt the lipid-packing and increase membrane permeability until complete disruption of cell membrane.

Therefore, measuring lipid packing of the cell membrane might be a novel method to evaluate the interaction between surfactant molecules and the cell membrane.

In the present study, a quantitative fluorescence microscopy technique has been employed to measure changes in the water content of cell membranes interacting with surfactant molecules.

Polarity-sensitive fluorescent probes such as Laurdan, Di-4-AN(F)EPPTEA and Di-4-ANEPPDHQ are useful tools to study lipid bilayers (Figure 30).

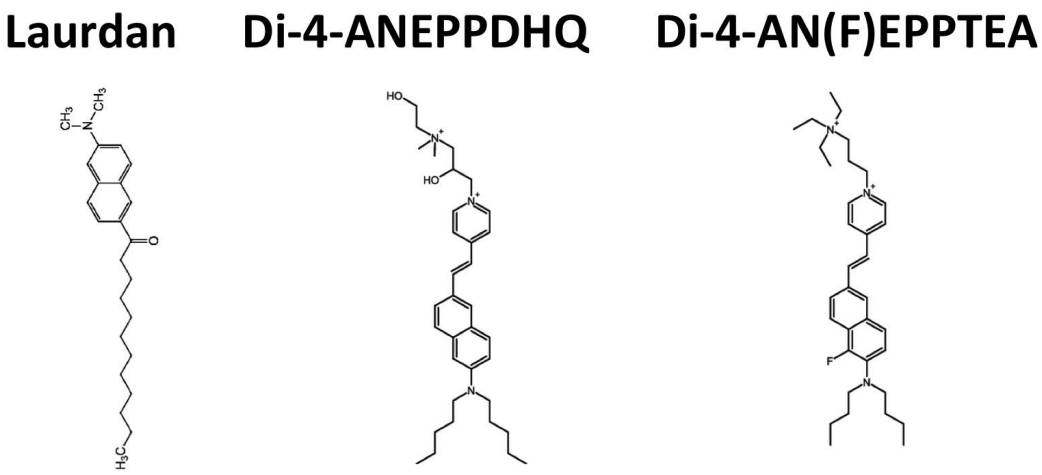

Figure 30. *Chemical structure of common polarity-sensitive fluorescent probes, namely Laurdan, Di-4-AN(F)EPPTEA and Di-4-ANEPPDHQ.*

These dyes change their emission spectrum depending on the environmental conditions (Parasassi et al., 1991; Amaro et al., 2017). Therefore, these fluorescent probes are able to detect changes in the membrane packing, thanks to their sensitivity to the polarity of the surrounding environment. More tightly packed (ordered) lipid environments accommodate a lower number of water molecules and are therefore relatively less polar than disordered environments. Variations in membrane water content thus cause wavelength shifts in the probe emission spectrum (Parasassi et al., 1998), which are quantified through a ratiometric parameter known as generalized polarization (GP)(Figure 31) (Jin et al., 2005).

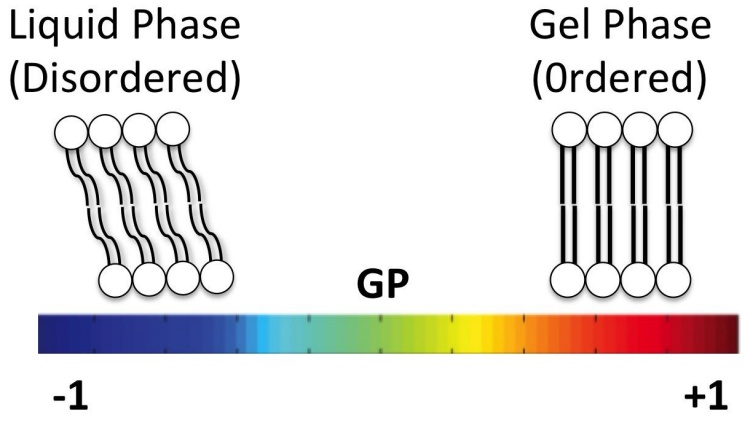

Figure 31*. Schematic representation of the lipid bilayer in its two phases: liquid (disordered) and gel (ordered). Lipid bilayers exist in either the liquid or gel phase, at a broad range of temperatures. The GP value varies from -1 to +1, which indicates the disordered and ordered phases, respectively.*

This technique has been used successfully to study bilayer properties in both artificial and natural membranes (Carugo et al., 2017).

Among the surfactant commonly employed in sclerotherapy, this study focuses specifically on polidocanol (POL), a polyethylene glycol ether of lauryl alcohol (Nastasa et al., 2015). POL is a non-ionic surfactant consisting of two moieties, a polar hydrophilic (dodecyl) head and an apolar hydrophobic (polyethylene oxide) chain. Liquid POL at a concentration of 0.50% (v/v) is used to treat telangiectasias and reticular veins, whilst varicose veins treatment typically requires a POL concentration of 1 – 3% (Van Deurzen et al., 2011).

Although the mechanism of action has not been clearly identified, it is known that POL interferes with cell membranes (Eckmann et al., 2005).

The sclerosing effect of POL arises because of the disrupting action of its polar head group on the non-covalent bond present within the cell's lipid bilayer, leading to membrane disruption (Parsi, 2014). Here, changes in membrane fluidity upon exposure to POL were quantified in order to evaluate the effect of the liquid/foamed sclerosant at the membrane level.

Initially, the robustness of the method was applied on two model cell lines. Afterwards, cells were exposed to different concentrations of liquid POL and subsequently foamed POL. The method here proposed represents a useful tool for quantifying the disruption effect of sclerosants on the lipid bilayer.

5.2 Materials and Methods

5.2.1 Cell culture and sample preparation

HUH7 (human hepatoma cell line) and PtK2 were employed as cellular membrane models.

HUH7 cells were grown in Dulbecco's Modified Eagle Medium (DMEM) with 10% fetal bovine serum (FBS) and 1% penicillin/streptomycin (Sigma-Aldrich, USA). PtK2 cells, a cell line derived from male Long-nosed potoroo (Potorous tridactylis) epithelial kidney cells, were grown in DMEM supplemented with 15% fetal bovine serum (FBS; Sigma-Aldrich, UK) and 1% l-glutamine (Sigma-Aldrich, UK). Cells were grown in T- 75 flasks and were passaged every three days at approximately 80% confluence.

For spectral imaging, approximately 1 x 10^6 cells were seeded in 80 µm diameter petri dishes containing one 75 µm x 25 µm x 0.17 µm glass coverslip (Logitech Ltd., Scotland) in 10 mL growth medium. Coverslips were sterilized in 70% ethanol for 30 min followed by washing with phosphate buffered saline (PBS) and 30 min UV exposure prior to seeding. Cells were grown in a temperature- and CO_2-controlled incubator at 37°C and 5% CO_2. Cells were incubated with 400 nM DDi-4-AN(F)EPPTEA (custom made by Prof. Leslie Loew, University of Connecticut), a fluorescent probe used to sense lipid order in cells (absorbance,

emission peaks in ethanol: 481, 725nm), in PBS (500 µL) for 5 min prior to spectral imaging. It was determined that PBS was a suitable choice of medium for both imaging quality and cell viability given the short duration of the experiments (1-2 minutes). In both experiments, the medium was gently replaced with fresh PBS prior to imaging (500 µL), and cells were kept at 37°C using the temperature-controlled chamber of the confocal microscope (Zeiss LSM 780, Carl Zeiss AG, Germany) for the duration of the experiments. All cell culture materials were purchased from Thermo Fisher Scientific (UK) unless stated otherwise.

5.2.2 Spectral imaging

Spectral imaging is an imaging technique that uses multiple bands across the spectrum from infrared to x-rays.

This method allows to obtain lambda stacks, which consist of an image collection using the same specimen field acquired at different wavelength bands.

Spectral imaging in this study was performed with an LSM 780 confocal microscope (Zeiss Microsystems, Mannheim, Germany) equipped with a 32-channel GaAsP detector array. Laser light at 488 nm was selected for fluorescence excitation of the probe. The λ-detection range was set between 560 and 650 nm.

The images were saved in .lsm file format and then analyzed with the freely available Fiji/ImageJ plugin (National Institutes of Health, Bethesda, MD), as described in (Sezgin et al. , 2014).

5.2.3 Treatment

Both cell lines were employed for testing the effect of liquid/foamed POL on lipid-packing. After incubation with the fluorescent probe, PBS was replaced with 500 µL of a liquid POL solution, which was directly injected into the microscope chamber that can hold 25 µm (diameter) round glass coverslips (Attofluor™ Cell Chamber, for microscopy, Thermofisher). The cell monolayer was exposed to POL during a minimum fixed time of 40 seconds. POL was employed at different volumetric concentrations of 1.00%, 0.50%, 0.06%, 0.03% and 0.015% in order to evaluate the minimum effective concentration.

Additionally, POL was utilised in foamed form, 500 µL of foam was injected either directly onto the cell monolayer or after priming the cell dish with 500 µL of PBS.

Experiments with foams included two types of test: (i) the injection of foams directly onto a monolayer of cells (referred to as ‘dry-test’) or (ii) upon covering cells with 500 µL of PBS

(referred to as 'wet-test'). These experiments replicate two different 'therapeutic scenarios': (i) the foam injected inside the vein lumen displaces blood completely and is thus directly in contact with the endothelial layer (dry-test), and (ii) the foam is separated from the cell by a layer of liquid.

5.2.4 Foam production

PCFs and PEM were employed to evaluate foam sclerotherapy efficacy. For details on foam production methods, refer to paragraph 4.2.1 (Foam production methods).

5.2.5 Image analysis

The images and videos were saved in .lsm file format and then analyzed with the freely available Fiji/ImageJ plugin (National Institutes of Health, Bethesda, MD), as described in Sezgin et al. Grey scale images were converted into LUT format.

Videos were recorded (1 frame per seconds) and saved in .lsm format. The duration of the experiment was 0-1 minutes, since the effect of POL becomes evident after few seconds from administration, as reported in literature and in Chapter 4. The video recording started at t_0 (i.e. cells were not yet treated) and the injection of the surfactant agent occurred between the first 1-5 seconds. Videos were then converted in .tif format using ImageJ. The frames were extracted using a Python script, which generated one image stack per time frame. Each stack contained images corresponding to all of the wavelength channels (total of 23), for a given time frame (1 s). The first image stack was employed as control (before treatment, t_0). Injection of the sclerosing agent occurred between t_1 and t_5, (1-5s), thus the offset taken in consideration was 5 seconds for all the experiments. The time points after t_5 thus correspond to measurements taken after administration. Images were not processed before GP calculation. Thresholds were evaluated automatically for each image and set to exclude background fluorescence from the GP calculations and to include only the fluorescence signal from the cell membranes.

5.2.6 Calculation of generalized polarization

The most used measure of lipid packing is the generalized polarization (GP) parameter, whose value is a relative index of lipid packing based on the red- or blue-shifted emission of the probe.

Spatial maps of generalized polarization (GP) were created from the image stacks using the

freely available GP Plugin published before by Sezgin *et al.* GP generally is calculated by using the fluorescence intensities measured at two specific wavelengths. These wavelengths are chosen as the wavelengths λ_{Ld} and λ_{Lo} of maximum emission of the probe in a reference liquid-disordered (Ld) and liquid-ordered (Lo) membrane environment, respectively. For DDi-4-AN(F)EPPTEA, λ_{Ld} is equal to 560 nm (blue-shifted) and λ_{Lo} is equal to 650 nm (red-shifted). The GP values are calculated by using the fluorescence signal intensities I_R and I_B at the red- and blue-shifted emission wavelengths λ_{Ld} and λ_{Lo}, respectively, as shown in Equation 1:

$$GP = \frac{I_B - I_R}{I_B + I_R}$$

[Eq.1]

The Java Fiji plug-in developed by *Sezgin et al.* allows an efficient analysis of spectral data (plug-in is available at https://github.com/ dwaithe/GP-plugin) (Sezgin et al., 2015). The algorithm produces a spatial GP map representing the GP value for each pixel of the image. A histogram of the GP map with general histogram statistics (median, min and max values, standard deviation) is generated. The GP value varies from -1 to +1, which indicate the disordered and ordered phases, respectively.

Cell images are also converted from the grey scale images into LUT file employing ImageJ.

5.2.7 Statistical analysis

The comparisons between treatments were performed using unpaired Student's t-test with Welch's correction. Statistical significance was assumed for p-value < 0.05. All statistical tests were performed with Prism software. Data were reported as the mean ± standard deviation

5.3 Results

5.3.1 GP membrane measurement of untreated cell membranes

Initially, the membrane GP (GP_m) value of HUH7 was measured without any treatment applied, in order to identify the physiological GP_m values.

Figure 1 shows the spectral imaging and GP analysis of live HUH7 cells labeled with Di-4-AN(F)EPPTEA. Figure 32(A, C, E, G and I) show composite images of HUH7 cells (LUT-files). Figure 32 (B, D, F, H and J) show representative pseudo-coloured maps of membrane generalized polarization (GP) over HUH7 cell membranes between 560 nm and 650 nm emission wavelengths.

It is evident from the GP_m maps, that there is no GP change in the control cells at different time points (0-40s).

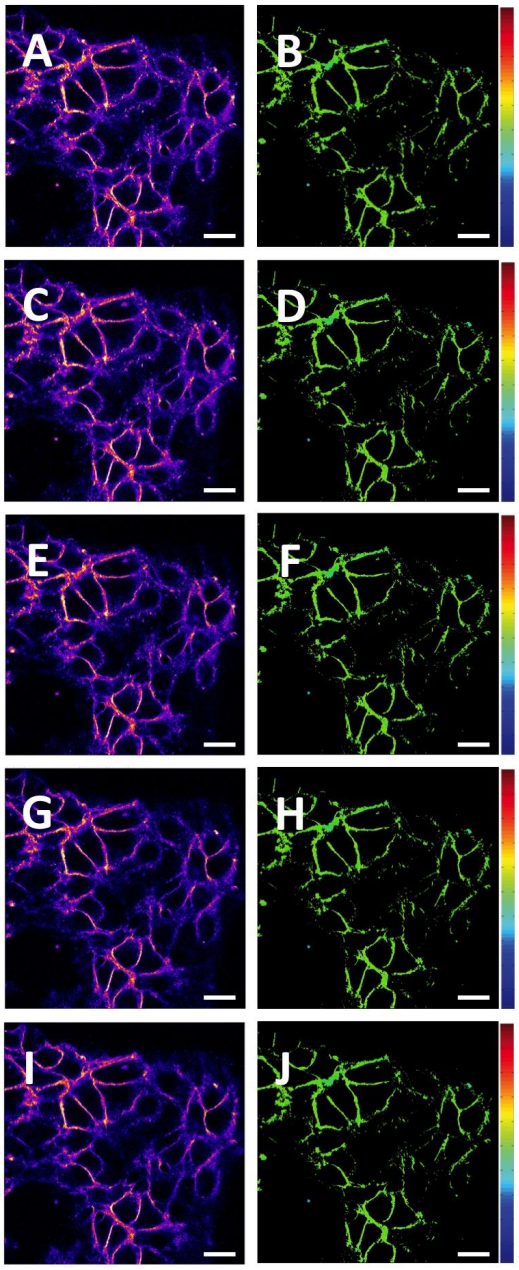

Figure 32. *Spectral GP imaging of live HUH7 cells. (A, C, E, G and I) HUH7 cells image stacks (grey scale images converted into LUT file). (B, D, F, H and J) Pseudo-colored GP maps (40 µm x 40 µm) of the equatorial plane of live HUH7 cells using the environment-sensitive membrane dye Di-4-AN(F)EPPTEA between 560 nm and 650 nm wavelength emission (scale bar 50 µm).*

GP images were converted into GP frequency plots to evaluate cell membrane hydration distribution at each time point (0-40 s). The resulting GP histograms are shown in Figure 33. The GP value remained stable throughout the measurement time (up to 40s). HUH7 showed

an average GP value of -0.259 + 0.13. The variation of GP between t_0 and t_{40} was 0.004 (coefficient of variation: 0.72%).

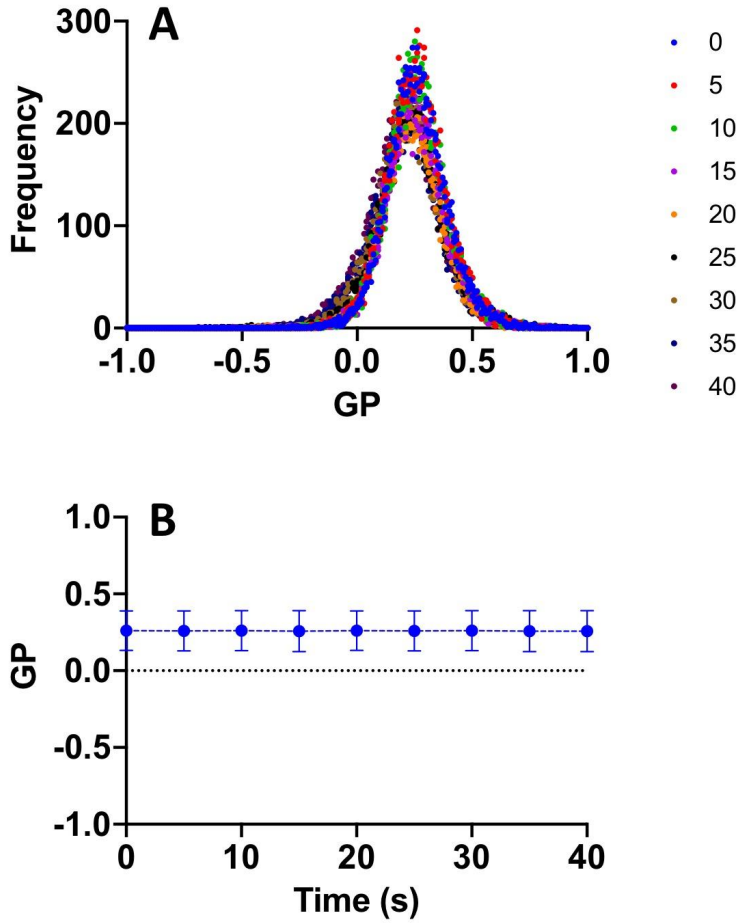

Figure 33. *Control HUH7 membrane GP measurements. (A) Histograms of GP values following Gaussian fitting indicating the variation of membrane GP up to 40s. (B) Average GP value up to 40s (blue line). Time point measurements were performed every 5 seconds. The experiment was repeated six times, and results are reported as mean value ± standard deviation.*

In order to evaluate the GP_m value into HUH7 live cells, the same measurement was repeated for several independent samples at the same experimental conditions. The membrane GP value measured for 12 different HUH7 cell cultures was 0.267 ± 0.13, with a minimum value of 0.248 and a maximum of 0.292 (Coefficient of variations 4.86%) (Figure 34).

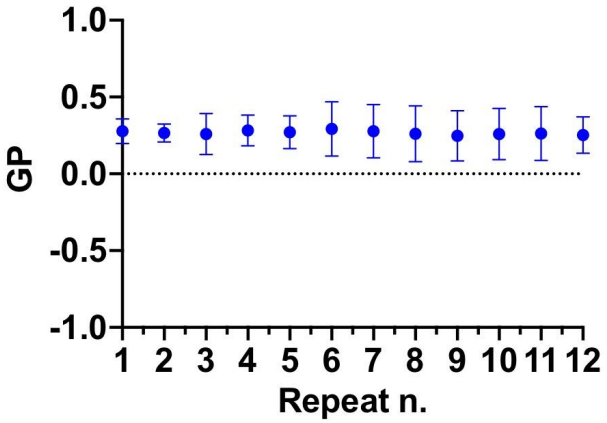

Figure 34. *Average membrane GP value in live HUH7, for 12 different independent samples (blue dots). The GP value was measured three times for each sample, and results are reported as mean value ± standard deviation.*

Afterwards, the control GP_m value of PtK2 cells was measured. The membrane GP value measured for 12 different PtK2 cell cultures was 0.173 ± 0.02, with a minimum value of 0.141 and a maximum of 0.170 (coefficient of variation: 16.30%) (Figure 35). PtK2 showed a lower average GP_m compared to HUH7 cell lines (p-value= 0.0057). A slight variability of GP_m values was identified between the same cell lines; comparing GP values of different samples for either cell lines.

Both cell line GP_m values are in line with values in the literature, which vary from 0.05 to 0.45 for different cells lines (Noutsi et al., 2016).

In order to reduce the variations associated with each measurement, the GP_m at time 0 for each sample (GPm_0) and the ΔGP_m were measured. ΔGP_m expresses the variation of GP_{m0} from time 0 and GP at a given time point t, GP_{mt}, as shown in Equation 2.

$$\Delta GP_m = GP_{mt} - GP_{m0}$$

[Eq.2]

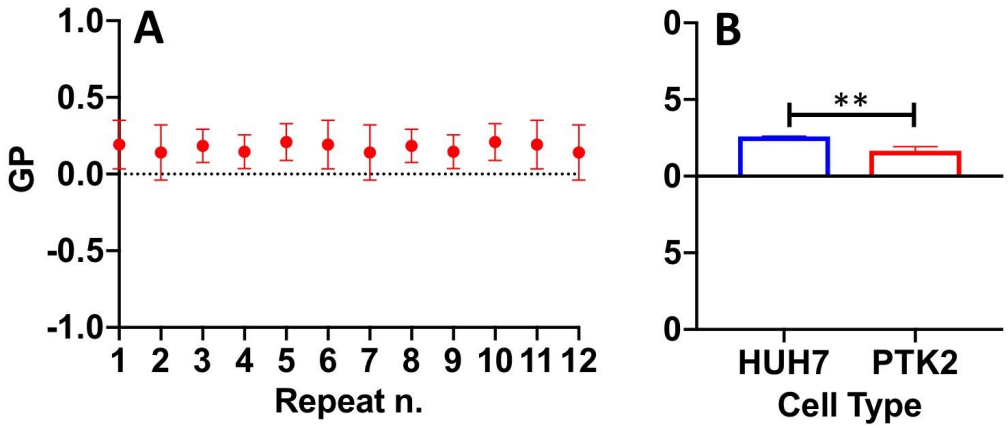

Figure 35. *Average membrane GP value in live HUH7 and PTK2. (A) Average membrane GP value in live PTK2, for 12 different independent samples (red dots). The GP_m value was measured three times for each sample, and results are reported as mean value ± standard deviation. (B) Comparison between physiological GP_m values of HUH7 and PTK2. The GP value was measured 12 times for each cell line using different samples, and results are reported as mean value ± standard deviation. Two asterisks (**) indicate that differences between mean values are very statistically significant (p-value < 0.01).*

5.3.2 GP membrane measurement of HUH7 and PtK2 treated with liquid polidocanol

After evaluating the robustness of the method, HUH7 cells were treated with liquid POL (0.06%).

Figure 36 shows representative pseudo-coloured membrane GP maps of HUH7 cells exposed to 0.06% POL. The decrease of the GP value is evident after 10 seconds of exposure.

As expected, the water content of the lipid bilayer increases during time after administration of the surfactant. This result is anticipated, because when surfactants are administered the lipid movements increases, and the membrane becomes more accessible to water molecules due to temporary defects and voids in the lipid bilayer (M'Baye et al., 2008).

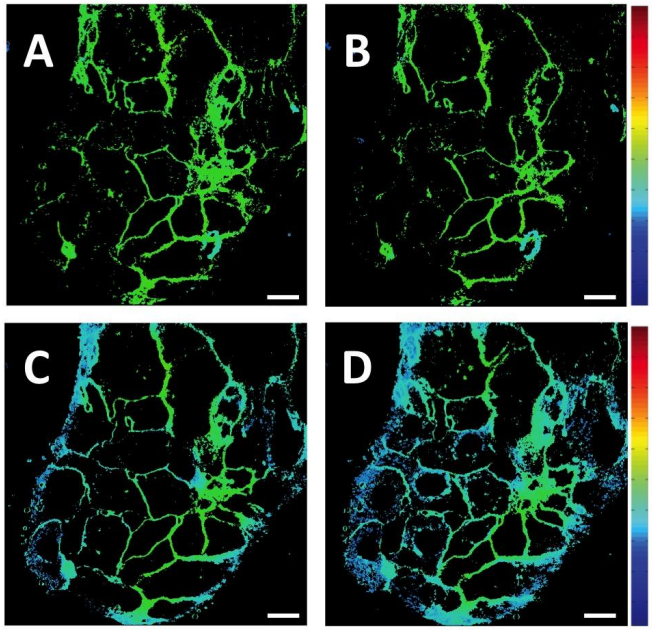

Figure 36. *Spectral GP imaging of live HUH7 cells treated with 0.06% liquid POL. GP maps (40 µm x 40 µm) of the equatorial plane of live HUH7 cells using the environment-sensitive membrane dye Di-4-AN(F)EPPTEA between 560 nm and 650 nm wavelength emission. Images correspond to different time points: (A) before POL injection (t_0), (B) 5s (t_{10}), (C) 15s (t_{20}) and (D) 35s (t_{40}) of exposure time with 0.06% POL (scale bar 50 µm).*

By analysing the GP frequency plots, a blue-shift in the emission spectrum of Di-4-AN(F)EPPTEA at 10s is evident (Figure 37). From 0 to 5s is the time window in which POL is injected. The decrease in GP_m becomes visible after 10s, followed by a progressive decrease during time. After 20s, GP decreased from 0.262 (GP_{20}) to 0.094, with a ΔGP_m equal to 0.167; and after 40s the GP value reached 0.014 (GP_{40}), corresponding to a variation of 0.248 from t_0 (ΔGP_m).

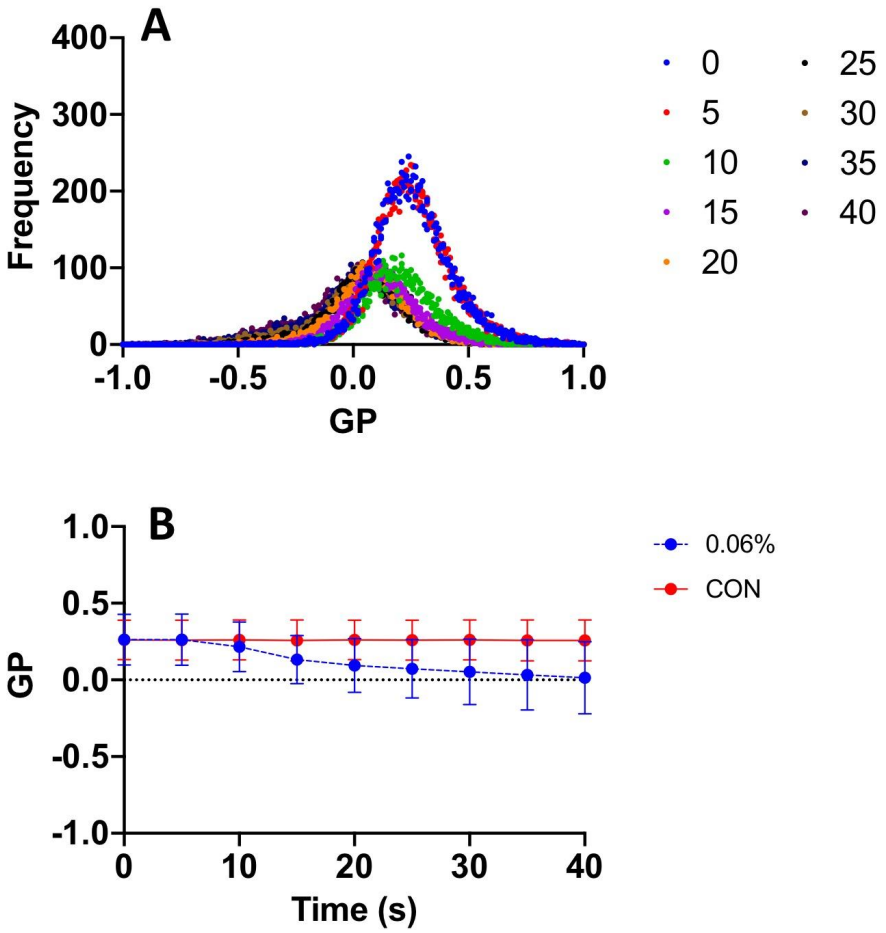

Figure 37. *GP_m measurement of HUH7 treated with 0.06% POL. (A) Histograms of GP_m values following Gaussian fitting indicating the variation of membrane GP over 40s. (B) Average GP_m value of HUH7 treated with 0.06% (blue line) compared to the control (red line) over time, up to 40s. Time point measurements were performed every 5 seconds. The experiment was repeated six times, and results are reported as mean value ± standard deviation.*

After 60s of treatment, it is evident from the GP maps that the membrane is completely disrupted and the lipids have diffused into the intracellular space. At this point the GP membrane is not measurable anymore (Figure 38).

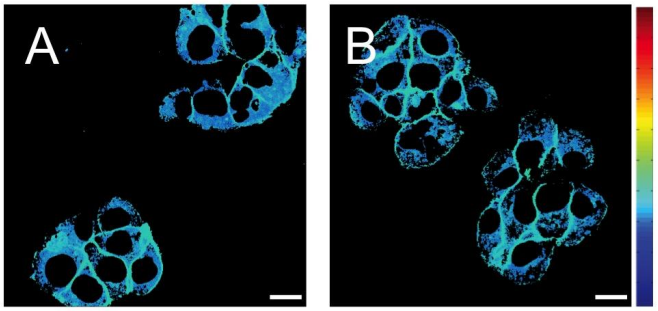

Figure 38. *Spectral GP imaging of live HUH7 cells treated with 0.06% liquid POL for 55s. GP maps (40 µm x 40 µm) of the equatorial plane of live HUH7 cells using the environment-sensitive membrane dye Di-4-AN(F)EPPTEA between 560 nm and 650 nm wavelength emission (scale bar 50 µm).*

The same experiment was repeated with the PtK2 cell line. The decrease in GP_m becomes visible after 10s, followed by a progressive decrease during time. Figure 39 shows the variation in the GP distribution curves variation over 40s of treatment. After 20 s, GP reduces from 0.209 to 0.020 (GP_{20}) with a ΔG equal to 0.189 and after 40s the GP value reached -0.115 (GP_{40}), corresponding to a variation of 0.259 from t_0 (ΔGP_m).

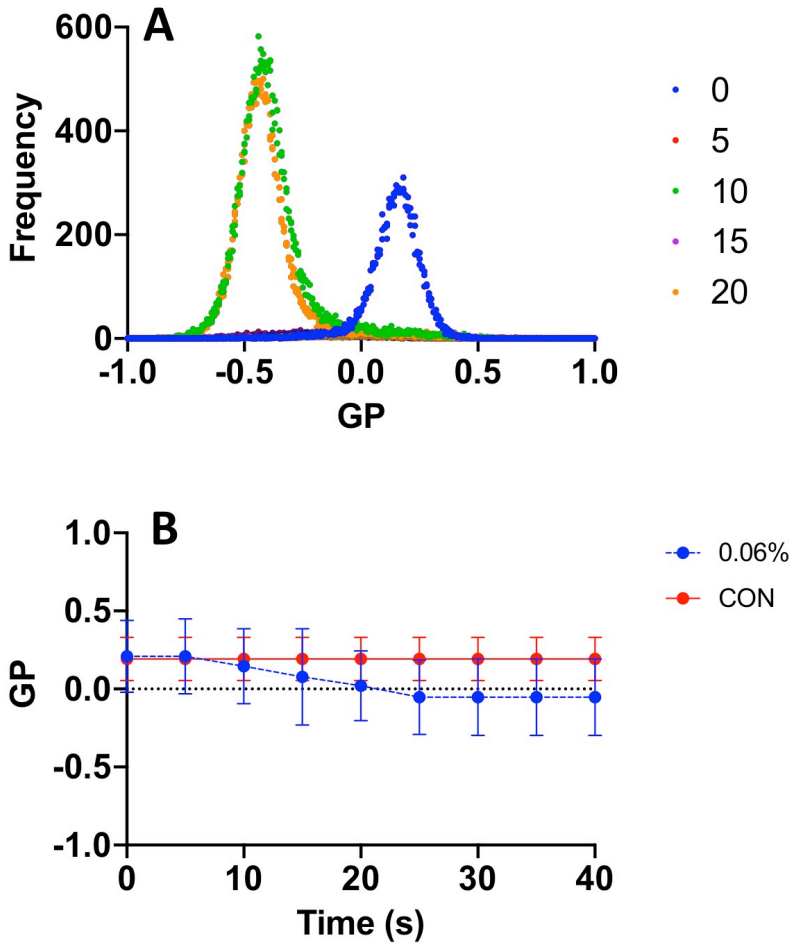

Figure 39. *GP measurement of PtK2 treated with 0.06%. (A) Histograms of GP values following Gaussian fitting indicating the variation of membrane GP over 40s. (B) Average GP value of PTK2 treated with 0.06% POL (blue line) compared to the control (red line) over time, up to 40s. Time point measurements were carried out every 5 seconds. The experiment was repeated six times, and results are reported as mean value ± standard deviation.*

Additionally, it was observed that the number of cells might have an impact on the ability of POL to affect cell membrane hydration. Notably, a lower cell number (<2 cells, confluence less than 10%) showed a greater decrease of GP, compared to higher cell numbers (>2 cells, >10%). In particular, cells at a lower number density experienced a faster decrease in the first 10s (GP_{m10} = -0.299 ± 0.17; ΔGP_m = 0.532), whereas cells at greater density had a GP_m of 0.209 ± 0.23 (ΔGP_m = 0.06). After 10s, the GP_m was not measurable any more since all the lipids migrated into the intracellular space; therefore the value reported indicate the intracellular GP (or GP_i), which is not directly comparable to GP_m (Figure 40). The reason behind this observation might be associated with differences in the ability of the surfactant molecule to diffuse between monolayer of cells or single cells.

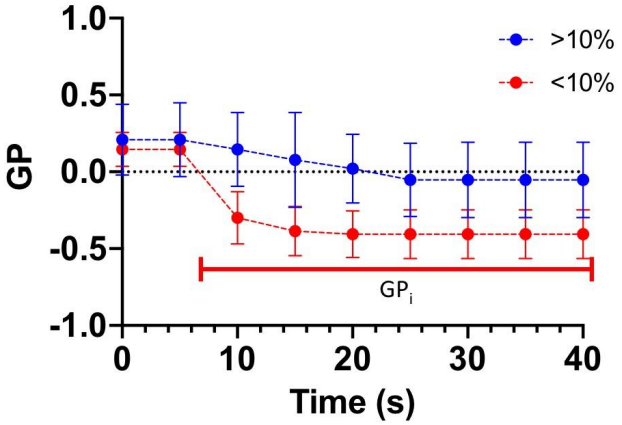

Figure 40. *PtK2 seeded at different density treated with 0.06% POL. Average GP value of PTK2 treated with 0.06% at confluence >10% (blue line) or <10% (red line) over time, up to 40s. At t_6, all the lipids moved into the intracellular space and the GP measurable is only the intracellular GP (GP_i). Time point measurements were carried out every 5 seconds. The experiment was repeated six times, and results are reported as mean value ± standard deviation.*

Figure 41 shows representative pseudo-coloured membrane GP maps of PtK2 cell membranes exposed to 0.06% POL. After 20 s of exposure, a GP_m decrease is evident. In Figure 41 (B, D) two single cells are analysed (zoom 4X). After 20s in the low density sample (<10%), the membrane appeared disrupted and the probe was internalized.

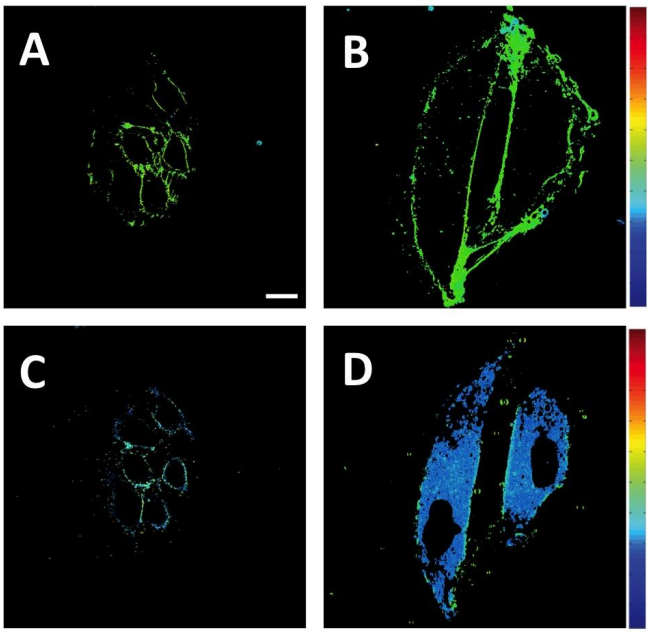

Figure 41. *Spectral GP imaging of live PtK2 cells treated with 0.06% liquid POL. GP maps (40 µm x 40 µm) of the equatorial plane of live PTK2 cells using the environment-sensitive membrane dye Di-4-AN(F)EPPTEA between 560 nm and 650 nm wavelength emission. Images correspond to different time points: (A, B) before injection (t_0), (C, D) after 15s of treatment time (t_{20}). Scale bar 50 µm).*

In order to understand the time point at which the membrane lost its structural integrity, the GP was evaluated every second (Figure 42). As it is evident from the GP maps, in the first 5 seconds the GP_m varied but the structure of the cell membrane was visible; after further 5 seconds of exposure (t_{10}) internalisation of the lipids occurred. This result shows how rapid is the effect of POL molecules in disrupting single cell membranes.

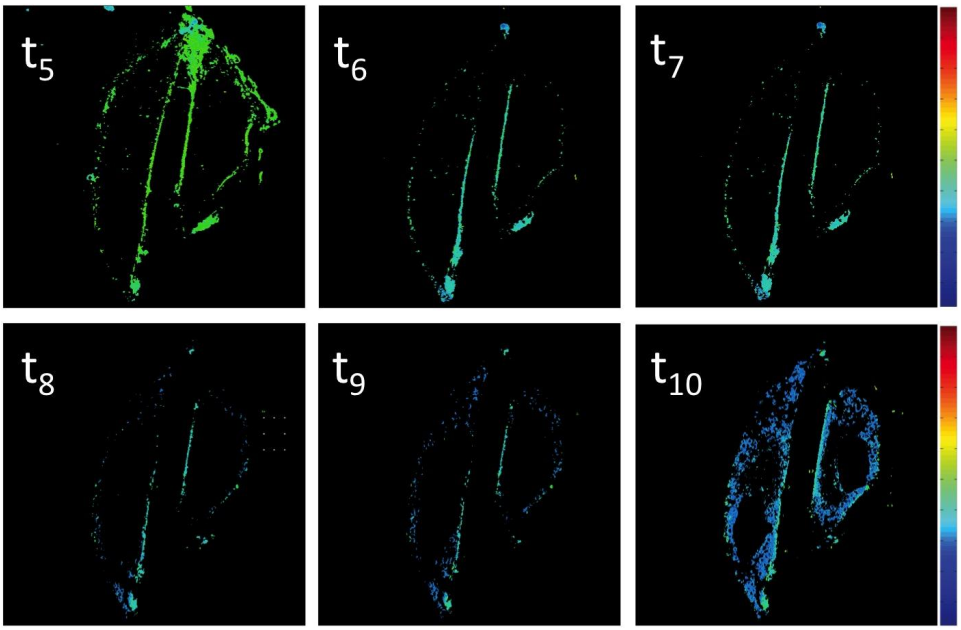

***Figure 42**. Spectral GP imaging of single PtK2 cells treated with 0.06% liquid POL. GP maps (40 µm x 40 µm) of the equatorial plane of live PTK2 cells using the environment-sensitive membrane dye Di-4-AN(F)EPPTEA between 560 nm and 650 nm wavelength emission. Images correspond to different time points: before POL injection (t_5) and 1s (t_6), 2s (t_7), 3s (t_8), 4s (t_9) and 5s (t_{10}) of exposure time with 0.06% POL. The yellow arrows indicate the intracellular movement of the lipids (scale bar 50 µm).*

In order assess variability between cell lines, and thus the potential generalization of the findings, another available cell line was adopted for comparison (PtK2).

Additionally, ΔGP_m results were analysed rather than the average GP value that can be more variable (Figure 33). ΔGP_m might be less influenced by the type of cell and by the starting GP_{m0}, which might slightly vary even for the same cell line (Figure 34 and 35A).

Figure 43 shows the comparison between PtK2 and HUH7 during treatment with 0.06% POL. Both cell lines present a similar GP trend over time. At this concentration of POL (0.06%) it is evident a gradual decrease of the GP_m. From 3s to 5s, the GP value remained unvaried, as this in the time window in which the injection occurred. After 20s, the ΔGP_m value was 0.189 (GP_{m20} = 0.02) for PtK22, and 0.167 (GP_{m20} = 0.094) for HUH7.

After 40s the ΔGP value was 0.259 (GP_{m40} = -0.050) for PTK22, and 0.248 (GP_{m40} = 0.014) for HUH7. Results are thus in agreement with the assumption that ΔGP might be not dependent on the cell type.

HUH7 cells have thus been employed as a cell model in the following experiments.

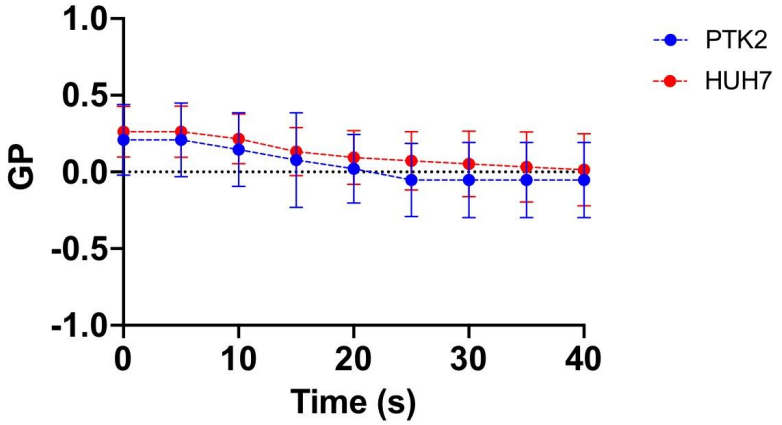

Figure 43. *Comparison membrane GP measurement of PTK2 and HUH7 treated with 0.06%. Average GP value of HUH7 (red line) compared to PTK2 (blue line) over time, up to 40s. Time point measurements were performed every 5 seconds. The experiment was repeated six times, and results are reported as mean value ± standard deviation.*

Subsequently, the sclerosing efficacy of liquid POL was investigated. The 1% POL solution was serially diluted in PBS in order to identify the minimum effective concentration for changing the lipid packing. Figure 44 shows the experimental GP frequency distribution corresponding to five different POL dilutions (A–E), such as 1.00%, 0.50%, 0.06%, 0.03% and 0.01%. As reported in Chapter 4, concentrations of POL below 0.02% rendered the treatment ineffective (50% inhibitory concentration of 0.024%). Cells treated with clinically relevant concentration - such as 1.00% POL - exhibited an evident blue shift after 5s of exposure (t_{10}-green dots), which is translated to an overall shift towards lower GP values (Figure 44). After 20s a dramatic reduction of the GP value is shown. The membrane GP is not measurable anymore, since the lipids have diffused mostly into the intracellular space. A similar trend, but with a slower rate of decrease, was observed while treating cells with 0.06% POL. At 1.00% and 0.50%, the frequency distribution of the GP_m shows two peaks after 5 seconds of exposure (t_{10}). This is caused by the coexistence of different lipid-packing phases before the complete disruption of the cellular membrane occurred.

The blue-shift becomes less evident when decreasing the POL concentration below 0.06%. At 0.03% POL, the shift is almost absent and at 0.01% no change in GP over time is appreciated.

.

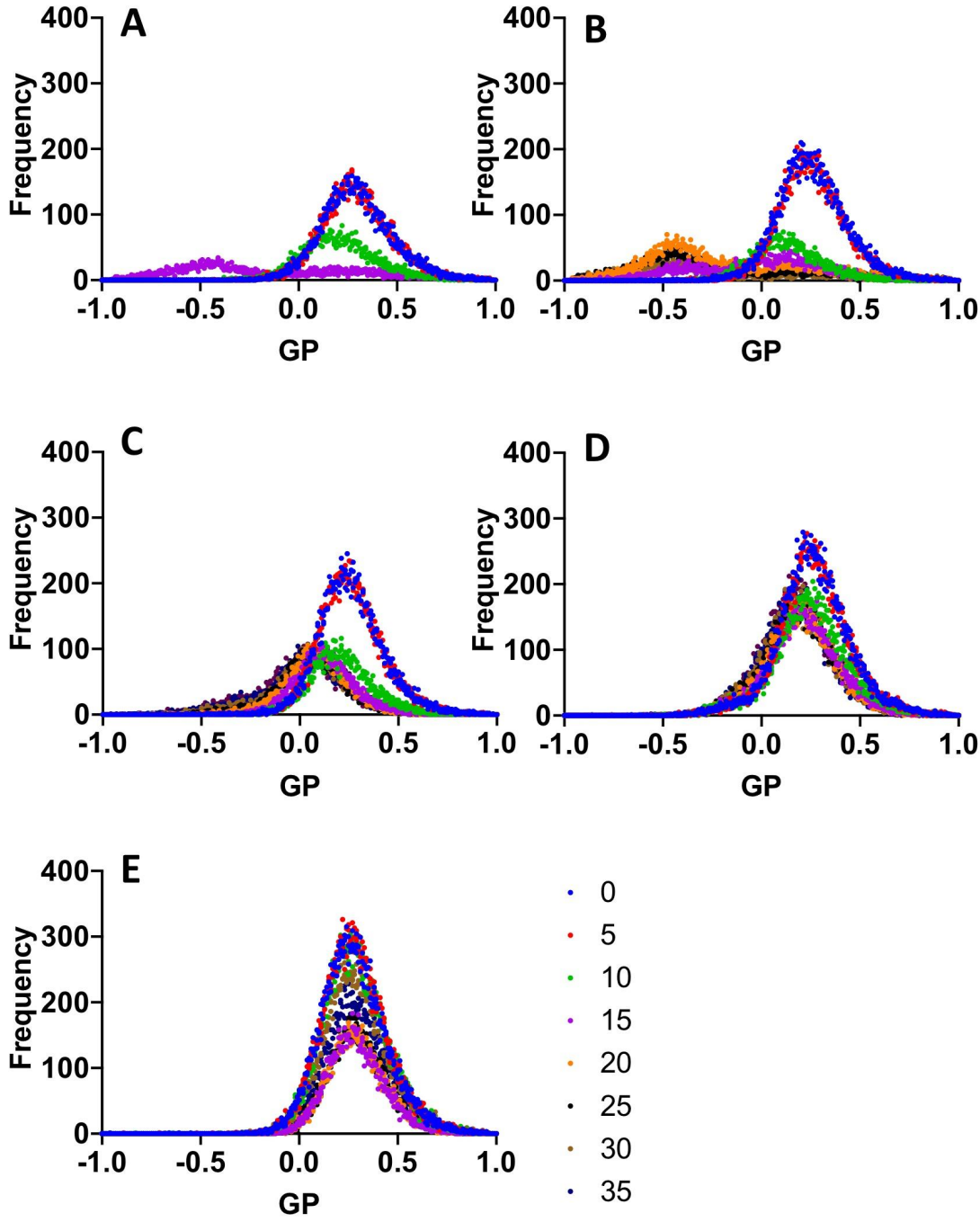

Figure 44. *GP measurement of live HUH7 treated with five different dilutions of liquid POL, namely (A) 1.00%, (B) 0.50%, (C) 0.06%, (D) 0.03%, and (E) 0.01%. Histograms of GP values following Gaussian fitting indicating the variation of GP distribution over time, up to 40s. Time point measurements were performed every 5 seconds.*

Figure 45 shows the average GP value for different POL dilutions. At 20s, the GP_m values for 1.00%, 0.50% and 0.06% POL are similar (0.32, 0.33 and 0.23 respectively), whereas GP_m for lower concentrations decreased significantly to 0.012 (0.03%) and 0.008 (0.001%). The

higher concentrations, 1.00% and 0.50%, caused complete cell membrane disruption in less than 15-25 seconds. At these time points, the fluorescence signal was almost absent and it was not possible to quantify a GP_m value. The GP_m value determined after 20s of treatment with POL 1.00% was -0.11 at 15s (ΔGP_m = 0.47). Concentrations lower than 0.50% showed a similar trend and a gradual decrease of GP_m over time. At 0.01% POL, the maximum ΔGP_m measured was 0.012, which was comparable to the control test.

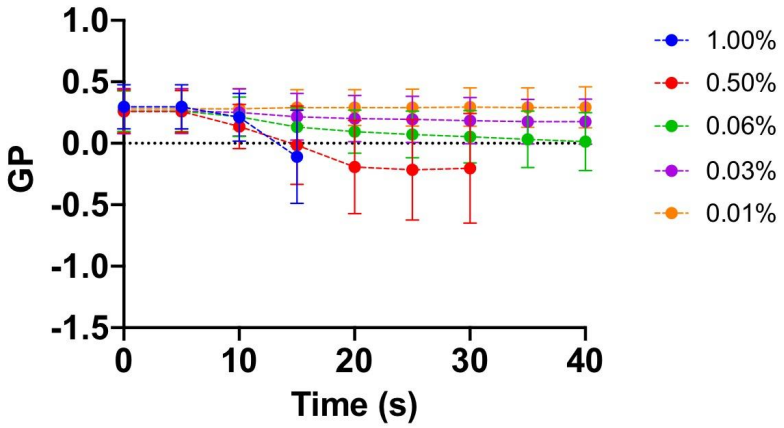

Figure 45. *Average GP_m measurement of live HUH7 treated with five different dilutions of liquid POL, namely 1.00% (blue line), 0.50% (red line), 0.06% (green line), 0.03% (purple line) and 0.01% (orange line). Average GP_m values were measured over time, up to 40s. Time point measurements were performed every 5 seconds. The experiment was repeated six times, and results are reported as mean value ± standard deviation.*

Figure 46 shows representative pseudo-coloured membrane GP maps of HUH7 at different concentrations of POL. After treatment with 1.00% POL, the cell membrane was completely disrupted after 15s. At 0.50% POL, complete disruption of the cell membrane occurred after 20-30s. At 0.06% POL, a blue shift was apparent and the membrane remained intact. Higher POL concentrations, such as 1.00% and 0.50% by volume, disrupted the cellular membrane in few seconds. At lower concentrations, the surfactant molecule interacts with the membrane more slowly, due to a smaller POL concentration gradient. Slight GP changes were visible at 0.03% POL, particularly at the cells in peripheral areas. At POL concentrations lower than 0.02%, as reported in the Chapter 4, polidocanol efficacy was dramatically reduced, indeed at concentrations ≤ 0.01%, the surfactant is incapable of lysing the cell membrane.

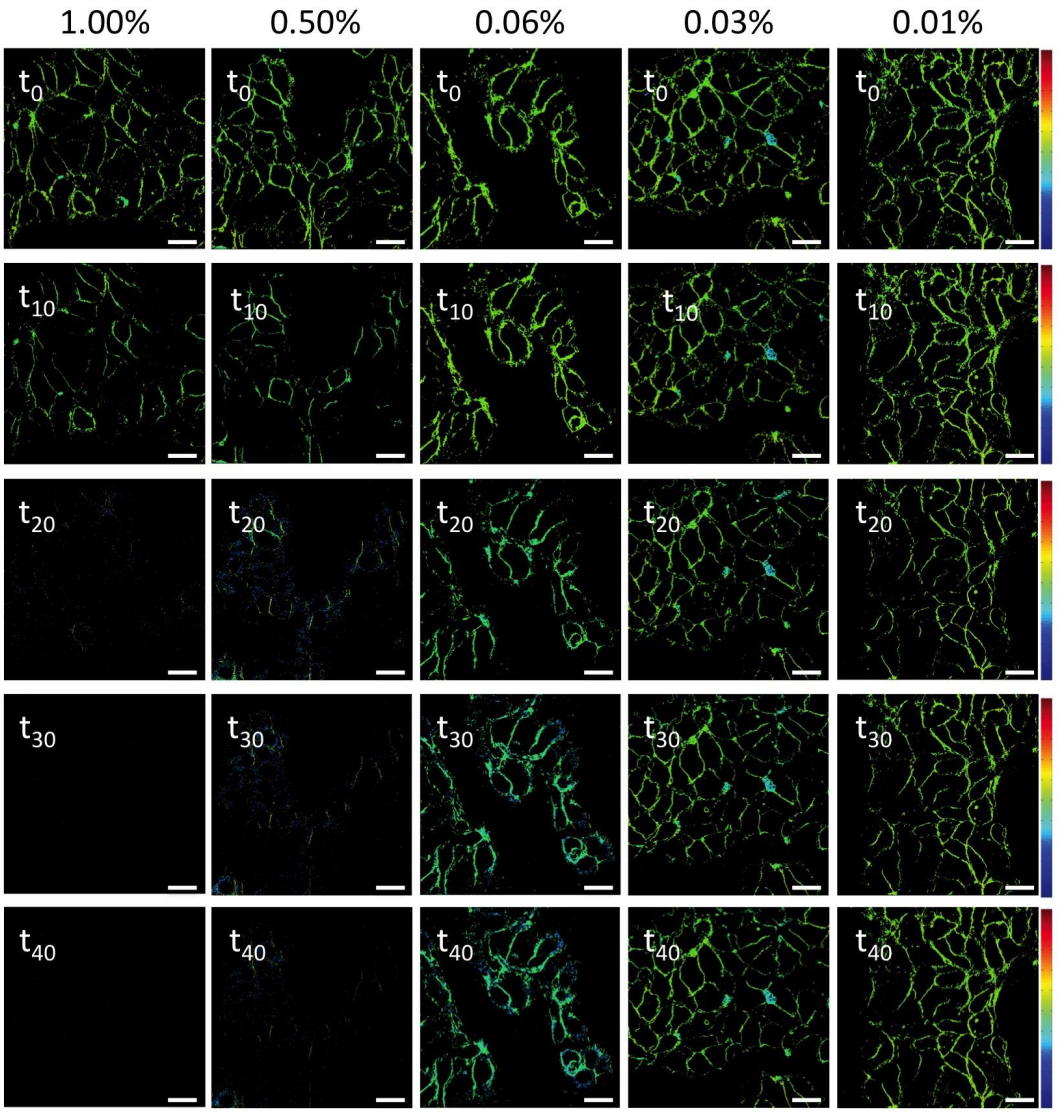

Figure 46. *Spectral GP imaging of live HUH7 treated with five different dilutions of liquid POL, namely 1.0%, 0.50%, 0.06%, 0.03% and 0.01%. HUH7 GP images (40 µm x 40 µm) of the equatorial plane of live cells using the environment-sensitive membrane dye DDi-4-AN(F)EPPTEA at t_0 (before injection) and after 10, 20, 30 and 40 s. Images were acquired between 560 nm and 650 nm wavelength emission (scale bar: 50 µm).*

At 60s after treatment with 0.06% POL, complete disruption of the membrane followed by internalization of the dye was observed. Zoomed-in images of cells (2x and 4x) clearly show the formation of several vesicles, which might be composed of the surfactant molecule and lipids (Figure 47).

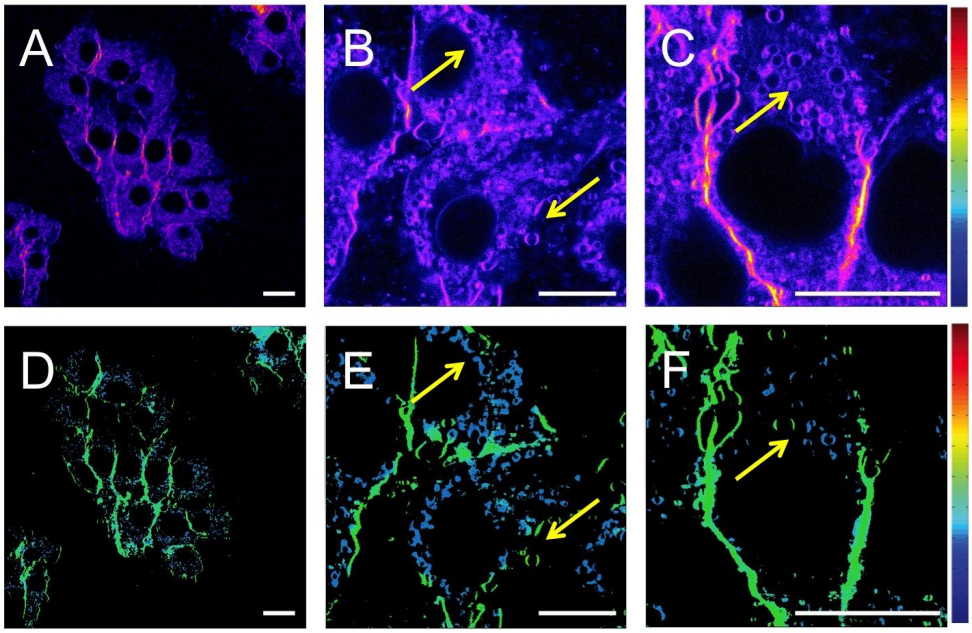

***Figure 47**. Spectral GP imaging of live HUH7 cells treated with 0.06% liquid POL. (A, B, and C) HUH7 cells image stacks (grey scale images converted into LUT file). (D, E and F) HUH7 GP images (40 µm x 40 µm) of the equatorial plane of live cells using the environment-sensitive membrane dye Di-4-ANEPPDHQ at t_{40}. Images were acquired between 560 nm and 650 nm wavelength emission (scale bar 50 µm).*

After treatment with POL at 0.06% it was possible to evaluate the difference in lipid-packing between cells surrounded by other cells (central zone) and cells partially in contact with other cells (peripheral zones). Figure 48 shows the effect of POL 0.06% after 95s of treatment (t_{100}). As previously mentioned, the area of the membrane not in contact with other cells might be more sensitive to POL. Indeed, these membrane segments showed a dramatic decrease in the GP value (arrows 1, 2 in Figure 48), whereas the segment of membrane located between two or more cells showed only a slight decrease on the thickness of the membrane (arrow 3 in Figure 48).

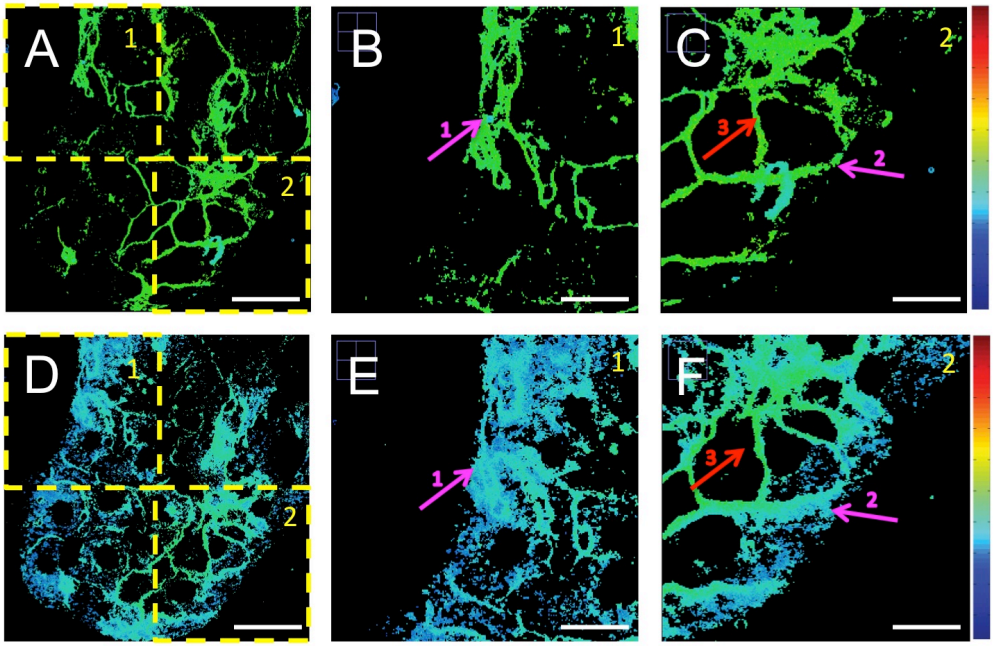

Figure 48. *Spectral GP imaging of live HUH7 cells treated with 0.06% liquid POL. HUH7 GP images (40 µm x 40 µm) of the equatorial plane of live cells using the environment-sensitive membrane dye Di-4-ANEPPDHQ at t_0 (A, D), t40 (B, E) and t100 (C, F). The purple arrows indicate segments of membrane not in contact with other cells, whereas the red arrows indicate segments of membrane between two or more cells. Images were acquired between 560 nm and 650 nm wavelength emission and zoomed in at 150% in ImageJ (scale bar 50 µm).*

The relatively limited (and slow) effect of POL at 0.03% allowed evaluating different particular characteristics. Figure 49 shows the effect of POL 0.03% before treatment t_0, and after 40s and 100s. As previously mentioned, the area of the membrane not in contact with other cells might be more sensitive to POL. Indeed, it is visible that these segments disappeared completely (arrow 2 in Figure 49) or showed a decrease in the GP value (arrow 1,3,5,6 in Figure 49), whereas segments of the membrane between two or more cells showed only a slight decrease on the thickness of the membrane (arrow 4,7,8 in Figure 49).

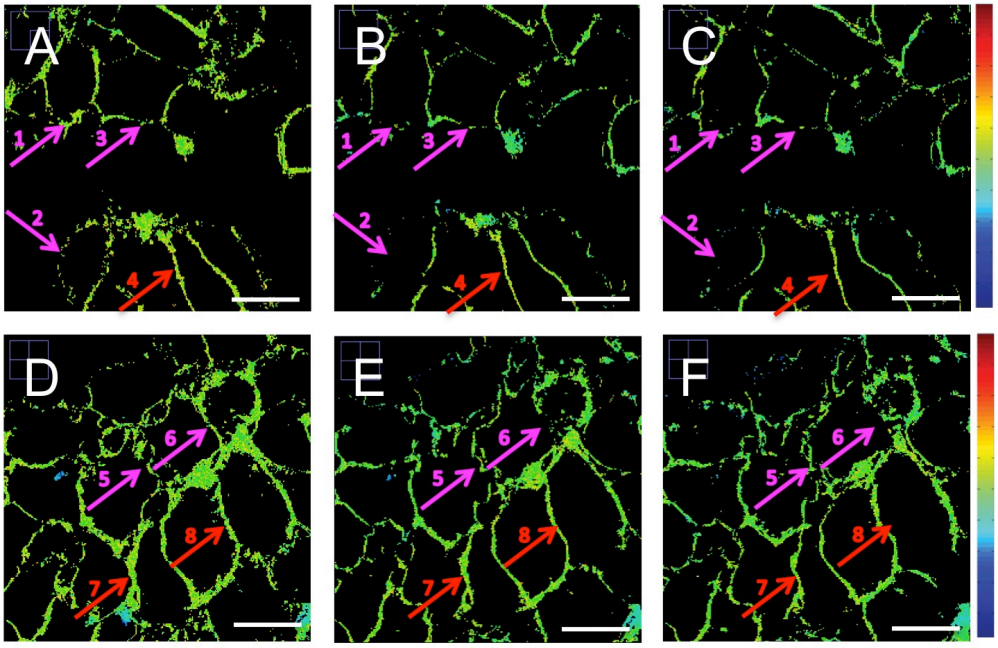

Figure 49. *Spectral GP imaging of live HUH7 cells treated with 0.03% liquid POL. HUH7 GP images (40 µm x 40 µm) of the equatorial plane of live cells using the environment-sensitive membrane dye Di-4-ANEPPDHQ at t_0 (A, D), t_{40} (B, E) and t_{100} (C, F). The purple arrows indicate segments of membrane not in contact with other cells, whereas the red arrows indicate segments of membrane between two or more cells. Images were acquired between 560 nm and 650 nm wavelength emission and zoomed in at 150% in ImageJ (scale bar 50 µm).*

5.3.3 GP membrane measurement of HUH7 treated with foamed polidocanol

In a subsequent phase of the study, the effects of sclerosing foams were investigated. POL-based foams were manufactured using PCF (TSS and DSS) and PEM methods. The first series of experiments involved the injection of foams directly onto a monolayer of cells (referred to as 'dry-test') or upon covering cells with 500 µL of PBS (referred to as 'wet-test').

HUH7 cells were exposed to TSS, DSS and PEM foams for a minimum of 20s. Figure 50 shows the GP frequency distribution of HUH7 cell membrane in the dry- and wet- test. In the dry-test, for all types of foam, the GP distribution exhibited a blue shift after 10s (green dots), which is translated to an overall shift towards lower GP values. With respect to the wet-test, a reduction in GP was observed but it was lower than in the dry-test. Bimodal peaks might be associated with the coexistence of different lipid-packing states.

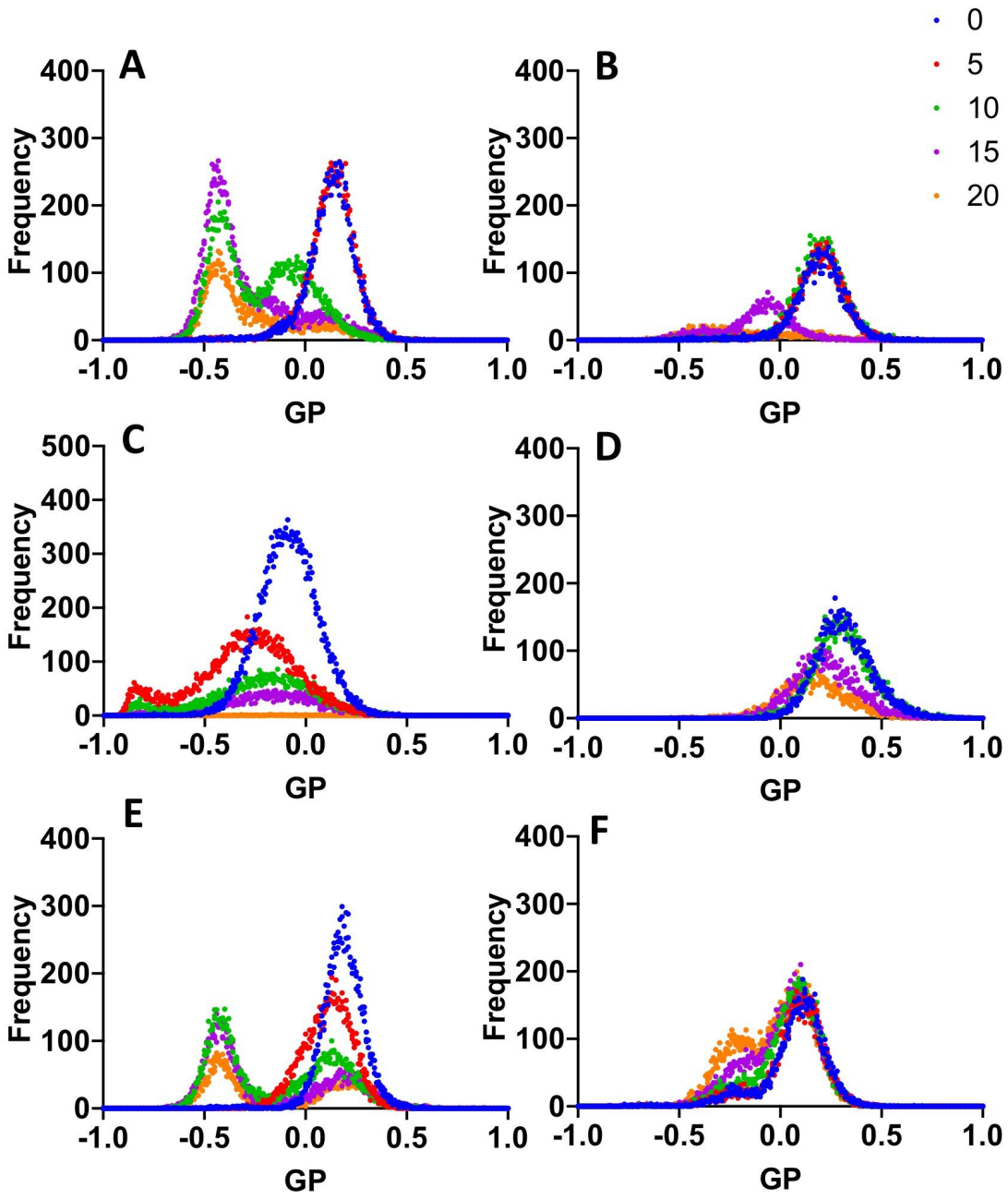

***Figure 50**. GP measurement of live HUH7 treated with TSS (A-B), DSS (C-D) and PEM (E-F). Experiments involved the injection of the foam directly onto the cells, referred to as dry-test (A, C, E), or onto a monolayer of cells covered by 500 µL of PBS, referred to as wet-test (B, D, F). Histograms of GP values following Gaussian fitting indicating the variation of the GP value over 20s. Time point measurements were performed every 5 seconds.*

Figure 51 reports the time variation of the average GP membrane, for all types of foam investigated. The data are reported in Table 8.

Table 8. ΔGP_m value obtained after treatment with PCFs and PEM in the dry- and wet-test.

	PEM		DSS		TSS	
	ΔGP_{m10}	ΔGP_{m20}	ΔGP_{m10}	ΔGP_{m20}	ΔGP_{m10}	ΔGP_{20}
Dry-test	0.349	0.423	0.266	0.257	0.297	0.32
Wet-test	0.05	0.376	0.007	0.145	0.031	0.12

Results show that, for all types of foam, directly contact with the cell monolayer is more effective in altering the lipid packing. With respect to the dry-test, slight changes occurred in the time window t_{10}-t_{20}, whereas in the wet-test a significant decrease of GP values occurred in the same time window.

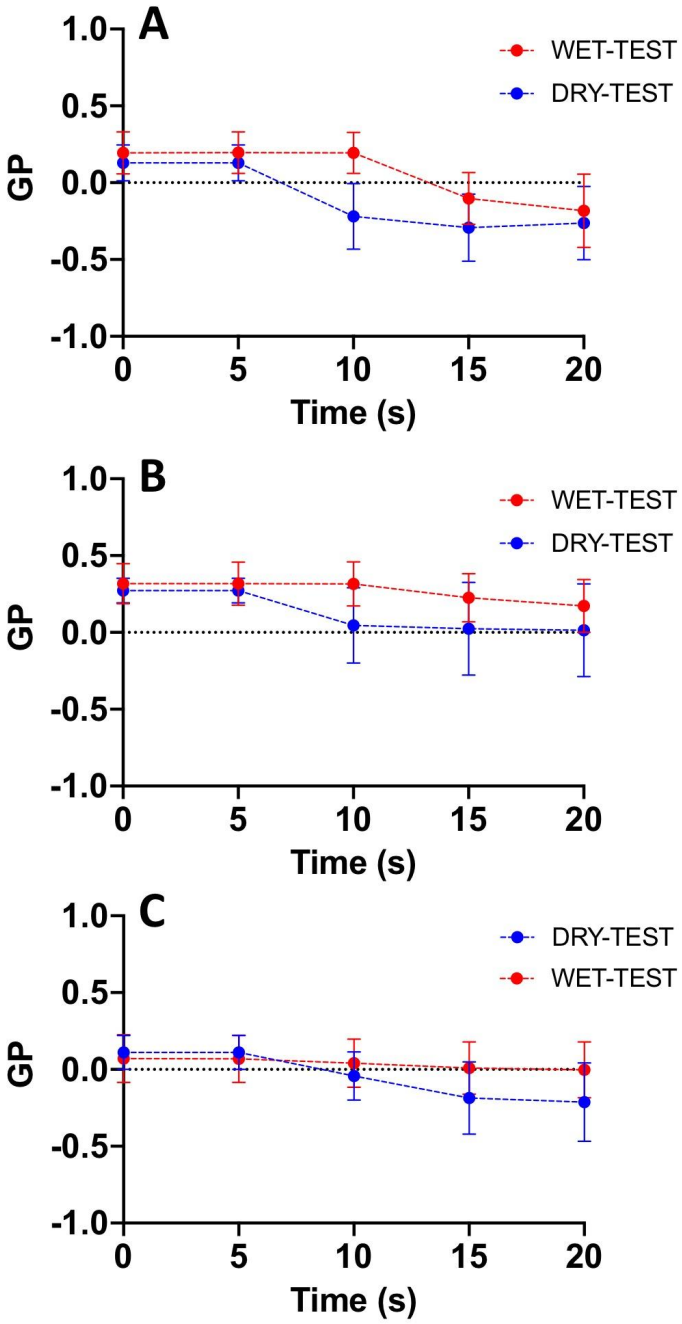

Figure 51. *Temporal evolution of the average GP of live HUH7 cells treated with (A) TSS, (B) DSS and (C) PEM foam in the dry-test (blue line) and wet-test (red line). Average GP values were measured, up to 20s. Time point measurements were carried out every 5 seconds. The experiment was repeated six times, and results are reported as mean value ± standard deviation.*

From the microscope images shown in Figure 52, immediate membrane disruption is observed after direct interaction with foamed POL. With respect to TSS and PEM treatments in the wet-test, at t_{20} few cellular membrane fragments were present. With respect to the wet-test, the GP shift was less rapid and evident only in some areas for either foam. Overall, DSS treatment showed a lower effectiveness in both tests.

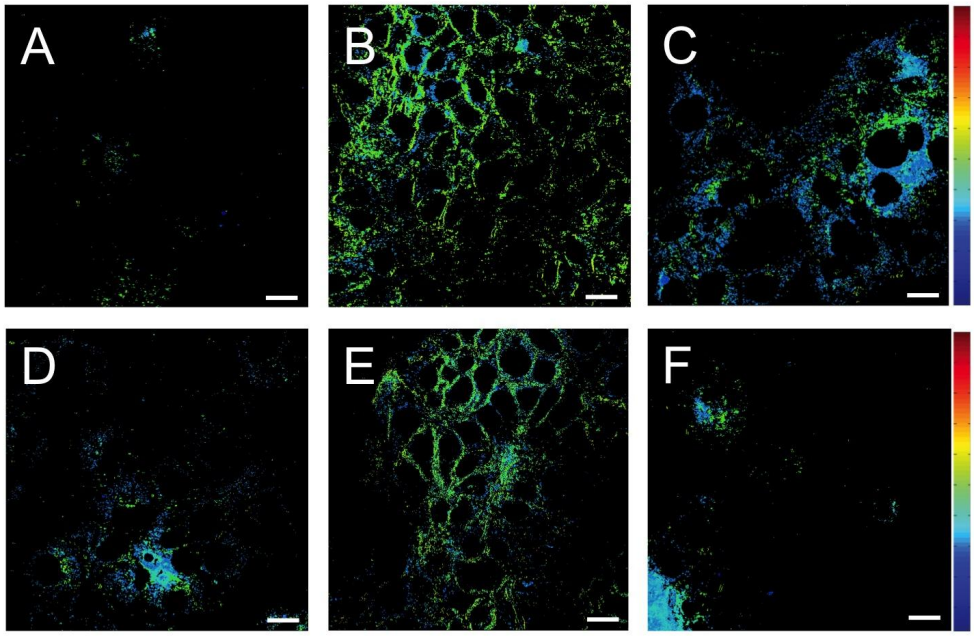

Figure 52. *Spectral imaging of live HUH7 cells treated with TSS (A-D), DSS (B-E) and PEM (C-F). The experiment involved the injection of the foam directly on the sample, called dry-test (A, B, C) or onto a monolayer of cells covered by 500 µL of PBS, called wet-test (D, E, F). HUH7 GP images (40 µm x 40 µm) of the equatorial plane of live cells using the environment-sensitive membrane dye DDi-4-AN(F)EPPTEA at t_{20}. Images were acquired at a wavelength range between 495 nm and 691 nm (scale bar 50 µm).*

Figure 53 shows the comparison between the three types of foams. PEM foams presented the highest ΔGP_m value (0.423) with a GP_{m20} of -0.293, which is similar to the one of liquid polidocanol (ΔGP_m = 0.40). TSS showed a ΔGP_m of 0.320 (GP_{m20} = -0.214). DSS resulted in the least effective membrane disruption, presenting the lowest value of ΔGP_m (0.257).

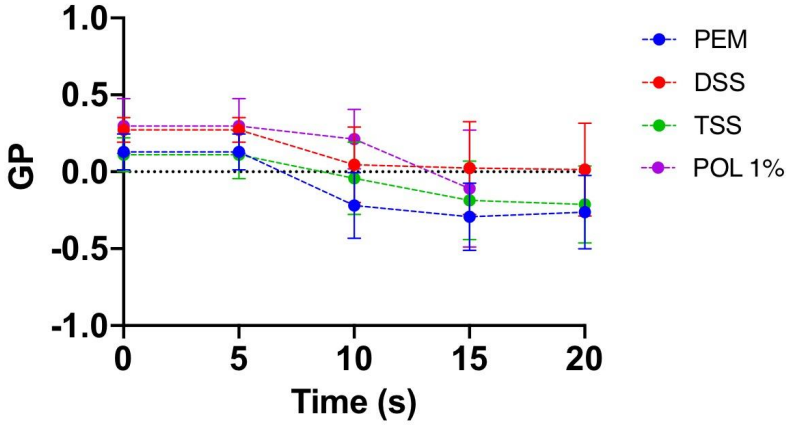

Figure 53. *HUH7 GP average measurement of live HUH7 treated with TSS, DSS and PEM foam. Average GP measurement of live HUH7 treated PEM (blue line), DSS (red line), TSS (green line) and POL (purple line). Time point measurements were taken every 5 seconds. The*

experiment was repeated six times, and results are reported as mean value ± standard deviation.

5.4 Discussion

It was recently observed that biological membranes could assume a number of distinct lipid packing states between the gel and the crystalline phase, which are mirror of the membrane functionality. The observation of coexisting gel (lipid packing ordered) and liquid-crystalline (lipid packing disordered) phases in phospholipid bilayers has been attempted using Di-4-AN(F)EPPTEA. This probe is able to quantify the extent of water content into the bilayer due to its dipolar relaxation effect.

Water content has been correlated with lipid packing and membrane fluidity. For instance, the emission spectrum of Di-4-AN(F)EPPTEA is centered at 560 nm if the membrane is in the ordered phase and at 650 nm when it is in the disordered phase. In this study, the generalized polarization (GP) was employed to determine changes in membrane fluidity as an indication POL's effectiveness.

A low GP value corresponds to higher membrane fluidity (thus greater disruption) and a higher GP value is associated with a more packed membrane (thus lower disruption).

Initially, the GP_m value of HUH7 was measured without any treatment applied, in order to identify the physiological GP value for this cell model (Figure 33). HUH7 cells showed a nearly constant GP value in the time window selected for the experiment (40s). The same measurement was repeated for several independent samples, at the same experimental conditions (Figure 34).

Afterwards, the control test was repeated using PtK2 live cells (Figure 35). Slight variability of the membrane GP values was identified between the same cells lines from either the cell lines tested (HUH7 cv= 4.46%, PtK2 cv=16.30%), which was in agreement with previous study.

The aim of this study is to determine membrane fluidity changes after treatment with POL. The question addressed are whether changes in fluidity are (i) time dependent, (ii) specific to certain cells, and (iii) can be correlated with the efficacy of POL.

The concentration of POL commonly used in the clinic for the treatment of varicose veins is 1.00% by volume. Being the disruptive effect of polidocanol almost immediate at these concentrations (10-20s), at the beginning of the study lower concentrations of surfactant have been employed (i.e., 0.06%), in order to capture the effect of POL at different time points. Notably, these lower concentrations of POL are still effective in damaging endothelial cells. As reported in the previous Chapter 4, POL at 0.06% concentration disrupts more than 50% of

cells cultured in a monolayer. Notably, there was a gradual change in membrane fluidity within a time window of 40s, with a final ΔGP of 0.248 (Figure 37). After 60s, the GP membrane was not measurable, confirming that the timescales selected for analysis are appropriate for evaluating GP at the membrane level (Figure 38). A similar result was obtained with the PtK2 cell line, with a ΔGP of 0.259 (Figure 39). However, the limitation of this study is that only two cell lines were employed. Furtherer test with other cell lines might be needed to understand that the effect of POL is not dependent by the type of cells.

Additionally, it was observed that the number of cells might have an impact on the ability of POL to affect cell membrane hydration (Figure 40). Notably, a lower cell number (<2 cells, confluence less than 10%) showed a greater decrease of GP, compared to higher cell numbers (>2 cells, >10%). This result might be due to the fact that polidocanol diffuses more rapidly into single cells compared to the one in contact with each other, where a smaller surface area is exposed to the drug transport. Additionally, molecules can passively cross the cellular barrier *via* diffusion by the paracellular route, or between the cells through tight junctions. The tight junction is a region where the outer leaflets of the membrane lipid bilayer of neighbouring cells are fused, thus restricting the movement of solutes through this space. Therefore, diffusion of POL molecules, which be more efficient in the areas of the cell membrane, which are not in direct contact with other cells. Considering that surfactants are clinically employed onto an endothelial monolayer, the more clinically relevant are the ones taken at higher cell density.

However, the single cell test was proven useful to evaluate the effect of POL at the single cell level and capture the time evolution of lipid-packing (Figure 42). Analyzing the GP-maps obtained in the first 10 seconds, it was possible to identify the moment where the membrane was completely disrupted (at t_{10} seconds).

Subsequently, the sclerosing efficacy of liquid POL was investigated at relevant clinical concentration (1-0.5%) and further dilutions (0.03%, 0.02%, 0.01%) in PBS. With respect to the treatment with 1% and 0.5% POL, the GP_m dramatically decreased within 10s (5s of exposure) and 20s (15s) respectively, with complete disruption of the cell membrane. This result justifies the choice of employing lower concentrations of POL - such as 0.06% - to evaluate temporal membrane GP changes due to exposure to POL (Figure 44). Indeed, at this concentration, the gradual decrease of GP_m could be measured. At t_{60} it was possible to observe the presence of vesicles, which might be composed by lipids and surfactant molecules. Slight GP changes were visible at 0.03% POL, particularly at the cells in peripheral areas.

At POL concentrations lower than 0.02%, as reported in Chapter 4 polidocanol efficacy was dramatically reduced; indeed at concentrations ≤ 0.01%, the surfactant is incapable of lysing the cell membrane and instead would cause the release of cytosolic calcium and pro-coagulant factors. These findings are generally in agreement with the results obtained in the i*n vitro* tests (Chapter 4). The ability of POL to penetrate and cross the membrane lipid bilayer was found to be concentration dependent. At the minimum saturation concentration (C_{sat}) POL molecules start producing large membrane fragments, whereas they start to solubilise the membrane at the critical solubilisation concentration (CSC).

The rapidity with which POL disrupts the cell membrane is fundamental in the sclerotherapy treatment, since the contact time between POL molecules and the endothelium is influenced by the blood flow. When the liquid polidocanol is injected, molecules need to interact immediately with the endothelial layer, before being deactivated and diluted by the blood flow.

As reported in the literature, initially there is a non-cooperative interaction between POL molecules and the lipid bilayer. As indicated by the results obtained at POL concentrations lower than 0.03%, surfactant monomers are absorbed into the lipid bilayer without affecting the membrane structure. Above the C_{sat}, surfactant monomers aggregate within the membrane to generate small fragments (cooperative interaction) as occurred with 0.06% POL treatment. Above the CSC, the bilayer is then disrupted and mixed surfactant-lipid micelles/vesicles. The formation of vesicles, composed by surfactant molecules and lipids, has been observed for the first time with a microscopy technique

In a second phase of the study, the effects of sclerosing foams (PEM and PCFs) were investigated. The dry- and wet-test were designed in order to evaluate two possible scenarios, which might occur in the clinical practice: (i) the foam injected inside the vein lumen displaces blood completely and is thus directly in contact with the endothelial layer (dry-test), and (ii) the foam is separated from the cell by a layer of liquid. The first case is the ideal therapeutic scenario, where bubbles coated with POL interact directly with the cell membrane. This condition might occur few seconds after foam injection, when the foam forms a plug that displaces blood and contacts directly with the inner vessel lumen. The second phase might happen subsequently, when the foam is separated from the endothelium by a layer of liquid, and the molecules of POL need to diffuse/drain through the liquid layer. Either phase depends on the mechanical properties (i.e. cohesiveness) of the foam. Indeed, more cohesive foams

remain longer in contact with the endothelial cells.

In the experiments designed in this study, the system is static, therefore the dynamic effect of the blood washing the foam is not present, and only the injection phase is replicated. Additionally, PBS has been employed instead of blood. However, the aim of the study is to understand the effect of polidocanol at the membrane level.

All types of foam showed a similar trend; GP decreased slowly when cells were not directly in contact with the foam (Figure 51). Results also suggest that POL molecules diffuse in the fluid layer and achieve similar end-point effects of foamed POL. Therefore, the main difference between the two tests is the velocity of the effect of POL molecules. When comparing the performance of all foams and liquid POL in the dry-test, PEM and TSS showed similar outcomes, whereas DSS presented the lower efficacy (and was comparable to liquid POL)(Figure 53). It should be noted that the similar behaviour between liquid and foamed POL was anticipated, since the experiments were carried out in static environment.

As reported in Chapter 4, at the time point investigated (from 0 to 20s), the effectiveness of POL *in vitro* is similar for all the types of foam (no statistically difference). Comparing the different types of foam, PEM showed the highest efficacy in disrupting the cell monolayer (Figure 24), which is in agreement with the results in this Chapter 4 (Figure 54).

5.5 Conclusion

The aim of this study was to investigate and quantify the effect of POL at the cellular membrane level, in order to understand more deeply its biological and physical mechanisms of action. A spectral imaging method was employed to determine the effect of POL on the lipid packing of cell membranes, using the environment-sensitive dye Di-4-AN(F)EPPTEA. A reduction in lipid-packing was regarded as an indication of the ability of POL to disrupt the cell membrane. This is the first study where spectral microscope imaging has been employed to assess membrane fluidity in live cells for evaluating the effect of surfactant molecules.

As reported in the literature, POL above at a certain concentration interacts with the cell membrane forming vesicles, composed by the surfactants molecule and the lipid bilayer, ultimately causing cell lysis. For the first time, the generation of vesicles upon interaction with POL has been observed with a microscopy technique. Additionally, the technique has been employed to quantify the level of disruption of cell membranes exposed to different types of liquid and foamed POL. Results showed that POL is able to cause a change in the lipid-packing state towards the liquid phase, translating into a reduction of the membrane GP. The

level of decrease in GP depends on the surfactant concentration, which is in agreement with previous findings (Chapter 4). Additionally, POL efficacy was associated with the number of cells and their spatial location (cells in peripheral areas were more sensitive to the treatment). Finally, the efficacy of foamed POL was evaluated, and results showed that PEM and TSS foams caused greater and faster membrane disruption.

Despite two different cell models were employed in this study, additional experiments with other cells types would be required to generalize these observations further. Additionally, all experiments were conducted in a static fluidic environment, which does not replicate all the events that occur during treatment. Future studies could focus on evaluating more in detail the morphological and structural differences resulting from the treatment. This study might have a great impact in measuring variations in the cell membrane after lipophilic drug treatments. Indeed, changes in cellular membrane properties might have an impact on the cellular uptake of various lipophilic molecules. In addition, membrane properties are expected to play a major role in pathogenesis of various diseases.

Chapter 6: Ex vivo evaluation of the biological performance of sclerosing agents

Chapter 6 describes the development of *ex vivo* vein models to quantify sclerosant-induced disruption of the endothelial layer, through quantification of the extravasation of a probe molecule.

Abstract

The sclerosing agent polidocanol (POL), in the form of liquid or foam, has been largely employed for the treatment of varicose veins by clinicians. It is widely accepted that surfactants disrupt the cell membrane causing endothelial cell (EC) death, vein wall damage, such as disruption of the *subintima* and mild alterations of the smooth muscle layer. Several histological studies have been reported, demonstrating that POL significantly compromises the vein wall's integrity by damaging the endothelium. Overall, these histological studies demonstrated the qualitative effects of the interaction between sclerosing agents and the vessel wall. Quantitative analyses mostly relied on microscopic measurements, which were however limited to regions of interest within the treated vessel.

Herein, methods for quantifying sclerosant-induced disruption of the endothelial layer in an *ex vivo* model have been proposed. For the first time, a comparison between different foam production techniques has been performed *ex vivo*. Results from this study can provide clinicians with some fundamental understanding of how different foam formulations may perform in the body.

6.1 Introduction

Sclerosing agents such as POL and STS, in the form of liquid or foam, have been largely used in the clinic for the treatment of varicose veins (Bush and Bush, 2017). It is widely accepted that surfactants disrupt the cell membrane causing (i) endothelial cell (EC) death microscopically, and (ii) macroscopic vein wall damage, such as disruption of the *subintima* (i.e. the elastic tissue located underneath the endothelium) and mild alterations of the smooth muscle layer (Goldman et al., 2017; Mol et al., 2007; Parsi et al., 2008). However, relatively little is known about their biological effects on the vessel wall. Limited *in vitro* studies have been performed to investigate the microscopic effects of sclerosants (Kobayashi et al., 2006). Most of these studies involve culturing of ECs over a plate, exposing cells to sclerosants, followed by staining with dyes to evaluate cell membrane lysis or cell death (Kobayashi et al., 2006; Mol et al., 2007; Parsi et al., 2008). Additionally, the *in vitro* models provide a 2D environment to investigate sclerosing effects in static conditions, and may not be suitable for replicating the clinical conditions. With respect to the macroscopic effects of sclerosants, several histological studies have been reported, demonstrating that POL significantly compromises the vein wall's integrity by damaging the endothelium. In most studies, segments of vein were treated with sclerosant, and stained afterwards with dyes to evaluate damage to the vessel wall (see Table 9).

Table 9. Summary of histological studies performed to investigate the macroscopic effects of sclerosants.

Author	Orsini	Ikponmwosa	Erkin	Whitely
Part treated	Vein segment	Vein segment	Vein segment	Vein segment
Treatment	3% STS foam (TSS 1:4)	1% and 3% STS foam	0.1-3% POL foam (TSS)	0.5-3% liquid STS and POL
Treatment Time	2-15-30 min	5 min	5 min	1-10 min
Method of Administration	Filling the vein	Injection with cannula	Soaking	Filling the vein
Analysis/ Outcome	Histological/ Staining/ Wall Damage	Histological/ Wall damage	Histological/Wall damage	Histological/ Staining/ Wall damage
Quantification method	H&E (Hematoxylin and eosin stain) and with Weigert and Weigert-Van Gieson methods	H&E (Hematoxylin and eosin stain)	H&E (Hematoxylin and eosin stain)	Up-regulation of p53 and intracellular adhesion molecule-1 (ICAM-1)

Orsini and Brotto have analyzed the immediate effects on the saphenous vein wall *in vivo*, upon sclerotherapy with STS foam produced with TSS at 1:4 liquid:RA ratio (Orsini and Brotto, 2007). Vein wall damage was rapid, with complete disruption of the endothelium occurring within the first 2 minutes. In the successive 15 and 30 minutes, edema of the s*ubintima* was observed, accompanied by progressive separation from the tunica media and initial formation of a thrombus.

Ikponmwosa *et al.* treated vein segments with 1% or 3% STS foam produced using TSS, at a 1:3 liquid:RA volume ratio (Ikponmwosa et al., 2010). Upon exposure to STS foam for 5 minutes, the percentage of EC loss was 86.3% (1% STS) and 92.2% (3% STS), whilst the percentage of *tunica media* injury was 8.9% (1% STS) and 12% (3% STS).

Erkin *et al.* treated varicose vein segments with a selected concentration of POL foam produced with the TSS method, at 1:4 liquid:RA ratio. Vein segments were immersed in foam for 5 minutes, and subsequently examined (Erkin et al., 2012). Treatment with POL foam caused endothelial swelling, necrosis, and intimal thickening. However, these effects were not statistically correlated to the concentration of sclerosant, except for the presence and extent of necrosis.

Whiteley *et al.* treated *ex vivo* human varicose veins with 1% or 3% STS and POL, for 1 or 10 minutes (Whiteley et al., 2017). Cell death and medial damage were directly correlated to surfactant concentration and treatment time. POL caused less damage to the endothelium and smooth muscle cells compared to STS.

Overall, these histological studies demonstrated the qualitative effects of the interaction between sclerosing agents and the vessel wall. Quantitative analyses mostly relied on microscopic measurements, which were however limited to regions of interest within the treated vessel. Therapeutic effects were largely dependent on treatment time and sclerosant concentration, although time at which the sclerosant was observed to become effective differed between investigations. This could be due to differences in the physical properties of the sclerosing agent used and the experimental conditions. To the best of my knowledge, there is no comparative quantitative analysis between different foam production or administration methods, and no previous *ex vivo* study has been carried out under dynamic flow conditions. Moreover, earlier studies only focused on spatially 'averaged' effects, whilst a spatially resolved analysis (i.e. looking at effects along the vessel) has not been carried out yet.

Herein, a method is proposed for quantifying sclerosant-induced disruption of the endothelial layer *ex vivo*. For the first time, a comparison between different foam production techniques has been performed. Results from this study can provide clinicians with some fundamental understanding of how different foam formulations may perform in the body.

In this Chapter different variables were analysed using the *ex vivo* model, which related on the background flow conditions (static or dynamic), and the type of carrier liquid (PBS or blood). These four parameters were combined to form four different experimental scenarios: (i) static conditions in the presence of PBS (S), (ii) static conditions in the presence of blood (SB), (iii) dynamic conditions with perfused PBS (D), and (iv) dynamic conditions with perfused blood (DB). The umbilical cords were treated with either foamed or liquid POL.

6.2 Material and Methods

6.2.1 Foam production methods

PCFs and PEM were employed to evaluate foam sclerotherapy efficacy. For details on foam production methods, refer to paragraph 4.2.1 (Foam production methods).

6.2.2 Ex vivo test method to evaluate the performance of sclerosants

This part of the study was carried out in accordance with the Human Tissue Act (2004) and the recommendations of Southampton & South West Hampshire Research Ethics Committee B with Governance provided by the University of Southampton Research Governance Office. Umbilical cords were collected from the Princess Anne Hospital (Southampton, UK) from non-complicated natural vaginal births following agreed ethical collection protocols (Local Research Ethical Committee (LREC); Ref: 07/H0502/83). The umbilical cord was cut from the placenta and sectioned into 10 cm long segments. A steel feeding cannula (16 G) was inserted into the vein. The cannula was clamped in place and attached to a 30 mL syringe filled with a physiological saline "cord buffer". The vein was washed until the fluid exiting the other end of the cord was clear.

The following experiments were carried out in two different conditions: (i) static and (ii) dynamic. Static condition refers to the absence of background flow during foam administration, whereas dynamic condition refers to the presence of a background flow during foam administration.

The umbilical vein (5 cm length) was filled with 2 mL of collagenase solution at 0.1% in phosphate buffered saline (PBS, Worthington Biochemical Corp., USA) or with POL (1%

v/v) or PBS (control). The treatment time was fixed at 10 minutes. In the clinical practice a volume of 6 to 8 mL is administered per session for the management of great saphenous varices, and no more than 3mL for the management of small saphenous veins. Generally, the volume injected depends on the size of the vessel to be treated. In this study, a volume of 4 mL was employed for treating a vein segment of 10 cm, as this volume was proven to be sufficient to completely fill the umbilical vein. Upon verification of the method, the effect of treatment time was investigated. The vein (5 cm) was treated with 2 mL of liquid POL 1% for 1, 5, and 10 minutes.

Static test.

Umbilical cords (10 cm in length) were treated with liquid and foamed POL (4 mL). The exposure time was fixed at 1 minute. As reported in the literature, there is a significant interaction between blood and sclerosants, therefore static tests in the presence of blood were also carried out. In the static test with blood, the vein washing process was omitted in order to make use of the blood that is already present in the cord.

Dynamic test.

In the dynamic test with blood, the experimental set-up consisted of an umbilical cord (10 cm) with a steel feeding cannula (16 G) inserted into the umbilical vein. The cannula was clamped in place and attached to a silicone inlet tube (OD: 4 mm) connected to a 30 mL syringe (BD Biosciences, USA) filled with PBS or whole human blood, placed into a syringe pump (IVAC P200 Syringe Pump, BD Biosciences, USA). A steady flow rate (62.5 mL/h) of PBS or blood was imposed using the syringe pump. The sclerosant (foamed or liquid) was injected in the inlet tube using a 25G needle (4 mL injected for 10 cm of umbilical cord). The treatment time was fixed at 1 minute unless otherwise specified (Figure 54).

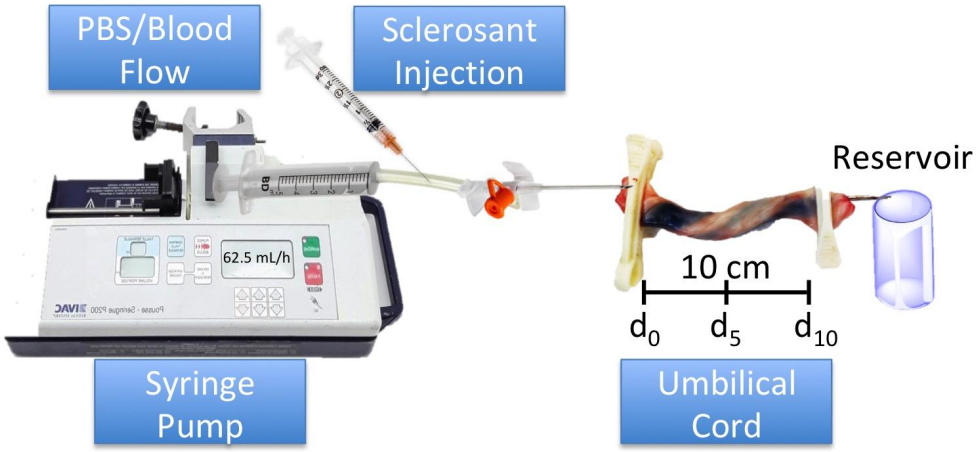

Figure 54. *Experimental set-up for ex vivo dynamic tests. A steady flow is imposed using a syringe pump. Foamed/liquid polidocanol is injected through the 25G needle into the inlet channel (silicone tube). The latter is connected to the umbilical cord (10 cm) using a steel feeding cannula (16 G) inserted into the vein. After treatment, each umbilical cord was sectioned in three segments by cutting it at the injection point (d_0), and at 5 cm (d_5) and 10 cm (d_{10}) from the injection point.*

Measurement of extravasation in the umbilical cord sample.

After treatment, the vein was washed with cord buffer, and filled with 4 mL of Evans blue (EB) (0.33% EB and 0.66% bovine serum albumin, BSA). The cord was then incubated at 37°C for 20 min, and the Evans Blue subsequently washed out using cord buffer (Figure 55). Each cord segment (10 cm) was cut in three smaller segments (1.5 cm) at the injection point (d_0), and at 5 cm (d_5) and 10 cm (d_{10}) from the injection point. Afterwards, the three segments were cut in three smaller pieces (each 0.5 cm long), which were weighed and inserted in 1.5 mL tubes. A formamide solution was added into each tube, and all tubes were transferred into a 62°C water bath and incubated overnight in order to extract EB from the tissue. Tubes were centrifuged at 13000 rpm for 20 minutes at 20°C. The supernatant was then transferred into a 96 well flat-bottomed plate. The EB stock solution was serially diluted to generate a standard curve. EB absorbance was then measured on a plate reading spectrophotometer, at a wavelength of 610 nm. The absorbance from a calibration standard curve was used to calculate unknowns, using the Prism software (©2017 GraphPad Software, Inc., USA) and applying a hyperbolic interpolation and regression (Figure 56).

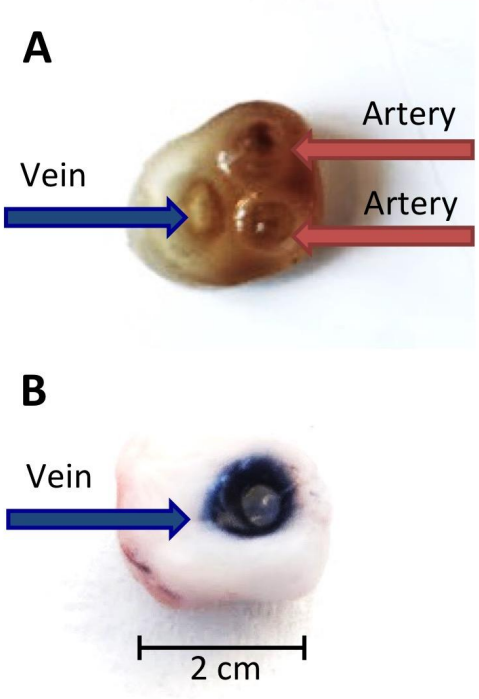

Figure 55. *Photographs of a segment of umbilical cord before and after treatment with liquid POL. (A) Transversal section of an umbilical cord before treatment. A normal cord contains two arteries and one vein, as indicated by the arrows. (B) Transversal section of an umbilical cord treated with liquid POL after injection of Evans Blue, from which extravasation of Evans Blue can be observed (scale bar 2 cm).*

Afterwards, the amount of extravasated Evans blue (in mg) per gram of tissue was calculated. The variation of extravasated EB_e at different points (d_n) is expressed in Equation 3:

$$\Delta EB_e = EB_{dn+5} - Eb_{dn} \qquad \text{[Eq. 3]}$$

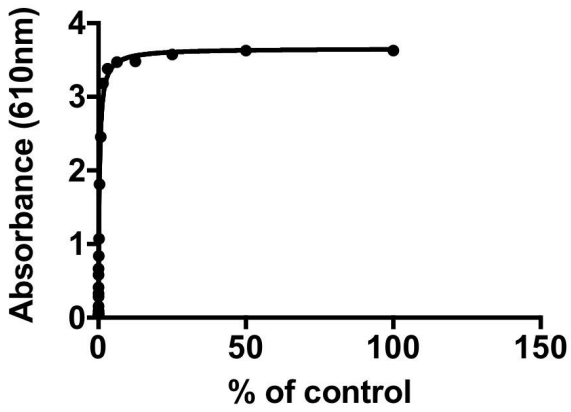

Figure 56. *Standard curve showing the absorbance (at 610 nm) at different concentrations of Evans Blue. The interpolating non-linear function (hyperbolic) can then be used to calculate the concentration of extravasated Evans Blue of experimental umbilical cord samples.*

6.2.3 Statistical analysis

Comparisons between treatments were performed using unpaired Student's t-test. Statistical significance was assumed for p-value < 0.05. All statistical tests were performed with Prism software. All data were reported as the mean ± SD of at least six independent experiments. The final level of extravasation of EB is obtained by the average of six segments of different cords (1.5 cm long); each of these segments was divided into three smaller segment (0.5 cm long), and three measurements were carried out on each small segment.

6.3 Results

6.3.1 Evaluation of the robustness of the method

In order to investigate the sclerosing performance of foams in a more realistic biological model, experiments using an *ex vivo* vein model were carried out. The reliability of the method was initially evaluated by quantifying endothelial damage induced by Type I collagenase, an enzyme that removes endothelial cells from the vessel wall by proteolysis of underlying collagen. The vein was exposed to the enzyme for 10 minutes. The same procedure was repeated using liquid POL (1% v/v) and PBS as a control (Figure 57). Following exposure to Evans Blue-conjugated BSA, control cords showed no leakage into the tissue surrounding the vein (the quantity of EB extravasated was 0.5 ± 0.2 mg EB/g tissue). The collagenase solution (positive control) showed a level of disruption equivalent to 42 ± 4.5 mg EB/g tissue, whereas liquid POL caused 21 ± 1.2 mg EB/g tissue of extravasation.

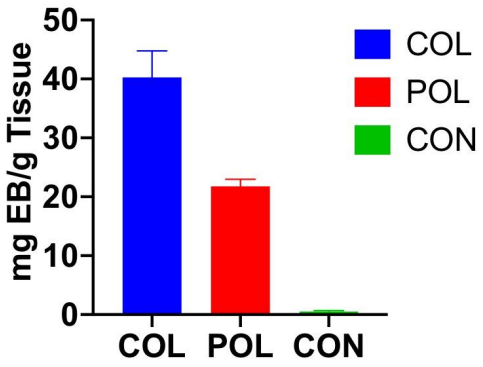

Figure 57. *Ex vivo validation of the Evans Blue (EB) method. Evaluation of the effect of collagenase, liquid polidocanol, and cord buffer as a control (2 mL, for a 5 cm vein segment). The vein wall was exposed to different collagen solutions (0.1% w/v) and POL (1% v/v) for 10 minutes. Data are reported as mg of extravasated EB for grams of tissue.*

6.3.2 Static test in the presence of PBS

Upon verification of the method, the effect of treatment time was investigated. The vein was treated with liquid POL 1% for 1, 5, and 10 minutes. Figure 58 (A) shows that endothelial disruption is directly proportional to exposure time (extravasation ranged from 1.55 ± 2 to 21 ± 1.2 to mg EB/g tissue).

The same experiment was subsequently performed using PCFs and PEM, using a constant exposure time of 1 minute. Figure 58 (B) shows that PEM was more effective in disrupting the endothelium compared to DSS and liquid POL; whilst no significant difference was observed between DSS and liquid POL. The DSS method in this test produced less disruption than PEM (corresponding to 1.3 ± 0.8 and 3.9 ± 2.1 mg EB/g tissue, respectively). When comparing mean values, it was found that there were statically significant differences between PEM vs. POL (p-value= 0.013) and PEM vs. DSS (p-value = 0.017).

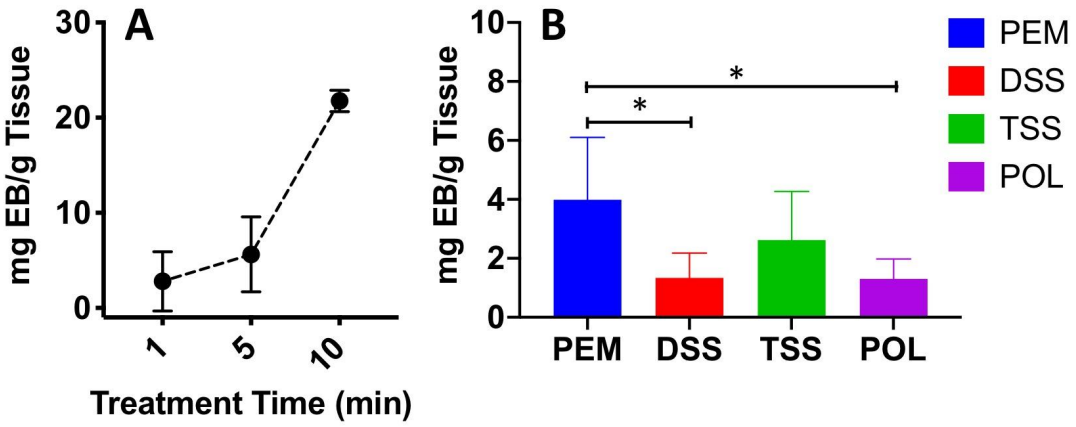

***Figure 58**. Ex vivo evaluation of the effect of liquid and foamed polidocanol on umbilical cord veins. (A) Evaluation of the effect of treatment time on umbilical cord vein, using liquid polidocanol (2 mL, for a 5 cm vein segment). The vein walls were exposed to polidocanol for 1, 5 and 10 minutes. Data are reported as mg of EB per grams of tissue, determined via Evans Blue method. The experiment was repeated four times. (B) Evaluation of the effect of foam on umbilical cord vein, using different types of sclerosing agent: PEM, DSS, TSS, and liquid POL (2 mL, for a 2 cm vein segment). The vein wall was exposed to the sclerosing agents for 1 minute. Data are reported as mg of EB per grams of tissue, determined via Evans Blue method. An asterisk (*) indicates p-value ≤ 0.05.*

6.3.3 Static test in the presence of whole human blood (SB)

As reported in the literature, circulating blood cells are known to deactivate sclerosants. The underlying mechanisms may include direct consumption of the active detergent in the process of inducing the lysis of erythrocytes, leukocytes, and platelets (Parsi et al., 2008).

In order to understand the interaction between blood components and the sclerosant molecules in this model, a new experiment was designed in which the umbilical vein was left primed with human whole blood, in order to mimic a physiological medium. The umbilical cords were treated with either foamed or liquid POL. Each umbilical cord was sectioned in 3 segments at the distance of 0 cm from the injection point (d_0), and at 5 cm (d_5), and 10 cm (d_{10}) from the injection site. As shown in Figure 59, DSS and POL had comparable performance, which remained relatively unchanged along the length of the vein and presented a maximum level of extravasation between 1.13 and 1.18 mg EB/g of tissue. PEM and TSS showed the highest level of disruption at d_5 (4.38 ± 3.2 mg EB/g and 3.05 ± 2.02 mg EB/g, respectively). At d_{10}, DSS and POL showed lower efficacy (0.75 ± 0.32 mg EB/g and 1.13 ± 0.9 mg EB/g, respectively).

Afterwards, the average level of EB extravasated through the endothelium was measured along the whole length of the cord. Statistical significance was evaluated between TSS and liquid POL (p-value = 0.033) and between PEM and liquid POL (p-value = 0.033). PEM and TSS showed the highest level of disruption (2.14 ± 1.08 mg EB/g and 2.13 ± 1.07, respectively), whereas DSS and POL induced the lowest level of disruption (1.13 ± 0.94 mg EB/g and 0.91 ± 0.52 mg EB/g).

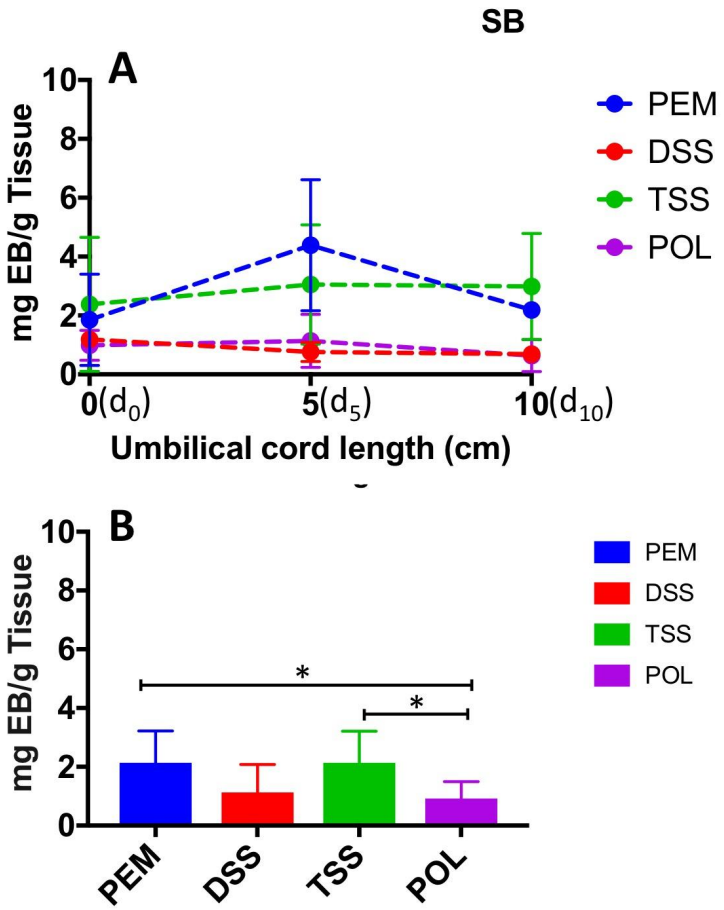

Figure 59. *Evaluation of the effect of PEM, PCFs and liquid POL treatment on umbilical cord vein in static condition, in the presence of blood. (A) Evaluation of the effect of PEM, PCFs and liquid POL treatment on umbilical cord vein at d_0, d_5 and d_{10}. The vein was left filled with whole human blood, and subject to 1 minute of treatment. Data are reported as mg of EB per grams of tissue, determined via Evans Blue method. The experiment was repeated six times. (B) Evaluation of the effect of PEM, PCFs and liquid POL treatment on umbilical cord vein (10 cm). The vein wall was exposed to the sclerosing agents for 1 minute. Data are reported as average of mg of EB per grams of tissue, determined via Evans Blue method. One asterisk (*) indicates p-value ≤ 0.05.*

The effect of blood on the performance of sclerosing agents was subsequently evaluated in static conditions (Figure 60). It is evident that differences appear for all types of treatment, where efficacy reduced in the presence of blood compared to PBS. However, no significant differences were found between the same types of treatment (see Table 10).

Table 10. Comparison between S and SB tests (average values of mg EB/g of tissue).

S (mg EB/g)	SB(mg EB/g)	$\Delta_{S\text{-}SB}$ (mg EB/g)	p-value
3.99	2.14	1.85	0.085
1.34	1.13	0.21	0.691
2.62	2.1	0.48	0.555
1.3	0.57	0.38	0.306

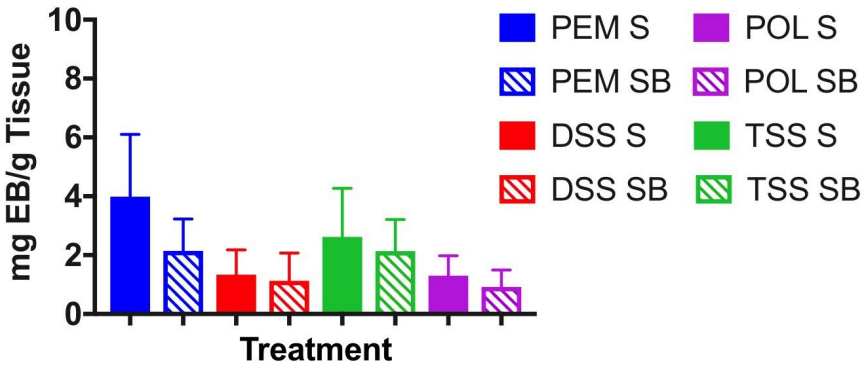

Figure 60. *Ex vivo evaluation of the effect of liquid/foamed POL in the presence (SB) or absence (S) of blood in static conditions. The vein was either prewashed (S) or filled with whole human blood (SB), and subject to 1 minute of treatment. Data are reported as mg of EB per grams of tissue, determined via Evans Blue method. The experiment was repeated six times.*

6.3.4 Dynamic test with PBS perfusion

In dynamic conditions, the spatial profile of treatment efficacy was similar to the one observed in static conditions (Figure 61). In these conditions, TSS showed the highest level of extravasation at 5 cm, whereas PEM showed the highest level at d_0. Either foam presented a gradual reduction in efficacy towards the final segment of the cord (from d_0 to d_5 ΔEB_e = 1.63 mg EB/g for PEM and ΔEB_e = 0.99 mg EB/g for TSS). The performance of DSS and POL remained almost constant along the length of the umbilical vein (variation of 0.48 mg EB/g, and 0.37 mg EB/g, respectively from d_0 to d_{10}). The highest level of disruption was achieved by PEM in proximity to the injection point (3.7 ± 2.3 mg EB/g), whereas POL reached the lowest level of disruption at 10 cm (0.5 ± 0.1 mg EB/g), a value comparable to the control.

Figure 61 shows the average performance of all treatments. PEM was statistically superior when compared to POL (p-value = 0.029). POL resulted in the lowest average level of EB extravasation (0.8 ± 0.31 mg EB/g), whereas PEM resulted in the highest level (3.2 ± 2.32 mg EB/g).

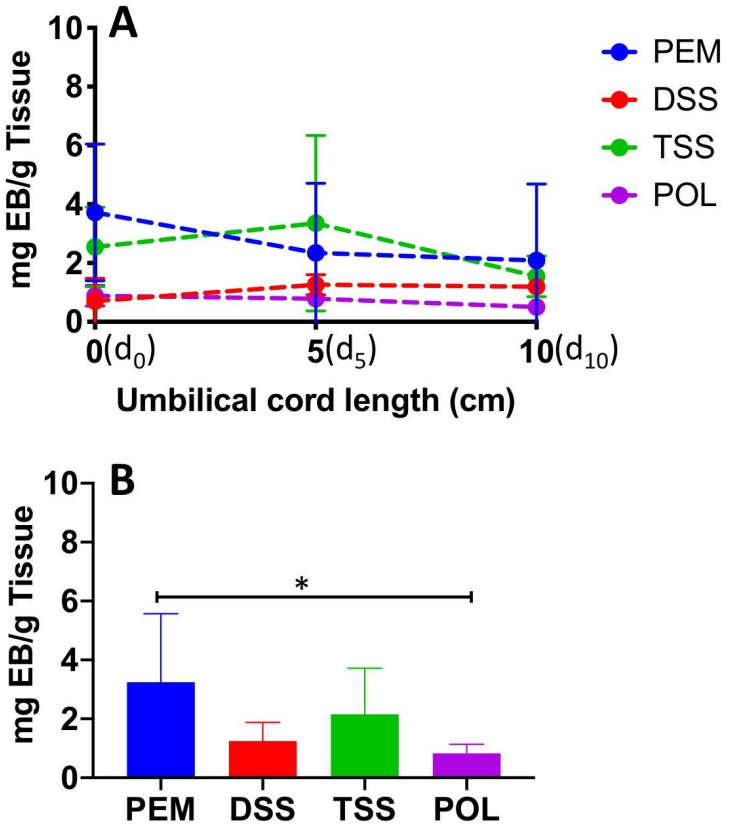

***Figure 61**. Ex vivo evaluation of the performance of liquid and foamed POL, under dynamic flow conditions. (A) Evaluation of the effect of PEM, PCFs and liquid POL treatment on the umbilical cord vein at d_0, d_5 and d_{10}. A steady flow of PBS (62.5 mL/h) was injected through the vein, which was subsequently treated with liquid/foamed POL for 1 minute. Data are reported as mg of EB per grams of tissue, determined via Evans Blue method. The experiment was repeated six times. (B) Evaluation of the effect of PEM, PCFs and liquid POL treatment on umbilical cord vein (10 cm). Data are reported as the average mg of EB per grams of tissue, determined via Evans Blue method. One asterisk (*) indicates p-value ≤ 0.05.*

6.3.5 Comparison between static and dynamic tests

Comparing dynamic with static experiments, a slight reduction in efficacy was observed for all treatments under dynamic flow conditions (see Table 11).

Table 11. Comparison between S and D tests (average values of mg EB/g of tissue).

Type of treatment	S(mg EB/g)	D(mg EB/g)	Δ_{S-D}(mg EB/g)	p-value
PEM	3.99	3.24	0.75	0.571
DSS	1.34	1.24	0.1	0.82
TSS	2.62	2.15	0.47	0.623
POL	1.3	0.82	0.48	0.146

The presence of background flow might reduce the time of contact between POL molecules

and the endothelium. However, no statistical differences were found between flow and no flow for all treatments (Figure 62). DSS foam showed the lowest difference in performance between dynamic (1.24 ± 0.63 mg EB/g) and static (1.34 ± 0.8 mg EB/g) conditions (Δ_{S-D}= 0.10 mg EB/g), whereas PEM showed the higher difference in performance (Δ_{S-D}= 0.75 mg EB/g).

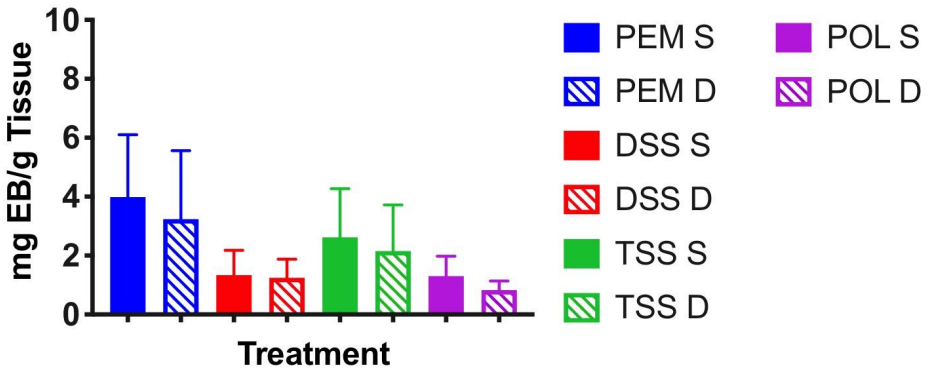

Figure 62. *Ex vivo evaluation of the effect of liquid/foamed sclerosant under static or dynamic conditions. The vein model in either static or dynamic (62.5 mL/h) conditions was exposed to 1 minute of treatment. Data are reported as mg of EB per grams of tissue, determined via Evans Blue method. The experiment was repeated six times.*

6.3.5 Dynamic test with blood perfused in the background

Afterwards, the dynamic test was repeated using whole human blood flowed continuously inside the vein. As shown in Figure 63, all treatments showed similar performance. For all types of treatment, the average value of extravasation was <2 mg of EB per g of tissue. This might be caused by direct consumption of the active detergent in the process of inducing the lysis of erythrocytes, leukocytes, and platelets.

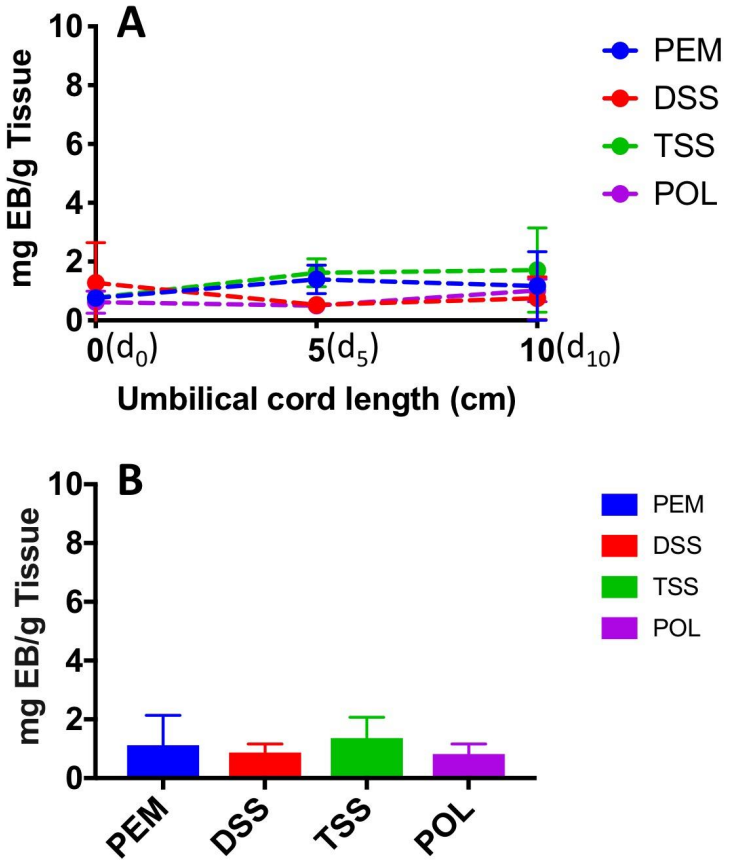

***Figure 63**. Ex vivo evaluation of the effect of liquid/foamed POL in dynamic conditions in the presence of blood. (A) Evaluation of the effect of PEM, PCFs and liquid POL treatment on umbilical cord vein at d_0, d_5 and d_{10}. The vein walls, exposed to a steady flow of whole human blood (62.5 mL/h), were subject to 1 minute of treatment. Data are reported as mg of EB per grams of tissue, determined via Evans Blue method. The experiment was repeated six times. (B) Evaluation of the effect of PEM, PCFs and liquid POL treatment on umbilical cord vein (10 cm). Data are reported as average of mg of EB per grams of tissue, determined via Evans Blue method.*

6.3.6 Comparison between dynamic and static test in presence of blood

Comparing the dynamic test DB (with blood perfused) and the static test SB (with blood resident inside the vein) there was no statistical difference in performance for all treatment types evaluated. However, a reduction in efficacy is evident for all the types of treatments (see Table 12).

Table 12. Comparison between SB and DB tests (average values of mg EB/g of tissue).

Type of treatment	SB(mg EB/g)	DB mg EB/g)	Δ_{DB-SB}(mg EB/g)	p-value
PEM	2.14	1.12	1.02	0.13
DSS	1.13	0.87	0.26	0.53
TSS	2.13	1.3	0.83	0.17
POL	0.91	0.82	0.09	0.74

POL showed lower variation in performance between dynamic and static conditions (Δ_{DB-B}= 0.09 mg EB/g) compared to PEM, which showed higher efficacy but also greater variation between the two conditions (Δ_{DB-SB}= 1.02 mg EB/g) (Figure 64).

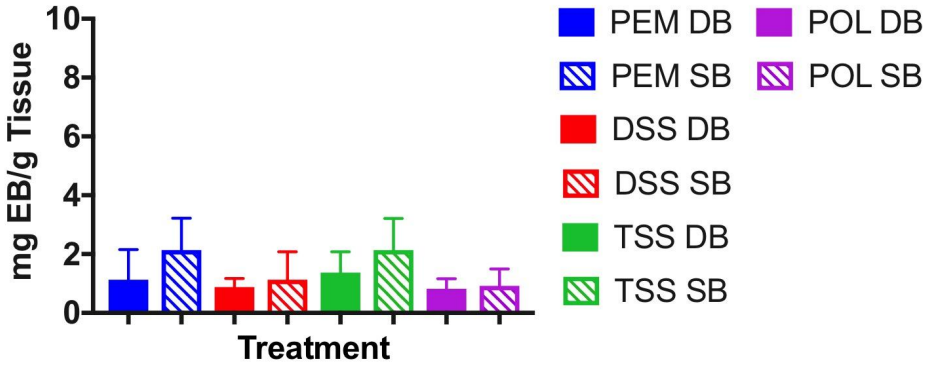

Figure 64. *Ex vivo evaluation of the performance of liquid/foamed sclerosants in dynamic and static conditions, in the presence of blood. A steady flow of blood (BD) or absence of flow (SB) were applied to the system. The vein was subject to 1 minute of treatment. Data are reported as mg of EB per grams of tissue, determined via Evans Blue method. The experiment was repeated six times.*

6.3.7 Evaluation of the effect of background liquid flow

Afterwards, the effect of a background fluid flow was analysed. In the DB test, all foams performed in a similar fashion, whereas in the D test TSS and PEM showed superior performance (Figure 65). The performance of liquid POL was independent from the type of medium. Overall, TSS and PEM showed a small decrease in the efficacy when blood was employed as a working fluid (see Table 13). However, differences are not is statistically significant.

Table 13. Comparison between D and DB test (average values of mg EB/g of tissue).

Type of treatment	D(mg EB/g)	DB(mg EB/g)	Δ_{DB-SB}	p-value
PEM	3.24	1.12	2.12	0.31
DSS	1.24	0.87	0.37	0.8
TSS	2.15	1.3	0.85	0.97
POL	0.82	0.82	0	1

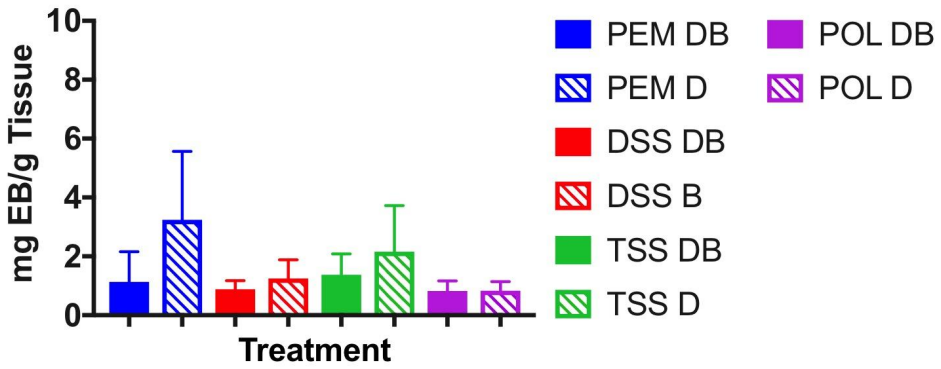

Figure 65. *Ex vivo evaluation of the effect of liquid/foamed sclerosants in dynamic conditions, in the presence/absence of blood. A steady flow of PBS (D) or blood (BD) was injected through the vein model. The vein was subject to 1 minute of treatment. Data are reported as mg of EB per grams of tissue, determined via Evans Blue method. The experiment was repeated six times.*

6.3.8 Effect of the anatomical structure of the umbilical cord on the effectiveness of sclerotherapy

All experiments reported in this Chapter have been carried out using healthy umbilical cords presenting left or right twist. Cords can present false knots or varices, which reflect vascular ectasia or tortuosity within the cord; these are rarely of clinical significance. False umbilical cord knots (pseudo-knots) are commonly formed variants in the umbilical cord anatomy. They represent an exaggerated looping of the umbilical cord vessels, causing focal dilatation that can be seen through the Wharton jelly (mucoid connective tissue that surrounds the umbilical vessels)(Figure 66).

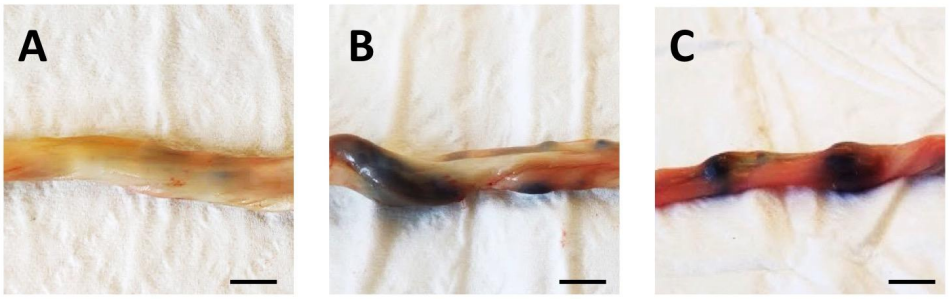

Figure 66. *Photographs showing representative umbilical cord anatomies. Umbilical cord showing (A) left twist, (B) single or (C) multiple pseudo knots. In the presence of pseudo knot, the umbilical vein is dilated and visible through the Wharton jelly (scale bar 2 cm).*

In a final phase of the study, cords presenting pseudo-knots in some region were taken in consideration in order to evaluate the effect of the sclerosants within a vessel with a non-physiological architecture. This enlarged and twisted veins might replicate the structure of

varicose veins. The test was carried out in static conditions (absence of blood).

As shown in Figure 67, in the presence of pseudo-knots the level of extravasation after treatment with PEM was significantly increased. The segment characterised by a normal left twist (segment 1) showed lower level of extravasation, which was consistent with the results reported earlier (in the range 2.34 - 8.06 mg of EB per g of tissue). With respect to segments containing varices (segment 2) the level of disruption reached values of 25.32 to 33.09 mg of EB, which are comparable to the ones obtained via collagenase-based treatment.

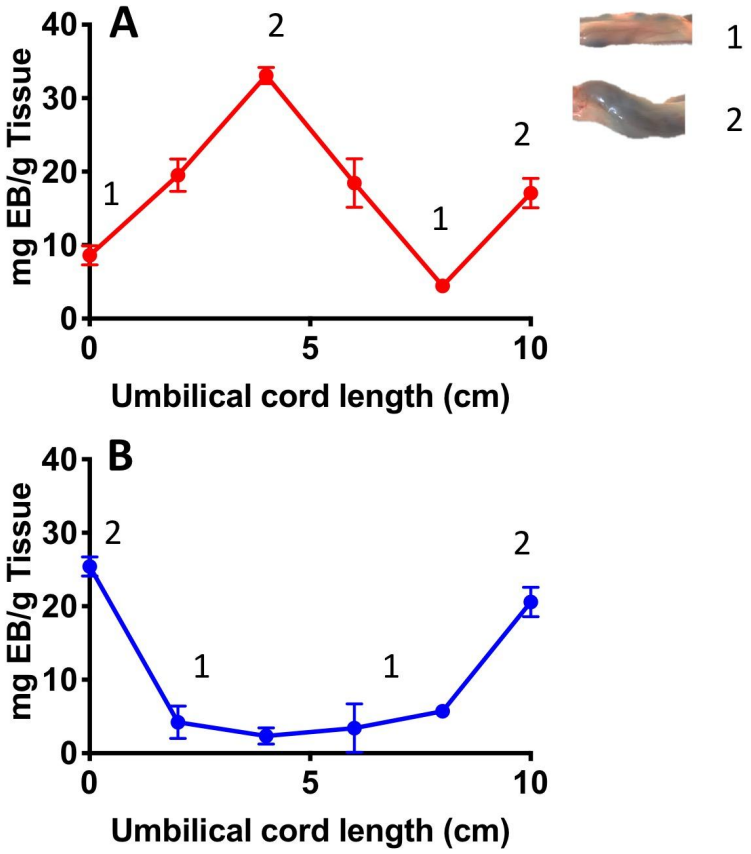

Figure 67. *Evaluation of the impact of umbilical cord anatomy. Umbilical cords presenting pseudo knots have been analysed. (A) Umbilical cord with two pseudo-knots in the position d_4 and d_{10} (4 cm and 10 cm from the injection point). (B) Umbilical cord with two pseudo-knots in the position d_0 and d_{10} (0 cm and 10 cm from the injection point). The veins were pre-washed and subject to 1 minute of treatment. Data are reported as mg of EB per grams of tissue, determined via Evans Blue method. The measurements are an average of three repeats.*

6.4 Discussion

In this chapter, four different variables were analysed in the *ex vivo* model, which depend on the background conditions such as (i) static or (ii) dynamic condition and the type of liquid in the background such as (iii) PBS (iv) and blood. These 4 parameters were combined in 4 possible scenarios: (i) static conditions in presence of PBS (S), (ii) static conditions in presence

of blood (SB), (iii) dynamic condition with perfused PBS (D) and (iv) dynamic conditions with perfused blood (DB). The umbilical cords were treated with either foamed or liquid POL.

The test carried out in static conditions with PBS (S) is the ideal scenario for sclerotherapy treatment, since the effect of "washing-out" due to background flow is not present, and the POL molecules are not consumed by blood components. In this test, there were statically significant differences between PEM vs. POL (p-value = 0.014) and PEM vs. DSS (p-value= 0.017) (Figure 58). PEM was more effective at disrupting the endothelium compared to DSS, as expected from the results obtained *in vitro*. TSS foam efficacy in disrupting the endothelium was slightly lower compared to PEM, but differences between mean values were not statistically significant (p-value= 0.238). This finding is in contrast with the *in vitro* results (Chapter 4), where DSS foam was consistently superior to TSS, although differences between PCFs significantly reduced with increasing the treatment time both *ex vivo* and *in vitro* (1 minutes). In this test the results depend only on the mechanical characteristics of the foam.

The test performed in static conditions with blood (SB) was designed to understand the interaction between blood components and sclerosant molecules.

As reported in the literature, the interaction between blood constituents and POL molecules is regarded as a potential source of sclerosant de-activation; with earlier studies describing reduction in sclerosant's lytic activity in the presence of whole blood. Sclerosant's dilution only plays a marginal role in this process; the primary underlying mechanism is associated with binding of surfactant molecules with plasma proteins, in particular albumin. This interaction causes direct consumption of active molecules, reducing the overall treatment efficacy.

Analysing the results along the length of the treated vein (10 cm in length) DSS and POL had comparable performance, which remained relatively unchanged along the length. PEM showed the highest level of disruption at 5 cm whereas TSS reached the highest value at 10 cm. PEM efficacy slightly decreased until the end of the cord. The higher level of disruption at d_5 might be associated with the ability of the foam to displace blood inside the vessel (Figure 59). The reasons behind this result might be the following: (i) dilution of active molecules, (ii) the first segment (nearby the injection site) might be exposed to a greater amount of active molecules over the time.

The effect of blood on the performance of sclerosing agents was subsequently investigated in static conditions (Figure 60). It is evident that differences appear for all types of treatment,

where efficacy reduced in the presence of blood. However, no significant difference between SB and S test has been found for the same type of treatment. This observation might be associated with the fact that foams are relatively effective in displacing blood away from the vein model, when this is in static conditions (i.e. stagnant). Results thus indicate that the presence of blood in static conditions doesn't influence the efficacy of treatment. Differences in efficacy were only observed between different types of sclerosing agent, as discussed previously. It should be noted that stagnant blood flow is likely to be a reasonable replication of the flow dynamic field within small varicose veins.

Additional experiments were performed in the presence of a sub-physiological background flow rate (62.5 mL/h), in order to investigate a more comprehensive range of end-point administration scenarios (Figure 61).
In dynamic conditions, the spatial profile of treatment efficacy was similar to the one observed in static conditions. In these conditions, TSS showed the highest level of extravasation at 5 cm, whereas PEM showed the highest level at d_0. Either foam presented a gradual reduction in efficacy towards the final segment of the cord. The performance of DSS and POL remained almost constant along the length of the umbilical vein. More cohesive foams might be more effective in the first segment of the vein, compared with less cohesive foam or POL, where the effect remains constant. Indeed, more cohesive foams act as a piston and form a uniform plug. Less cohesive foams instead tend to dilute after a certain distance.
Comparing the average performance of all treatments, POL resulted in the lowest average level of EB extravasation (0.8 ± 0.31 mg EB/g), whereas PEM resulted in the highest level (3.2 ± 2.32 mg EB/g).

Comparing dynamic with static experiments, a slight reduction in efficacy was observed for all treatments under dynamic flow conditions (see Table 11). However, no statistical differences were found between static and dynamic conditions, for all treatments (Figure 62). The presence of background flow might reduce the time of contact between POL molecules and the endothelium, but interestingly, at the flow rate investigated and within this specific vein model, the background flow rate might not be sufficient to significantly decrease the effectiveness of treatment.

Afterwards, the dynamic test was repeated using whole human blood flown continuously

inside the vein. This test has been designed in order to understand the effect of the background flow (PBS or blood) in the final outcome. Indeed, the sclerosant molecules injected in the liquid or foamed form are washed out/diluted by the blood flow, which - at the same – interacts with sclerosing agent. As shown in Figure 63, all treatments showed a similar performance. For all types of treatment, the average value of extravasation was <2 mg of EB per g of tissue.

Comparing the dynamic test DB (with blood infused) and the static test SB (with blood resident inside the vein) there was no statistical difference in performance for all treatment types evaluated (Figure 64). However, a reduction in efficacy is evident for all types of treatments. DSS showed lower variation in between dynamic and static conditions ($\Delta_{SB\text{-}DB}$= 0.26 mg EB/g) compared to PEM, which showed higher efficacy but also greater variation between the two conditions ($\Delta_{SB\text{-}DB}$= 1.02 mg EB/g).

Afterwards, the effect of fluid flowed in the background was analysed. In the DB test all foams performance were equivalent, whereas comparing in the D test (Figure 65). TSS and PEM showed the best performance. The performance of liquid POL was independent from the type of medium, showing similar behaviour between the DB test and D test ($\Delta_{DB\text{-}D}$= 0.00 mg EB/g). Overall, TSS and PEM showed a small decrease in efficacy when blood was employed as a working fluid. However, none of the changes is statistically significant. Therefore there is no statistical difference between foam types and between DB and D. These results show that, at a background flow rate of 62.5 mL/h in this model, the nature of the carrier liquid doesn't significantly influence the final treatment outcome.

All the experiments reported in this Chapter have been carried out using healthy umbilical cords presenting left or right twist. Cords can present false knots or varices might resemble the structure of varicose veins, which are generally tortuous and swollen. As shown in Figure 67, in the presence of the pseudo-knots the level of extravasation after treatment with PEM was significantly increased. The segment characterized by a normal left twist showed lower level of extravasation, which was consistent with the results reported earlier. With respect to segments containing varices the level of disruption reached values of 25.32 to 33.09 mg of EB, which are comparable to the ones obtained *via* collagenase-based treatment (Figure 57).
One potential explanation could be that, in the presence of a constriction, the shear stress

acting on the vessel wall increases, which may enhance mechanical damage to the vessel wall. Moreover, a smaller inner diameter in a vascular constriction would also promote contact between the bubbles and the inner lumen of the vessel.

6.5 Conclusion

The present study represents a systematic comparison of the biological performance of different sclerosing liquid/foam formulations in a more realistic biological model.

Experiments were performed *ex vivo* using umbilical cord veins in static and dynamic conditions, both in the presence and absence of whole blood. Sclerosant-induced disruption of the endothelium was determined from extravasation of a BSA-conjugated dye. Initially, the ability of the method to provide a quantification of endothelial disruption was assessed, using collagenase to actively cause endothelial damage. Afterwards, veins were treated with liquid POL 1% for 1, 5 and 10 minutes. A direct correlation between contact time and endothelial disruption was observed, consistently with *in vitro* experiments using sclerosing foams (Chapter 4).

Summarizing all the results reported, PEM showed better performance (statistically different) compared to DSS (in the presence of PBS) and POL (in the presence of PBS and blood) in static conditions and in the presence of PBS. In dynamic conditions, PEM presented better performance (statistically different) compared to POL only in the case where PBS was flowed in background. When blood was perfused inside the umbilical veins, all treatments presented similar efficacy. This might indicate that all the specific properties of the foams, which may influence the final outcome, are not relevant in this specific model. In the future work, more conditions might be taken into consideration, such as the effect of the blood flow rate.

All tests were conducted using healthy umbilical cords presenting left or right twist. Cords presenting false knots or varices might resemble the structure of varicose veins, which are generally tortuous and swollen. Results showed that after treatment with PEM the segment containing varices were dramatically disrupted compared to segment without varices. These segments might be employed to resemble some architectural features of varicose veins. Further experiments are needed in order to deeply understand the effect of these anatomical features on the treatment outcomes, and whether they might be a good model to replicate the structure of varicose veins. Previous tests were carried out using common umbilical cord veins (i.e. left twisted, without false knots) in order to specifically investigate the effect of fluidic conditions on the efficacy of sclerosing agents.

In this Chapter a quantitative method for evaluating sclerotherapy efficacy has been proposed. *Ex vivo* models may help understanding the biological effects of sclerosants on a real vascular tissue, and have been employed in both static and dynamic conditions, to replicate stagnant and sub-physiological blood flow. However, this model would not allow for monitoring endothelial disruption *in situ*, but only provide a post-treatment evaluation.

Therefore the development of 3D vein-on-a-chip devices, which can replicate the physiological and pathological (varicose) structure of lower limb veins, might be useful for evaluating *in situ* the effect of treatment and correlate the mechanical properties of foams with their biological effect.

Chapter 7: Vein-on-a-Chip devices for evaluating the mechanical properties of sclerosing foams

Chapter 7 covers the development of a more complex *in vitro* model, referred to as vein-on-a-chip. The chapter describes the production of the devices, followed by the design of a new set-up to quantify and compare the flow behaviour of sclerosing foams. The method was employed to evaluate physical properties of foams, which are correlated to their biological performance.

Abstract

Foam sclerotherapy is clinically employed to treat varicose veins. It involves intravenous injection of foamed surfactant agents causing endothelial wall damage and vessel shrinkage, leading to subsequent neovascularization. Foam production methods used clinically include manual techniques, such as the Double Syringe System (DSS) and Tessari (TSS) methods. Pre-clinical *in vitro* studies are conducted to characterize the performance of sclerosing agents; however, the experimental models used often do not replicate physiologically relevant physical and biological conditions.

In this study, vein-on-a-chip (VOC) models were developed and employed for the first time to characterize the flow behaviour of sclerosing foams. VOCs were fabricated in polydimethylsiloxane (PDMS) by replica molding, and were designed to mimic qualitative geometrical characteristics of veins. Foam behaviour was investigated as a function of different physical variables, namely (i) geometry of the vein model (i.e., physiological *vs.* varicose vein), (ii) foam production technique, and (iii) flow rate of a blood surrogate.

The experimental set-up consisted of a VOC positioned on an inclined platform, a syringe pump to control the flow rate of a blood substitute, and a pressure transducer. The static pressure of the blood surrogate at the VOC inlet was measured upon foam administration. The recorded pressure-time curves were analysed to quantify metrics of foam behaviour, with a particular focus on foam expansion and degradation dynamics. Results showed that DSS and TSS foams had similar expansion rate in the physiological VOC, whilst DSS foam had lower expansion rate in the varicose VOC compared to TSS foam. The degradation rate of DSS foam was lower than TSS foam, in both model architectures. Moreover, the background flow rate had a significant effect on foam behaviour, enhancing foam displacement rate in both types of VOC.

7.1 Introduction

Venous incompetence in the lower limbs is a common disease. Varicose veins have long been considered a cosmetic problem but – if left untreated – they may lead to more advanced form of chronic venous dysfunction, such as chronic venous insufficiency (CVI) (Spiridon and Corduneanu, 2017). Varicose veins are generally treated in order to prevent venous stasis, reflux, hypertension, and ulceration (Gloviczki et al., 2011). Sclerotherapy is a minimally invasive technique for treating varicose veins, and involves the intravenous injection of a sclerosing solution to cause endothelial damage, vessel shrinkage, and subsequent neovascularization (Goldman et al., 2017). Foam sclerotherapy is a development of liquid sclerotherapy, where the sclerosing solution is mixed with a gas in order to produce a 'microfoam' (bubble diameter: 100-500 μm) (Eckmann, 2009). The use of foamed sclerosants offers significant benefits, particularly in the treatment of larger lower-extremity veins (Hamel-Desnos et al., 2003; Smith, 2009; Ouvry et al., 2008). Notably, a limitation of liquid sclerotherapy is that the sclerosing agent mixes rapidly with blood and is 'consumed' or de-activated by blood cells and plasma proteins, respectively (Connor et al., 2015; Parsi et al., 2008). On the other hand, cohesive foam displaces blood away from the diseased vein, reducing the extent of sclerosant's deactivation and leading to a greater contact time with the endothelial layer. As a result, sclerosing foams can be more effective in damaging the vessel wall, and this is achieved at lower concentrations of active molecule compared to their liquid counterparts (Goldman, Weiss, and Guex, 2017).

The flow behavior of sclerosing foams is therefore an important determinant of their ability to fully prime the target vein, and to provide sufficient contact time with the endothelial layer to result in effective therapeutic outcomes. The ideal foam should be sufficiently viscous and have low bubble size dispersity, to result in adequate handling stability and cohesiveness upon injection (Star, Connor, and Parsi, 2018). Increasing the quantity of surfactant agent may result in greater foam stability; however, this is undesirable as higher concentrations of sclerosant may lead to increased risk of side effects (J D Peterson and Goldman, 2012). Phlebologists often generate foams manually; these types of foam are referred to as physician-compounded foams (or PCFs). The two most common techniques utilized for producing PCFs are (i) the double syringe system (DSS) and (ii) the Tessari (TSS) methods (Tessari, Cavezzi, and Frullini, 2001). Both techniques involve mixing of a liquid sclerosant solution with a gas or gas mixture, which is achieved by passing the liquid and gas between two syringes joined together *via* a connector (Jia et al., 2007). The gas phase most commonly used is room

air (RA); its high nitrogen (N_2) content results in a foam that is more stable than N_2-free PCFs. However, the low solubility of nitrogen in blood may be responsible for increased risk of gas embolism and neurological events. Other gases employed are clinical grade carbon dioxide (CO_2), or CO_2 and oxygen (O_2) mixtures (Jennifer D. Peterson and Goldman, 2011). Foams produced with these gases are reported to be less stable than RA-foams, due the high solubility of CO_2 in blood, but the risk of embolism is largely reduced (Cavezzi and Tessari, 2009; Jennifer D. Peterson and Goldman, 2011). However, they may be less effective in displacing blood, which could limit their therapeutic efficacy. The characteristics of PCFs can depend on many variables, including (i) the type of gas (Jennifer D. Peterson and Goldman, 2011; Larmignat et al., 2008), (ii) the liquid:gas volume ratio (typically in the range 1:3-1:7), (iii) the type of surfactant (polidocanol or sodium tetradecyl sulfate) and its volumetric concentration (typically in the range 0.5-3%) (Hanwright et al., 2005; Van Deurzen et al., 2011), (iv) the type of connector used (straight connector in DDS and a 3-way valve in TSS) (Rao and Goldman, 2005), and (v) the number of passes between syringes (in the range 5-10) (Jennifer D. Peterson and Goldman, 2011). This large parametric space often limits the possibility of comparing results from different studies; thus, there is a growing need to establish standardized methodological approaches to evaluate physical stability of PCFs (C. Hamel-Desnos et al., 2007).

Foam stability is often evaluated *in vitro* by measuring macroscopic or microscopic parameters, such as foam half time (FHT), foam drainage time (FDT), bubble size distribution, and foam dwell time (FDT) (Critello, Fiorillo, and Matula, 2017; Carugo et al., 2016; Kruglyakov et al., 2008). In a typical experiment, a defined volume of foam is produced and delivered into a vessel, where changes to its physical properties are monitored as a function of time. FHT is the time required for half of the volume of sclerosing solution to revert to liquid (Nastasa et al., 2015). FDT is instead the time at which visible liquid drainage begins (Kruglyakov et al., 2008). Both parameters can be measured by observing drainage in a standing column of foam, and quantifying the height (or volume) of the liquid phase over time. This can be determined by analysing photographic images of the foam column at increasing time points, or it can be inferred from changes in back-scattering or transmission of an incident light beam. These indicators of foam stability are however strongly dependent on the type and size of vessel in which the foam is contained (Carugo et al., 2015). Foam bubble size distribution can be measured by optical microscopy or light scattering techniques (Osei-Bonsu, Shokri, and Grassia, 2015; Watkins and Oliver, 2017). The measured bubble size may however be

strongly influenced by the invasiveness of the method used, and the time elapsed between foam production and analysis. A technique commonly used involves the injection of a foam sample between two glass plates, where foam containment in a small environment reduces the drainage and coarsening rates to facilitate imaging (Carugo et al., 2016).

The characterization methods reported above have been largely employed in the literature as a means to evaluate stability of sclerosing foams, and have been particularly useful for comparing different foam formulations (McAree et al., 2012; Cameron et al., 2013; Bai et al., 2017). However, the experimental systems used (i.e., syringes or vials) do not reflect dynamic conditions that are relevant to the end-point usage of the foam. Recently, Carugo *et al.* developed a model for the analysis of sclerosing foam behaviour under more clinically relevant conditions. The model consisted of a 4 or 10 mm inner diameter polytetrafluoroethylene tubing, placed onto a platform with an adjustable inclination angle. Foam was injected into the tube, which was initially primed using a blood substitute, and its expansion/degradation rates were quantified using computational-based image analysis software. The model allowed to measure the foam dwell time, which is the time take taken for a foam plug to recede over a unit distance (Carugo et al., 2015). It was however designed for usage under static fluidic conditions, and it did not replicate the varicose vein architecture.

In order to address these limitations of previous test methods, the work in this study aims to develop physical models replicating qualitative architectural characteristics of varicose veins and to employ them as a screening platform for comparing the flow behaviour of different foam formulation methods. The developed biomimetic-inspired vein model (referred to as vein-on-a-chip, or VOC) allows recapitulating features of physiological and varicose veins, including circular cross-section, tortuous and swollen vessel morphologies, and physiologically relevant flow conditions. VOCs were employed to compare the flow performance of polidocanol-based PCFs, as a function of vessel geometry (straight *vs.* curved centerline), foam production technique (PCF *vs.* TSS), and volumetric flow rate.

7.1.1 Limitations of *in vitro* and *ex vivo* models in sclerotherapy

The *in vitro* and *ex vivo* models reported Chapter 4 and 6 allow quantifying the biological effects of sclerosants, but they present some limitations. The 2D *in vitro* model does not replicate physiologically relevant characteristics and conditions such as (i) the physiological and pathological vein structure, (ii) the 3D endothelial layer, and (iii) the presence of a background blood flow. These limitations are addressed by *ex vivo* models, which however do

not allow real-time visualization of the biological effects of sclerosants, but only a post-treatment analysis of a sacrificed vein.

In this Chapter, the development of a new biomimetic-inspired vein model (referred to as vein-on-a-chip or VOC) is described. The VOCs allow to (i) recreate physiological and varicose vein structures (circular section, tortuous and swollen channel shape), (ii) to mimic a 3D endothelium layer (see Chapter 8), to (iii) recreate both static and dynamic conditions (blood flow).

7.2 Materials and methods.

7.2.1 Vein-on-a-chip (VOC) models: design and manufacturing

VOCs were fabricated *via* replica moulding. Firstly, the 3D vein architecture was designed in SolidWorks (Dassault Systemes SolidWorks Corporation, USA). Two different designs were generated to model both physiological and varicose veins. The physiological vein model comprised of a straight channel, whilst the varicose vein model comprised of a serpentine-like channel that replicated qualitatively varicose vein geometry. In both models, channel length and inner diameter were set to 70 mm and 4 mm, respectively (Figure 68).

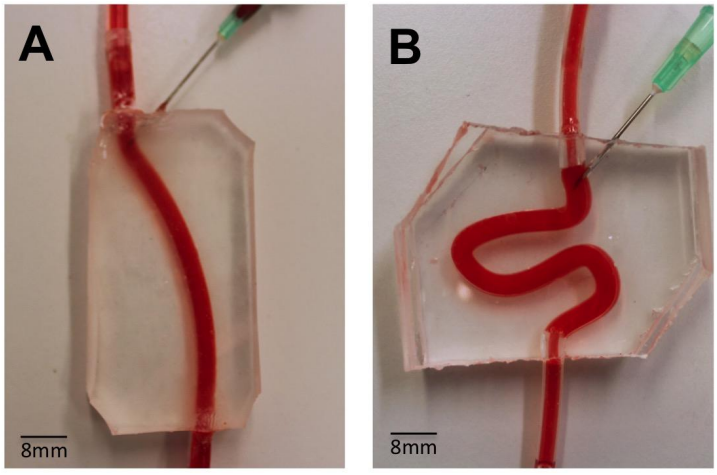

Figure 68. *Assembled VOCs representing simplified physiological (A) and varicose (B) vein models, and demonstration of perfusion using a red dye. These models were employed to test the flow behavior of foams. The main channel was punctured with a needle (21 G), in order to mimic the clinical process of injection more closely (scale bar 8mm).*

The inner diameter replicated the average diameter of veins treated with sclerotherapy (Genovese, 2002), while the length was selected so that the model could accommodate at least 1 mL of foam. The volume of foam injected clinically depends on the size of the vessel

segment to be treated (Chwała et al., 2015).

The VOC manufacturing process is illustrated in Figure 69. Firstly, positive moulds of the design were 3D printed using an Objet350 Connex printer (Haycroft Works, Buckholt Drive, UK). Two specular moulds were fabricated, each with a semi-circular channel cross-section, in order to obtain a model with a fully circular cross-section by combining the two moulds. In addition, alignment pins were added to the mould design in order to facilitate the alignment process. Polydimethylsiloxane (PDMS) prepolymer and curing agent (Sylgard® 184, Dow Corning Corporation, USA) were mixed at a weight ratio of 10:1 (w/w), and then poured onto the 3D-printed moulds. PDMS was then cured in an oven, at 65°C for 1 hour, and allowed to solidify. The two specular PDMS layers were then aligned together and permanently bonded *via* treatment with oxygen plasma (Tepla 300 Plasma Asher, PVA TePla AG, Germany). The main channel was punctured with a 16G needle (BD Biosciences, UK) in order to replicate the clinical foam administration process (Goldman et al., 2017). Inlet/outlet ports were connected with silicone tubing (4 mm outer diameter, Cole-Palmer, UK).

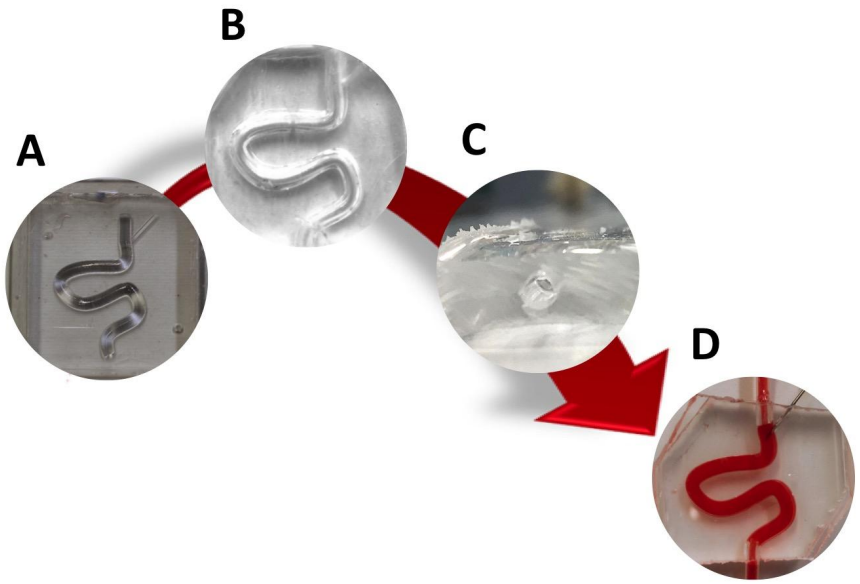

Figure 69. *Schematic of VOCs production via replica molding. Firstly, (A) a CAD design of positive molds was generated and 3D printed. Secondly, (B) two PDMS layers were produced from the molds, aligned together, and permanently bonded via oxygen plasma treatment to obtain a fully circular channel cross-section (C). Finally, the main channel was punctured with a 21G needle (D).*

7.2.2 Foam production

PCFs and PEM were employed to evaluate foam sclerotherapy efficacy. For details on foam production methods, refer to paragraph 4.2.1 (Foam production methods).

7.2.3 Characterization of the flow behavior of foams: experimental set-up

The experimental set-up consisted of a VOC lodged onto a 3D printed inclined platform (inclination angle of 25°), to replicate patient's leg elevation as in the clinical procedure. The inlet tube was connected to the VOC using a three-way stopcock. A blood substitute (30% v/v glycerol in purified water) with a fluid dynamic viscosity, μ, of 0.003 Pa · s and density, ρ, of 1078 kg/m^3 (Pries, Neuhaus, and Gaehtgens, 1992) was conveyed through the vein model using a 10 mL syringe (BD Biosciences, USA). A steady flow of the blood substitute was imposed using a syringe pump (NE-1000 Programmable Single Syringe Pump, New Era Pump Systems, Inc., USA). A pressure transducer (Research Grade Blood Pressure Transducer, 230 VAC, 50 Hz, Harvard apparatus, UK) was positioned in line with the inlet tubing, and located 30 mm proximally to the VOC inlet. The pressure transducer was connected to a National Instruments I/O module (NI-DAQ, USB-6008, National Instrument, UK). The NI-DAQ system supports analog and digital inputs, and communicates with the NI-DAQ software (National Instrument, UK). A MATLAB® (The MathWorks Inc., USA) script was employed to store pressure data in an automated fashion (Figure 70).

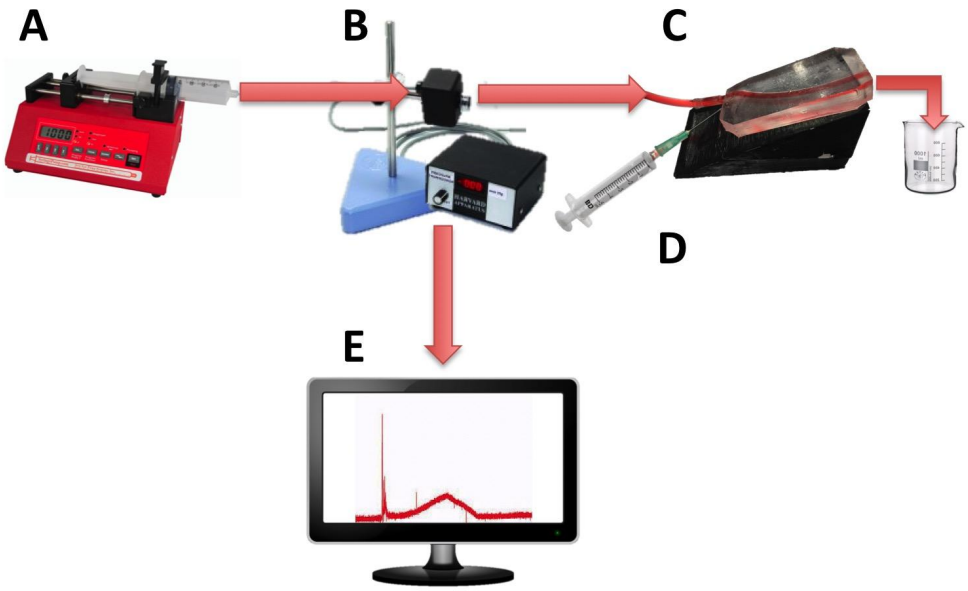

Figure 70. *Schematic illustrating the set-up for evaluating the flow behaviour of foams in the VOC model. A steady flow is imposed using a syringe pump (A), and a pressure transducer (B) is positioned in line with the inlet tubing and prior to the VOC (C). The foam is injected through the 16G needle into the main channel (D). The pressure transducer is connected to a National Instruments I/O module. The NI-DAQ system supports analog and digital inputs, and communicates with the NI-DAQ software. A Matlab code is employed to store pressure data in an automated fashion (E).*

7.2.4 Characterization of the flow behavior of foams: experimental procedures

As described earlier, the 30 mL syringe was filled with a blood substitute, which was conveyed through the VOC at constant flow rates. A clinically relevant volume of foam (1 mL) (Eckmann, 2009) was injected manually into the VOC through a needle, using a silicon-free plastic syringe with capacity of 5 mL. The static pressure of the blood surrogate at the VOC inlet was measured before, during and after injection of foam, for a fixed time of 100 seconds. The static pressure was set to 0 mmHg before injecting the foam. Results were transferred to a personal computer and analyzed as described in the following paragraphs. The volumetric flow rates investigated were 62.5, 72.0, and 125.0 mL/h. The corresponding inlet Reynolds number was calculated using Equation 4, where ρ is the density of the blood surrogate (kg/m^3), v is the mean velocity of the blood surrogate (m/s), D is the hydraulic diameter of the vein model (m), and μ is the dynamic viscosity of the blood surrogate (Pa · s).

$$Re = \frac{\rho v D}{\mu}$$

[Eq. 4]

The Reynolds number in these experiments ranged from 1.65 to 3.34, which is approximately 100-200 times lower than physiological values (Raju et al., 2004), in order to replicate quasi-static or impaired flow conditions occurring in diseased veins (Table 14).

Table 14. Flow rate and Reynolds number calculation.

Flow rate (mL/h)	Velocity (m/s)	Reynolds number
62.5	0.00136	1.65491
72.0	0.00159	1.92805
125.0	0.00275	3.34195

7.2.5 Computational foam analysis system

A computational foam analysis system (CfAS) was developed with the aim of analyzing the pressure recordings upon foam injection. The analysis system was designed using MATLAB R2016a software (The MathWorks Inc., USA) with a flexible user-intended interface. The software read the experimental pressure measurements and performed a sequence of semi-automated operations, allowing extraction of relevant parameters from the pressure-time data.

The pressure-time curve could be divided into three phases (Figure 60): (i) an initial spike due to the foam injection procedure, (ii) an almost linear increase in pressure due to the expansion of the foam within the VOC, and (iii) an almost linear decrease in pressure caused by foam degradation and 'washing out'. The CfAS calculated the slope of phases (ii) and (iii), which were referred to as expansion rate (ER) and degradation rate (DR), respectively. In addition, expansion time (ET) and degradation time (DT) were also quantified.

A representative pressure profile is illustrated in Figure 71, from which four different phases can be identified:

(i) *Foam injection*. This phase was associated with a rapid pressure spike, likely due to the insertion of the needle within the VOC or other mechanical perturbations associated with the injection procedure. Peak pressure values in this phase ranged from 10 mmHg to 50 mmHg.

(ii) *Foam plug expansion*. While the foam plug expanded within the VOC, the backpressure increased almost linearly. This is due to the significantly higher effective viscosity of foams compared to the blood surrogate, as reported in previous studies (Wong et al., 2015), leading to increased hydraulic resistance. The linear pressure increase is coherent with previous studies investigating foam behavior in a tube model, which revealed an almost linear increase in foam plug length during expansion (Carugo et al., 2015). The CfAS allowed quantifying the slope of the plug expansion phase, which was herein referred to as expansion rate (ER). It is hypothesized that more cohesive foams would fractionate more slowly and dilute less rapidly with the blood substitute, thus resulting in lower ER and higher peak pressures. The expansion time (ET) was also calculated from the pressure-time curve; higher ET corresponds to a longer contact time between the foam and the inner surface of the VOC.

(iii) *Foam plug degradation*. Once expansion was complete, the foam plug underwent degradation. This is due to a combination of processes, including foam drainage, coarsening, and the 'washing out' action exerted by the background flow of a blood substitute. Foam degradation resulted in a reduction in hydraulic resistance, leading to an almost linear drop in VOC backpressure. As for the degradation phase, the shape of the pressure profile during degradation is consistent with prior studies (Carugo et al., 2015). The CfAS allowed quantifying the slope of the plug degradation phase, which was referred to as degradation rate (DR). It is hypothesized that more cohesive foams would destabilize more slowly, thus resulting in lower DR. The degradation time (DT) was also calculated from the pressure-time curve; higher DT corresponds to a longer contact time between the foam and the inner surface of the VOC.

(iv) *Residual pressure*. The pressure level at the end of the degradation phase could be equal or greater than the initial pressure (i.e., at the time of injection). Because of gravitational separation, bubbles accumulated at the top surface of the vein model. If sufficiently stable, they would remain in place for the duration of the pressure recording (up to 100 sec), causing the residual pressure to be greater than the initial pressure.

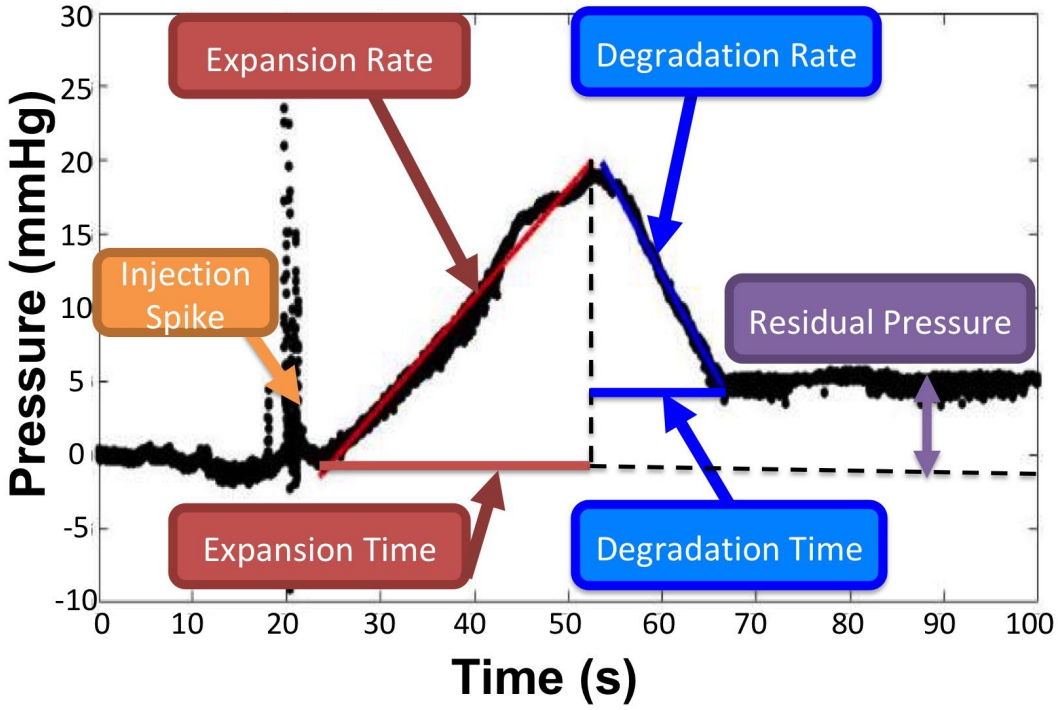

Figure 71. *Representative pressure vs. time curve obtained by the CfAS. The plots were divided into three phases: (i) an increase of the pressure due to the expansion of the foam inside the channel, (ii) a decrease of the pressure caused by the degradation of the foam, and (iii) an initial peak due to the injection.*

7.2.6 Statistical analysis

Comparisons between foam production methods were performed using an unpaired Student's t-test for two groups analysis, or one way ANOVA in the case of more than two groups. Statistical significance was assumed for p-value < 0.05. All statistical tests were performed with Prism software (GraphPad Software Inc., USA). All data were reported as the mean ± SD of at least six independent repeats of the same experiment.

7.3 Results

The VOC models developed in this study have been employed to characterize the flow behaviour of sclerosing foams, by measuring static pressure of a blood surrogate at the VOC inlet.

Representative pressure-time curves obtained by CfAS, for both DSS (blue line) and TSS (red line) foams are shown in Figure 5. Both VOC geometries, i.e. straight (Figure 72A-B) and serpentine-like (Figure 72C-D), showed similar pressure profiles containing the four phases discussed earlier. As a control test, pressure was measured without injecting the foam, at a constant background flow rate of 72 mL/h (Figure 72E). As expected, no pressure variation was detected in these experiments for both VOC geometries. In addition, tests were also performed where foams were injected in the absence of background flow (Figure 72F). In this case, only the pressure spike corresponding to foam injection was present, due to the absence of a background pressure-driven flow.

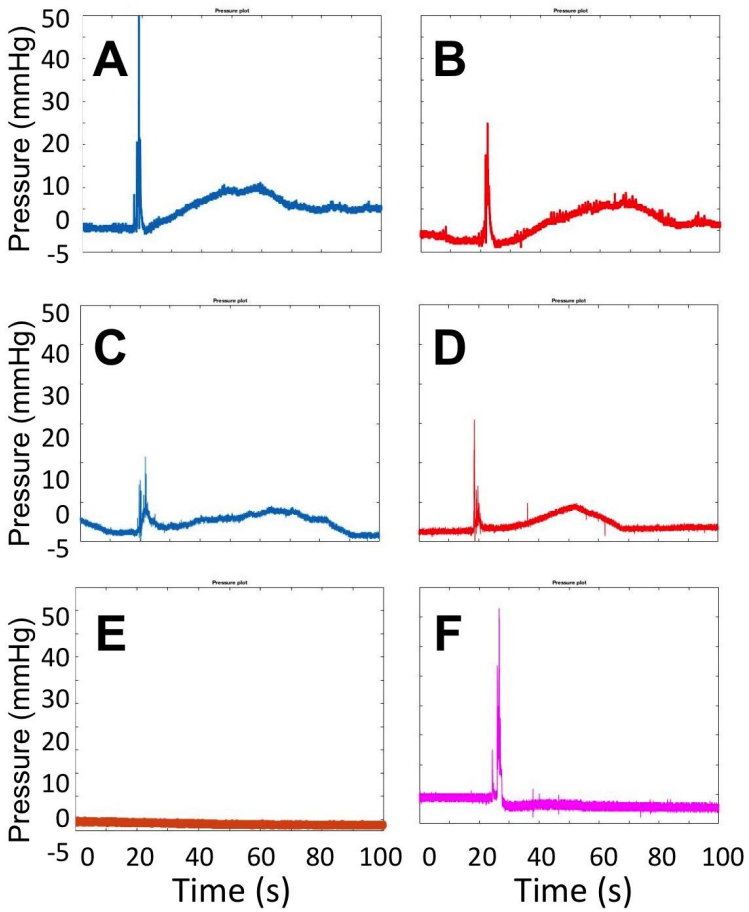

Figure 72. *Pressure plots obtained from the CfAS while injecting DSS (A, C) and TSS (B, D) foams. The upper panels show the recordings obtained using the straight channel geometry, whereas the lower panels show the recording obtained using the serpentine-like channel geometry. As a control test (E), the pressure was measured without injecting foam, at a background constant flow rate (72 mL/h). The pressure inside the vein models was also measured while injecting the foam in the absence of a blood-surrogate flow (F).*

Figure 73 shows the ER values determined for both TSS and DSS foams at all flow rates investigated, using both physiological (Figure 73A) and varicose (Figure 73B) VOCs. Lower ER is herein regarded as a therapeutically favorable property of foams, as it is indicative of

higher foam cohesion and longer persistence in the vein. In the physiological VOC, TSS and DSS had comparable ER at all flow rates investigated. Values were equal to 0.25 ± 0.01 mmHg/s (62.5 mL/h), 0.26 ± 0.01 mmHg/s (72.0 mL/h), and 0.33 ± 0.04 mmHg/s (125.0 mL/h) for TSS; and 0.27 ± 0.03 (62.5 mL/h), 0.32 ± 0.06 mmHg/s (72.0 mL/h), and 0.37 ± 0.02 mmHg/s (125.0 mL/h) for DSS. On the other hand, in the varicose VOC model, DSS foam had lower ER compared to TSS, particularly at the highest flow rate (0.49 ± 0.03 mmHg/s for TSS and 0.29 ± 0.08 mmHg/s for DSS). Differences in foam behavior may be attributed to their bubble size distribution and drainage kinetics (Carugo et al., 2015).

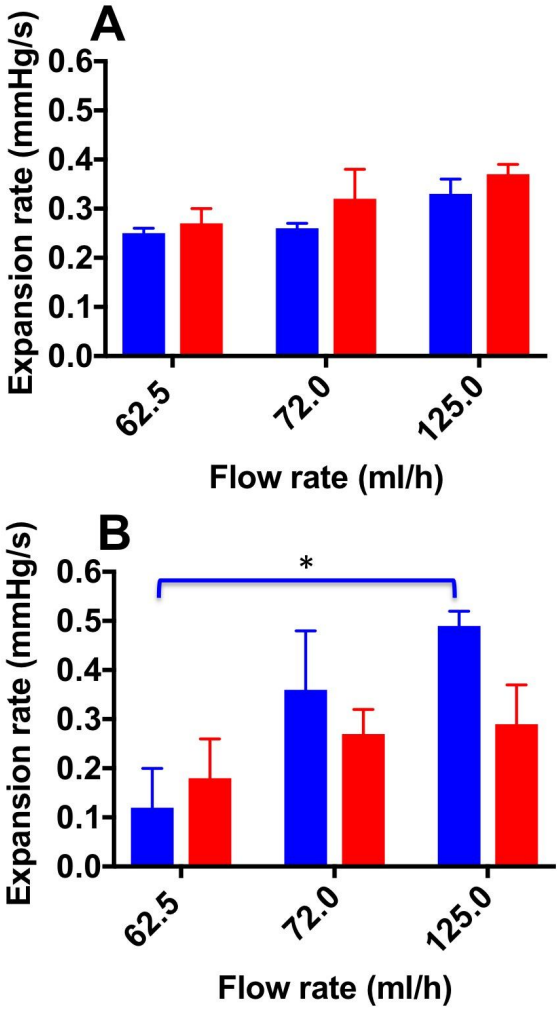

Figure 73. *Expansion rate values at the different flow rates investigated, and different foam production methods (TSS blue bars, DSS red bars). Measurements were obtained from the straight (A) and curved (B) channel geometry. Data represent the average of 6 measurements ± SD. An asterisk (*) indicates that differences between mean values are statistically significant (p-value < 0.05). The experiment was repeated six times, and results are reported as mean value ± standard deviation.*

A one-way ANOVA was conducted to evaluate whether ER of both types of foam depended on the inlet flow rate. With respect to the TSS group, a significant difference was observed

between all flow rates investigated; indeed, the average ER value increased with increasing the inlet flow rate.

Figure 74 shows the ET values determined for both TSS and DSS foams, at all flow rates investigated. As expected, the expansion time (ET) was slightly higher for TSS at 62.5 mL/h and 72.0 mL/h (39.9 ± 1.00 and 28 ± 8.00 s, respectively) compared to DSS (29.9 ± 5.00 and 23 ± 2.00 s, respectively).

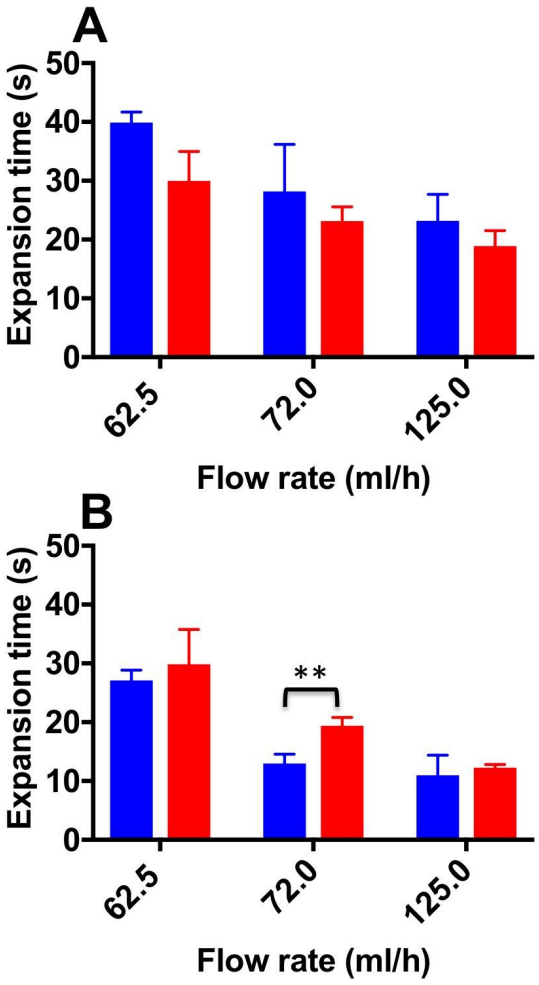

Figure 74. *Expansion time values at the different flow rates investigated, and different foam production methods (TSS blue bars, DSS red bars). Measurements were obtained from the straight (A) and curved (B) channel geometry. Two asterisks (**) indicate that differences between mean values are very statistically significant (p-value < 0.01). The experiment was repeated six times, and results are reported as mean value ± standard deviation.*

However, in the physiological VOC no statistical difference was determined between PCFs. In the varicose VOC, TSS foam had lower ET compared to DSS foam at all flow rates investigated, consistently with the expansion rate data reported previously. Statistical difference between TSS and DSS was found at 72.0 mL/h (12.98 ± 1.60 s and 19.35 ± 1.430 s

for TSS and DSS, respectively). In both VOC models, increasing the background flow caused a reduction of ET, likely due to a 'washing out' effect of the blood surrogate, as discussed earlier. In the varicose vein model, DSS foam demonstrated greater ability to oppose this effect, resulting in higher contact time with the vessel wall.

Figure 75 shows DR values determined for both TSS and DSS foams, at all flow rates investigated. In the physiological VOC, at the lowest flow rate (62.5 mL/h), DSS foam had a lower DR (0.26 ± 0.01 mmHg/s) compared to TSS foam (0.32 ± 0.03 mmHg/s). Significant difference in DR between TSS (0.45 ± 0.06 mmHg/s) and DSS (0.37 ± 0.09 mmHg/s) foams was found at 72.0 mL/h. At the highest flow rate (125.0 mL/h) both types of foam had similar DR (0.48 ± 0.03 mmHg/s for TSS and 0.47 ± 0.07 mmHg/s for DSS), suggesting that foam degradation performance is dominated by the background flow at these higher flow rates. A one-way ANOVA was performed to evaluate the effect of background flow rate on DR, for both types of PCF. With respect to the DSS group, a significant difference was observed with increasing the inlet flow rate; indeed, the average DR value increased with increasing the flow rate. With respect to TSS group, no significant difference was found by varying the flow rate. Both foams had comparable degradation performance across the two VOC geometries, suggesting that once a foam plug has been established into the vein, its degradation dynamics is not significantly affected by the vessel architecture.

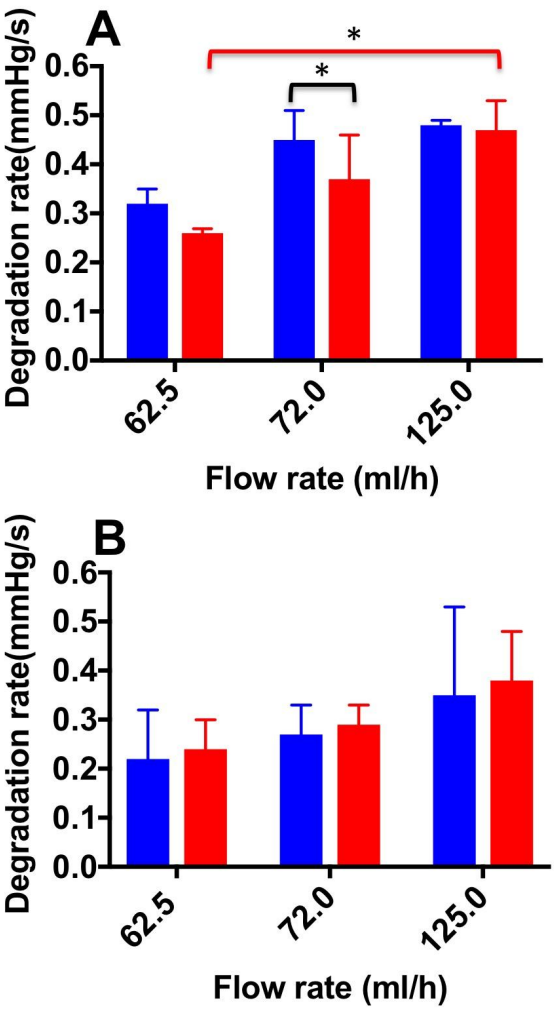

Figure 75. *Degradation rate values at the different flow rates investigated, and different foam production methods (TSS blue bars, DSS red bars). The measurements were obtained from the straight (A) and curved (B) channel geometry. An asterisk (*) indicates that differences between mean values are statistically significant (p-value < 0.05). The experiment was repeated six times, and results are reported as mean value ± standard deviation.*

Figure 76 shows DT values determined for both TSS and DSS foams at all flow rates investigated. In the physiological VOC model, at the lower flow rate (62.5mL/h), DSS foam had a statistically higher DT (20.73 ± 2.60 s) compared to TSS foam (15.46 ± 2.30 s). At the intermediate flow rate, the average DT value was still higher compared to TSS (16.38 ± 3.70 s and 10.90 ± 3.40 s, respectively). At the highest flow rate (125.0 mL/h) both PCFs had comparable DT (9.97 ± 5 s for TSS and 7.8 ± 5.6 s for DSS). As expected, foams with lower degradation rate had a longer degradation time. Similar observations were made using the varicose VOC model, where at the lowest flow rate (62.5 mL/h) DSS foam had statistically higher DT (24.8 ± 6.20 s) compared to TSS. Differences between foam types reduced with increasing the inlet flow rate. At 125.0 mL/h, both types of foam presented similar DT (9.1 ±

5.3 s for TSS and 11.07 ± 4.1 s for DSS). A one-way ANOVA was conducted to compare the effect of flow rate on DT for both types of foam. With respect to the DSS group, results show that there is a significant difference between DTs measured at increasing flow rates, for both types of geometry. Moreover, DT was not significantly influenced by the VOC geometry, as for the degradation rate. With respect to the TSS group, no significant difference was found by varying the background flow rate.

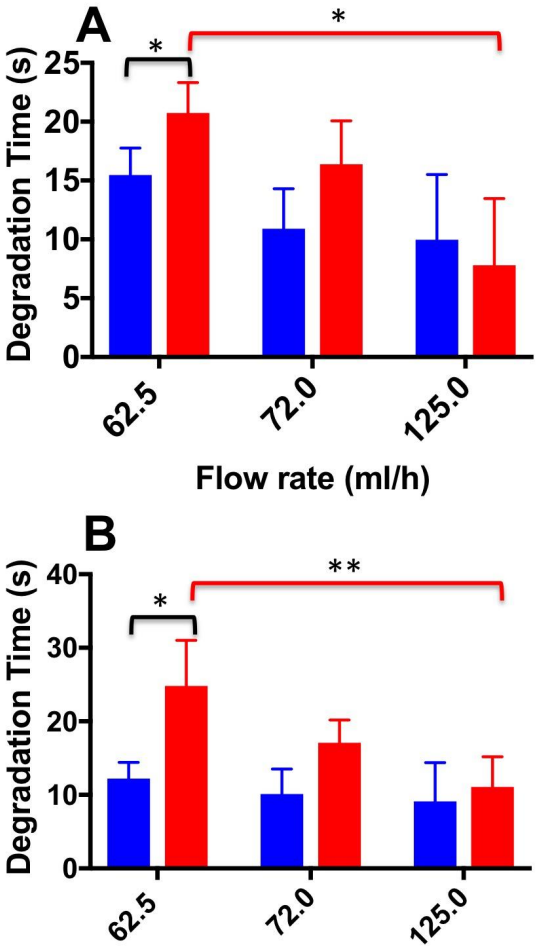

Figure 76. *Degradation time values at the different flow rates investigated, and different foam production methods (TSS blue bars, DSS red bars). The measurements were obtained from the straight (A) and curved (B) channel geometry. An asterisk (*) indicates that differences between mean values are statistically significant (p-value < 0.05) and two asterisks (**) indicate that differences between mean values are very statistically significant (p-value < 0.01). The experiment was repeated six times, and results are reported as mean value ± standard deviation.*

7.4 Discussion

In this study, a novel experimental method to quantify and compare the flow behaviour of sclerosing foams was developed. The method provided a quantitative determination of fluid pressure upon foam administration, within models of either physiological or varicose veins

(referred to as vein-on-a-chip, or VOC).

When cohesive foam is injected into the VOC, it forms a plug that displaces the blood substitute. The foam plug however degrades over time, due to its intrinsic instability and the 'washing out' action of the background flow. Using the developed model system, it was possible to characterize these phenomenological behaviours for the first time, by measuring the static pressure of a blood surrogate at the VOC inlet.

It is well known that sclerosing foams produced using different techniques differ in their 'static' physical properties. In this study, for the first time the dynamic flow behaviour of sclerosing foams were evluated, by analysing their expansion and degradation within qualitative models of both physiological and varicose veins. In particular, the behaviour of different PCFs was compared, at varying volumetric flow rates (in the range 62.5 – 125.0 mL/h).

Overall, the results reported in this study show that TSS and DSS foams had comparable expansion rate in the physiological vein model, whereas TSS had faster expansion rate in the varicose model (Figure 73). Therefore, DSS foam has the ability to expand more slowly within a varicose vein model architecture, resulting in longer contact time (ET) with the vein wall upon injection (Figure 74). These results are consistent with prior studies showing that DSS foams are more cohesive than TSS foams in a tube model, in the absence of a background flow rate (Carugo et al., 2015).

Results also demonstrated that the flow field within the target vein could significantly influence the expansion dynamics of sclerosing foams. DSS foam was slightly less sensitive to changes in the background flow rate, suggesting that more cohesive foams may offer higher resistance to the 'washing out' effect of the blood flow during expansion. Reducing blood flow rate during administration (i.e. *via* vein compression) may thus be preferable to enhance therapeutic efficacy.

With respect to the degradation dynamics of PCFs, at the lowest flow rate investigated DSS foam had lower degradation rate compared to TSS foam (Figure 75). This was likely due to the slower coarsening and drainage rate of DSS foams, coherently with previous studies (Carugo et al., 2015). Increasing the inlet flow rate resulted in PCFs having comparable degradation rate, suggesting that foam degradation performance is dominated by the background flow in these conditions. Interestingly, there was no significant difference in the degradation dynamics between the two VOC geometries investigated; suggesting that once a foam plug has been established into the vein, its degradation dynamics is not significantly

affected by the vessel architecture (Figure 76).

It is important to highlight that expansion and degradation dynamics taken at the lowest flow rate are likely to be more representative of the flow conditions in a diseased (i.e. varicose) vein. In these conditions, DSS presented a slightly superior performance compared to TSS.

7.5 Conclusion

In this study, the development of vein-on-a-chip models replicating the qualitative architecture of physiological and varicose veins were described, and their utility as model platforms to screen the flow behaviour of sclerosing foams, upon different formulation and administration conditions, was evaluated.

A simple method to manufacture vein models was developed, which aimed at generating channels with circular section and with a geometry that recapitulates some characteristics of the varicose vein. An experimental protocol was also established to investigate the flow performance of foams at conditions relevant to their clinical administration. Notably, the experimental set-up replicated some aspects of the clinical process of foam injection, including the use of a needle, patient's leg elevation, and the presence of a background blood flow.

Fluid pressure at the VOC inlet was measured during foam administration, which revealed different phases of the foam expansion and degradation dynamics. Particular emphasis was given to expansion and degradation of the foam plug, as indicators of its therapeutic efficacy.

As reported in previous studies (Carugo et al., 2015), the cohesiveness of foams is highly dependent on their rheological properties, which in turn are influenced by the bubble size distribution and foam drainage kinetics. Previous results showed that foam produced using the DSS method were more stable and presented longer dwell time compared to TSS foams (Carugo et al., 2015). Consistently with these previous observations, in our dynamic study DSS foam had longer degradation time and slower degradation rate than TSS foam. With respect to the expansion dynamics, no significant difference between the two foam formulations was found in the physiological vein model, whereas DSS had slower expansion in the varicose model. Differences in foam behaviour across different model geometries could be attributed to the broader bubble size distribution of TSS foam compared to DSS foam; although these aspects merit further investigation.

In conclusion, the vein-on-a-chip models and experimental methods developed in this study provide a novel technology platform to measure the behaviour of different formulations of sclerosing foams, at physical conditions that resemble their clinical administration. They could

therefore be employed as an additional test method in the pre-clinical pipeline, to innovate foam formulation and administration procedures.

It should be noted that the VOC models reported in this study do not replicate the presence of venous valves or branching structures, which may affect the flow behaviour of foams. Future research may focus on the incorporation of these additional architectural and functional characteristics. Moreover, a more faithful replication of the physiological boundary conditions (including changes due to clinical practices; i.e. vein compression) could be considered in the future.

Chapter 8: Development of more complex VOC

Chapter 8 describes the development of a method to create channel networks within a hydrogel matrix in a facile, rapid and reproducible way, and using only natural hydrogels. The method was used for the production of both scaffold (i.e. extra-vascular compartment) and perfusable channel networks. Particular attention was devoted to the use of replica or sacrificial molding techniques to generate the scaffold.

Abstract

Microfluidics has been increasingly employed in vascular tissue engineering. Microvascular models are typically made of PDMS, and consist of microchannels lined with endothelial cells, recapitulating key vascular properties such as the size scale, the 3D structure, and physiologically relevant haemodynamic parameters.

Although PDMS-based microdevices have allowed significant progress in the development of physiologically relevant models of the vascular system, the material and surface properties of PDMS do not represent the ones of native ECM. Therefore, hydrogel-based microfluidics is gaining interest as an alternative method for producing models that more closely mimic the *in vivo* microenvironment. Nonetheless, being a relatively recent technology, further efforts need to be put in place in order to be able to (i) fabricate capillary-sized channels (i.e., due to the resolution of current bio-printers); (ii) standardize the fabrication techniques; and (iii) produce complex vascular networks. Therefore, hydrogel-based microdevices often present simpler architectures and the production process is frequently more complex in comparison to PDMS-based methods. For these reasons, PDMS microdevices are commonly employed to characterize mechanical effects on ECs, whereas hydrogel-based devices are the preferred option for performing permeability assays. A more effective integration between microfabrication techniques and tissue engineering methods is therefore needed in order to obtain more realistic vascular models, where physiologically relevant geometrical/mechanical characteristics are combined with biochemical/biophysical properties.

In this chapter PDMS- and hydrogel-based VOCs devices have been designed and produced in order to recreate vasculature models. Particularly, a new method for generating channels inside hydrogel scaffolds has been proposed. This method allows manufacturing of channels with different size and geometry in a controlled manner.

8.1 Introduction

8.1.1 PDMS-based microfluidic devices

Microfabrication techniques allow the construction of biomimetic vasculature channels, which cannot be recapitulated using current *in vitro* systems. These manufacturing techniques include soft- and photo-lithography (Qin et al., 2010), laser ablation and more recently new methods such as bioprinting (Murphy and Atala, 2014), needle-casting (Buchanan et al., 2014) and sacrificial templating (Wang et al., 2014) approaches. With respect to the first two methods, the microdevices are commonly made of plastic or silicon-based (i.e., PDMS) materials (Choi et al., 2013); whereas in the last three methods they are made of hydrogels (Li et al., 2012).

Microfluidics has been increasingly employed in vascular tissue engineering. Microfluidic devices are often fabricated using PDMS, a silicon elastomer that offers several advantages, including: (i) cost-effectiveness, (ii) biocompatibility, and (iii) optical transparency. In addition, it can be molded into different architectures at high throughput, allowing fabricating channel networks with geometries comparable to physiological vascular systems. It is thus a suitable substrate for the growth of different cell types, under flow perfusion or in static conditions, and is compatible with real time monitoring of environmental parameters (i.e., via integration with optical or other sensors).

PDMS microdevices typically consist of microchannels lined with endothelial cells, recapitulating key vascular properties such as the size scale, the 3D structure, and physiologically relevant haemodynamic parameters. Areas of application for these devices include the study of (i) morphogenesis of ECs and the regulation of angiogenesis (Herbert and Stainier, 2011) (Staton et al., 2009); (ii) haemodynamics and the effect of shear stress on EC morphology and function (Buchanan et al., 2014); (iii) regulation of vascular permeability (Sukriti et al., 2014).; (iv) pathological conditions such as tumor vasculature and thrombosis(Buchanan et al., 2013); and (v) the production of vascular systems for tissue engineering and organ-on-chip constructs.

Morphogenesis and angiogenesis.

The formation of new blood vessels from existing vessels, referred to as angiogenesis, is a complex multistep process controlled by pre-existent ECs, that occurs in response to

inadequate oxygen and nutrient supply (Herbert and Stainier, 2011). After the activation of angiogenic cues, ECs change their behaviour losing their cell–cell junction contacts, activating proteases that degrade the basement membrane, and becoming invasive and motile in order to initiate sprouting of new blood vessels. Angiogenesis is essential to several physiological and pathological processes, such as wound healing and tumour growth. The traditional *in vitro* platforms for studying angiogenesis consist of a monolayer of ECs seeded on hydrogels (Staton et al., 2009);. Although *in vitro* models allowed an understanding of the angiogenic factor(s) involved in this process, these static environments present a lack of chemical gradients and mechanical cues that would be otherwise produced *in vivo.*

Vickerman *et al.* developed a microfluidic device to study the morphogenesis of ECs. The microdevice developed was made of PDMS and presented two parallel flow channels integrated with a 3D scaffold in order to recreate the *in vivo* 3D microarchitecture. The production procedure included a surface treatment (using oxygen plasma) to render the PDMS hydrophilic, followed by gel microinjection. This platform allowed visualizing the sprouting and migration of ECs at microscopic level, which is not possible using the traditional models. Using time-lapse recording, authors showed the different phases of angiogenesis; i.e. the 'lead-cell' invading the underlying 3D collagen matrix and extending filopodial projections, while the other ECs on the monolayer remained non-invasive. Afterwards, filopodia underwent dynamic projection and retraction, followed by morphological changes. The invading cells subsequently formed sprouts with open-lumen structures (Vickerman et al., 2008).

Chung and colleagues proposed a platform to evaluate and quantify capillary growth and endothelial cell migration from ECs monolayer in mono and co-culture (comprising cancer cells and smooth muscle cells). The device contained three independent flow channels separated by a 3D collagen gel, where ECs were cultured in the center microfluidic channel in direct contact with the collagen scaffolds on either side. In order to quantify the migration of ECs into the scaffold, the device was monitored over time in response to multiple biophysical, biochemical or co-culture conditions, including different scaffold stiffness, vascular endothelial growth factor (VEGF) gradients, and cell type (Chung et al., 2009). The results obtained from the cell migration assay demonstrated that tumor cells could attract ECs and induce capillary formation, whereas in presence of smooth muscle cells the effect of attraction was minimal.

Song *et al.* investigated how fluid and chemical factors affect sprouting. They designed a

microfluidic platform with two parallel channels (lined with human umbilical vein endothelial cells, HUVECs) and seven apertures of 3D collagen I gel matrix that allow the contact between the vessel walls and the intervessel matrix. HUVECs were stimulated with VEGF in order to induce the cell migration into the bulk of the 3D matrix, and in parallel were exposed to fluid shear stress. Results showed that fluid shear stress inhibits vessel morphogenesis *via* the nitric oxide (NO) pathway, and the interstitial flow increases the rate of morphogenesis (Song and Munn, 2011). The same group described a microfluidic device used to reproduce the vascular anastomosis process, where the sprouts connect with other vascular segments. Using the same devices, they were able to recreate the conditions necessary for anastomosis: extension of endothelial sprouts away from an existing vessel into a 3D matrix, and connection of this sprout with another endothelial-lined structure to form a new circuit.

Zheng *et al*. developed a microfluidic vascular network for long-term cell culture. They investigated the angiogenic remodeling, focusing specifically on the interactions between ECs and perivascular cells, and between blood components and the endothelium. Particularly, the microfluidic device allowed producing endothelialized vessels with physiologically relevant geometries such as bifurcations and junctions. These studies reproduced important characteristics of microvessels observed *in vivo*, in both healthy and pathological scenarios (Tsai et al., 2012).

Another example of co-culture was presented by Kim and colleagues. They described a microfluidic-based platform where the ECs were co-culture with stromal fibroblasts, pericytes, or cancer cells. This approach allowed controlling the heterotypic cell–cell interactions, which are fundamental in physiological morphogenesis of ECs to produce networks of microvessels. The microfluidic chip was fabricated using standard photolithography and soft-lithography techniques. It consisted of five parallel channels: a ECs culture central channel and two lateral stromal cell culture channels, separated by two fluidic channels. Microspots were added into the channels to reproduce the surface tension of ECM and to create a route for the paracrine interactions between ECs and stromal cells during angiogenesis. They monitored the growth of angiogenic sprouts in the platform over 7 days. After one day, the ECs displayed elongated morphology and after 2 days they started to self-assemble into a tubule-like structure. Furthermore, perfusable microvascular networks were visible by day 4 to 5. This work demonstrated the importance of the co-culture approach, which allows modeling the cross-talking between ECs and perivascular or stromal cell types, which is essential to control the formation and function of new blood vessels (Kim et al., 2013). Furthermore, Zanotelli *et al.*

presented a microdevice lined with human induced pluripotent stem cell-derived endothelial cells (iPSC-ECs) cultured in PEG-hydrogel. The results showed that iPSC-ECs cultured in PEG-hydrogels were consistent with *in vivo* vasculogenesis and angiogenesis, indeed they self-assembled into vascular networks under physiological shear stress and were viable for 14 days (Zanotelli et al., 2016).

Haemodynamic and mechanical stimulation studies

Endothelial cells are exposed to various haemodynamic forces associated with blood flow. These include fluid shear (a force tangential to the endothelium), the tensile stress, and a normal stress caused by the static pressure (Buchanan et al., 2014). Microfluidic devices have been used to investigate the haemodynamics inside microvascular networks, thanks to their ability to reproduce microvascular geometries, down to the capillary level. One of the first PDMS-based microvascular platform was designed to model red blood cells (RBC) deformation as observed i*n vivo* (Shevkoplyas et al., 2003). In addition, microfluidic devices have also been used to investigate the deformation of leukocytes, revealing that cell deformation is due to the activation of a cytoskeletal remodeling process, which affects the viscoelastic mechanical behavior of cells. This mechanism also governs leukocytes transmigration across the endothelium.

Endothelial cells are continuously subject to shear forces caused by blood flow. The fluid flow in the cardiovascular system is extremely heterogeneous, ranging from pulsatile flow in large and small arteries, to continuous or intermittent flow in capillaries and veins (Ives et al., 1986). The study of shear-induced bio-effects is very relevant for understanding many pathological conditions. Notably, mechanical forces are involved in cardiovascular diseases and are implicated in the control of ECs morphology and function. However, traditional *in vitro* models are limited by the inability to accurately mimic the fluid dynamic environment within a real vessel. On the other hand, *in vivo* models suffer from the difficulty in measuring and monitoring experimental variables.

Esch and colleagues investigated the effect of shear stress on ECs in PDMS channels (50–60 μm diameter) with semicircular and square cross-section. They demonstrated that shear stress had greater impact on endothelial confluence and cell adhesion than the geometry of the channel (Esch et al., 2011).

Hattori *et al.* proposed a microfluidic device, which provides three different wall shear stress

levels (from 0.1 to 1.0 Pa) within three distinct, parallel microchannels. Using this microdevice they were able to evaluate the effect of different shear stress levels on ECs morphology and gene expression by direct microscopic observation. The results demonstrated that higher shear stress levels (from 3.0 to 7.9 Pa) were necessary for developing an optimal monolayer. Indeed at lower shear stress (0.5 Pa) ECs has not completely covered the channels and may not respond normally to environmental stimuli (Hattori et al., 2014).

In order to characterize the effects of varying wall shear stress (WSS) levels more in detail, Booth and colleagues developed a multiple channel microfluidic platform to produce an even wider range of WSS values. Using this device, they could also monitor permeability, trans-endothelial electrical resistance and protein expression upon flow stimulation (Booth et al., 2014).

Endothelial Barrier Function

The endothelial barrier function is the ability of the vessel wall to modulate the passage of macromolecules, ions, and water across the endothelium. The regulation of endothelial permeability is essential for maintaining homeostasis (i.e., water and solute balance). Endothelial barrier dysfunction occurs during inflammation or in pathological conditions (Sukriti et al., 2014). Generally, microfluidic devices designed to study the endothelial barrier permeability are made by sandwiching porous filters between PDMS layers or utilizing hydrogels to allow for diffusion of solutes.

Tien's group developed a microfluidic platform to create three-dimensional microvascular tubes (diameter average was from 55 to 150 μm) that exhibited long-term barrier function and reactivity to cytokines. Firstly, they used standard lithography to generate the silicon mechanical support chamber for the hydrogel. Secondly, they suspended a needle in the chamber and the collagen was added in order to surround the needle. Upon jellification, the needle was removed and ECs were seeded inside the channel. After few days ECs started to produce tubes, which showed three important characteristics: (i) the presence of a strong endothelial barrier; (ii) no leukocytes adhesion (as it occurs in physiological conditions), and (iii) the active response to inflammatory mediators (histamine, thrombin, and TNF-α) by increasing permeability and enhancing adhesion of leukocytes (as occur in pathological conditions) (Chrobak et al., 2006). Furthermore, they investigated how chronic exposure to different forms of mechanical stress affected the barrier permeability. They applied different flow regimes to quantify the effects of shear stress, transmural pressure, and average luminal

pressure on the vascular microchannel. Results showed that increasing the flow rate made the barrier function stronger, and wall shear stress greater than 1.5-2.0 Pa resulted in the generation of a functional endothelial barrier inside the collagen gel microchannel.

Furthermore, Sato and colleagues designed a model of the microcirculation containing both blood and lymphatic vessels with rectangular section (65 μm in height and 300 μm in width) for studying vascular permeability. The microfluidic device contained upper and lower channels that were partly aligned, and separated by a porous membrane where blood vascular endothelial cells (BECs) and lymphatic endothelial cells (LECs) were co-cultured. Particularly, they investigated the interaction between BECs and LECs. The model was employed to measure the permeability coefficient upon formation of tight endothelial junctions inside the microdevice. Notably, permeability was lower than the values reported for isolated mammalian venules. Results also showed that the BECs and LECs barrier was affected by the presence of histamine, which induced changes in the localization of proteins associated with tight and adherent junctions. Moreover, BECs and LECs maintained their physiological function in the microfluidic co-culture platform, even if they formed tighter cell-cell junctions in comparison to the real *in vivo* barrier (Sato et al., 2015).

Manneschi *et al.* proposed a microfluidic chip with two parallel microchannels (200 μm in width and 50 μm in height) connected laterally *via* an array of micropillars to create a permeable vascular barrier. A double-step lithographic process combined with a replica molding approach was employed to fabricate the device. Particularly, they produced 80 different arrays of micropillars with three cross-sectional geometries (rectangular, elliptical and curved), two orientations (perpendicular and parallel to the flow direction), and a variety of width and gap sizes between the pillars, ranging from 10 to 20 μm and 2 to 5 μm, respectively. The curved pillars provided higher bending stiffness, lower adhesive interactions, and smaller intrachannel separation distances compared to the conventional rectangular pillars. In order to measure the micropillar membrane permeability, fluorescent dextran molecules, nanoparticles and microparticles were employed. They were injected into the upper channel of the microchip and their permeation across the micropillar membrane into the lower channel was continuously monitored *via* optical microscopy. In addition, permeability was measured in the presence of hyaluronic acid hydrogel in order to model the extravascular matrix, and the results showed that under those conditions the permeability was significantly reduced (Manneschi et al., 2016).

Vascular diseases

Vascular disease is a leading cause of death and illness in developed countries. One of the most common diseases is atherosclerosis, the accumulation of lipids and fibrous structures in large arteries. The dynamic environment of microfluidic devices allows to study the atherosclerotic process (Chan et al., 2015). To investigate how the geometry of vascular constrictions (i.e., plaques) influenced thrombus formation, Westein *et al.* developed a microfluidic platform with multiple flow channels containing stenotic features of different dimensions (microchannels of 300 μm and half- circular stenoses of 600 or 1000 μm in width) (Westein et al., 2013). Tsai *et al.* reported on a microdevice to investigate the occlusion and thrombosis process. The microdevice was lined with human lung microvascular endothelial cells (HLMVECs), which were incubated without and with the presence of TNF-α and then exposed to whole blood under physiological flow conditions. Results revealed an increase in leukocyte adhesion to endothelial cells in the presence of TNF-α, leading to an increase in microchannel obstruction and an approximately 80% decrease in flow compared with the control (Tsai et al., 2012).

Ingber's group described a long-term cell culture microfluidic device for investigating the process of thrombus formation. The device made of PDMS includes six independent microchannels (400 μm in width, 100 μm in height, 2 cm in length) lined with ECs that are chemically fixed. They demonstrated that this platform has the ability to show in real time the thrombus genesis, and measure platelet function by flowing whole blood taken from patients receiving antiplatelet medications. Afterwards, they compared the results obtained by microfluidic platform with conventional method such as light transmission aggregometry (LTA). The data obtained from the microfluidic platform were similar to the data obtained by the LTA and in addition the microfluidic platform required lower time to complete the assay (15 min) compared to the aggregometry (approximately 2 hours) (Jain et al., 2016).

Microfluidic devices offer the opportunity to study the process of tumor development in a dynamic environment. Typically, in these models ECs are co-cultured with tumor cells. Buchanan *et al.* developed a three-dimensional microfluidic tumor vascular model for co-culturing tumor and endothelial cells under varying fluid shear stress conditions. The device presents a central microchannel embedded within a collagen hydrogel, where tumor-relevant hydrodynamic stress levels were generated and quantified using micro-particle image velocimetry. Findings revealed that low flow (3 μL/min) conditions significantly increases the expression of proangiogenic genes (Buchanan et al., 2013).

All the examples reported earlier described microfluidic devices mainly employed for understanding the physiological ECs behavior or pathological conditions (tumor vasculature and thrombosis) and all replicating small vessels (50 and 400 μm in diameter). In particular, there is no established model of physiological and pathological veins, which could be employed in pre-clinical testing to investigate the pathogenesis and treatment of venous pathologies, such as thrombosis and insufficiency, which affect approximately 25% of Western adults.

8.1.2 Hydrogel –based microfluidic devices

The use of PDMS as a material for generating biomimetic vascular models has some limitations (Subramaniam and Sethuraman, 2014), due to (i) its hydrophobicity, (ii) surface adsorption of molecules, and (iii) lack of ECM. PDMS hydrophobicity does not allow cell attachment onto its surface; the latter could be made hydrophilic by treatment with oxygen plasma, but it will revert to its hydrophobic state when exposed to air (Bodas and Khan-Malek, 2007). PDMS can adsorb small, hydrophobic molecules from a solution and this needs to be considered in applications involving quantitative molecular analyses (for example in drug screening, where fixed volumes of drug are used to determine a dose–response) (van Meer et al., 2017). Finally, PDMS is generally coated with ECM proteins (collagen, fibronectin, or laminin) in order to promote cell attachment. However, ECM components are typically present only as a thin layer of proteins adsorbed onto a rigid PDMS surface. In this type of culture conditions, permeability assays are not possible because of the lack of a 3D ECM (Han et al., 2016). Therefore, alternative materials should be investigated in order to develop a model that more closely replicates the physical properties of a tissue substrate, and that allows for evaluating extra-vasation of therapeutic or probe molecules (i.e., resulting from endothelial damage).

Towards this, hydrogels have been recently employed in vascular tissue engineering (Bertassoni et al., 2014; Billiet et al., 2012b). Notably, they present properties similar to the ones of native extracellular matrix (ECM), such as high content of water, biocompatibility, biodegradability, as well as tunable physical and chemical properties (Caliari and Burdick, 2016; Deligkaris et al., 2010). Key characteristics of hydrogels that should be evaluated for a specific application include: (i) mechanical properties, (ii) gelation mechanism, (iii) biocompatibility, and (iv)

degradation process.

8.1.3 Mechanical Properties of hydrogels

The substrate stiffness affects many cellular behaviors such as growth, migration and proliferation, as well as resistance to apoptosis (Pal, 2014; Wells, 2008). A mechanical property of hydrogels that is commonly investigated is the Young's modulus (E), also known as elastic modulus. It is a mechanical property of linear elastic, solid materials and defines the relationship between stress (force per unit area) and strain (proportional deformation) in the elastic portion of the physical stress–strain curve, as indicated in Equation 5.

$$E = \frac{FL}{A\Delta L}$$

[Eq. 5]

Where E is the Young's modulus (Pa), F is the force (N), L is the original length (m), A is the actual cross-sectional area (m^2), and ΔL is the change in length (m). It is often expressed in kPa, MPa or GPa.

The Young's modulus of tissues ranges from 0.1 kPa to 1 MPa (Liu et al., 2015), depending on the type of tissue. With respect to the vascular wall, several factors influence its mechanical properties such the volume fraction of elastin and collagen, and the volume or number of cells, such as SMCs (Messas et al., 2013). Ideally, hydrogel scaffolds for vascular tissue engineering should replicate the native mechanical properties of extra-vascular tissues (E = 0.2-0.6 MPa) (Pukacki et al., 2000).

8.1.4 Gelation mechanism of hydrogels

The gelation mechanism depends on the type of hydrogel used. With respect to natural hydrogels for example, gelatin and agarose undergo a thermal gelation (Djabourov and Leblond, 1987; Fernández et al., 2008), whereas alginate undergoes a chemical cross-linking gelation (Braccini and Pérez, 2001). Gelatin or agarose are prepared by heating a powder suspension above 80 °C until it fully dissolves, followed by cooling down to 25°C to form a stable gel. Conversely, alginate gelation occurs through ionic cross-linking between multivalent cations and alginate's molecular structures.

Gelation time is another important parameter affecting the generation of vascularized scaffolds. Gelation must be completed rapidly, in order to produce channel walls that can

mechanically sustain perfusion of embedded channels. The gelation time depends on the production method, and on the quantity and concentration of the hydrogel (Xiong et al., 2005).

8.1.5 Hydrogel biocompability and cellular attachment

Biocompatibility is an essential requirement for materials used in the generation of tissue engineering constructs. Cells can be embedded into the scaffold matrix, or can adhere onto its inner or outer surfaces (Naahidi et al., 2017). The ability to promote cellular attachment is an important characteristic of scaffolds containing perfusable vascular networks, particularly for recreating the endothelial layer lining the inner surfaces of the vessels. Cell attachment depends on the type of cell and hydrogel employed (Schneider et al., 2004).

8.1.6 Hydrogels degradation

Degradation of hydrogels is an important process since the embedded cells need space and time to spread, grow, proliferate and migrate producing their own functional ECM (Cha et al., 2009). If the degradation is too rapid, the dissolution of the supporting hydrogel may lead to collapse of the engineered vascular structures. On the other hand, if the degradation is too slow, cell proliferation and tissue formation might be delayed. The mechanisms of degradation are generally through hydrolysis, enzyme-mediated, or a combination of both processes (Kong et al., 2004; Jain et al., 2017).

In summary, the ideal hydrogel for generating a vascularized tissue construct should have (i) adequate mechanical properties to maintain vessels' integrity and allow perfusion, (ii) short gelation time in order to decrease the depletion of oxygen during the production process, and (iii) high biocompatibility and tendency to promote cell attachment.

8.1.7 Types of natural hydrogels employed in this study

Agarose

Agarose is a linear polysaccharide derived from marine red algae. It consists of residues of β-1,3 D-galactose linked to α-1,4 3,6-anhydro-αl-galactose. The gelation process of agarose is thermal-reversible (Figure 77). When a homogeneous agarose solution is cooled down to a temperature lower than approximately 60°C (i.e., this critical temperature depends on molecular weight, and concentration/number of side groups) gelation occurs due to the

intramolecular hydrogen-bonding between OH-4 of the D-galactopyranosyl residue and the adjacent hemiacetal oxygen atom of the anhydro-cY-L-galactopyranosyl residue(Xiong et al., 2005).

Agarose has been widely used in tissue engineering thanks to its mechanical and biocompatible properties, which are similar to the ones of soft tissue. Therefore, it can support cell adhesion with chemical modifications, while providing adequate permeation of oxygen and nutrients for cell growth (Zarrintaj et al., 2018).

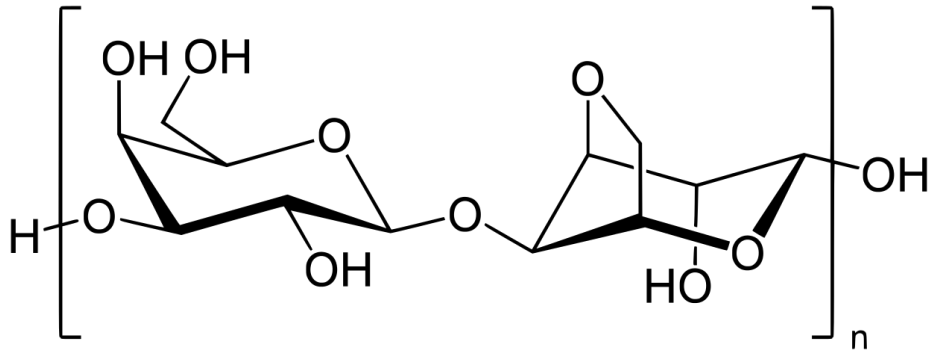

Figure 77. *Agarose polymeric unit:1,3 linked β-d-galactose residue; 1,4 linked 3,6-anhydro-α-l-galactose residue (source: https://en.wikipedia.org/wiki/Agarose#/media/File:Agarose_polymere.svg).*

Gelatin

Gelatin is a pure protein polymer, obtained by thermal denaturation of natural collagen (usually porcine or bovine), which is the structural pillar as well as the most common protein in animal organisms (Hoque et al., 2015).

There are two main types of gelatin: type A (isoionic point from 7 to 9) that is derived from collagen with exclusively acid pretreatment, and type B (isoionic point from 4.8 to 5.2) that is the result of an alkaline pretreatment of collagen. The gelation process of gelatin is thermal-reversible. When a homogeneous gelatin solution is cooled to a temperature lower than approximately 35°C the gelation process occurs (Bigi et al., 2001).

Gelatin is a colorless, odorless, non-irritating, biocompatible, and biodegradable material. Because of these characteristics it has a long history of safe use in a wide range of medical, pharmaceutical, and cosmetic applications as well as in the food industry. It has also been widely employed in tissue engineering as a template matrix for cell cultures (Huang et al., 2005).

Alginate

Alginate is a polysaccharide derived from brown algae. It comprises linear copolymers containing blocks connected with ties of β-D-mannuronic (M) and α-L-guluronic (G) residues. Blocks are composed of consecutive G residues (GGGGGG), consecutive M residues (MMMMMM), and alternating M and G (GMGMGM) residues (Lee and Mooney, 2012).

The most common method to prepare hydrogels is by combining an aqueous alginate solution with ionic cross-linking agents, such as divalent cations (Ca^{2+}, Ba^{2+}, or Sr^{2+}). The divalent cations bind to G blocks of alginate chains forming an intermolecular gel network. Ionic cross-linking between multivalent cations and alginate takes place instantaneously (Braccini and Pérez, 2001)(Figure 78).

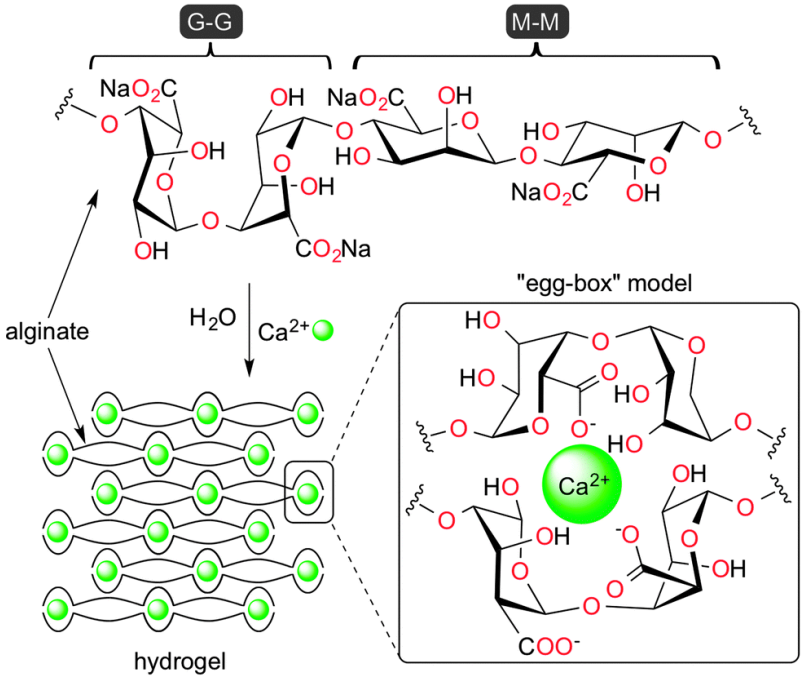

Figure 78. *Chemical structure of alginate: G-blocks and M-blocks. An ionic cross-linking occurs in the presence of divalent cations (Ca^{2+}), with the hydrogel formation characterized by the presence of the typical egg-box structure (source: Kühbeck, D., Mayr, J., Häring, M., Hofmann, M., Quignard, F., and Díaz Díaz, D. (2015). Evaluation of the nitroaldol reaction in the presence of metal ion-crosslinked alginates. New J. Chem. 39, 2306–2315).*

Ionically gelified alginate can be dissolved by treatment with chelating agents for divalent cations, such as citrate and ethylenediaminetetraacetic acid (EDTA) or hexametaphosphate.

Two main techniques have been developed to provide controlled introduction of gelling ions into alginates, referred to as external and internal gelation (Kaklamani et al., 2014). External gelation involves the diffusion of ions from a large outer reservoir into to the alginate solution. This is commonly used for preparation of hydrogel beads, which form instantaneously when

an alginate solution is dropped into a solution containing gelling ions (Chan et al., 2006).
Internal gelation is characterized by a controlled release of gelling ions from an inert source that is dissolved or suspended within the alginate solution. Examples of sources of gel-forming ions include carbonate salts ($SrCO_3$ or $CaCO_3$), calcium EDTA, calcium citrate, calcium sulfate ($CaSO_4$), calcium alginate (Ca-alginate), and calcium gluconate. The release of ions can be induced for example by a change in pH. Compared to external gelation, in this method gelling ions are released in a controlled fashion (Lupo et al., 2014).
In addition, covalently cross-linked gels can be prepared from chemically modified alginates. For instance, by covalently conjugating methacrylate groups onto the alginate backbone, covalently cross-linked hydrogels can be prepared in the presence of a photoinitiator and UV light.
Compared with ionic gelation, photocrosslinking allows the formation of more stable alginate hydrogels, with mechanical properties and biodegradation rates that can be adjusted by varying the degree of alginate methacrylation (Rouillard et al., 2011).

8.1.8 Fabrication of hydrogel –based microfluidic devices

The production of hydrogel scaffolds containing perfusable microfluidic channels is still a significant challenge in tissue engineering or vascular modeling. Integrating a microfluidic vascular network within a hydrogel-based scaffold enhances perfusion of the scaffold, and thus delivery of oxygen and nutrients to the embedded cells. It also opens new research avenues for recreating the spatial complexity of 3D *ex vivo* tissues (Buchanan et al., 2013; Golden and Tien, 2007).

Researchers have proposed several methods to form vascular networks in hydrogels, which can be classified into two types: (i) methods relying on angiogenesis, where ECs are used in combination with progenitor cells (subject to specific stimuli) for promoting the formation of capillaries (Chen and Kaji, 2017), and (ii) generation of pre-formed channels, where ECs are seeded in order to recreate the endothelial layer (Choi et al., 2013). The first method is particularly suitable for studying angiogenesis, however the formed vascular structures are not able to sustain perfusion. Alternatively, approaches based on pre-formed channels allow the formation of endothelialized vessel models that can be easily perfused. In addition, ECs exposed to the right physical and chemical cues can promote angiogenesis, which will be guided by the pre-formed channel network.

Following recent advances in microengineering technologies, several methods for fabricating pre-vascularized scaffolds have been reported, such as (i) molding(Takei et al., 2006; Chrobak et al., 2006; Linville et al., 2016), (ii) soft lithography(Ling et al., 2007; Zheng et al., 2012), (iii) photopatterning (Du et al., 2011; Zhu et al., 2017), (iv) bioprinting (Lee et al., 2010; Lee et al., 2014; Gao et al., 2017), and (v) modular assembly (Du et al., 2011; McGuigan and Sefton, 2006). These will be reviewed in the following paragraphs.

Molding

Molding is a common method applied to the fabrication of microchannels within hydrogel blocks, and is based on the use of different templates, typically in the form of micro-needles, and metallic or polymeric wires (Chrobak et al., 2006; Linville et al., 2016). Generally, micro-needles are simply inserted into a hydrogel-filled chamber and are gently removed upon gelation, in order to form a straight channel. This method is limited to the fabrication of simple architectures consisting of straight microchannels, and suffers from low reproducibility. Takei *et al.* employed this approach for producing a tube (500 μm in diameter) within a collagen block (Takei et al., 2006).

Chrobak *et al.* demonstrated production of hydrogel channels with a significantly smaller diameter (i.e., down to 75 μm) using a silicone chamber incorporating micro-needles and filled with collagen (Chrobak et al., 2006b).
Recently, Linville *et al.* proposed the use of glass needles as a mold to generate 20 μm diameter channels in a collagen matrix. Although the molding process is simple, rapid and low-cost, the channel architecture is again limited by the simplicity of the mold's shape, which is usually a single or a parallel of straight channels (Linville et al., 2016).

Soft lithography

Soft lithography has been largely employed for fabricating microfluidic channel networks. Generally, a positive master with predefined vascular patterns is employed for producing replicas of a channel network, which is then bonded permanently to a flat surface, or to another channel replica, to form an enclosed fluidic structure (Qin et al., 2010a). The master (or positive mold) can be made of different materials, such as SU-8, PDMS, or poly vinyl alcohol (PVA). The channel network often incorporates inlet/outlet ports, allowing perfusion with medium as well as seeding of ECs. The bonding process depends on the type of hydrogel

used, and can be either chemical cross-linking or thermal. Ling *et al.* produced a microfluidic channel within agarose hydrogel using this approach. The agarose channel was generated from silicon masters; upon gelation, the patterned agarose layer was sealed with another thin agarose layer by heating. Different designs of rectangular channels were created, with a width in the range 50 to 1000 μm (Ling et al., 2007). Zheng *et al.* produced collagen microfluidic channels using a silicon case. After gelation, the patterned collagen layer was sealed with a collagen slab, applying high pressure. The method allowed the production of parallel channels with a diameter of 120 μm.

The main advantage of soft lithographic approaches is high accuracy and reproducibility (Zheng et al., 2012). However, they are not suitable for the production of 3D constructs, as they rely on a stack of individual layers.

Photopatterning

Photopatterning involves the use of UV light to selectively crosslink a polymeric precursor solution. This approach has been applied to produce hydrogel tissue constructs containing microfluidic channels. In this process, a thin layer of a photosensitive polymer is exposed to UV light through a mask, in order to selectively crosslink only specific areas (Gumuscu et al., 2015).

Du *et al.* employed a two-step photolithographic method to fabricate concentric tubular constructs, with inner diameter of ~100 μm. The tube consisted of outer gel micro-rings formed by UV exposure through a first photomask, and internal rings formed by UV exposure through a second photomask. The concentric micro-rings arrays were subsequently assembled in oil (Du et al., 2011).

Zhu *et al.* produced microchannel networks by photopatterning, using gelatin methacrylate and hyaluronic acid. By employing a network shaped mask design, a network structure with continuous variation of diameter from 50 μm to 250 μm was generated (Zhu et al., 2017).

This method is rapid and reproducible, however photocrosslinkable materials and UV light can be toxic for cells. In addition, the limited penetration depth of UV light in hydrogels makes the method only applicable for the production of thin constructs.

Bioprinting

Bioprinting is a rapid prototyping technology, which allows producing functional living tissues

through computer-aided, layer-by-layer deposition of multiple types of cells and biomaterials. Printers can simultaneously deposit biomaterial scaffolds and cells, at precisely controlled 3D-locations.

The characteristics of bioprinted constructs depend on different factors such as process parameters (nozzle tip size, shear at nozzle, temperature in ejection reservoirs, and impact pressure on the surface) and material parameters (polymer viscosity, crosslink density, etc.) (Mandrycky et al., 2016).

Lee *et al*. developed a bioprinting approach to construct a perfusable channel in a collagen scaffold. Gelatin was used as a sacrificial material to create the channels. The collagen precursor was printed layer-by-layer and polymerized by $NaHCO_3$, and then a 20% gelatin solution containing HUVECs was printed in a straight pattern to generate the channel (Lee et al., 2010b).

V. K. Lee *et al.* recently proposed a methodology using 3D bio-printing technology to produce a functional *in vitro* channel with perfused open lumen, using only cells and biological matrices. The channel was produced via layer-by-layer printing of a collagen scaffold and a cell-gelatine mixture (Lee et al., 2014).

In another study, Gao *et al.* printed blood vessels approximately 2 mm in diameter made of two printed layers of cells, containing smooth muscle cells and fibroblasts respectively. Afterwards endothelial cell were seeded into the inner surfaces of the device (Gao et al., 2017).

Although bioprinting allows the fabrication of complex structures mimicking physiological environments, there are numerous parameters affecting the properties of the end-product that need to be controlled. However, being a relatively recent technology, it is envisaged that further improvements will be made in the near future.

Sacrificial Molding

Sacrificial molding involves the production of a template (or master), usually by molding or bioprinting processes. Templates are then positioned into a chamber, which is filled with hydrogel precursors. After complete hydrogel gelation, the template is sacrificed by melting or dissolution, in order to form a microchannel architecture (Gelber and Bhargava, 2015).

Glass and polymer fibers are commonly used as sacrificial materials in this method. In addition, hydrogels themselves can be used as sacrificial material, exploiting some of their properties such as low melting point or reversible gelation.

Tocchio *et al.* proposed a versatile sacrificial molding technique using poly vinyl alcohol (PVA). The PVA solution was poured on the mold and allowed to dry. The dried PVA layer was leveled in order to remove the polymer excess; afterwards, the sacrificial template was immersed into the gel. After gelation, the PVA template was dissolved in water, creating the microfluidic channel architecture within the gel. A channel with feature size of 500 μm and minimum dimension of 100 μm could be achieved with this method (Tocchio et al., 2015).

Miller *et al.* proposed as sacrificial mold made of 3D printed rigid filament networks of carbohydrate glass. A suspension of cells in an ECM prepolymer made of a mixture of hydrogels was poured to cover the sacrificial mold. After crosslinking the ECM, the glass filaments were dissolved to form vessels. The process allows producing a monolithic tissue construct with a vascular network that matches the original 3D printed structure (Miller et al., 2017).

Golden *et al.* produced microfluidic channels in hydrogels using gelatin as sacrificial mold material. A PDMS microfluidic device containing the channel architecture was used for making the gelatin mold. The liquid gelatin was poured into the channels and allowed to gelify; afterwards the PDMS device was opened and the gelatin mold was removed using tweezers. The gelatin mold was encapsulated in a liquid hydrogel precursor (type I collagen, fibrinogen, Matrigel). Afterwards the hydrogel precursor was polymerized and the gelatin was removed by heating, leaving a network of interconnected channels in the gel scaffold (Golden and Tien, 2007).

In conclusion, sacrificial molding is a low-cost and rapid method, which allows generation of relatively complex channel architectures within a gel. The advantages of using a natural material as sacrificial mold, such as gelatin, are: (i) it does not need a solvent for removing the mold, and (ii) it avoids release of structural particles that might be toxic for cells. This approach presents also some disadvantages: (i) complexity of manipulation and positioning of the gelatin molds to achieve a fully planar structure, given the flexibility of the material, and (ii) swelling of the gelatin inside the hydrogel, which causes the formation of larger channels than the original templates in PDMS. In general, sacrificial molding is also limited to the production of planar networks and/or stacks of planar networks.

Modular assembly

Modular assembly utilizes building units to generate large constructs, through manual, physical or chemical assembly procedures.
Du *et al.* produced PEG modified hydrogel units that were assembled through a directed bottom-up approach. PEG units with well-defined geometry were created by a photolithographic technique. The units were assembled into a tubular structure characterized by multi-level interconnected lumens. SMCs were encapsulated into the external layer, whereas HUVECs were encapsulated into the internal layer, recreating the architecture of the physiological vascular wall (Du et al., 2011).

McGuigan *et al.* proposed the fabrication of microscale cylindrical constructs using collagen. However, as collagen has weak mechanical properties, the modulus in this system cannot sustain perfusion at high-pressure. Therefore, the same group reported on a modified procedure using gelatin crosslinked with glutaraldehyde (McGuigan and Sefton, 2006).
Liu *et al.* proposed a similar strategy utilizing star shape modules. Modules were assembled by a cross-linker, through a Micheal-type addition reaction. Scaffolds showed high cell viability and high permeability to different chemical species, which is beneficial for nutrients' transport within the construct (Liu et al., 2010).
Despite it has potential for generation of complex vascular networks, the modular assembly approach is generally complex and time-consuming and only simple tubular structures can be achieved.

In conclusion, the ideal vascularized scaffold is made of a natural material, which must be (i) cost-effective, (ii) biocompatible and suitable for ECs attachment, and (iii) rigid enough to allow perfusion of embedded channels and provide support to the cells. The ideal production method should be (i) cost-effective and rapid, (ii) reproducible, (iii) should not require complex tools, and (iv) should be flexible enough to produce channels with different sizes, including branched and other complex geometries.

The aim of this chapter is to create more complex VOC models, starting from PDMS-based endotheliazed VOC to hydrogels-based model. This new method allows creating channels within a hydrogel matrix in a simple, rapid and reproducible way, using natural hydrogels, such as agarose, gelatin and alginate. It brings together two different approaches: (i) molding and (ii) sacrificial molding. Combining these two techniques allows for the production of both

a scaffold (extra-vascular compartment) and a perfusable microfluidic channel. An agarose mold is used for constructing the scaffold, whereas a gelatin sacrificial mold is employed for producing channels inside the scaffold.

8.2 Materials and Methods

8.2.1 Small PDMS vein-on-a-chip (VOCs) fabrication and design

After validation of relatively large VOC production (Chapter 7), the production of smaller vein-on-a-chips has been carried out. The production protocol employed is the same reported in Paragraph 7.2.1.

The production of models with smaller dimension presents different advantages: (i) devices are easy to handle and can be stored inside a common cell culture petri dish; (ii) they are less expensive to produce, as less material is needed to generate positive and negative molds, and lower amounts of proteins are needed for coating the inner surfaces of the device prior to cell seeding. Finally, (iii) production times are reduced, particularly the endothelialization phase.

The new models of veins (1 mm in diameter, 50 mm long), replicated physiological and pathological vein architectures. As shown in Figure 79, different types of physiological veins have been generated.

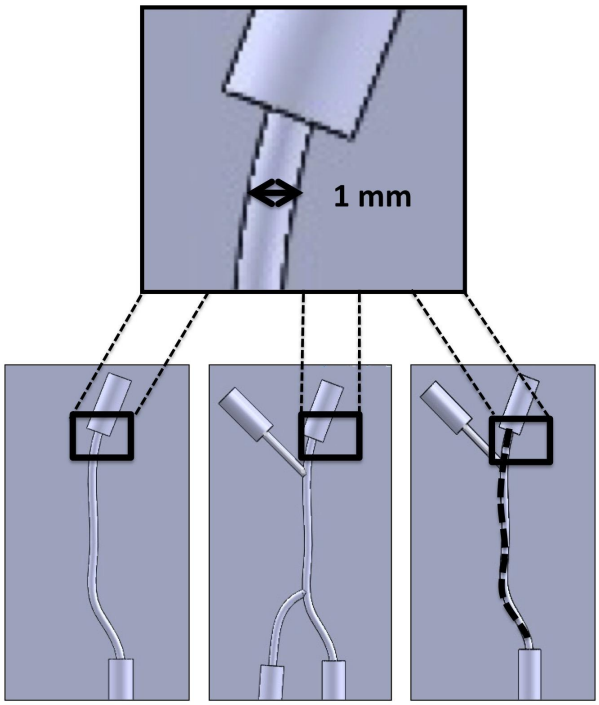

Figure 79*. CAD drawings of VOC models (1mm diameter, 50 mm long) representing physiological veins. The devices were characterized by one inlet/one outlet, two inlets/two outlets, or*

two-inlets/one outlet.

Devices were characterized by one inlet and one outlet, which can be punctured with a needle to replicate the injection process; or two inlets/two outlets or two inlets/one outlet, where the foam can be injected through a cannula (Figure 80).

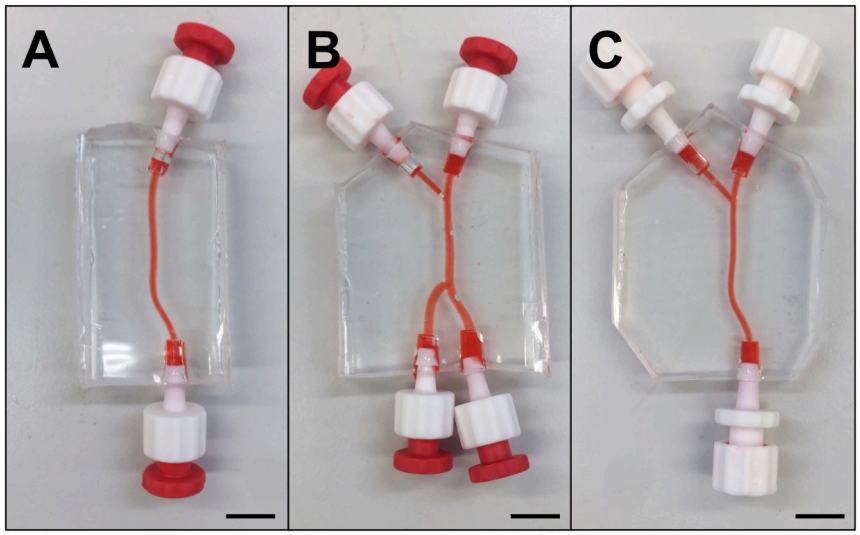

***Figure 80**. Images of VOC models (1mm diameter, 50 mm length) representing physiological veins. The devices are characterized by (A) one inlet and one outlet, (B) two inlets and two outlets, or (C) two inlets one outlet. Channels were perfused with red food dye (scale bar 4 mm).*

In addition, varicose vein models were developed, which were characterised by variations in diameter along the vessel and tortuosity, replicating more closely the real appearance of varicose veins. (Figure 81-82).

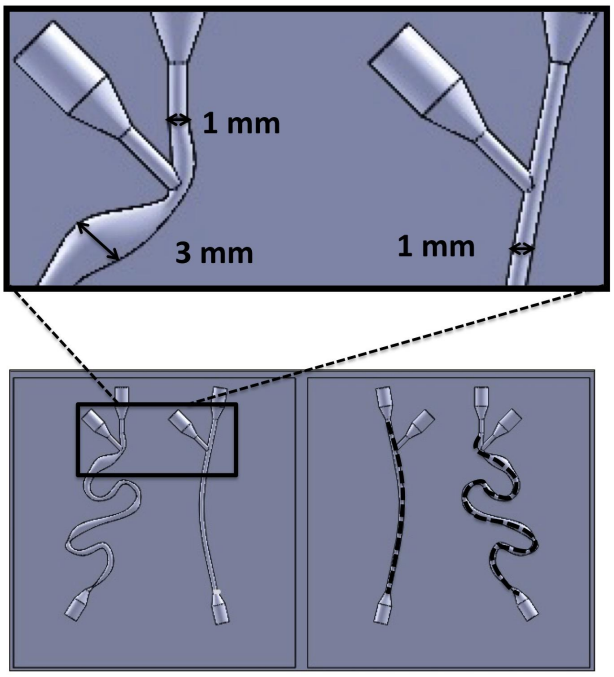

***Figure 81**. CAD drawings of the VOC models (1mm in diameter, 50 mm long) representing physiological and varicose vein (1-3 mm in diameter, 70 mm long). Devices are characterized by two inlets and one outlet.*

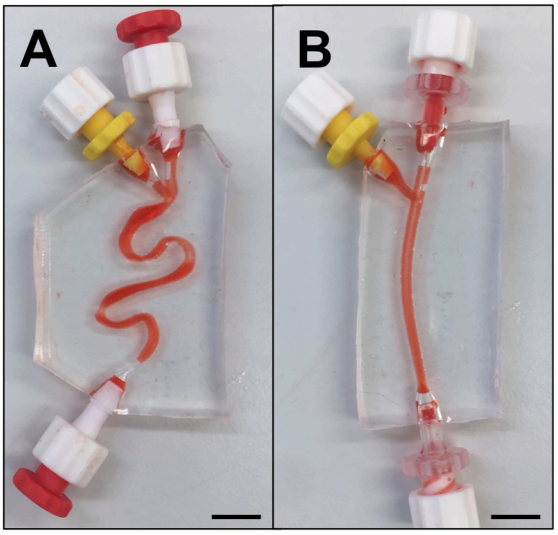

***Figure 82.** Images of VOC models (1mm in diameter, 50 mm long) representing physiological and varicose veins (1-3 mm in diameter, 70 mm long). Devices are characterized by two inlets and one outlet. Channels were perfused with red food dye (scale bar 4 mm).*

8.2.2 Branching vasculature models: fabrication and design

The main focus of the project is on the production of vein models for evaluating the sclerotherapy efficacy into a biomimetic model. The developed method is versatile and can

potentially be employed beyond the modeling of veins, to include arterial networks. These models could be used to investigate other vascular diseases. Herein, examples of arterioles-on-a-chip (AOCs) are reported, which will be successively employed for the validation of the endothelialization process in channels with smaller diameter compared to veins (Figure 83).

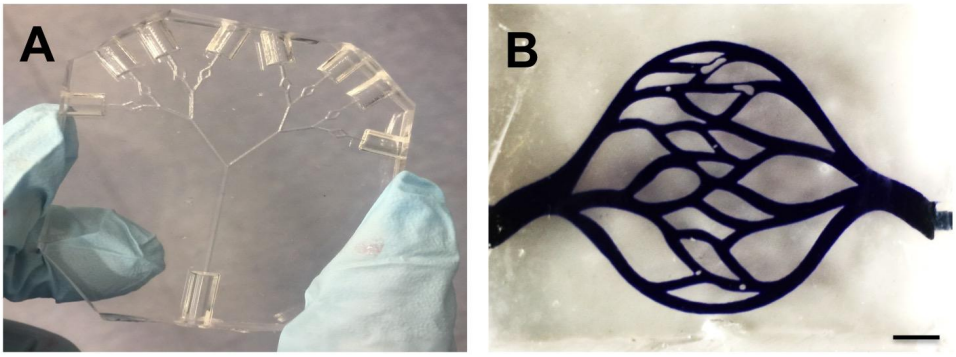

Figure 83*. Arterioles-on-a-chip models (A) of smaller arterioles tree network (200 µm in diameter, 50 mm length) and (B) larger arterioles network (1-2 mm in diameter, 50 mm length). The channels were perfused with blue food dye. Scale bar 2mm.*

8.2.3 Cell seeding in PDMS based device

HUVECs were initially attached to flat PDMS layers (2 mm thick) to investigate the ECs attachment onto the silicon surface. The PDMS layers were first washed with 70 % ethanol. Then, they were rinsed with HBSS to remove any trace of ethanol. Each layer was then placed into a 24 well plate. Wells were filled with 200 µL of different types of protein solutions diluted in HBSS: (i) 50 µL/mL of rat type I collagen (100 µg/ mL; Gibco™, UK), (ii) 100 µL/mL of fibronectin (Sigma, UK), and (iii) 0.06-1.79 mg/mL of Geltrex™ (Thermo Fisher Scientific, UK). The matrix proteins were allowed to adhere to the PDMS at 37 °C in a 5 % CO_2 incubator (Sanyo Electric Co., Ltd., Japan) for 1 hour. The protein solutions were then removed and HUVECs (2 x 10^4 cells\mL) were seeded in each well and in 750 mL of HM (HUVECs Medium, Thermo Fisher, UK) was added. The 24 well plates were positioned into the incubator.

In a second step of the study, cells were seeded in the VOC models. The PDMS devices were washed 4 times with 70% ethanol for sterilization. Then, HBSS was flushed inside the channels to remove ethanol traces. Afterwards, the inner surfaces of the device were coated with 1 mL of different proteins: (i) rat type I collagen, (ii) fibronectin, or (iii) Geltrex™. The device was subsequently placed at 37°C in a 5% CO_2 incubator for 1 hour, followed by

rinsing with HM.

HUVECs suspension was injected into the protein-coated channels (4 or 5 × 10^5 cells\mL), and the device was incubated for 2 hours. In order to achieve complete coating, the device was turned upside down and primed with a fresh HUVEC suspension. The device was then incubated overnight to promote cell attachment.

8.2.4 Image acquisition

Bright field images were acquired with an optical microscope (Olympus, CKX41, Japan), while fluorescent images were acquired using an epi-fluorescence microscope (Leitz, Germany). Images were taken of live samples every 24-48 h, with either phase contrast or fluorescence microscopy. HUVECs nuclei were stained using Acridine orange (1 : 1000 dilution, Thermo Fisher Scientific, UK). HUVECs in the microchannels were initially washed with phosphate buffered saline (PBS) to remove any cell media, and afterwards incubated with Acridine orange for 15 minutes.

Cylindrical scaffold images were acquired with stereo microscope (Nikon, Japan) (1x magnification). The diameter of the scaffold was measured using the microscope images in ImageJ (National Institutes of Health, U.S).

8.2.5 Agarose mold templates preparation

The agarose mold templates were generated by 3D-printing. Molds were designed in SolidWorks (Dassault Systemes SolidWorks Corporation, USA) and subsequently 3D printed (Objet350 Connex, Haycroft Works, Buckholt Drive, UK). Different designs of the molds were produced in order to obtain scaffolds with different shapes and sizes, to demonstrate the flexibility of the fabrication method. Figure 84 shows three different types of mold: (A) a mold comprising 6 cylinders, 5 mm in width and height; (B) 6 cubes, with edge length of 5 mm; and (C) 6 disks, 15 mm in width and 2 mm in height.

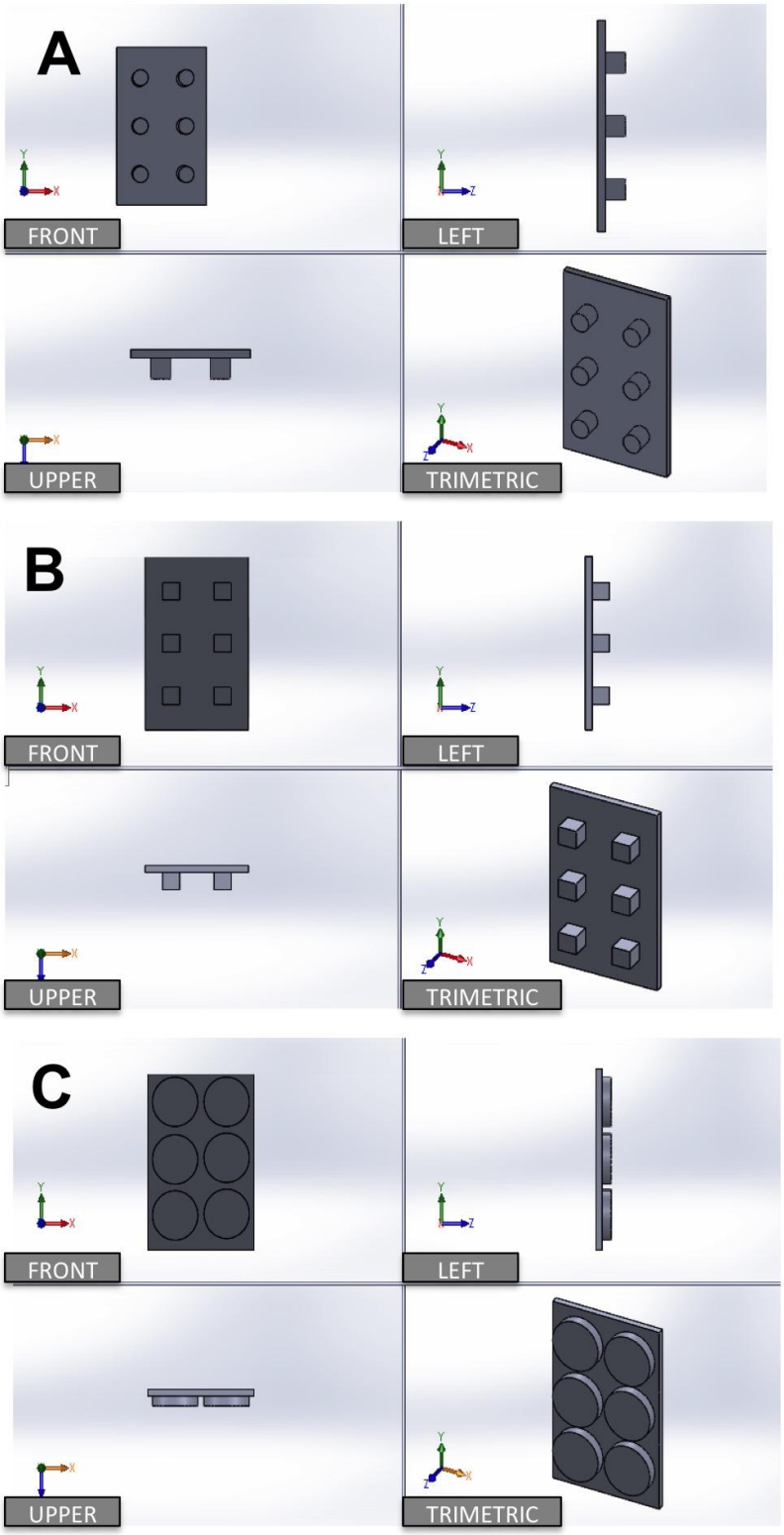

Figure 84. *CAD drawings of 3D printed agarose mold templates in different perspective views. Molds comprised of (A) 6 cylinders (5mm in width, 5 mm in height), with edge length of 5 mm, (B) 6 cubes, 5mm in width and depth, and (C) 6 disks, 15 mm in width and 2 mm in height.*

8.2.6 Alginate preparation

A 1 or 2% (w/v) alginate solution was prepared by dissolving the sodium alginate powder (Sigma-Aldrich Co. LLC., USA) in PBS (Thermo Fisher Scientific, UK), under mechanical

stirring. The solution was sterilized and filtered with syringe filters (0.22 µm, Corning®, Sigma, UK), under a sterile hood. The alginate solution obtained was stored in a refrigerator at +4 °C.

8.2.7 Agarose preparation

The gelling solutions used in the experiment contained calcium chloride ($CaCl_2$) (Sigma-Aldrich Co. LLC., USA) at 1.5 % (w/v) in ultrapure water. In addition, a 0.15% $CaCl_2$ solution was prepared for storing the produced scaffolds. Filtration and sterilization was carried out with syringe filters (0.22 µm, Corning®, Sigma-Aldrich Co. LLC., USA). The calcium solutions were stored in a refrigerator at +4°C.

The 1% agarose solution was prepared by dissolving the agarose powder (Sigma-Aldrich Co. LLC., USA) in the 1.5 % (w/v) calcium chloride ($CaCl_2$) solution. The agarose solution was then heated using a microwave (SHARP Compact) at 700W for 5 minutes, in order to solubilize the agarose until the solution became optically transparent.

Agarose was additionally employed for evaluating endothelial cell attachment. Hydrogels scaffold were prepared from either 1% or 2% agarose solutions in phosphate-buffered saline (PBS). Therefore, 700 µl of the agarose solution are poured into each well of a 24-well plate (Greiner-CELLSTAR®, 662160). The plate was placed into the hood at room temperature for 10min allowing for cooling and gelation of the agarose solution.

7.2.8 Alginate scaffold preparation

In order to fabricate the agarose mold, the 3D-printed positive mold was washed with 5% Biocleanse (Fisher Scientific Ltd, UK) and allowed to dry into a fume hood. The 1% agarose/1.5% $CaCl_2$ solution was poured into a 10 cm diameter Petri dish (Greiner-CELLSTAR®, Starlab, UK). The 3D-printed mold was placed onto the surface of the agarose solution in the Petri dish. The mold was gently shacked with tweezers to remove potential air bubbles. The agarose solution was then allowed to dry at room temperature until gelation occurred, which takes approximately 10 minutes. Upon gelation, the 3D-printed mold was gently removed using tweezers.

To form the alginate construct, the sterilized 2% alginate hydrogel solution was pipetted over the agarose mold. The gelation process takes about 30 minutes at room temperature (for 100 µl of alginate solution). After gelation, the alginate hydrogel scaffolds were removed carefully using a spatula and placed into a multiwell plate for further experiments (Figure 85).

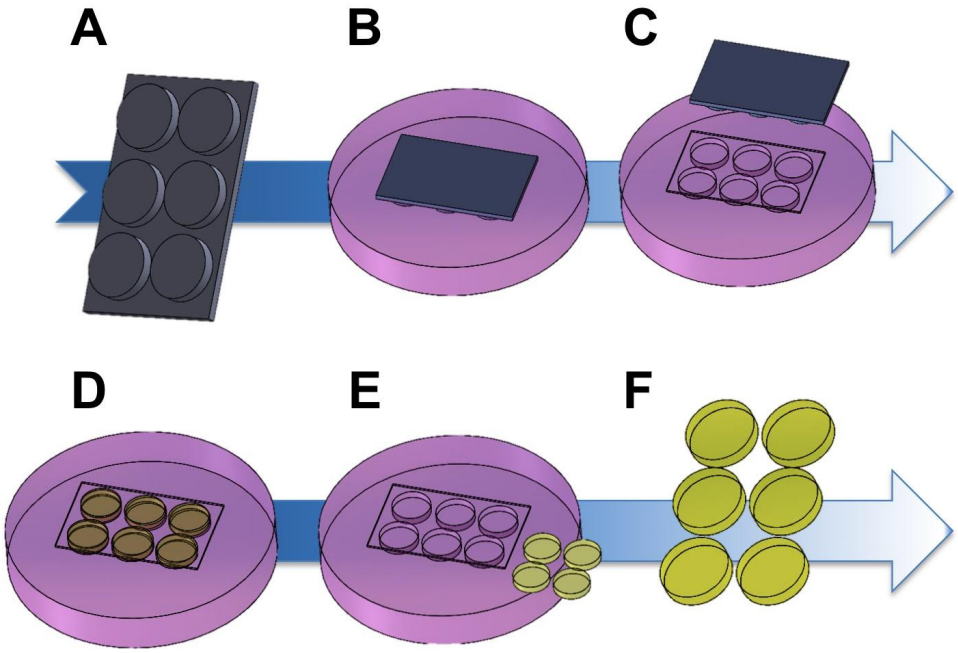

Figure 85. *Schematic of alginate scaffold production. (A) A 3D printed template was employed for generating negative patterns onto the agarose gel. (B) 1% agarose/1.5% $CaCl_2$ was heated in a microwave and was poured into a petri dish. The 3D printed mold was gently positioned on surface of the mixture and allowed to solidify for 30 minutes. (C-D) Once the agarose-$CaCl_2$ mold was solidified the 3D printed mold was gently removed and the chosen volume of alginate was poured into the wells. After 30 minutes, the scaffolds were extracted and left soaking 20 minutes into 0.15 5% $CaCl_2$ solution.*

8.2.9 Collagen Coating

In order to improve HUVECs' attachment on the agarose and alginate surface, coating with collagen is often performed. A thin layer of collagen over the gel surface might improve HUVECs' attachment and growth (Relou et al., 1998), since collagen is an extracellular matrix for HUVECs in the blood vessels. After gelation of agarose/alginate, collagen (GIBCO®, A10483-01) was diluted 100x with a Hank's balanced salt solution (HBSS). The collagen solution is gently mixed and applied on the agarose or alginate hydrogel into the 24-well plate; 250µl of solution are used for each well. The wells were left in the incubator for at least 1 hour to achieve effective coating. Then the excess collagen solution on the hydrogels surface was removed, and the collagen coated agarose/alginate hydrogel was ready for cell seeding.

8.2.10 HUVECs attachment onto hydrogel surface

HUVEC attachment on the different hydrogels was evaluated to assess their bio-compatibility. The cell suspension was diluted with culture medium to achieve a concentration of $2x10^5$

cells/mL (Thermofisher.com, 2017). Cells were then seeded into a 24-wells plate with the hydrogel blocks and 1mL for each well.

8.2.11 PDMS template for preparation of sacrificial mold

PDMS templates were obtained *via* replica molding. The channel architecture was designed in SolidWorks (Dassault Systemes SolidWorks Corporation, USA). The microfluidic hydrodynamic focusing (MHF) geometry, commonly employed in microfluidics, has been chosen, characterized by three inlets, which replicate junctions between multiple channels, and one outlet. This simple channel geometry facilitates the validation process of the method. Afterwards, positive molds were 3D printed (Objet350 Connex, Haycroft Works, Buckholt Drive, UK).

A PDMS pre-polymer and curing agent (Sylgard® 184, Dow Corning Corporation, USA) were mixed at a weight ratio of 10:1, and then poured over the 3D-printed molds. PDMS was then cured in an oven (65°C) for 1 hour, and peeled off from the mold in order to obtain the final negative PDMS template (Figure 86).

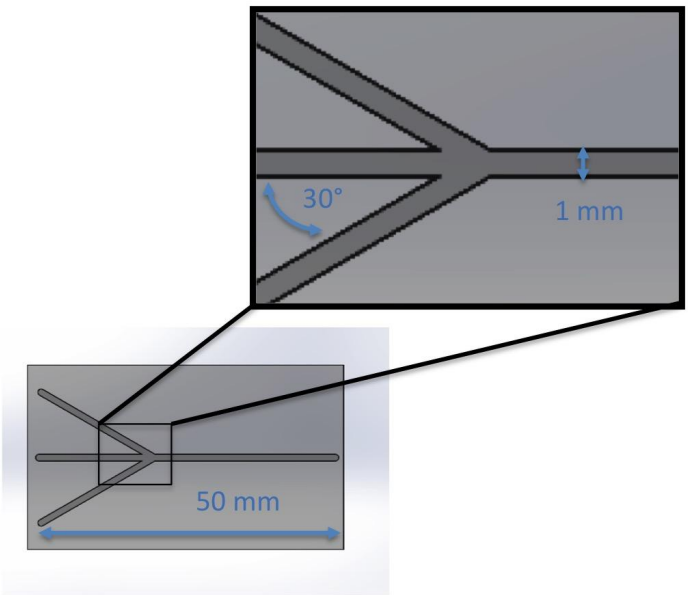

Figure 86. *Schematic drawing of the PDMS template employed for the fabrication of the gelatin mold. In this study a microfluidic hydrodynamic focusing geometry has been employed, characterized by three inlets and one outlet (depth: 1 mm, width: 1mm, length of main channel: 50 mm).*

8.2.12 Gelatin preparation

For construction of the sacrificial mold, 30% (w/v) gelatin solution was prepared by dissolving

bovine gelatine powder (Sigma-Aldrich Co. LLC., USA) in dH_2O, and heating it using a microwave (at 500W) until the gelatin was fully melted.

8.2.13 Sacrificial mold production

The sacrificial mold was made of gelatin, and generated from the negative PDMS templates. The gelatin solution was poured onto the negative PDMS template and allowed to gelify for 15 minutes at 4°C. Tweezers were used to remove the sacrificial mold from the PDMS template.

8.2.14 Construction of vascularized alginate scaffolds

The alginate scaffold was made from a negative agarose mold. The agarose mold was produced using the procedure described in paragraphs 8.2.7. In this case, the mold employed was a parallelepiped (50 mm long, 30 mm high, and 10 mm deep), which allowed producing a negative chamber into the agarose gel, deep enough to allow the production of a scaffold that can contain channels inside (Figure 87).

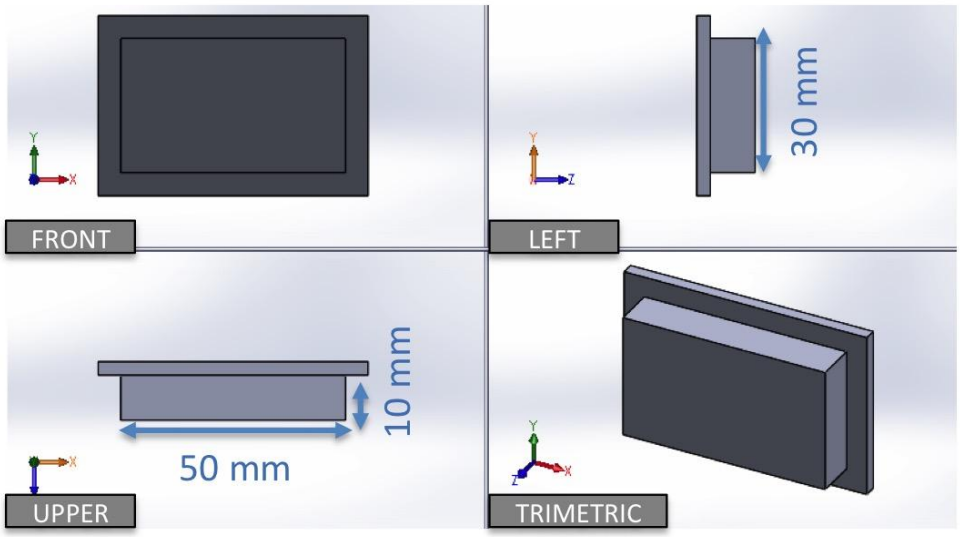

Figure 87. *CAD drawings of 3D printed agarose mold in different perspective views. The mold employed was a parallelepiped (50 mm long, 30 mm high, and 10 mm deep), which allows producing a negative chamber into the agarose gel.*

The latter was filled with few microliters of alginate in order to make a thin layer of gel, and the sacrificial mold was immediately and carefully positioned into the middle of the chamber, which was then completely filled with the alginate solution. A flat sheet of 1% agarose/1.5% $CaCl_2$ can be used as a lid to allow the gelation process to occur from all boundary surfaces.

After gelation (60 minutes), the alginate scaffold was removed using a spatula. The scaffold was stored into a 10 cm diameter culture dish filled with 0.15 % $CaCl_2$ solution, in order to complete the gelation process (for at least 30 minutes). Afterwards, the scaffold was placed in an incubator (Sanyo Electric Co., Ltd., Japan) at 37°C to melt the sacrificial mold contained inside the alginate scaffold. Melting took about 10 min to take place, depending on the size and architecture of the channel design. The alginate scaffold was then allowed to cool down at environmental temperature, and the last residues of gelatin contained inside the alginate scaffold were removed by pipetting PBS into the channels. The scaffold was flushed with sterilized PBS, 3 to 5 times, to wash away the gelatin. The alginate scaffold was then ready to be used for further experiments (Figure 88).

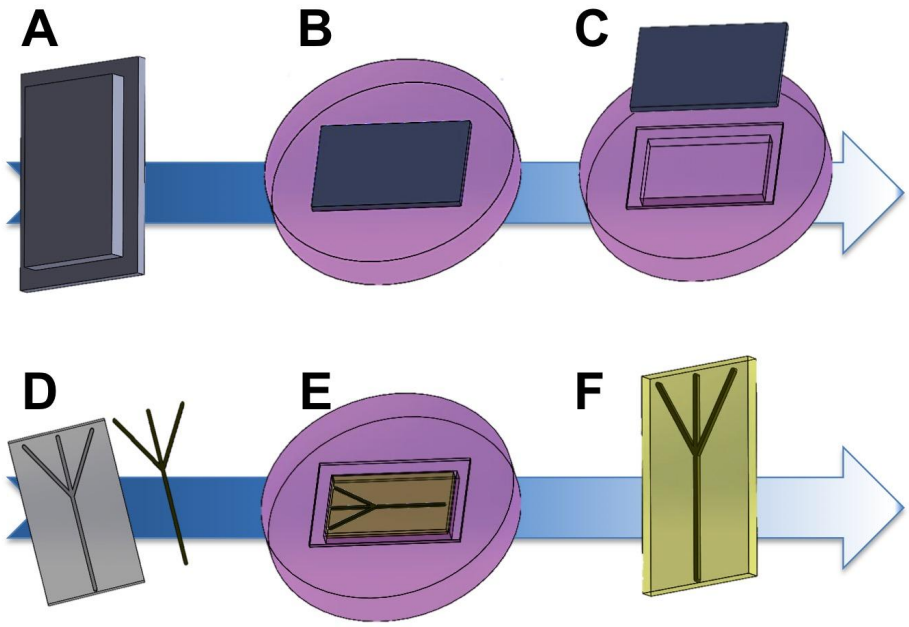

Figure 88. *Schematic of the production of an alginate scaffold containing microfluidic channels. (A) 3D printed parallelepiped (50 mm long, 30 mm high, and 10 mm deep) template was employed for generating a negative chamber onto the agarose gel. (B) 1% agarose/1.5% $CaCl_2$ was heated in a microwave, poured into a petri dish, and the 3D printed mold was gently positioned on the surface of the mixture and allowed to solidify for 30 minutes. (C) Once the agarose-$CaCl_2$ mold was solidified, the 3D printed mold was gently removed. (D) In parallel, the gelatin sacrificial mold was generated by replica molding. (E) The agarose chamber was filled with 2 mL s of alginate in order to make a thin layer of gel, and the gelatin sacrificial mold was then positioned into the middle of the chamber, which was then completely filled with alginate solution. A flat sheet of 1% agarose/1.5% $CaCl_2$ can be used as a lid to allow the gelation process to occur from all boundaries. After gelation, the alginate scaffold was removed using a spatula.*

8.2.15 Endothelialization of the inner channels

The alginate scaffold containing microchannels was produced as described in paragraph 8.2.14 and coated as described 8.2.9. HUVECs were seeded at a concentration of 4 x 10^6 cells/mL,

and injected into the channel using a pipette until full priming was achieved. The priming volume was of approximately 500 µL. The alginate hydrogel scaffold was then placed into a 10 cm diameter petri dish, which was filled with culture medium to cover the scaffold.

The petri was after positioned into the incubator at 37 °C in a 5 % CO_2 (Sanyo Electric Co., Ltd., Japan) for at least 2 hours, allowing the HUVECs to adhere on the lower surface of the channels. HUVECs attachment was microscopically observed after 24 hours.

8.3 Results

8.3.1 Cell seeding and channel functionalization in PDMS-based devices

Initially, flat PDMS layers were coated with collagen for 1 hour. Then, a HUVECs suspension (2 x 10^4 cells/mL) was added onto the flat PDMS layers. As a control, the same coating was carried out onto plastic 24 well plates. In Figure 89, it can be seen that cells added to tissue culture plastic (controls) controls have > 90 % confluence. In the collagen coated PDMS layer, the attachment was similar to the control but with small areas where cells were not attached, maybe due to inhomogeneous coating or low number of cells seeded.

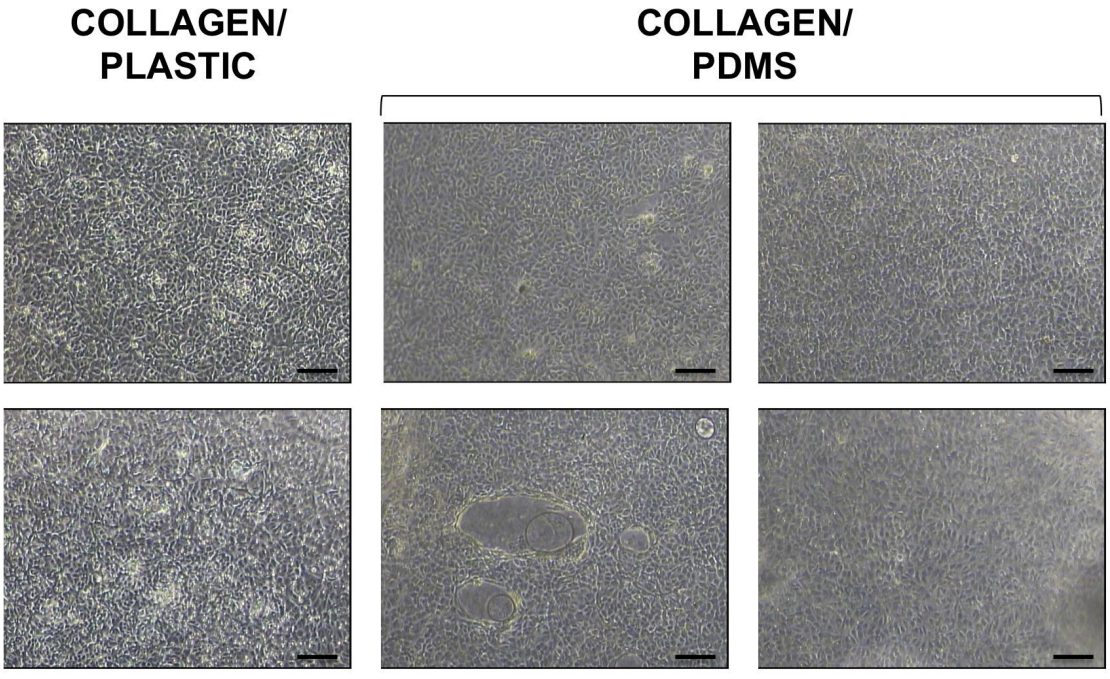

Figure 89. *Surface modification of well plates and PDMS using collagen. HUVECs exhibit similar adhesion and morphology on either substrate. On the left, the photographs (4X magnification) show HUVECs attached on the plastic coated with collagen after 48 hours, whereas on the right HUVECs were let to attach on PDMS coated with collagen after 48 hours. In either substrate, cells exhibited good attachment with typical elongated shape, although the monolayers attached onto PDMS show areas without cells. Scale bars are 200 µm.*

PDMS pre-coated with fibronectin was found to promote attachment of HUVECs to a similar extent as traditional cell culture dishes made of polystyrene (Figure 90).

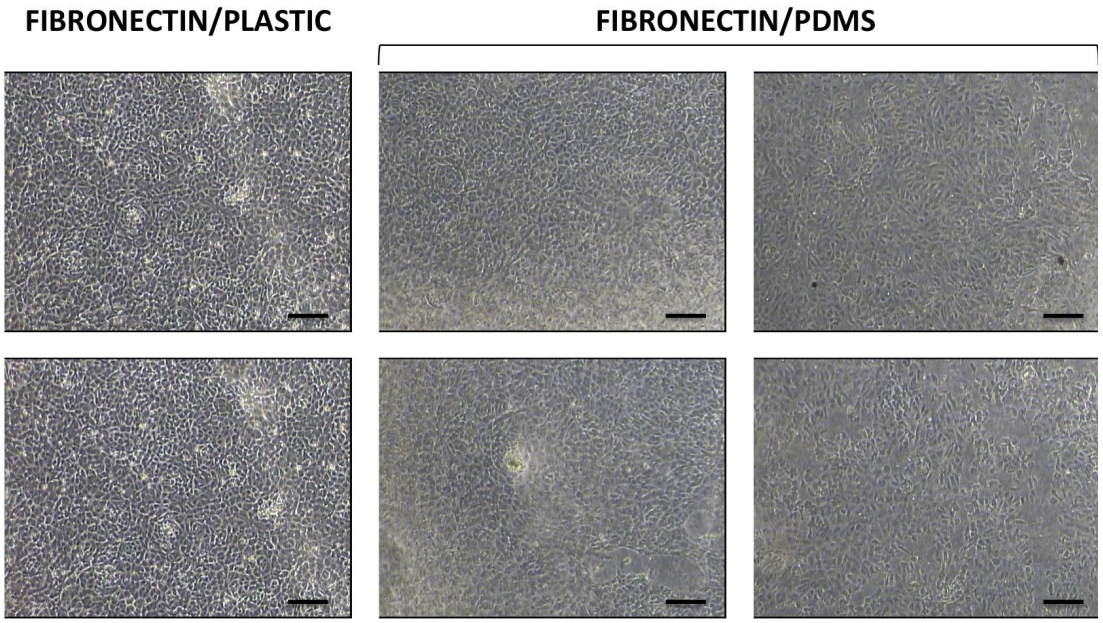

Figure 90. *Surface modification of well plates and PDMS using fibronectin. HUVECs exhibit similar adhesion and morphology on either substrate. On the left, the photographs (4x magnification) show HUVECs attached on the plastic coated with fibronectin after 48 hours, whereas on the right the photographs (4X magnification) show HUVECs attached on the PDMS coated with fibronectin after 48 hours. In either substrate, the cells exhibited good attachment with a typical long shape. Scale bars are 200 µm.*

Geltrex™ was employed at two different concentrations: 60-90 µg/mL and 1.18-1.78 mg/mL. The protein matrix enhanced HUVECs attachment on PDMS surfaces; however, in a similar manner to collagen coated PDMS, there are areas where there was no cell attachment (Figure 91). Results show higher cell coverage area with the higher concentration of Geltrex™, with greater confluence after 48 hours.

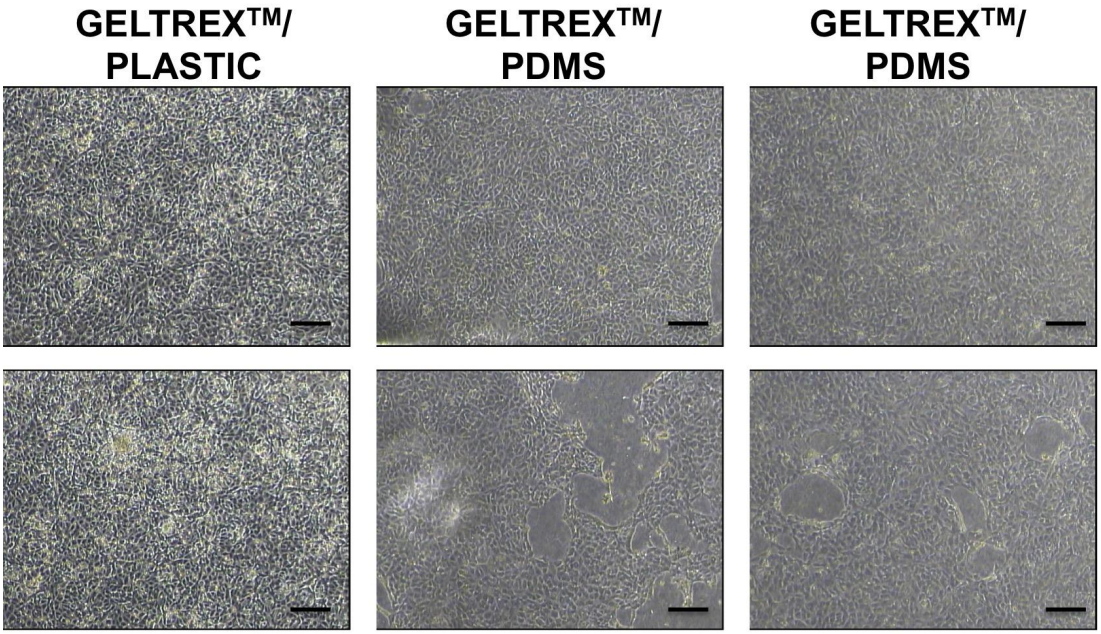

Figure 91. *Surface modification of well plates and PDMS using Geltrex™. HUVECs cells exhibit similar adhesion and morphology on either substrate. On the left the photographs (4X magnification) show HUVECs attached on the plastic coated with Geltrex™ after 48 hours, whereas on the right the photographs (4X magnification) show HUVECs attached on the PDMS coated with Geltrex™ after 48 hours (scale bars are 200 µm).*

Results indicated that PDMS alone, made at a common 10:1 monomer:curing agent weight ratio, did not allow HUVECs attachment. Coating is necessary to achieve confluent monolayers similar to those obtained on traditional tissue culture plastics. Comparing the three types of ECM proteins used, fibronectin and collagen resulted in the most effective cell coatings (Figure 92).

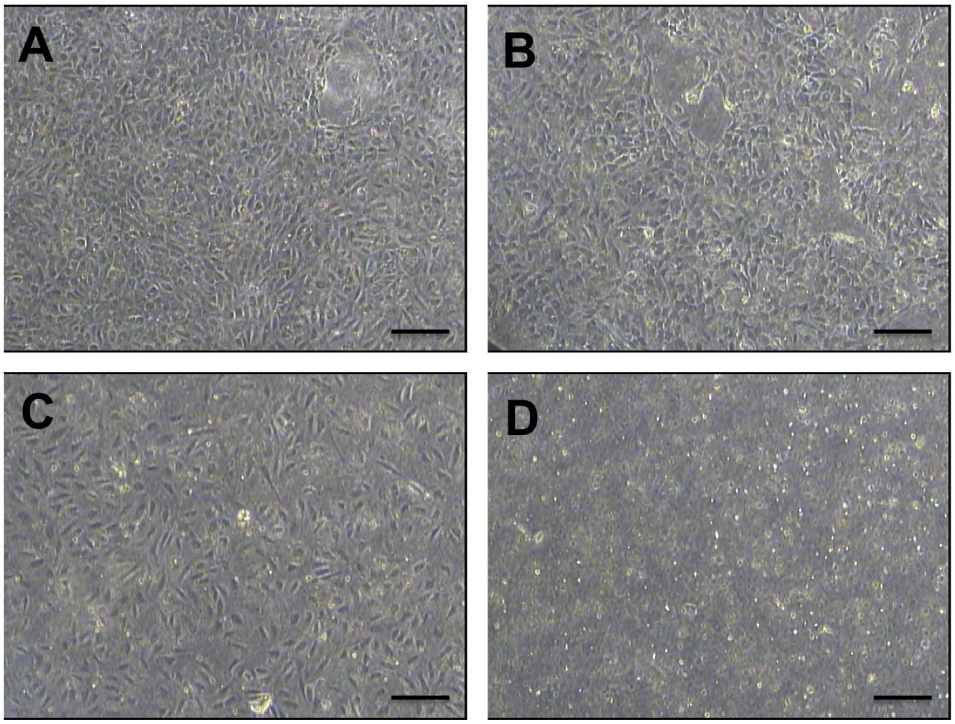

Figure 92. *Comparison between surface modification of PDMS with collagen (A), fibronectin (B), Geltrex™ (higher concentration) (C), and PDMS uncoated (D) as control. HUVECs exhibit similar adhesion and morphology whene fibronectin and collagen coating are performed, whereas they exhibit a lower growth rate with Geltrex™. In the untreated PDMS, no cells adhered. Images (4X magnification) were taken after 48 hours from seeding (scale bars are 200 µm).*

After investigating HUVECs behaviour onto a flat PDMS surface, experiments were repeated inside the circular VOC channels (1 mm inner diameter). Channels were coated with collagen or fibronectin for 1 hour. Then, HUVECs (5 x 10^5 cells/mL) were injected into the VOCs and incubated for 2 hr. Devices were then rotated of 180°, followed by fresh HUVECs injection and overnight incubation to achieve complete cell lining. Images were captured after 24 (Figure 93) and 48 hours (Figure 94) using an inverted optical microscope (objective magnification 4X) with phase contrast.

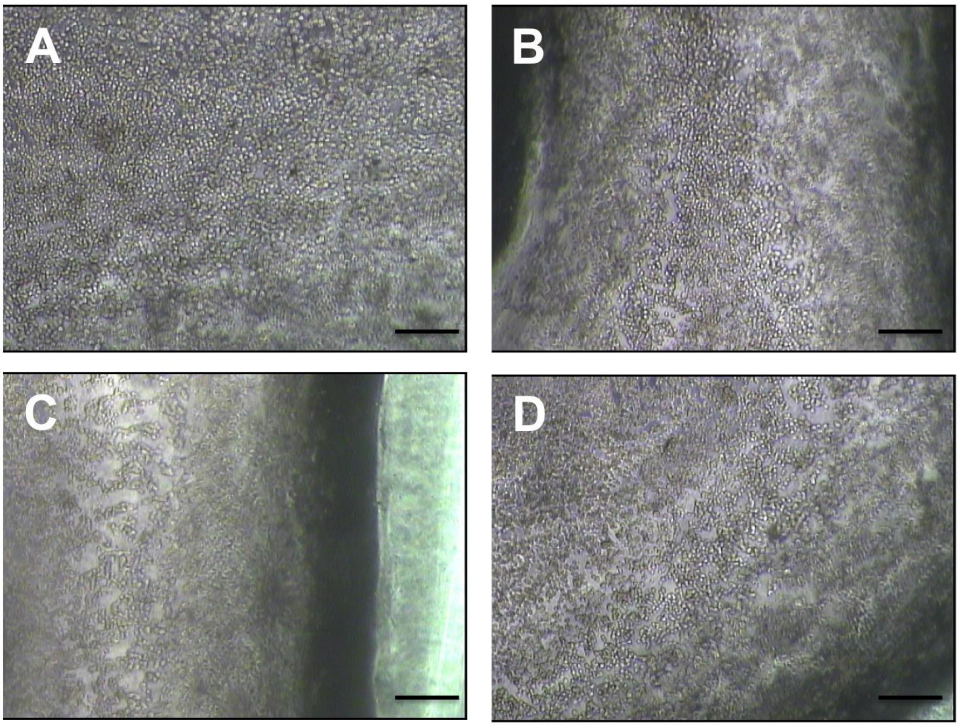

Figure 93. *HUVECs cultured in fully circular channels after 24 hours. Images on the left show the lower channel wall coated with collagen (A) and fibronectin (C), respectively. Photographs on the right show the upper channel wall coated with collagen (B) and fibronectin (D), respectively. Images (4X magnification) were taken after 24 hours (scale bars are 200 µm).*

As shown in Figure 94, HUVECs were attached and uniformly spread over the protein-coated surface on both lower and upper walls of the circular channels. Particularly, fibronectin coating resulted in more effective seeding, with a larger surface area covered with HUVECs and fewer areas without cells. It is important to highlight that VOC devices have larger channel (1 mm in diameter) compared to microchannels typically used in vasculature-on-a-chip devices (10-400 µm), making the cell coating process more challenging, given the larger surface area to be covered. However, despite channels were larger in this study, it was possible to obtain a homogenous coating using a lower seeding concentration of cells compared to previous studies (generally 5×10^5 - 1.25×10^7cells/mL).

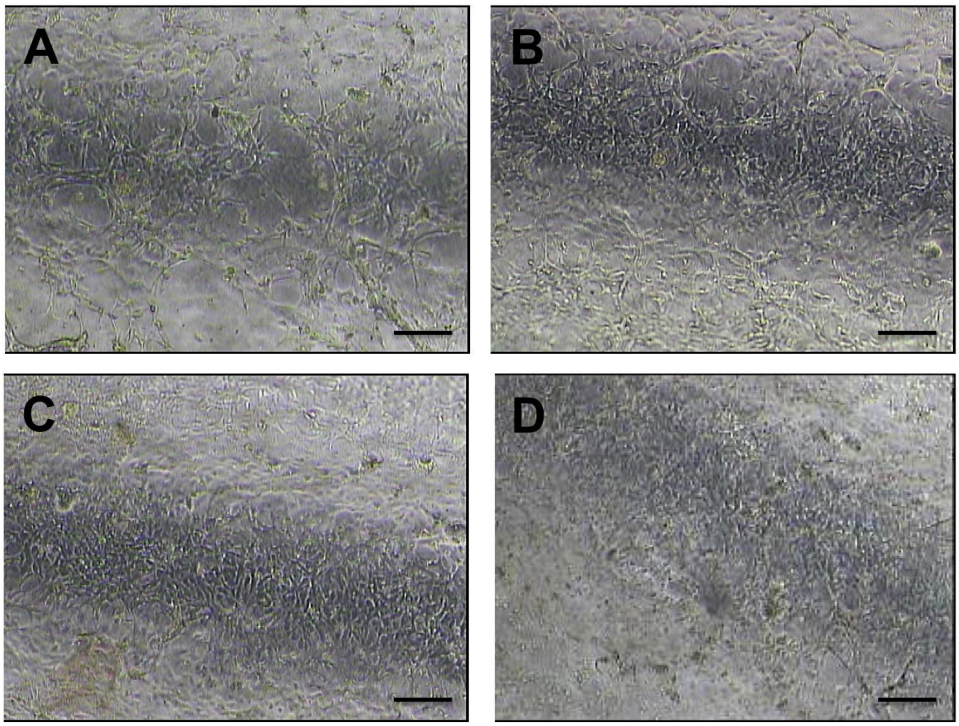

Figure 94. *HUVECs cultured in fully circular channels after 48 hours. Images on the left show the lower channel wall coated with collagen (A) and fibronectin (C), respectively. Photographs on the right show the upper channel wall coated with collagen (B) and fibronectin (D), respectively. Images (4X magnification) were taken after 48 hours (scale bars are 200 µm).*

8.3.2 HUVECs fluorescence images in PDMS vasculature models

After the initial validation of the ECs seeding protocol, HUVECs were cultured in different types of microfluidic channels. ECs attachment was evaluated in the VOCs models (1 mm diameter) and in the arteriolar models (200 µm diameter). The latter have been produced with the same technique described for VOCs. The only differences are the channel network design and the vessel diameter.

With respect to the VOCs design (1 mm in diameter) cell attachment was evaluated after 48 h. Cell nuclei were labeled with Acridine orange (green) and imaged using a fluorescence microscope (Figure 95).

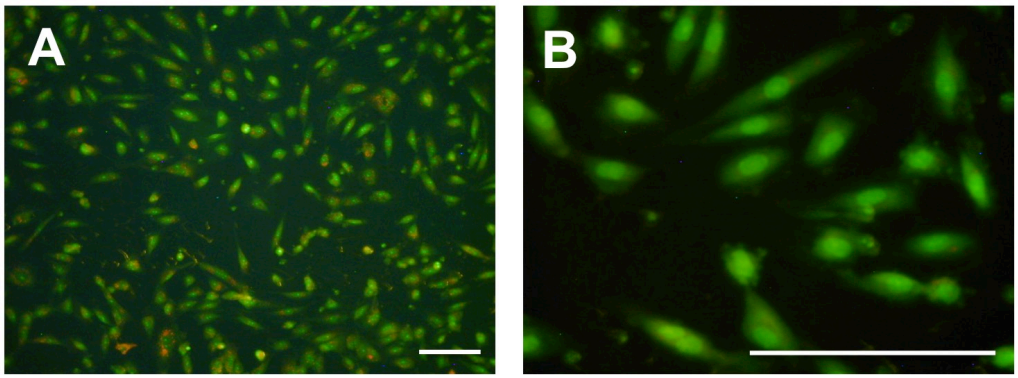

Figure 95. *Fluorescence images of HUVECs culture into a 24-well-plates. After 48h, cell nuclei were labeled with Acridine Orange (green) and imaged with fluorescence microscopy. (A) 4X and (B) 10x, (scale bar 200 µm).*

The attachment of ECs over the channel walls was evaluated. As shown in Figure 96, the number of the cells at regions close to the inlet of the device is higher when compared to regions close to the outlet, showing a decrease of cell number along the channel. These results might be due to the seeding method itself.

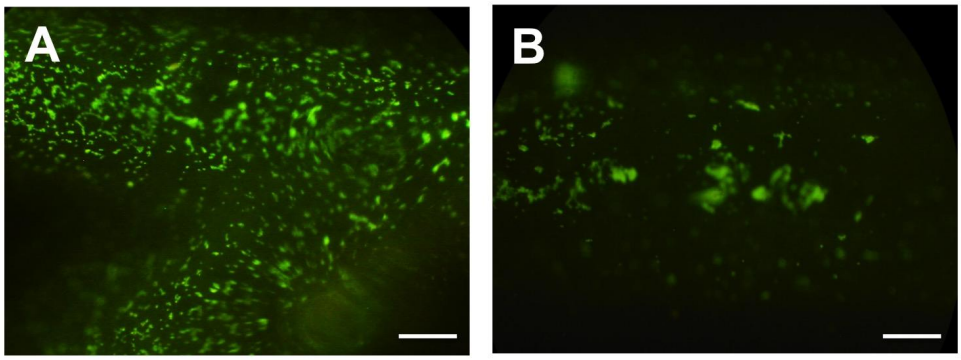

Figure 96*. Fluorescence images of HUVECs into the VOCs (1 mm in diameter) in the inlet (A) and in the outlet (B) regions along the channel. HUVECs were cultured in a PDMS channel and allowed to cover all surfaces. After 48h, cell nuclei were labeled (green) and imaged with fluorescence microscopy (scale bar 200 µm).*

Indeed, cells are generally injected from the inlet/s of the channel, to achieve complete priming. Afterwards, cells are allowed to sediment and attach onto the channel surface, for at least 2h. This approach might not allow cells to reach the end of the channel, as they may sediment in the proximal regions. In this project, it is fundamental to obtain a homogeneous monolayer of ECs in order to recreate the physiological vessel wall. Therefore, cell seeding was performed from both inlets and outlets, in order to obtain a more homogeneous endothelialization of the microfluidic channel (Figure 97).

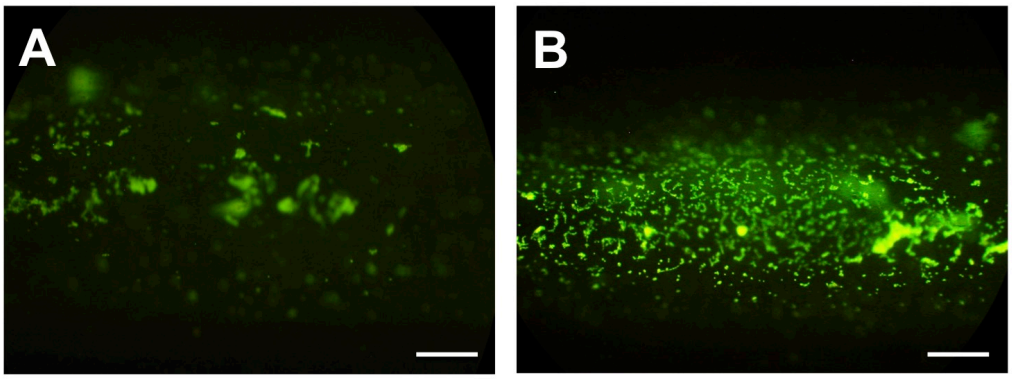

Figure 97. *Fluorescence images of HUVECs into the VOCs (1 mm in diameter) in the outlet region injected only from the inlet (A) or from the inlet/outlet (B) along the channel. HUVECs were cultured in a PDMS channel and allowed to cover all surfaces. After 48h, cell nuclei were labeled (green) and imaged with fluorescence microscopy (scale bar 200 µm).*

Therefore the total number of cells injected was divided into two samples, and injected in two phases: injection from the inlet followed by the injection from the outlet, in order to assure the complete coverage of the channel length. The second injection was performed after 2 hours from the first seeding (Table 15).

Table 15. Cell seeding approach in the microfluidic device.

Seeding	Segment (outlet)
Inlet	207
Inlet and outlet	570
Increase in %	175%

Following the procedure reported above, the cell attachment was homogenous along the entire device as is shown on Figure 98. The number of cell in the outlets was generally slightly smaller in all chips, compared to the inlet region. However, employing the two-phases method for seeding led to more uniform coverage compared to the one phase seeding.

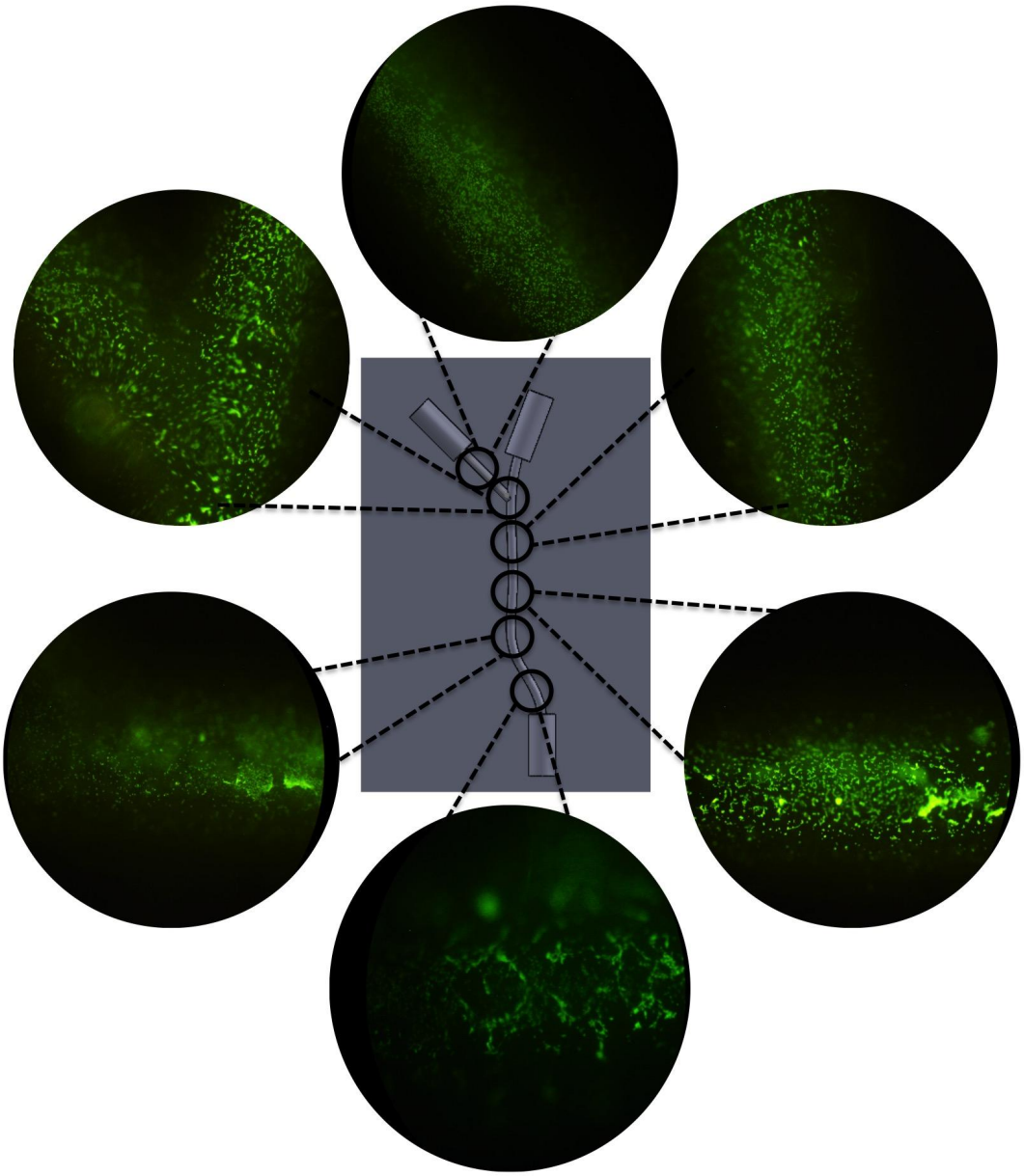

Figure 98. *ECs covering of the microfluidic channel wall. Fluorescence images of HUVECs into the VOCs (1 mm in diameter) in different regions along the channel. HUVECs were cultured in a PDMS channel and allowed to cover all surfaces. After 48h, cell nuclei were labeled (green) and imaged with fluorescence microscopy.*

With respect to the arteriolar model having 200 µm diameter channels, cell attachment was more homogeneous along the microfluidic tree, using the same initial cell concentration (Figure 99). These results might be due to the fact that the diameter of the channel is 5 times lower compared to VOCs. These results confirmed that endothelialization was more effective in smaller channels. Indeed, culturing ECs in the larger vein model requires higher volume of ECM proteins, higher number of cells, and more time to achieve a homogenous monolayer.

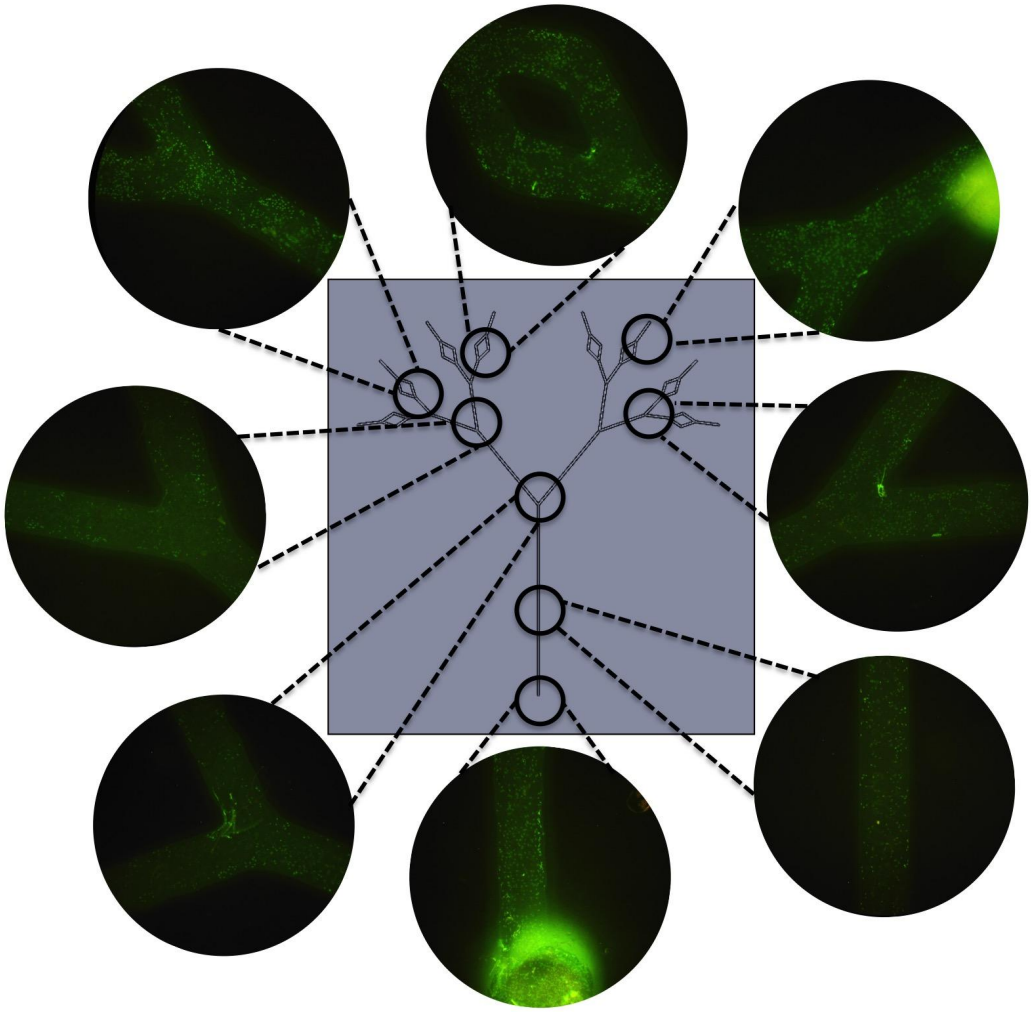

Figure 99. *ECs covering of the microfluidic channel wall. Fluorescence images of HUVECs within an arterioles-on-a-chip (0.2 mm diameter) at different regions along the channel network. HUVECs were cultured in the PDMS microfluidic device and allowed to cover the inner surfaces. After 48h, cell nuclei were labeled (green) and imaged with fluorescence microscopy.*

Afterwards, the number of cells in the microfluidic channels was evaluated after 24 hours and 48 hours. The cell counting plugin of ImageJ was employed for this purpose, and images were taken at two different regions of the microfluidic network as shown in the figure 100-101.

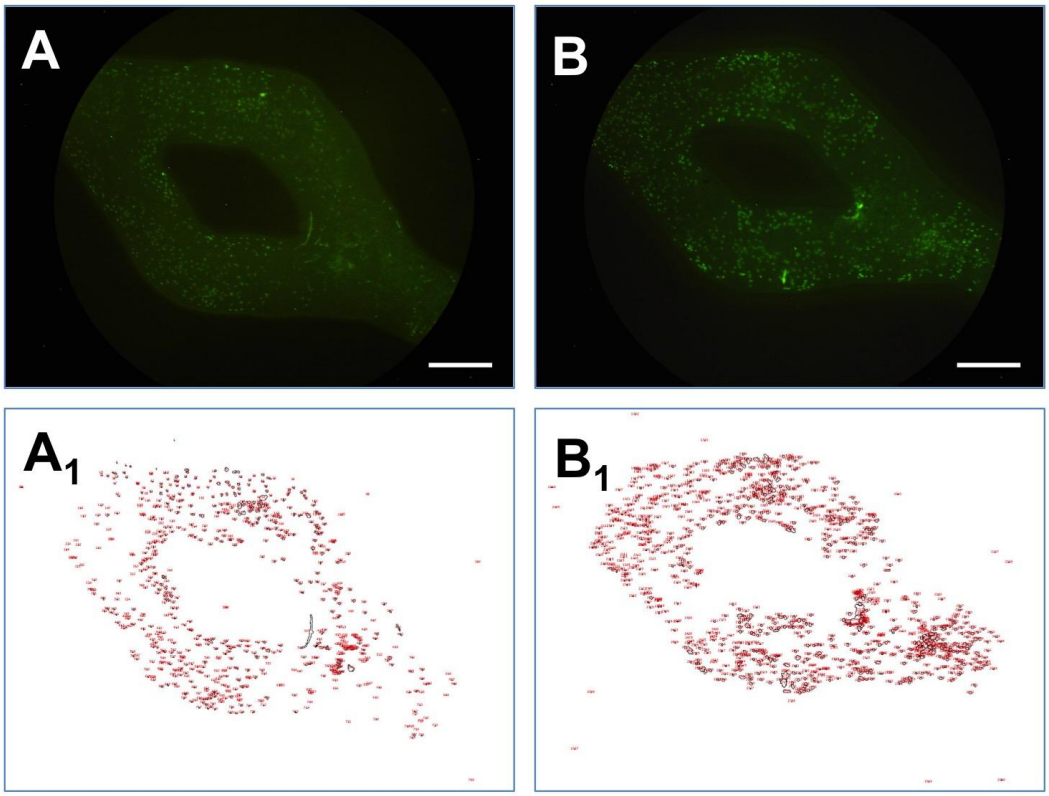

Figure 100. *Fluorescence images of HUVECs in the same vascular segment of a arterioles-on-a-chip device (0.2 mm diameter) after 24 h (A) and 48 h (B), and corresponding cell edges analysis images obtained through the analyze particles tools of ImageJ employed for cell counting (A_1 and B_1). HUVECs were cultured in the PDMS microfluidic channels and allowed to cover all inner surfaces. After 24 and 48h cells nuclei were labeled (green) and imaged with fluorescence microscopy. Scale bars are 200 μm.*

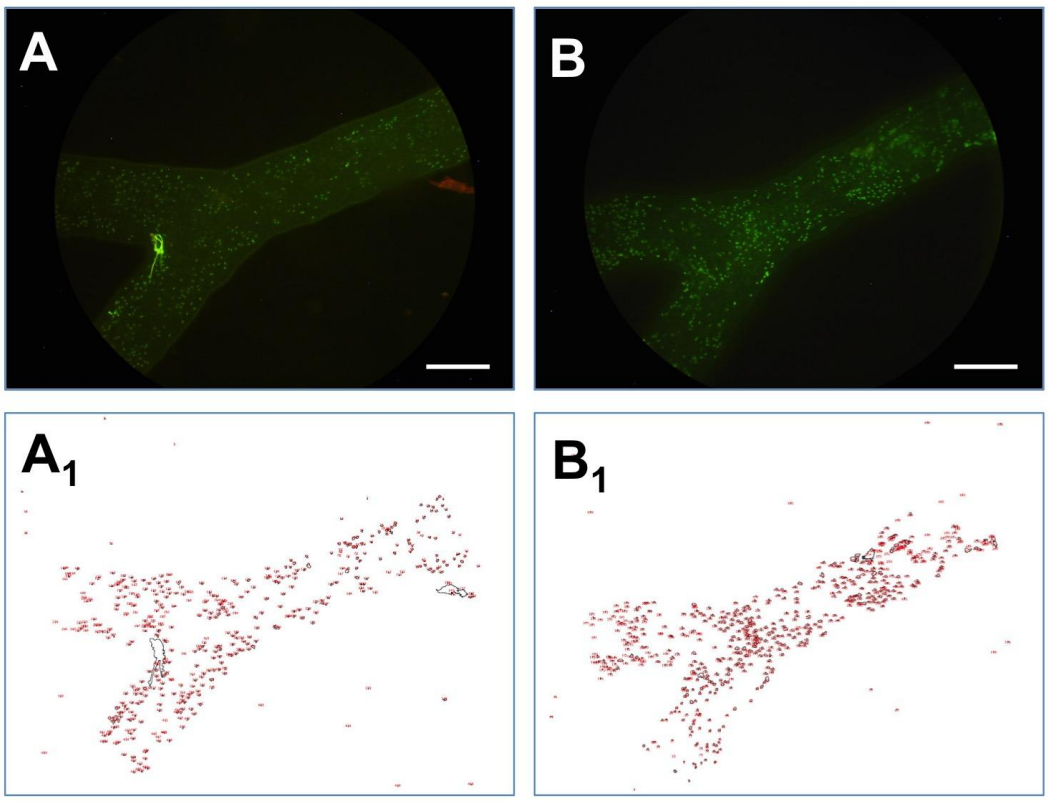

Figure 101. *Fluorescence images of HUVECs in the same vascular segment of a arterioles-on-a-chip device (0.2 mm diameter) after 24 h (A) and 48 h (B), and corresponding cell edges analysis images obtained through the analyze particles tools of ImageJ employed for cell counting (A_1 and B_1). HUVECs were cultured in the PDMS microfluidic channels and allowed to cover all inner surfaces. After 24 and 48h cells nuclei were labeled (green) and imaged with fluorescence microscopy. Scale bars are 200 µm.*

The counting was repeated four times for each segment. After cell counting, the percentage increase in cell number in the two selected areas was 21% and 43% (30% average) respectively, showing a significant increase in % coverage area after 48 hours (see Table 16).

Table 16. Cell counting into the microfluidic channel network after 48 h.

N of cells		
Time (h)	Segment 1	Segment 2
24	470	873
48	569	1247
Increase in %	21%	43%

One important consideration is that the aim of the project is to produce a biomimetic vasculature platform, which will be employed for drug testing. The platform should be produced with low cost, easily, in short time and with a robust method. For this reason 48 hours of cell culture will be considered as the optimal time in further experiments. With this

approach, a vasculature platform could be manufactured in 3 days, employing a relatively low lower number of ECM proteins and cells, achieving efficient covering of the microfluidic vessels.

8.3.3 Alginate scaffold preparation

Herein, a novel method to create microchannels inside natural hydrogels has been proposed, which is simple to perform, rapid and reproducible. The method brings together two different approaches: (i) molding and (ii) sacrificial molding. It allows producing a scaffold containing perfusable microfluidic channels. An agarose mold is used for constructing the scaffold, whereas a gelatin sacrificial mold is employed for producing the channels inside the scaffold. Hydrogels employed in this method were chosen based on their characteristics.

First at all, the hydrogel employed for the scaffold fabrication must allow ECs attachment and growth onto its surface. Therefore, the evaluation of cell attachment on agarose and alginate (2% w/v) with absence and presence of collagen was the first experiment performed (Figure 102).

Cell attachment was compared with plastic wells (the plastic was primed with gelatin 0.2 %, prior to HUVECs seeding).

HUVECs seeded on agarose tended to form spheroids instead of generating a confluent monolayer, with and without coating with collagen.

With respect of the alginate gel, cell attachment was evident in the case of the gel coated with collagen. For this reason, agarose was employed as molding material while alginate as a scaffold material in further experiments.

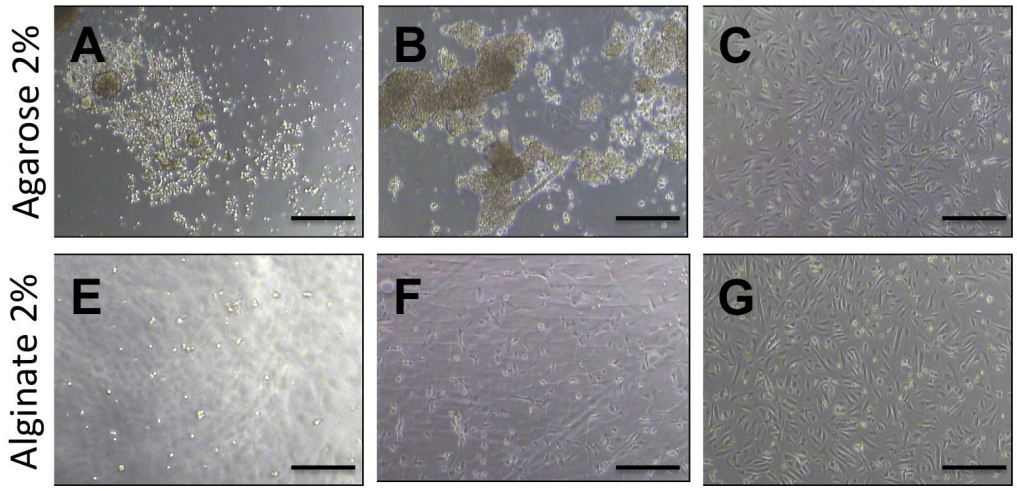

Figure 102. *Evaluation of cell attachment on agarose and alginate gels with (B, F) and without (A, E) collagen coating (2% w/v). At the top, photographs (4X magnification) show HUVECs seeded on the agarose gel after 48 hours, whereas the photographs at the bottom (4X magnification) show HUVECs seeded on alginate gel after 48 hours. Both substrates were compared to the control (C, G), where cells were seeded onto a plastic well. Scale bar 200 μm.*

8.3.4 Generation of a calcium/agarose mold by replica molding

In this study, 3D printed templates with cylindrical, cubic and discoid geometry have been proposed in order to demonstrate the versatility of the method in producing simple geometries. As shown in Figure 103, cylindrical and cubic alginate scaffolds can be obtained with this method. However, other geometries could be fabricated, depending on the specific application of the scaffold.

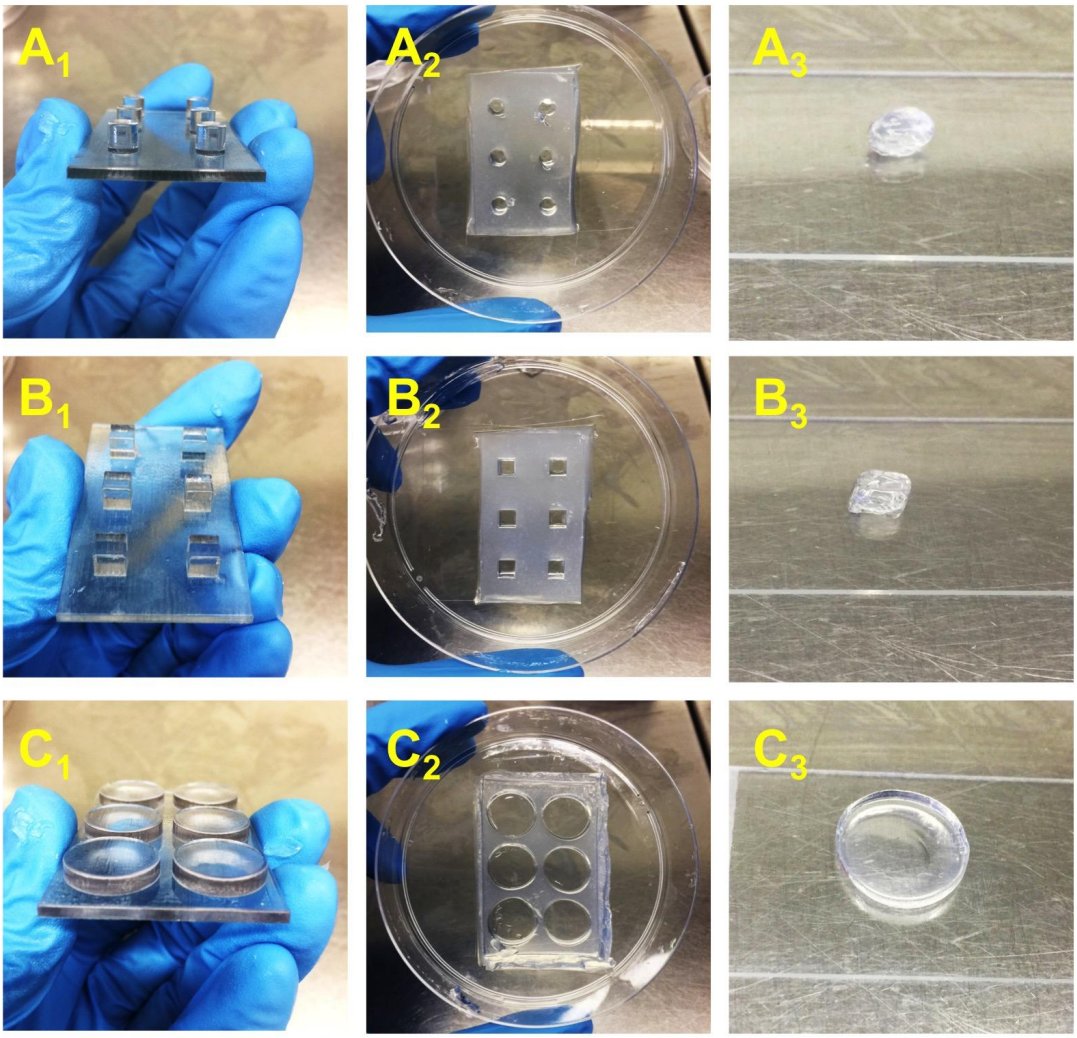

Figure 103. *Photographs of the alginate scaffold production process, using different types of 3D printed molds, such as (A_1) cylindrical, (B_1) cubic, and (C_1) discoid. For each type of mold the agarose mold obtained is shown (A_2-B_2-C_2). The obtained (A_3) cylinder, (B_3) cube, and (C_3) disk of alginate are also shown.*

After validating the versatility of the method, the production of a cylinder with 5 mm diameter and 5 mm height was evaluated (Figure 104). The 3D printed mold contained 6 identical cylinders, to demonstrate high-throughput production. The quantity of alginate pippeted was 100 µl per well, which gelified in approximately 30 minutes at room temperature.

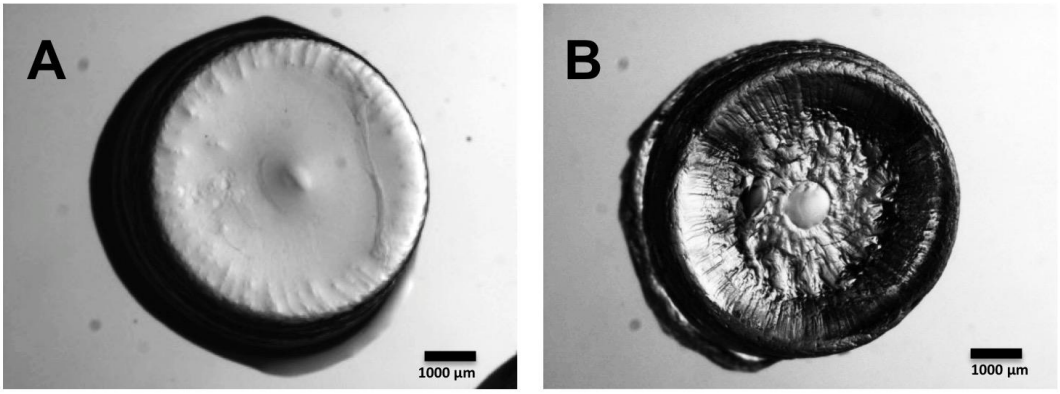

Figure 104. *Microscope images of two alginate cylinders fabricated by the agarose molding technique. Images were taken when the scaffold was stored into 0.15% $CaCl_2$ (A), or into at open air (B) for 30 minutes. (1X magnification, scale bars are 1000 µm).*

Afterwards, a study of the gelation time inside the agarose mold was carried out. Samples were analyzed at different time points during gelation. After one minute, the alginate scaffold was only partially gelified. Complete gelation occurred after 30 minutes. The scaffold could be left in the mold until 110 minutes, after which dehydration occurred causing shrinkage of the gel (Figure 105). The diameter of the scaffold was measured using the microscope images in ImageJ, taken at 30 to 70 minutes of gelation time, and no variation in diameter was detected.

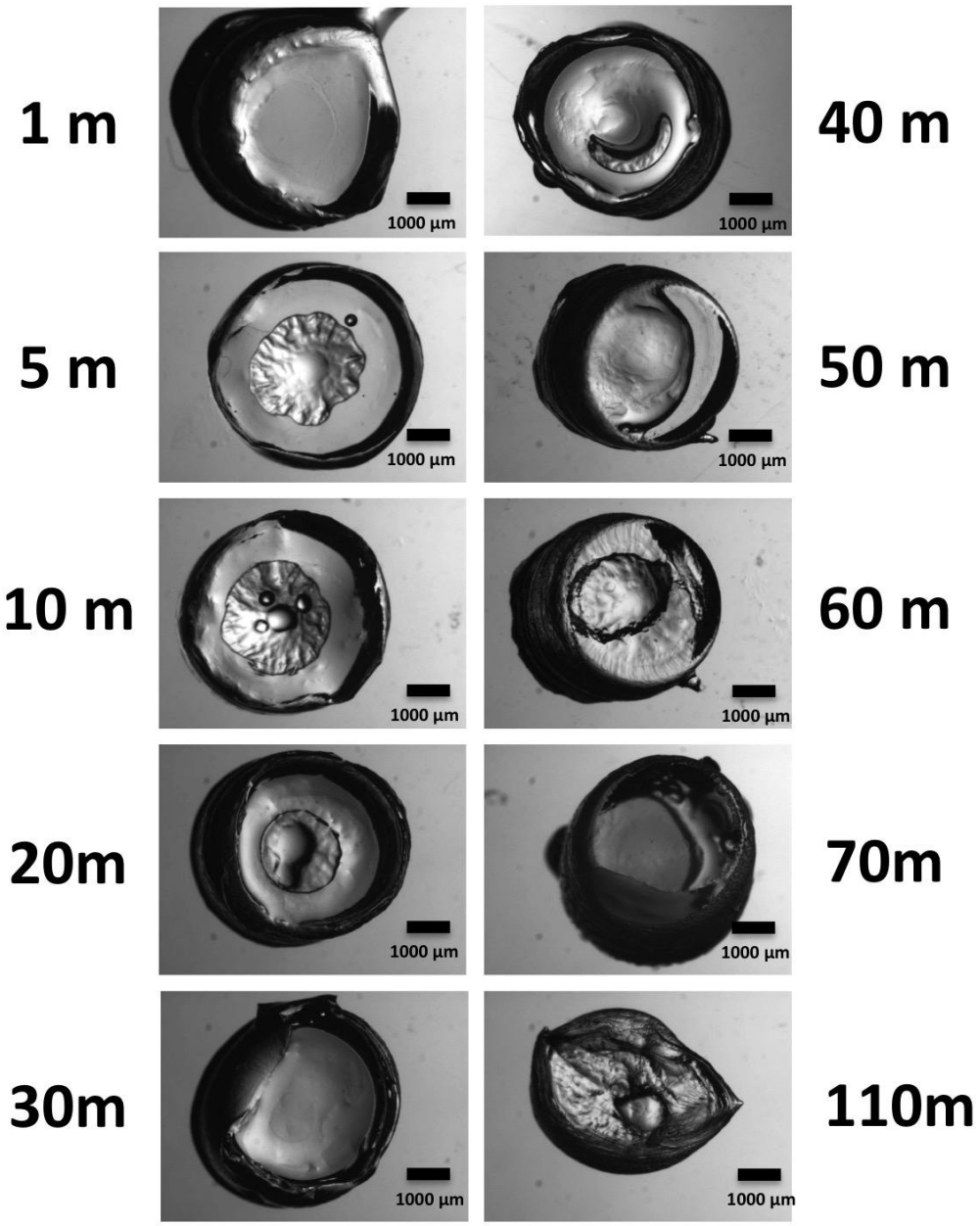

Figure 105. *Evaluation of the effect of alginate gelation time. Microscope images of alginate cylinders fabricated by agarose molding after 1-110 minutes from the beginning of the gelation process (1X magnification). The cylinder are completed gelified after 30 minutes. The ideal gelation time is between 30-70 minutes, after which dehydration occurs, causing shrinkage of the gel (scale bars are 1000 µm).*

8.3.5 Construction of vascularized alginate scaffolds

In a second step of the study, the same fabrication technique was employed for the production of alginate scaffolds containing microfluidic channels.

The hydrogel scaffold was produced via molding technique. The shape of the scaffold was defined by the agarose mold, while the inner microchannels were produced using gelatin sacrificial molds. Figure 106 shows the hydrogel scaffolds constructed using the agarose

molding/gelatin sacrificial molding technique. The 3D printed agarose mold was produced using the procedure described in paragraphs 8.2.5.

In this case, the mold employed was a parallelepiped, which allows producing a negative chamber into the agarose gel. Simultaneously, the sacrificial mold made of gelatin was produced using the molding technique. For the production of the microfluidic channels, the MHF geometry has been chosen, characterized by three inlets, which replicate junctions between multiple channels, and one outlet. MHF is a common geometry employed in microfluidics and has a simple channel structure, which facilitates the validation process of the method.

Afterwards, the agarose chamber was filled with few microliters of 2 % alginate in order to make a thin layer of gel, immediately the 30% gelatin sacrificial mold was positioned into the middle of the chamber, which was completely filled with the alginate solution. A flat sheet 1% agarose/1.5% $CaCl_2$ gel can be used as a lid to allow the gelation process to occur from all surfaces. Generally, 60 minutes were needed to form a firm hydrogel scaffold. After gelation, the alginate scaffold was removed using a spatula.

The scaffold was stored into a 10 cm diameter culture dish filled with 0.15% $CaCl_2$ in order to finalize the gelation process for at least 30 minutes. After gelation, the edges of the scaffold were cut in order to open the inlets and outlet, and allow the gelatin removal. Then, the sacrificial mold made of gelatin was melted by leaving the hydrogel scaffold into the incubator at 37°C. Warm PBS was finally used to perfuse the microchannel (Figure 106).

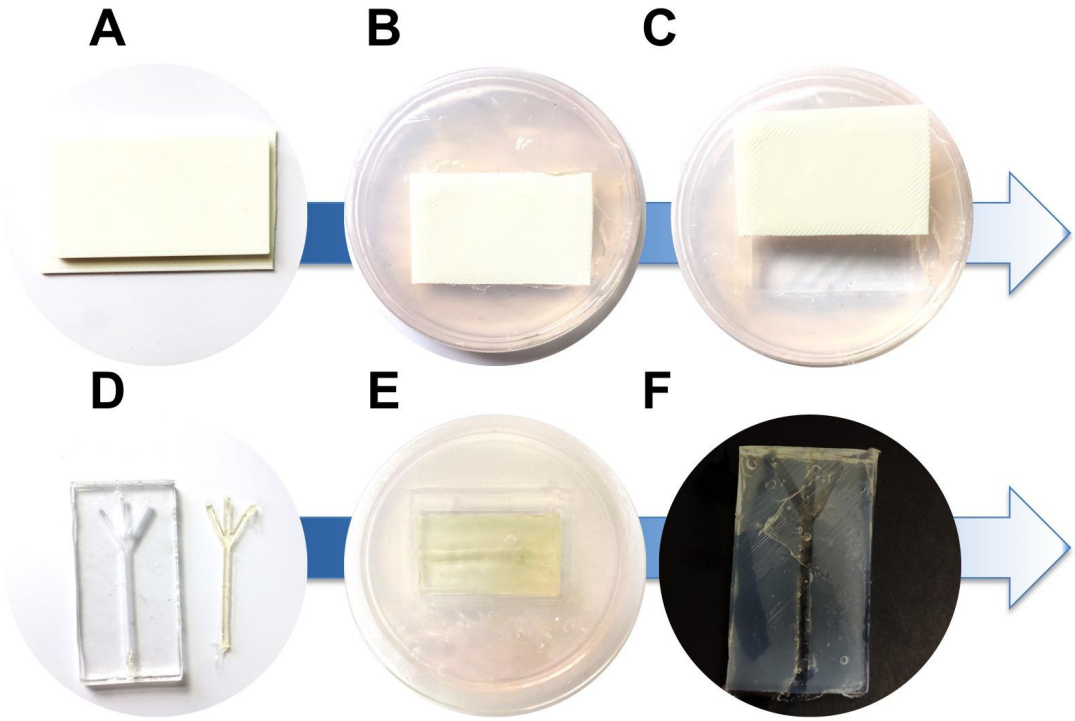

Figure 106. *Photographs of an alginate scaffold containing microfluidic channels, and illustration of the production process. (A) The 3D printed parallelepiped template was employed for generating a chamber into the agarose gel. (B) 1% agarose/1.5% $CaCl_2$ was heated in the microwave and poured into a petri dish. The 3D printed mold was gently positioned on the surface of the mixture and allowed to solidify for 30 minutes. (C) Once the agarose-$CaCl_2$ mold was solidified, the 3D printed mold was gently removed. (D) In parallel, the gelatin sacrificial mold was generated by replica molding. (E) The agarose chamber was filled with few microliters of alginate in order to make a thin layer of gel, and the gelatin sacrificial mold was positioned into the middle of the chamber, which was then completely filled with the alginate solution. A flat sheet of 1% agarose/1.5% $CaCl_2$ can be used as a lid to allow the gelation process to happen from all the boundaries. After gelation, the alginate scaffold was removed using a spatula.*

The same procedure was employed to recreate a varicose vein model (4mm inner diameter). The gelatin sacrificial mold was obtained using a simple serpentine-vein structure. The steps described before were followed as shown Figure 107. This method allowed producing a more complex geometry in a controlled manner. These results show the tunability of the method, which allows creating different types of vessel geometries, from 1 mm diameter to larger sizes (4 mm is the maximum size studied). With respect to the bigger channels, the channel section presented ellipitical geometry, due to the softness of the material; this limitation might be overcome varying the composition of the gel to increase stiffness.

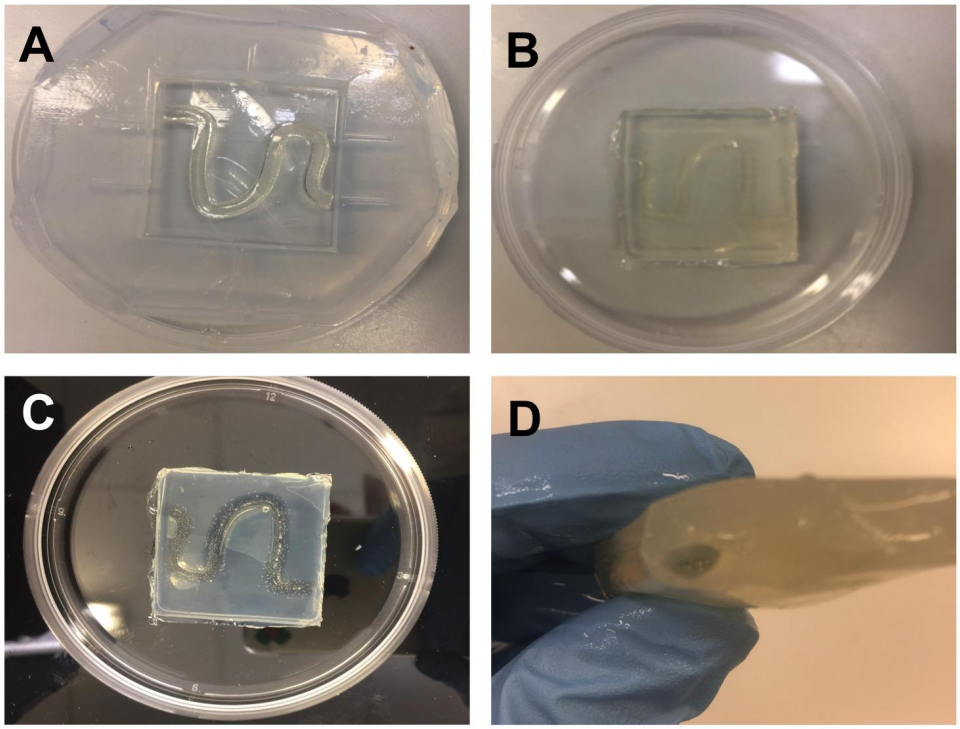

Figure 107. *Photographs of an alginate scaffold containing vascular channels, and illustration of some steps of the production process. (A) The gelatin vessel structure was placed onto the agarose chamber, which was filled with few milliliters of alginate. (C) After gelation, the alginate scaffold was removed using a spatula and the gelatin was removed by melting, in order to obtain an empty channel (D).*

8.3.6 Endothelialization of the channels in alginate scaffold

Endothelial cell adhesion inside the hydrogel microchannels was investigated. The alginate gel was coated with collagen, in order to improve the attachment of endothelial cells onto the channel.

After the preparation of the scaffold, HUVECs ($5x10^5$ cell/mL) were injected into the microchannel. Subsequently, the alginate hydrogel scaffolds were carefully transferred into a 10 cm diameter petri dish filled with medium. The obtained scaffold was left into the incubator for 2 days. The results are shown in Figure 108, showing HUVECs attached on the microchannel inner surfaces.

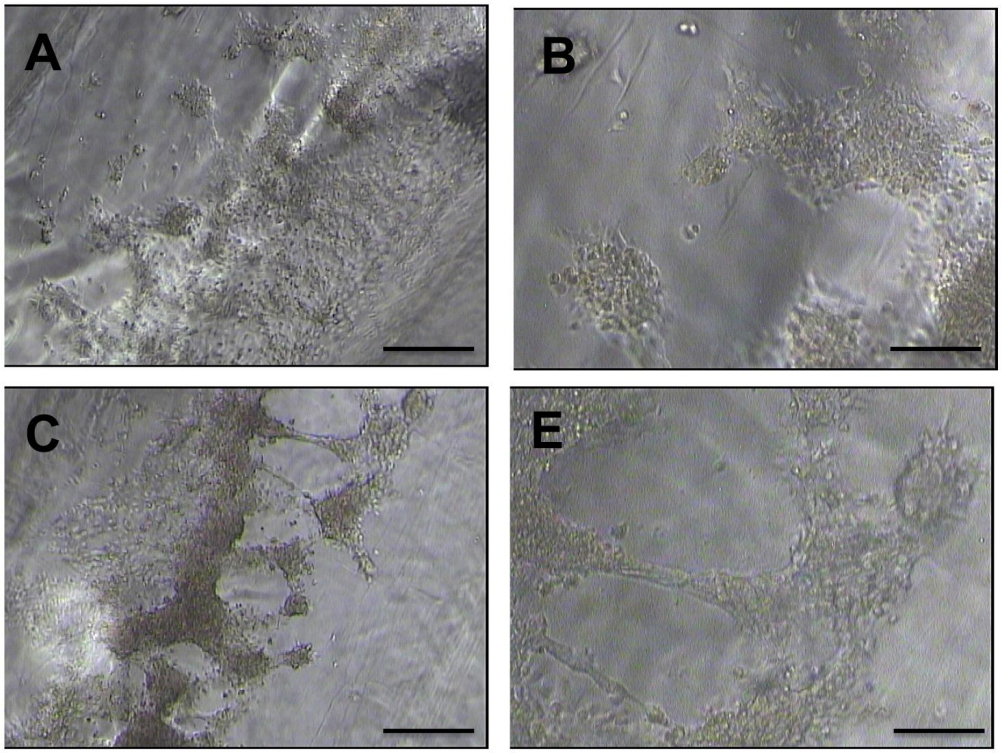

Figure 108. *Evaluation of HUVECs attachment on the surfaces of the channels. Microscope photographs show HUVECs attached on the alginate channel lumen, (A-C) taken at 4X magnification and (B-D) at 10X magnification, after 48 hours. Scale bars are 200 μm.*

Results of preliminary experiments show that HUVECs do not cover the whole channel lumen. Several reasons might be responsible for this behaviour. First, the concentration of HUVECs employed for this experiments might be low considering the surface area of the channel. Second, the culture medium used in this project is M199 with 20% fetal bovine serum, without any cell growth supplement, which could be added to promote cells growth. Third, coating with cellular certain peptides (e.g., GRGD, RGDS), might improve cell attachment. However, a reasonable number of cells adhered onto the alginate surface, showing that the hydrogel itself allowed ECs attachment. It should be noted that this was the first attempt to seed ECs into the microfluidic hydrogel scaffold, thus further experiments are required to optimise the process.

8.4 Discussion

8.4.1 Cell seeding in PDMS-based devices

With the aim of developing VOC models coated with an endothelial monolayer, the behaviour of HUVECs when cultured on PDMS surfaces was investigated. PDMS has been extensively used for cell culture at microfluidic level, because of its optical transparency, low

cost, gas permeability, and biocompatibility. However, it is not an ideal substrate surface for cell attachment, due to its hydrophobicity (Bodas and Khan-Malek, 2007).

In the physiological environment, ECs are attached on the ECM that is fundamental to control cell morphology and proliferation. ECM is composed of glycosaminoglycans and fibrous proteins, including collagen and fibronectin. Both matrix proteins have structural and adhesive functions. Coating with ECM proteins inside PDMS channels has shown an improvement in cell adhesion. In this study, different types of matrix proteins were investigated: collagen rat type I, fibronectin, and Geltrex™. Comparing the three types of ECM proteins used, fibronectin and collagen resulted in the most effective cell coating (Figure 89-92).

After investigating HUVECs behaviour onto a flat PDMS surface, experiments were repeated inside the circular VOC channels (1 mm inner diameter). Fibronectin coating resulted in more effective seeding, with a larger surface area covered with HUVECs and fewer areas without cells (Figure 93-94). Additionally, in order to obtain a homogenous coverage, cell seeding was performed from both inlets and outlets, in order to obtain a more homogeneous endothelialization of the microfluidic channel (Figure 98). It was also demonstrated that the number of cells increased after 48h inside the microfluidic channel (Figure 100-101). It is important to underline that the results here reported are obtained from preliminary test and further improvements are needed such as (i) cell culture under continuous steady flow and (ii) implementation of the medium with growth factors. However, this simple seeding method allowed creating homogenous endothelium in relative small devices (0.2-1 mm in diameter) and is important to underline that the aim of the project is to create vasculature platform with low cost and in a short time period.

8.4.2 Cell seeding in alginate-based device

The use of PDMS as a material for generating biomimetic vascular models has some limitations, due to (i) its hydrophobicity, (ii) surface adsorption of molecules, and (iii) lack of ECM.

Therefore, alternative materials should be investigated in order to develop a model that more closely replicates the physical properties of a tissue substrate, and that allows for evaluating extravasation of therapeutic or probe molecules (i.e., resulting from endothelial damage).

Herein, a novel method to create microchannels inside natural hydrogels has been proposed, which is simple to perform, rapid and reproducible. The method brings together two different

approaches: (i) molding and (ii) sacrificial molding. It allows producing a scaffold containing perfusable microfluidic channels. An agarose mold is used for constructing the scaffold, whereas a gelatin sacrificial mold is employed for producing the channels inside the scaffold. Hydrogels employed in this method were chosen based on their characteristics. HUVECs seeded on agarose tended to forming spheroids instead of generating a confluent monolayer, with and without the coating with collagen.

With respect of the alginate gel, cell attachment was evident in the case of the coated gel with collagen. For this reason, agarose was employed as molding material while alginate as a scaffold material in further experiments (Figure 102).

Agarose has been selected as a material for molding because of its simple gelation method and, on the other hand, it is not a suitable candidate for ECs attachment. Gelatin has been used as the sacrificial molding material since it can be easily removed as it melts at 37 °C, which is the temperature of a cell incubator (Sanyo Electric Co., Ltd., Japan). Finally, alginate has been employed as a scaffold material for different reasons: (i) it undergoes a tunable crosslinking gelation process, (ii) its stiffness is sufficient to allow generation of perfusable channels, and (iii) it has acted as an effective substrate for ECs attachment.

The calcium/agarose mold in this study was made by replica molding. 3D printed templates were employed for generating negative patterns onto the agarose gel. In a first phase of the study, cell-free scaffolds were evaluated. Scaffolds were produced dispersing the agarose in a $CaCl_2$ solution; this mixture solution was heated in the microwave and was poured into a petri dish. At this point, the 3D printed mold was gently positioned on the surface of the mixture and allowed to solidify for 30 minutes. Once the mold agarose-$CaCl_2$ was solidified, the 3D printed mold was gently removed and the 100 µl volume of alginate was poured into the wells. Once gelling achieved (after 30 minutes) the scaffolds were extracted and immersed for 20 minutes into the gelling bath ($CaCl_2$ 0.15% solution), as reported in Materials and Methods section.

When the alginate is added in to the agarose mold, it is crosslinked by calcium ions diffusing from the agarose mold at room temperature. In this way the diffusion of ions occurs from one gel to the other, in a controllable manner. After approximately 30 minutes (i.e. the gelation time depends on the size of the mold), the alginate constructs can be easily removed from the mold.

In the more common external gelation process, when the alginate solution comes into contact with divalent cations, gelation occurs immediately. The gelation time influences the shape of

the hydrogel, indeed when it occurs rapidly the surface can appear less smooth and homogenous, and it might be difficult to control the shape of the scaffold. In the method presented here, gelation occurred due to the diffusion of Ca_2 ions from the agarose gel into the alginate gel, indeed it occurred more rapidly in the areas of contact between the two gels and more slowly within the scaffold. Achieving a slower gelation time reduces conformational distortions of the gel, making the method suitable for generating different scaffold architectures.

In a second step of the study, the same fabrication technique was employed for the production of alginate scaffolds containing microfluidic channels.

In this case, the mold employed was a parallelepiped, which allows producing a negative chamber into the agarose gel. Simultaneously, the sacrificial mold made of gelatin was produced using the molding technique. For the production of the microfluidic channels, the MHF geometry has been chosen, characterized by three inlets, which replicate junctions between multiple channels, and one outlet. MHF is a common geometry employed in microfluidics and has a simple channel structure, which facilitates the validation process of the method (Figure 106).

The same procedure was employed to recreate a varicose vein model (4mm inner diameter). The gelatin sacrificial mold was obtained using a simple serpentine-vein structure. The steps described before were followed as shown Figure 107.

Endothelial cell adhesion inside the hydrogel microchannels was investigated. The alginate gel was coated with the collagen in order to improve the attachment of the endothelial cells onto the channel. Results of preliminary experiments show that HUVECs do not cover the whole channel lumen. Several reasons might be responsible for this behaviour. First, the concentration of HUVECs employed for this experiments is low considering the surface area of the channel. Second, the culture medium used in this project is HM with 20% fetal bovine serum, without any cell growth supplement, which could be added to promote cells growth. Third, coating with cellular certain peptides (e.g., GRGD, RGDS), might improve cell attachment. However, a reasonable number of cells adhered onto the alginate surface, showing that the hydrogel itself allowed ECs attachment. It should be noted that this was the first attempt to seed ECs into the microfluidic hydrogel scaffold, thus further experiments are required to optimise the process.

The new technique proposed here allows creating different channel geometries with a size greater than 1 mm in diameter. Smaller sizes might be obtained exploiting the ability of the

gelatin gel to shrink when it dehydrates.

The limitations of the following vascularized device are the following: (i) difficult to continuously perfuse, (ii) fragile to handle, (iii) more complex and laborious fabrication and diffusion of molecules through the bulk (not isolated in the channel).

8.5 Conclusions

In this Chapter, a simple method was employed to attach EC onto PDMS-based microfluidic devices. Homogenous endothelializiation is fundamental for generating reliable vascular models. Further improvements may be carried out in the future such as, cell culture in dynamic conditions and the improvement of the media composition in order to increase cell growth rate. The device might be employed to correlate the results obtained *in vitro* (Chapter 4) with the mechanical proprieties measured in the VOC models.

Secondly, a rapid, low-cost and simple method to create hydrogel scaffolds for tissue engineering and vascular research was demonstrated. The use of agarose molds allowed production of alginate scaffolds with cylindrical and cubic geometry, and of different sizes. However, multiple geometries could be fabricated, based on the final application of the hydrogel scaffold.

Afterwards, the agarose molding method was employed in association with the sacrificial molding technique in order to obtain alginate scaffolds with channels inside.

The 3D-printed replica molding and gelatin sacrificial molding techniques allowed rapid prototyping of the scaffold. Alginate hydrogel gelation by an agarose mold containing cross-linking moieties, allowed controlling the gelation process dynamics. After validation of the production method, ECs were seeded into the microchannels to recreate the endothelial layer. Although HUVECs did not cover the whole microchannel lumen, cell attachment inside the scaffold for 48 hours showed potential to form an endothelial layer. Future work could focus on the improvement of cell attachment and growth. In addition, perfusion of the channel has been carried out using a pipette; thus, additional efforts could be devoted to the production of connection ports in order to allow for continuous flow perfusion. Although current results demonstrate the potential of the developed technique for producing vascularised scaffolds, further improvements are needed for application in vascular research or pre-clinical testing.

This technique could however be employed for the fabrication of vein-on-chips models made of hydrogels rather than PDMS. Alginate-based VOCs could provide new *in vitro* platform for evaluating the effect of sclerotherapy on endothelial cells, potentially allowing for a more

robust *in vitro/ex vivo* correlation. Additionally, the same fabrication approach could be applied to other application areas, such as the generation of vascular models for investigating diffusion of drugs or other drug delivery vehicles. In this case, the use of hydrogels as a constitutive material is fundamental, because it allows measuring the diffusion of molecules across the endothelial layer, which is not achievable using PDMS-based devices.

Chapter 9: Conclusion and Future Work

Chapter 9 summarises the final conclusions, limitations and avenues for future work.

9.1 Summary of key results

In this study, three models have been developed in order to gain a more comprehensive understanding of the physical and biological effects of sclerosing agents. These include: (i) 2D *in vitro* models, (ii) *ex vivo* models, and (iii) 3D vein-on-a-chip.

In Chapter 4, a simple quantitative 2D *in vitro* method to quantify the efficacy of sclerosing agents was proposed. The method allows investigating different clinical parameters such as exposure time, injected volume, concentration of sclerosant, and needle bore size amongst others. The present study represents the first systematic comparison of the biological performance of different sclerosing foam formulations, and a first attempt to correlate biological performance with foam physical properties. Overall, analyzing the results obtained using the *in vitro* model, PEM was the most effective foam for disrupting the endothelial layer in a variety of tests and over different timescales of treatment. This was attributed to the slower drainage dynamics of PEM compared to PCFs, and – potentially – to the enhanced polidocanol mobility conferred by its gas formulation. It was also shown that reducing the injection needle diameter, increasing the volume of injected foam, and increasing the treatment time, all contributed towards increasing treatment efficacy (for all types of foam).

In Chapter 5 variations in the lipid-packing of cell membranes have been employed to evaluate the bio-physical effects of sclerosing agents. For the first time, a quantitative microscopy technique has been employed to quantify the level of disruption of cell membranes subject to sclerotherapy.

As reported in the literature, POL above at a certain concentration interacts with the cell membrane forming vesicles, composed by the surfactant molecules and the lipid bilayer, ultimately causing cell lysis. For the first time, the generation of vesicles upon interaction with POL has been observed with a microscopy technique. Results also showed that POL is able to cause a change in the lipid-packing state towards the liquid phase, translating into a reduction of the membrane GP. The level of decrease of GP depends on the surfactant concentration. Results were in agreement with findings obtained in-vitro (Chapter 4). Additionally, POL efficacy on disrupting the cellular membrane might be associated with the number of cells and the spatial location (cells in peripheral area might be more sensitive to POL molecules). The efficacy of foamed POL (PEM and PCFS) was also tested. Results showed that PEM and TSS caused greater and faster membrane disruption.

In order to investigate sclerosants' effectiveness in a more realistic biological environment, a three-dimensional *ex vivo* model has been proposed, as an additional method of evaluation (Chapter 6). Chapter 6 provides a systematic comparison of the biological performance of different sclerosing liquid/foam formulations in a more realistic biological model. Experiments were performed *ex vivo* using umbilical cord veins in static and dynamic conditions, both in the presence and absence of whole blood. Summarizing all the results reported, PEM showed superior performance (statistically different) compared to the DSS (in presence of PBS) and POL (in presence of PBS or blood), in static condition and in the presence of PBS. In dynamic conditions PEM and TSS presented better performance (statistically different) compared to DSS and POL, but only when PBS was employed as background fluid.

In Chapter 7 the design and fabrication of VOC is discussed, together with an experimental system for evaluating the mechanical properties of foams. Initially, a simple method of VOC production was designed in order to obtain robust models, replicating the physiological and pathological architecture of veins.

In parallel to the production of VOCs, an experimental set-up for the investigation of the mechanical properties of foams was developed. It was designed to replicate a clinical process of sclerosant injection, by utilising physiologically relevant vein diameter, geometry, and inclination angle (i.e. replicating leg elevation), and replicating bulk physical properties of blood. The static fluid pressure at the inlet of the vein model was measured before, during and after injection of a sclerosant. Rates of pressure variation were strongly dependent on the mechanical properties of the foams; and two physical parameters (defined as expansion rate ER, and degradation rate, DR) were defined to quantify foam cohesiveness during and after injection. Results showed that, at the lowest flow rate investigated, DSS had the lowest ER in both straight and curved channels. At the highest flow rate investigated all types of foam were comparable in the straight channel, while in the curved channel TSS foam showed the highest ER value compared to DSS. Therefore, DSS presented slower ER compared with TSS, suggesting that it undergoes a slower expansion in the vessel and thus offers higher contact time with the vein wall upon injection.

In Chapter 8, different chemical treatments were performed in order to promote HUVECs' adhesion over the surface of the vein models; coating with fibronectin resulted in more efficient seeding, thus resulting in a larger surface area covered with HUVECs. The method

proposed in Chapter 8 thus allows creating a homogenous endothelium inside relatively large devices (0.2-1 mm in diameter).

Afterwards, a fast, low-cost and simple method to create hydrogel scaffolds for tissue engineering and vascular research was demonstrated. The use of agarose molds allowed production of alginate scaffolds with cylindrical and cubic geometry, and of different sizes. However, multiple geometries could be fabricated, based on the final application of the scaffold. Afterwards, the agarose molding method was employed in association with a sacrificial molding technique in order to obtain alginate scaffolds containing channel networks. A scaffold with a simple channel geometry followed by a more complex structure were generated, to demonstrate the rapid prototyping potential of the method. After validation of the production method, ECs were seeded into the channels to recreate the endothelial layer.

In summary, this study has proposed three models and associated quantitative methods for evaluating the effect of sclerosants. Each model represents an evolution of the previous one, and allows understanding of specific mechanistic aspects of sclerotherapy treatments. At the same time results obtained using the different models can be integrated to generate a comprehensive analysis of sclerosants' behaviour, from the cellular level to vascular effects. Two-dimensional models provide fundamental information of the mechanisms of action of sclerosing molecules and allow evaluating different therapeutic parameters such as concentration, exposure time, and gas composition. The *ex vivo* model may help understanding the biological effects of sclerosants on a real vascular tissue, and physical three-dimensional models (VOCS) instead allow evaluating fluid dynamic aspects of the treatment.

Overall, these technological developments and research findings can form the basis for a novel technological pipeline to accelerate clinical translation of innovative sclerosing agents

9.2 Limitations and future work

In Chapter 4 a simple 2D *in vitro* method to quantify the efficacy of foam sclerotherapy has been developed. However, this *in vitro* model is only two-dimensional, whereby a monolayer of endothelial cells cultured onto a plastic well mimics a limited portion of the vessel wall treated by the foam and does not fully reflect the clinical setting for foam sclerotherapy, because it is employed in static conditions and thus does not replicate foam-induced blood

displacement, and also does not provide a faithful replication of the varicose vein architecture. Therefore, a more realistic biological model, i.e. a three-dimensional *ex vivo* vein model, as a further method of evaluation should be utilized to understand more in detail the effect of the sclerosant onto the endothelium.

The major limitation in Chapter 5 was that all tests were carried out in static conditions, which doesn't fully replicate all the events that occur in the real treatments. However, the aim of the study is to investigate and quantify the effect of POL molecules at the cellular membrane, in order to understand more deeply the biological and physical interaction occurring. Another limitation of this study is that only two cell lines were employed. Therefore, in the future work further cell line should be employed. Additionally, the morphologic and structural changes after the treatment should be investigated more in details. This study might be relevant to the measurement of variations in the cell membrane after drug treatments. Indeed, the cellular membrane properties might have a significant impact on the cellular uptake of various lipophilic molecules. In addition, membrane properties are expected to play a major role in pathogenesis of various diseases.
The *ex vivo* models presented in Chapter 6 may help understanding the biological effects of sclerosants on a real vascular tissue, and have been employed in both static and dynamic conditions, to replicate stagnant and physiological blood flow. However, this model would not allow for monitoring endothelial disruption *in situ*, but only provide a post-treatment evaluation.

For these reasons, 3D vein-on-a-chip models made of PDMS were proposed, which recreate the circular section of the vessel lumen and the tortuosity of varicosities (Chapter 7). VOC allow analysing the treatment outcome *in situ*, using microscopy techniques, and can be integrated with pressure sensors to correlate mechanical with biological performance of foams. In chapter 7-8, a simple and robust method was proposed for fabricating VOC and cover the channel lumen with endothelial cells. Future work may include the use of these devices for evaluating the effect of sclerosants *in situ*. The same quantitative methods employed together with the 2D models could be applied in order to evaluate the effect of the treatment in the 3D space. The devices could allow correlating the fluid-dynamic aspects with the biological effects of the treatment.

Despite the PDMS-based VOCs provide a useful model to investigate the flow behavior of sclerosing foams and its relation to biological performance, VOC models do not fully replicate the physical properties of the vascular and extra-vascular compartments of a vein. In order to overcome this limitation, the development of hydrogel models was investigated (Chapter 8). The new method described in Chapter 8 shows great potential in recreating a model, which can mimic the characteristics of a real vein. Although current results demonstrate the potential of the developed technique for producing vascularised scaffolds, further improvements are needed for application in vascular research or pre-clinical testing. Future work will focus on the improvement of cell attachment and growth. In addition, perfusion of the channel has been carried out using a pipette; so, additional efforts will be devoted to the production of connection ports in order to allow for continuous flow perfusion.

References

1. Agarwal, A., Goss, J.A., Cho, A., McCain, M.L., and Parker, K.K. (2013). Microfluidic heart on a chip for higher throughput pharmacological studies. Lab. Chip *13*, 3599.

2. Albanese, G., and Kondo, K.L. (2010). Pharmacology of sclerotherapy. Semin. Interv. Radiol. *27*, 391–399.

3. Alòs, J., Carreño, P., López, J.A., Estadella, B., Serra-Prat, M., and Marinel-lo, J. (2006). Efficacy and Safety of Sclerotherapy Using Polidocanol Foam: A Controlled Clinical Trial. Eur. J. Vasc. Endovasc. Surg. *31*, 101–107.

4. Alvares, D.S., Viegas, T.G., and Ruggiero Neto, J. (2017). Lipid-packing perturbation of model membranes by pH-responsive antimicrobial peptides. Biophys. Rev. *9*, 669–682.

5. Amaro, M., Reina, F., Hof, M., Eggeling, C., and Sezgin, E. (2017). Laurdan and Di-4-ANEPPDHQ probe different properties of the membrane. J. Phys. Appl. Phys. *50*, 134004.

6. Anderson, J.R., Chiu, D.T., Wu, H., Schueller, O.J., and Whitesides, G.M. (2000). Fabrication of microfluidic systems in poly (dimethylsiloxane). Electrophoresis *21*, 27–40.

7. Baker, B.M., Trappmann, B., Stapleton, S.C., Toro, E., and Chen, C.S. (2013). Microfluidics embedded within extracellular matrix to define vascular architectures and pattern diffusive gradients. Lab. Chip *13*, 3246–3252.

8. Baliyan, V., Tajmir, S., Hedgire, S.S., Ganguli, S., and Prabhakar, A.M. (2016). Lower extremity venous reflux. Cardiovasc. Diagn. Ther. *6*, 533–543.

9. Bertassoni, L.E., Cecconi, M., Manoharan, V., Nikkhah, M., Hjortnaes, J., Cristino, A.L., Barabaschi, G., Demarchi, D., Dokmeci, M.R., Yang, Y., et al. (2014). Hydrogel bioprinted microchannel networks for vascularization of tissue engineering constructs. Lab Chip *14*, 2202–2211.

10. Bhadriraju, K., and Chen, C.S. (2002). Engineering cellular microenvironments to improve cell-based drug testing. Drug Discov. Today *7*, 612–620.

11. Bhise, N.S., Manoharan, V., Massa, S., Tamayol, A., Ghaderi, M., Miscuglio, M., Lang, Q., Shrike Zhang, Y., Shin, S.R., Calzone, G., et al. (2016). A liver-on-a-chip platform with bioprinted hepatic spheroids. Biofabrication *8*, 14101.

12. Bigi, A., Cojazzi, G., Panzavolta, S., Rubini, K., and Roveri, N. (2001). Mechanical and thermal properties of gelatin films at different degrees of glutaraldehyde crosslinking. Biomaterials *22*, 763–768.

13. Bikerman, J.J. (1973). Foams (Berlin, Heidelberg: Springer Berlin Heidelberg).

14. Billiet, T., Vandenhaute, M., Schelfhout, J., Van Vlierberghe, S., and Dubruel, P. (2012a). A review of trends and limitations in hydrogel-rapid prototyping for tissue engineering. Biomaterials *33*, 6020–6041.

15. Bodas, D., and Khan-Malek, C. (2007). Hydrophilization and hydrophobic recovery of PDMS by oxygen plasma and chemical treatment—An SEM investigation. Sens. Actuators B Chem. *123*, 368–373.

16. Booth, R., Noh, S., and Kim, H. (2014). A multiple-channel, multiple-assay platform for characterization of full-range shear stress effects on vascular endothelial cells. Lab. Chip *14*, 1880.

17. Bountouroglou, D.G., Azzam, M., Kakkos, S.K., Pathmarajah, M., Young, P., and Geroulakos, G. (2006). Ultrasound-guided Foam Sclerotherapy Combined with Sapheno-femoral Ligation Compared to Surgical Treatment of Varicose Veins: Early Results of a Randomised Controlled Trial. Eur. J. Vasc. Endovasc. Surg. *31*, 93–100.

18. Braccini, I., and Pérez, S. (2001). Molecular Basis of Ca^{2+} -Induced Gelation in Alginates and Pectins: The Egg-Box Model Revisited. Biomacromolecules *2*, 1089–1096.

19. Bradbury, A., Evans, C., Allan, P., Lee, A., Ruckley, C.V., and Fowkes, F.G.R. (1999). What are the symptoms of varicose veins? Edinburgh vein study cross sectional population survey. Bmj *318*, 353–356.

20. Brittenden, J., Cotton, S.C., Elders, A., Ramsay, C.R., Norrie, J., Burr, J., Campbell, B., Bachoo, P., Chetter, I., Gough, M., et al. (2014). A Randomized Trial Comparing Treatments for Varicose Veins. N. Engl. J. Med. *371*, 1218–1227.

21. Buchanan, C.F., Voigt, E.E., Szot, C.S., Freeman, J.W., Vlachos, P.P., and Rylander, M.N. (2013b). Three-dimensional microfluidic collagen hydrogels for investigating flow-mediated tumor-endothelial signaling and vascular organization. Tissue Eng. Part C Methods *20*, 64–75.

22. Buchanan, C.F., Verbridge, S.S., Vlachos, P.P., and Rylander, M.N. (2014). Flow shear stress regulates endothelial barrier function and expression of angiogenic factors in a 3D microfluidic tumor vascular model. Cell Adhes. Migr. *8*, 517–524.

23. Bush, R., and Bush, P. (2017). Evaluation of sodium tetradecyl sulfate and polidocanol as sclerosants for leg telangiectasia based on histological evaluation with clinical correlation. Phlebol. J. Venous Dis. *32*, 496–500.

24. Caliari, S.R., and Burdick, J.A. (2016). A practical guide to hydrogels for cell culture. Nat. Methods *13*, 405.

25. Campbell, B. (2006). Varicose veins and their management. BMJ *333*, 287.

26. Carugo, D., Ankrett, D.N., O'Byrne, V., Wright, D.D.I., Lewis, A.L., Hill, M., and Zhang, X. (2015). The role of clinically-relevant parameters on the cohesiveness of sclerosing foams in a biomimetic vein model. J. Mater. Sci. Mater. Med. *26*.

27. Carugo, D., Ankrett, D.N., Zhao, X., Zhang, X., Hill, M., O'Byrne, V., Hoad, J., Arif, M., Wright, D.D., and Lewis, A.L. (2016). Benefits of polidocanol endovenous microfoam (Varithena®) compared with physician-compounded foams. Phlebology *31*, 283–295.

28. Carugo, D., Aron, M., Sezgin, E., Bernardino de la Serna, J., Kuimova, M.K., Eggeling, C., and Stride, E. (2017). Modulation of the molecular arrangement in artificial and biological membranes by phospholipid-shelled microbubbles. Biomaterials *113*, 105–117.

29. Cavezzi, A., and Tessari, L. (2009). Foam sclerotherapy techniques: different gases and methods of preparation, catheter versus direct injection. Phlebology *24*, 247–251.

30. Ceulen, R.P., Sommer, A., and Vernooy, K. (2008). Microembolism during foam sclerotherapy of varicose veins. N. Engl. J. Med. *358*, 1525–1526.

31. Cha, C., Kohman, R.H., and Kong, H. (2009). Biodegradable Polymer Crosslinker: Independent Control of Stiffness, Toughness, and Hydrogel Degradation Rate. Adv. Funct. Mater. *19*, 3056–3062.

32. Chan, J.M., Wong, K.H., Richards, A.M., and Drum, C.L. (2015). Microengineering in cardiovascular research: new developments and translational applications. Cardiovasc. Res. *106*, 9–18.

33. Chan, L.W., Lee, H.Y., and Heng, P.W.S. (2006). Mechanisms of external and internal gelation and their impact on the functions of alginate as a coat and delivery system. Carbohydr. Polym. *63*, 176–187.

34. Chen, L.-J., and Kaji, H. (2017). Modeling angiogenesis with micro- and nanotechnology. Lab. Chip *17*, 4186–4219.

35. Chiu, J.-J., and Chien, S. (2011). Effects of Disturbed Flow on Vascular Endothelium: Pathophysiological Basis and Clinical Perspectives. Physiol. Rev. *91*, 327–387.

36. Choi, J.S., Piao, Y., and Seo, T.S. (2013). Fabrication of a circular PDMS microchannel for constructing a three-dimensional endothelial cell layer. Bioprocess Biosyst. Eng. *36*, 1871–1878.

37. Chrobak, K.M., Potter, D.R., and Tien, J. (2006a). Formation of perfused, functional microvascular tubes in vitro. Microvasc. Res. *71*, 185–196.

38. Chung, S., Sudo, R., Mack, P.J., Wan, C.-R., Vickerman, V., and Kamm, R.D. (2009). Cell migration into scaffolds under co-culture conditions in a microfluidic platform. Lab Chip *9*, 269–275.

39. Cohen-Addad, S., Höhler, R., and Pitois, O. (2013). Flow in Foams and Flowing Foams. Annu. Rev. Fluid Mech. *45*, 241–267.

40. Connor, D.E., Cooley-Andrade, O., Goh, W.X., Ma, D.D.F., and Parsi, K. (2015). Detergent Sclerosants are Deactivated and Consumed by Circulating Blood Cells. Eur. J. Vasc. Endovasc. Surg. *49*, 426–431.

41. Cooper, D.G., Hillman-Cooper, C.S., Barker, S.G.E., and Hollingsworth, S.J. (2003). Primary varicose veins: The sapheno-femoral junction, distribution of varicosities and patterns of incompetence. Eur. J. Vasc. Endovasc. Surg. *25*, 53–59.

42. Dalsing, M.C., Ricotta, J.J., Wakefield, T., Lynch, T.G., and Ouriel, K. (1998). Animal Models for the Study of Lower Extremity Chronic Venous Disease: Lessons Learned and Future Needs. Ann. Vasc. Surg. *12*, 487–494.

43. DeLaney, M.C., Bowe, C.T., and Higgins, G.L. (2010). Acute stroke from air embolism after leg sclerotherapy. West. J. Emerg. Med. *11*.

44. Deligkaris, K., Tadele, T.S., Olthuis, W., and van den Berg, A. (2010). Hydrogel-based devices for biomedical applications. Sens. Actuators B Chem. *147*, 765–774.

45. Denayer, T., Stöhr, T., and Van Roy, M. (2014). Animal models in translational medicine: Validation and prediction. New Horiz. Transl. Med. *2*, 5–11.

46. Diaz Jose A., Saha Prakash, Cooley Brian, Palmer Olivia R., Grover Steven P., Mackman Nigel, Wakefield Thomas W., Henke Peter K., Smith Alberto, and Lal

Brajesh K. (2019). Choosing a Mouse Model of Venous Thrombosis. Arterioscler. Thromb. Vasc. Biol. *39*, 311–318.

47. Dietzek, C.L. (2007). Sclerotherapy: Introduction to Solutions and Techniques. Perspect. Vasc. Surg. Endovasc. Ther. *19*, 317–324.

48. DiMasi, J.A., Feldman, L., Seckler, A., and Wilson, A. (2010). Trends in Risks Associated With New Drug Development: Success Rates for Investigational Drugs. Clin. Pharmacol. Ther. *87*, 272–277.

49. Dinic, J., Biverståhl, H., Mäler, L., and Parmryd, I. (2011). Laurdan and di-4-ANEPPDHQ do not respond to membrane-inserted peptides and are good probes for lipid packing. Biochim. Biophys. Acta BBA - Biomembr. *1808*, 298–306.

50. Djabourov, M., and Leblond, J. (1987). Thermally Reversible Gelation of the Gelatin-Water System. In Reversible Polymeric Gels and Related Systems, P.S. Russo, ed. (Washington, DC: American Chemical Society), pp. 211–223.

51. Doke, S.K., and Dhawale, S.C. (2015). Alternatives to animal testing: A review. Saudi Pharm. J. *23*, 223–229.

52. Du, Y., Ghodousi, M., Qi, H., Haas, N., Xiao, W., and Khademhosseini, A. (2011). Sequential assembly of cell-laden hydrogel constructs to engineer vascular-like microchannels. Biotechnol. Bioeng. *108*, 1693–1703.

53. DuRaine, G.D., Brown, W.E., Hu, J.C., and Athanasiou, K.A. (2015). Emergence of scaffold-free approaches for tissue engineering musculoskeletal cartilages. Ann. Biomed. Eng. *43*, 543–554.

54. Eckmann, D.M. (2009). Polidocanol for endovenous microfoam sclerosant therapy. Expert Opin. Investig. Drugs *18*, 1919–1927.

55. Eckmann, D.M., Kobayashi, S., and Li, M. (2005). Microvascular Embolization Following Polidocanol Microfoam Sclerosant Administration. Dermatol. Surg. *31*, 636–643.

56. Eklöf, B., Rutherford, R.B., Bergan, J.J., Carpentier, P.H., Gloviczki, P., Kistner, R.L., Meissner, M.H., Moneta, G.L., Myers, K., Padberg, F.T., et al. (2004). Revision of the CEAP classification for chronic venous disorders: Consensus statement. J. Vasc. Surg. *40*, 1248–1252.

57. Elmore, S. (2007). Apoptosis: a review of programmed cell death. Toxicol. Pathol. *35*, 495–516.

58. Erkin, A., Kosemehmetoglu, K., Diler, M.S., and Koksal, C. (2012). Evaluation of the Minimum Effective Concentration of Foam Sclerosant in an Ex-vivo Study. Eur. J. Vasc. Endovasc. Surg. *44*, 593–597.

59. Esch, E.W., Bahinski, A., and Huh, D. (2015). Organs-on-chips at the frontiers of drug discovery. Nat. Rev. Drug Discov. *14*, 248.

60. Esch, M.B., Post, D.J., Shuler, M.L., and Stokol, T. (2011). Characterization of in vitro endothelial linings grown within microfluidic channels. Tissue Eng. Part A *17*, 2965–2971.

61. Fernández, E., López, D., Mijangos, C., Duskova-Smrckova, M., Ilavsky, M., and Dusek, K. (2008). Rheological and thermal properties of agarose aqueous solutions and hydrogels. J. Polym. Sci. Part B Polym. Phys. *46*, 322–328.

62. Gao, Q., Liu, Z., Lin, Z., Qiu, J., Liu, Y., Liu, A., Wang, Y., Xiang, M., Chen, B., Fu, J., et al. (2017). 3D Bioprinting of Vessel-like Structures with Multilevel Fluidic Channels. ACS Biomater. Sci. Eng. *3*, 399–408.

63. Gelber, M.K., and Bhargava, R. (2015). Monolithic multilayer microfluidics via sacrificial molding of 3D-printed isomalt. Lab. Chip *15*, 1736–1741.

64. Genovese, G. (2002). Venous anatomy of the lower limb. Soc. Ital. Flebol.

65. Gillet, J.-L., Guedes, J.M., Guex, J.-J., Hamel-Desnos, C., Schadeck, M., Lauseker, M., and Allaert, F.A. (2009). Side-effects and complications of foam sclerotherapy of the great and small saphenous veins: a controlled multicentre prospective study including 1025 patients. Phlebology *24*, 131–138.

66. Gius, J.A. (1960). Arteriovenous Anastomoses and Varicose Veins: Observations with the Operation Microscope. Arch. Surg. *81*, 299–310.

67. Gloviczki, P., Comerota, A.J., Dalsing, M.C., Eklof, B.G., Gillespie, D.L., Gloviczki, M.L., Lohr, J.M., McLafferty, R.B., Meissner, M.H., Murad, M.H., et al. (2011). The care of patients with varicose veins and associated chronic venous diseases: Clinical practice guidelines of the Society for Vascular Surgery and the American Venous Forum. J. Vasc. Surg. *53*, 2S–48S.

68. Golden, A.P., and Tien, J. (2007). Fabrication of microfluidic hydrogels using molded gelatin as a sacrificial element. Lab. Chip *7*, 720.

69. Goldman, M.P., Weiss, R.A., and Guex, J.-J. (2017). Sclerotherapy: treatment of varicose and telangiectatic leg veins.

70. Gómez-Sjöberg, R., Leyrat, A.A., Pirone, D.M., Chen, C.S., and Quake, S.R. (2007). Versatile, Fully Automated, Microfluidic Cell Culture System. Anal. Chem. *79*, 8557–8563.

71. Groot, R.D., and Rabone, K.L. (2001). Mesoscopic Simulation of Cell Membrane Damage, Morphology Change and Rupture by Nonionic Surfactants. Biophys. J. *81*, 725–736.

72. Gu, T., and Sjöblom, J. (1992). Surfactant structure and its relation to the Krafft point, cloud point and micellization: Some empirical relationships. Colloids Surf. *64*, 39–46.

73. Gumuscu, B., Bomer, J.G., van den Berg, A., and Eijkel, J.C.T. (2015). Photopatterning of Hydrogel Microarrays in Closed Microchips. Biomacromolecules *16*, 3802–3810.

74. Hamel-Desnos, C., Desnos, P., Wollmann, J.-C., Ouvry, P., Mako, S., and Allaert, F.-A. (2003). Evaluation of the efficacy of polidocanol in the form of foam compared with liquid form in sclerotherapy of the greater saphenous vein: initial results. Dermatol. Surg. *29*, 1170–1175.

75. Hattori, K., Munehira, Y., Kobayashi, H., Satoh, T., Sugiura, S., and Kanamori, T. (2014). Microfluidic perfusion culture chip providing different strengths of shear stress for analysis of vascular endothelial function. J. Biosci. Bioeng. *118*, 327–332.

76. Heerklotz, H. (2008b). Interactions of surfactants with lipid membranes. Q. Rev. Biophys. *41*, 205–264.

77. Herbert, S.P., and Stainier, D.Y.R. (2011). Molecular control of endothelial cell behaviour during blood vessel morphogenesis. Nat. Rev. Mol. Cell Biol. *12*, 551–564.

78. Hoque, M.E., Nuge, T., Yeow, T.K., Nordin, N., and Prasad, R. (2015). Gelatin based scaffolds for tissue engineering-A review. Polym. Res. J. *9*, 15.

79. Hua, X.Y., and Rosen, M.J. (1991). Dynamic surface tension of aqueous surfactant solutions: 3. Some effects of molecular structure and environment. J. Colloid Interface Sci. *141*, 180–190.

80. Huang, T.-W., Chen, S.-L., Bai, C.-H., Wu, C.-H., and Tam, K.-W. (2013). The Optimal Duration of Compression Therapy Following Varicose Vein Surgery: A Meta-analysis of Randomized Controlled Trials. Eur. J. Vasc. Endovasc. Surg. *45*, 397–402.

81. Huh, D., Hamilton, G.A., and Ingber, D.E. (2011). From 3D cell culture to organs-on-chips. Trends Cell Biol. *21*, 745–754.

82. Hutmacher, D.W., and Cool, S. (2007). Concepts of scaffold-based tissue engineering?the rationale to use solid free-form fabrication techniques. J. Cell. Mol. Med. *11*, 654–669.

83. Ikponmwosa, A., Abbott, C., Graham, A., Homer-Vanniasinkam, S., and Gough, M.J. (2010). The Impact of Different Concentrations of Sodium Tetradecyl Sulphate and Initial Balloon Denudation on Endothelial Cell Loss and Tunica Media Injury in a Model of Foam Sclerotherapy. Eur. J. Vasc. Endovasc. Surg. *39*, 366–371.

84. Irodi, A., Keshava, S.N., Agarwal, S., Korah, I.P., and Sadhu, D. (2011). Ultrasound Doppler evaluation of the pattern of involvement of varicose veins in Indian patients. Indian J. Surg. *73*, 125–130.

85. Ives, C.L., Eskin, S.G., and McIntire, L.V. (1986). Mechanical effects on endothelial cell morphology: in vitro assessment. Vitro Cell. Dev. Biol.-Plant *22*, 500–507.

86. Jain, A., van der Meer, A.D., Papa, A.-L., Barrile, R., Lai, A., Schlechter, B.L., Otieno, M.A., Louden, C.S., Hamilton, G.A., Michelson, A.D., et al. (2016). Assessment of whole blood thrombosis in a microfluidic device lined by fixed human endothelium. Biomed. Microdevices *18*.

87. Jain, A., Barrile, R., van der Meer, A.D., Mammoto, A., Mammoto, T., De Ceunynck, K., Aisiku, O., Otieno, M.A., Louden, C.S., Hamilton, G.A., et al. (2018). Primary Human Lung Alveolus-on-a-chip Model of Intravascular Thrombosis for Assessment of Therapeutics. Clin. Pharmacol. Ther. *103*, 332–340.

88. Jain, E., Hill, L., Canning, E., Sell, S.A., and Zustiak, S.P. (2017). Control of gelation, degradation and physical properties of polyethylene glycol hydrogels through the chemical and physical identity of the crosslinker. J. Mater. Chem. B *5*, 2679–2691.

89. Jia, X., Mowatt, G., Burr, J.M., Cassar, K., Cook, J., and Fraser, C. (2007). Systematic review of foam sclerotherapy for varicose veins. Br. J. Surg. *94*, 925–936.

90. Jin, L., Millard, A.C., Wuskell, J.P., Clark, H.A., and Loew, L.M. (2005). Cholesterol-Enriched Lipid Domains Can Be Visualized by di-4-ANEPPDHQ with Linear and Nonlinear Optics. Biophys. J. *89*, L04–L06.

91. Jones, M.N. (1992). Surfactant interactions with biomembranes and proteins.

Chem. Soc. Rev. *21*, 127.

92. Jones, G.T., Grant, M.W., Thomson, I.A., Hill, B.G., and van Rij, A.M. (2009). Characterization of a porcine model of chronic superficial varicose veins. J. Vasc. Surg. *49*, 1554–1561.

93. Kaklamani, G., Cheneler, D., Grover, L.M., Adams, M.J., and Bowen, J. (2014). Mechanical properties of alginate hydrogels manufactured using external gelation. J. Mech. Behav. Biomed. Mater. *36*, 135–142.

94. Kendler, M., Fellmer, P.T., and Wetzig, T. (2012). Varicose vein surgery. JDDG J. Dtsch. Dermatol. Ges. *10*, 157–164.

95. Kendler, M., Averbeck, M., Simon, J.C., and Ziemer, M. (2013). Histology of saphenous veins after treatment with the ClariVein® device - an ex-vivo experiment: Histology ClariVein. JDDG J. Dtsch. Dermatol. Ges. *11*, 348–352.

96. Kent, P.J., Maughan, J., Burniston, M., Nicholas, T., Parkin, A., and Robinson, P.J. (1999). Perforation-Invagination (PIN) Stripping of the Long Saphenous Vein Reduces Thigh Haematoma Formation in Varicose Vein Surgery. Phlebology *14*, 43–47.

97. Kim, S., Lee, H., Chung, M., and Jeon, N.L. (2013). Engineering of functional, perfusable 3D microvascular networks on a chip. Lab. Chip *13*, 1489.

98. Kimlin, L., Kassis, J., and Virador, V. (2013). 3D *in vitro* tissue models and their potential for drug screening. Expert Opin. Drug Discov. *8*, 1455–1466.

99. Kobayashi, S., Crooks, S., and Eckmann, D.M. (2006). Dose- and Time-Dependent Liquid Sclerosant Effects on Endothelial Cell Death. Dermatol. Surg. *32*, 1444–1452.

100. Koehler, S.A., Hilgenfeldt, S., and Stone, H.A. (2000). A Generalized View of Foam Drainage: Experiment and Theory. Langmuir *16*, 6327–6341.

101. Kong, H.J., Kaigler, D., Kim, K., and Mooney, D.J. (2004). Controlling Rigidity and Degradation of Alginate Hydrogels via Molecular Weight Distribution. Biomacromolecules *5*, 1720–1727.

102. Krijnen, R.M., de Boer, E.M., and Bruynzeel, D.P. (1997). Epidemiology of venous disorders in the general and occupational populations. Skin *11*, 29.

103. Kuni, F.M., Shchekin, A.K., Rusanov, A.I., and Grinin, A.P. (2004). Concentrations of Monomers and Cylindrical Micelles above the Second CMC.

Colloid J. *66*, 174–185.

104. Kühbeck, D., Mayr, J., Häring, M., Hofmann, M., Quignard, F., and Díaz Díaz, D. (2015). Evaluation of the nitroaldol reaction in the presence of metal ion-crosslinked alginates. New J. Chem. *39*, 2306–2315.

105. Lee, K.Y., and Mooney, D.J. (2012). Alginate: Properties and biomedical applications. Prog. Polym. Sci. *37*, 106–126.

106. Lee, V.K., Kim, D.Y., Ngo, H., Lee, Y., Seo, L., Yoo, S.-S., Vincent, P.A., and Dai, G. (2014). Creating perfused functional vascular channels using 3D bio-printing technology. Biomaterials *35*, 8092–8102.

107. Lee, W., Lee, V., Polio, S., Keegan, P., Lee, J.-H., Fischer, K., Park, J.-K., and Yoo, S.-S. (2010). On-demand three-dimensional freeform fabrication of multi-layered hydrogel scaffold with fluidic channels. Biotechnol. Bioeng. n/a-n/a.

108. Li, L.-M., Wang, X.-Y., Hu, L.-S., Chen, R.-S., Huang, Y., Chen, S.-J., Huang, W.-H., Huo, K.-F., and Chu, P.K. (2012). Vascular lumen simulation and highly-sensitive nitric oxide detection using three-dimensional gelatin chip coupled to TiC/C nanowire arrays microelectrode. Lab. Chip *12*, 4249.

109. Ling, Y., Rubin, J., Deng, Y., Huang, C., Demirci, U., Karp, J.M., and Khademhosseini, A. (2007a). A cell-laden microfluidic hydrogel. Lab. Chip *7*, 756.

110. Linville, R.M., Boland, N.F., Covarrubias, G., Price, G.M., and Tien, J. (2016). Physical and Chemical Signals That Promote Vascularization of Capillary-Scale Channels. Cell. Mol. Bioeng. *9*, 73–84.

111. Liu, B., Liu, Y., Lewis, A.K., and Shen, W. (2010). Modularly assembled porous cell-laden hydrogels. Biomaterials *31*, 4918–4925.

112. Liu, J., Zheng, H., Poh, P., Machens, H.-G., and Schilling, A. (2015). Hydrogels for Engineering of Perfusable Vascular Networks. Int. J. Mol. Sci. *16*, 15997–16016.

113. Liu, J.-J., Fan, L.-H., Xu, D.-C., Li, X., Dong, Z.-H., and Fu, W.-G. (2016). The endovenous laser treatment for patients with varicose veins. Pak. J. Med. Sci. *32*, 55–58.

114. Lupo, B., Maestro, A., Porras, M., Gutiérrez, J.M., and González, C. (2014). Preparation of alginate microspheres by emulsification/internal gelation to encapsulate cocoa polyphenols. Food Hydrocoll. *38*, 56–65.

115. Mak, I.W., Evaniew, N., and Ghert, M. (2014). Lost in translation: animal models

and clinical trials in cancer treatment. Am. J. Transl. Res. *6*, 114.

116. Mandrycky, C., Wang, Z., Kim, K., and Kim, D.-H. (2016). 3D bioprinting for engineering complex tissues. Biotechnol. Adv. *34*, 422–434.

117. Manneschi, C., Pereira, R.C., Marinaro, G., Bosca, A., Francardi, M., and Decuzzi, P. (2016). A microfluidic platform with permeable walls for the analysis of vascular and extravascular mass transport. Microfluid. Nanofluidics *20*.

118. Maschmeyer, I., Lorenz, A.K., Schimek, K., Hasenberg, T., Ramme, A.P., Hübner, J., Lindner, M., Drewell, C., Bauer, S., Thomas, A., et al. (2015). A four-organ-chip for interconnected long-term co-culture of human intestine, liver, skin and kidney equivalents. Lab Chip *15*, 2688–2699.

119. Mata, A., Fleischman, A.J., and Roy, S. (2005). Characterization of polydimethylsiloxane (PDMS) properties for biomedical micro/nanosystems. Biomed. Microdevices *7*, 281–293.

120. Mazurek, R., Dave, J.M., Chandran, R.R., Misra, A., Sheikh, A.Q., and Greif, D.M. (2017). Vascular Cells in Blood Vessel Wall Development and Disease. In Advances in Pharmacology, (Elsevier), pp. 323–350.

121. McAree, B., Ikponmwosa, A., Brockbank, K., Abbott, C., Homer-Vanniasinkam, S., and Gough, M.J. (2012). Comparative Stability of Sodium Tetradecyl Sulphate (STD) and Polidocanol Foam: Impact on Vein Damage in an In-vitro Model. Eur. J. Vasc. Endovasc. Surg. *43*, 721–725.

122. McGuigan, A.P., and Sefton, M.V. (2006). Vascularized organoid engineered by modular assembly enables blood perfusion. Proc. Natl. Acad. Sci. *103*, 11461–11466.

123. Meer, B.J., de Vries, H., Firth, K.S.A., van Weerd, J., Tertoolen, L.G.J., Karperien, H.B.J., Jonkheijm, P., Denning, C., IJzerman, A.P., and Mummery, C.L. (2017). Small molecule absorption by PDMS in the context of drug response bioassays. Biochem. Biophys. Res. Commun. *482*, 323–328.

124. Meer, G., Voelker, D.R., and Feigenson, G.W. (2008). Membrane lipids: where they are and how they behave. Nat. Rev. Mol. Cell Biol. *9*, 112–124.

125. Meissner, M.H. (2005). Lower extremity venous anatomy. In Seminars in Interventional Radiology, (Copyright\copyright 2005 by Thieme Medical Publishers, Inc., 333 Seventh Avenue, New York, NY 10001, USA.), pp. 147–156.

126. Messas, E., Pernot, M., and Couade, M. (2013). Arterial wall elasticity: State of the

art and future prospects. Diagn. Interv. Imaging *94*, 561–569.

127. Michael Balls (2010). The principles of humane experimental technique: timeless insights and unheeded warnings. ALTEX - Altern. Anim. Exp. *27*.

128. Miller, A., Lilach, N., Miller, R., and Kabnick, L. (2017). A preclinical animal study of a novel, simple, and secure percutaneous vessel occluder for the treatment of varicose veins. J. Vasc. Surg. Venous Lymphat. Disord. *5*, 114–120.

129. Mol, W., Furukawa, H., Sasaki, S., Tomaru, U., Hayashi, T., Saito, A., Nagao, M., Saito, N., Hata, S., and Yamamoto, Y. (2007). Evaluation of the Sclerotherapeutic Efficacy of Ethanol, Polidocanol, and OK-432 Using an In Vitro Model. Dermatol. Surg. *0*, 071009211231009.

130. Murad, M.H., Coto-Yglesias, F., Zumaeta-Garcia, M., Elamin, M.B., Duggirala, M.K., Erwin, P.J., Montori, V.M., and Gloviczki, P. (2011). A systematic review and meta-analysis of the treatments of varicose veins. J. Vasc. Surg. *53*, 49S–65S.

131. Murphy, S.V., and Atala, A. (2014). 3D bioprinting of tissues and organs. Nat. Biotechnol. *32*, 773–785.

132. Naahidi, S., Jafari, M., Logan, M., Wang, Y., Yuan, Y., Bae, H., Dixon, B., and Chen, P. (2017). Biocompatibility of hydrogel-based scaffolds for tissue engineering applications. Biotechnol. Adv. *35*, 530–544.

133. Napolitano, A., Dean, D., Man, A., Youssef, J., Ho, D., Rago, A., Lech, M., and Morgan, J. (2007). Scaffold-free three-dimensional cell culture utilizing micromolded nonadhesive hydrogels. BioTechniques *43*, 494–500.

134. Nastasa, V., Samaras, K., Ampatzidis, C., Karapantsios, T.D., Trelles, M.A., Moreno-Moraga, J., Smarandache, A., and Pascu, M.L. (2015). Properties of polidocanol foam in view of its use in sclerotherapy. Int. J. Pharm. *478*, 588–596.

135. Necas, M. (2010). Duplex ultrasound in the assessment of lower extremity venous insufficiency. Australas. J. Ultrasound Med. *13*, 37–45.

136. Norotte, C., Marga, F.S., Niklason, L.E., and Forgacs, G. (2009). Scaffold-free vascular tissue engineering using bioprinting. Biomaterials *30*, 5910–5917.

137. Noutsi, P., Gratton, E., and Chaieb, S. (2016). Assessment of Membrane Fluidity Fluctuations during Cellular Development Reveals Time and Cell Type Specificity. PLOS ONE *11*, e0158313.

138. Ohkubo, T., Kinoshita, H., Maekawa, T., Kunida, K., Kimura, H., Kuroda, S.,

and Fujii, T. (2018). Development of a microfluidic cell culture and monitoring system for intracellular signaling studies. bioRxiv 453100.

139. Ombrellino, M., and Kabnick, L.S. (2005). Varicose vein surgery. In Seminars in Interventional Radiology, (Copyright\copyright 2005 by Thieme Medical Publishers, Inc., 333 Seventh Avenue, New York, NY 10001, USA.), pp. 185–194.

140. O'Neill, R., McCarthy, H.O., Montufar, E.B., Ginebra, M.-P., Wilson, D.I., Lennon, A., and Dunne, N. (2017). Critical review: Injectability of calcium phosphate pastes and cements. Acta Biomater. *50*, 1–19.

141. Orsini, C., and Brotto, M. (2007). Immediate Pathologic Effects on the Vein Wall of Foam Sclerotherapy. Dermatol. Surg. *33*, 1250–1254.

142. Owen, D.M., Rentero, C., Magenau, A., Abu-Siniyeh, A., and Gaus, K. (2012). Quantitative imaging of membrane lipid order in cells and organisms. Nat. Protoc. *7*, 24–35.

143. Pal, S. (2014). Mechanical Properties of Biological Materials. In Design of Artificial Human Joints & Organs, (Boston, MA: Springer US), pp. 23–40.

144. Pang, Z., Al-Mahrouki, A., Berezovski, M., and Krylov, S.N. (2006). Selection of surfactants for cell lysis in chemical cytometry to study protein-DNA interactions. ELECTROPHORESIS *27*, 1489–1494.

145. Parasassi, T., De Stasio, G., Ravagnan, G., Rusch, R.M., and Gratton, E. (1991). Quantitation of lipid phases in phospholipid vesicles by the generalized polarization of Laurdan fluorescence. Biophys. J. *60*, 179–189.

146. Parasassi, T., Krasnowska, E.K., Bagatolli, L., and Gratton, E. (1998). Laurdan and Prodan as polarity-sensitive fluorescent membrane probes. J. Fluoresc. *8*, 365–373.

147. Parsi, K. (2014). Interaction of detergent sclerosants with cell membranes. Phlebology *30*, 306–315.

148. Parsi, K., Exner, T., Connor, D.E., Ma, D.D.F., and Joseph, J.E. (2007). In Vitro Effects of Detergent Sclerosants on Coagulation, Platelets and Microparticles. Eur. J. Vasc. Endovasc. Surg. *34*, 731–740.

149. Parsi, K., Exner, T., Connor, D.E., Herbert, A., Ma, D.D.F., and Joseph, J.E. (2008). The Lytic Effects of Detergent Sclerosants on Erythrocytes, Platelets, Endothelial Cells and Microparticles are Attenuated by Albumin and other Plasma Components in Vitro. Eur. J. Vasc. Endovasc. Surg. *36*, 216–223.

150. Partearroyo, M.A., Ostolaza, H., Goñi, F.M., and Barberá-Guillem, E. (1990). Surfactant-induced cell toxicity and cell lysis: a study using B16 melanoma cells. Biochem. Pharmacol. *40*, 1323–1328.

151. Pascarella, L., Schmid-Schönbein, G.W., and Bergan, J. (2005). An animal model of venous hypertension: The role of inflammation in venous valve failure. J. Vasc. Surg. *41*, 303–311.

152. Peterson, J.D., and Goldman, M.P. (2011). An Investigation into the Influence of Various Gases and Concentrations of Sclerosants on Foam Stability: Dermatol. Surg. *37*, 12–17.

153. Peterson, J.D., and Goldman, M.P. (2012). An investigation of side-effects and efficacy of foam-based sclerotherapy with carbon dioxide or room air in the treatment of reticular leg veins: a pilot study. Phlebol. J. Venous Dis. *27*, 73–76.

154. Phan, C.M. (2018). Chapter 4 - Ionization of Surfactants at the Air–Water Interface. In Physical Chemistry of Gas-Liquid Interfaces, J.A. Faust, and J.E. House, eds. (Elsevier), pp. 79–104.

155. Piazza, G. (2014). Varicose Veins. Circulation *130*, 582–587.

156. Poder, T.G., Fisette, J.-F., Bédard, S.K., and Despatis, M.-A. (2018). Is radiofrequency ablation of varicose veins a valuable option? A systematic review of the literature with a cost analysis. Can. J. Surg. J. Can. Chir. *61*, 128–138.

157. Polacheck, W.J., Li, R., Uzel, S.G.M., and Kamm, R.D. (2013). Microfluidic platforms for mechanobiology. Lab. Chip *13*, 2252–2267.

158. Pukacki, F., Jankowski, T., Gabriel, M., Oszkinis, G., Krasinski, Z., and Zapalski, S. (2000). The Mechanical Properties of Fresh and Cryopreserved Arterial Homografts. Eur. J. Vasc. Endovasc. Surg. *20*, 21–24.

159. Qin, D., Xia, Y., and Whitesides, G.M. (2010). Soft lithography for micro- and nanoscale patterning. Nat. Protoc. *5*, 491–502.

160. Quinn, P.J., and Wolf, C. (2009). The liquid-ordered phase in membranes. Biochim. Biophys. Acta BBA - Biomembr. *1788*, 33–46.

161. Rangamani, P., Lipshtat, A., Azeloglu, E.U., Calizo, R.C., Hu, M., Ghassemi, S., Hone, J., Scarlata, S., Neves, S.R., and Iyengar, R. (2013). Decoding Information in Cell Shape. Cell *154*, 1356–1369.

162. Rao, J., and Goldman, M.P. (2005). Stability of Foam in Sclerotherapy:

Differences between Sodium Tetradecyl Sulfate and Polidocanol and the Type of Connector Used in the Double-Syringe System Technique. Dermatol. Surg. *31*, 19–22.

163. Rasmussen, L.H., Lawaetz, M., Bjoern, L., Vennits, B., Blemings, A., and Eklof, B. (2011). Randomized clinical trial comparing endovenous laser ablation, radiofrequency ablation, foam sclerotherapy and surgical stripping for great saphenous varicose veins. Br. J. Surg. *98*, 1079–1087.

164. Raven, K. (2012). Study finds up to $5 billion in potential trial cost savings. Nat. Med. *18*, 1159–1159.

165. Rouillard, A.D., Berglund, C.M., Lee, J.Y., Polacheck, W.J., Tsui, Y., Bonassar, L.J., and Kirby, B.J. (2011). Methods for Photocrosslinking Alginate Hydrogel Scaffolds with High Cell Viability. Tissue Eng. Part C Methods *17*, 173–179.

166. Šachl, R., Štěpánek, M., Procházka, K., Humpolíčková, J., and Hof, M. (2008). Fluorescence Study of the Solvation of Fluorescent Probes Prodan and Laurdan in Poly(ε-caprolactone)-block-poly(ethylene oxide) Vesicles in Aqueous Solutions with Tetrahydrofurane. Langmuir *24*, 288–295.

167. Saint-Jalmes, A. (2006). Physical chemistry in foam drainage and coarsening. Soft Matter *2*, 836.

168. Saint-Jalmes, A., Vera, M.U., and Durian, D.J. (1999). Uniform foam production by turbulent mixing: new results on free drainage vs. liquid content. Eur. Phys. J. B-Condens. Matter Complex Syst. *12*, 67–73.

169. Sato, M., Sasaki, N., Ato, M., Hirakawa, S., Sato, K., and Sato, K. (2015). Microcirculation-on-a-Chip: A Microfluidic Platform for Assaying Blood- and Lymphatic-Vessel Permeability. PLOS ONE *10*, e0137301.

170. Schneider, G.B., English, A., Abraham, M., Zaharias, R., Stanford, C., and Keller, J. (2004). The effect of hydrogel charge density on cell attachment. Biomaterials *25*, 3023–3028.

171. Sell, H., Vikatmaa, P., Albäck, A., Lepäntalo, M., Malmivaara, A., Mahmoud, O., and Venermo, M. (2014). Compression Therapy Versus Surgery in the Treatment of Patients with Varicose Veins: A RCT. Eur. J. Vasc. Endovasc. Surg. *47*, 670–677.

172. Sezgin, E., Sadowski, T., and Simons, K. (2014). Measuring Lipid Packing of Model and Cellular Membranes with Environment Sensitive Probes. Langmuir *30*, 8160–8166.

173. Sezgin, E., Waithe, D., Bernardino de la Serna, J., and Eggeling, C. (2015).

Spectral Imaging to Measure Heterogeneity in Membrane Lipid Packing. ChemPhysChem *16*, 1387–1394.

174. Sheng, J.J. (2011). Chapter 7 - Surfactant Flooding. In Modern Chemical Enhanced Oil Recovery, J.J. Sheng, ed. (Boston: Gulf Professional Publishing), pp. 239–335.

175. Shevkoplyas, S.S., Gifford, S.C., Yoshida, T., and Bitensky, M.W. (2003). Prototype of an in vitro model of the microcirculation. Microvasc. Res. *65*, 132–136.

176. Singer, S.J., and Nicolson, G.L. (1972). The Fluid Mosaic Model of the Structure of Cell Membranes. Science *175*, 720.

177. Smith, P.C. (2009). Foam and liquid sclerotherapy for varicose veins. Phlebology *24*, 62–72.

178. Song, J.W., and Munn, L.L. (2011). Fluid forces control endothelial sprouting. Proc. Natl. Acad. Sci. *108*, 15342–15347.

179. Song, J.W., Bazou, D., and Munn, L.L. (2012). Anastomosis of endothelial sprouts forms new vessels in a tissue analogue of angiogenesis. Integr. Biol. *4*, 857.

180. Spiridon, M., and CORDUNEANU, D. (2017). Chronic venous insufficiency: a frequently underdiagnosed and undertreated pathology. Ma Edica *12*, 59.

181. Staton, C.A., Reed, M.W., and Brown, N.J. (2009). A critical analysis of current in vitro and in vivo angiogenesis assays. Int. J. Exp. Pathol. *90*, 195–221.

182. Su, C.-C., Chen, C.-W., Ho, W.-T., Hu, F.-R., Lee, S.-H., and Wang, I.-J. (2015). Phenotypes of trypsin- and collagenase-prepared bovine corneal endothelial cells in the presence of a selective Rho kinase inhibitor, Y-27632. Mol. Vis. *21*, 633–643.

183. Subramaniam, A., and Sethuraman, S. (2014). Biomedical applications of nondegradable polymers. In Natural and Synthetic Biomedical Polymers, (Elsevier), pp. 301–308.

184. Sukriti, S., Tauseef, M., Yazbeck, P., and Mehta, D. (2014). Mechanisms regulating endothelial permeability. Pulm. Circ. *4*, 535–551.

185. Sumpio, B.E., Riley, J.T., and Dardik, A. (2002). Cells in focus: endothelial cell. Int. J. Biochem. Cell Biol. *34*, 1508–1512.

186. Sun, Y., Qi, X., Sun, H., Zhao, H., and Li, Y. (2016). Understanding about How

Different Foaming Gases Effect the Interfacial Array Behaviors of Surfactants and the Foam Properties. Langmuir *32*, 7503–7511.

187. Surendran, S., Ramegowda, K.S., Suresh, A., Raj, S.B., Lakkappa, R.K.B., Kamalapurkar, G., Radhakrishnan, N., and Kartha, C.C. (2016). Arterialization and anomalous vein wall remodeling in varicose veins is associated with upregulated FoxC2-Dll4 pathway. Lab. Invest. *96*, 399–408.

188. Takei, T., Sakai, S., Ono, T., Ijima, H., and Kawakami, K. (2006). Fabrication of endothelialized tube in collagen gel as starting point for self-developing capillary-like network to construct three-dimensional organs in vitro. Biotechnol. Bioeng. *95*, 1–7.

189. Tessari, L., Cavezzi, A., and Frullini, A. (2001). Preliminary Experience with a New Sclerosing Foam in the Treatment of Varicose Veins. Dermatol. Surg. *27*, 58–60.

190. Tocchio, A., Tamplenizza, M., Martello, F., Gerges, I., Rossi, E., Argentiere, S., Rodighiero, S., Zhao, W., Milani, P., and Lenardi, C. (2015). Versatile fabrication of vascularizable scaffolds for large tissue engineering in bioreactor. Biomaterials *45*, 124–131.

191. Tsai, M., Kita, A., Leach, J., Rounsevell, R., Huang, J.N., Moake, J., Ware, R.E., Fletcher, D.A., and Lam, W.A. (2012). In vitro modeling of the microvascular occlusion and thrombosis that occur in hematologic diseases using microfluidic technology. J. Clin. Invest. *122*, 408–418.

192. Valenzuela, G.C., Wong, K., Connor, D.E., Behnia, M., and Parsi, K. (2013). Foam Sclerosants are More Stable at Lower Temperatures. Eur. J. Vasc. Endovasc. Surg. *46*, 593–599.

193. Van Deurzen, B., Ceulen, R.P., Tellings, S.S., Van Der Geld, C., and Nijsten, T. (2011). Polidocanol Concentration and Time Affect the Properties of Foam Used for Sclerotherapy: Dermatol. Surg. *37*, 1448–1455.

194. Vickerman, V., Blundo, J., Chung, S., and Kamm, R. (2008). Design, fabrication and implementation of a novel multi-parameter control microfluidic platform for three-dimensional cell culture and real-time imaging. Lab. Chip *8*, 1468.

195. Wang, L., Sun, B., Ziemer, K.S., Barabino, G.A., and Carrier, R.L. (2009). Chemical and physical modifications to poly(dimethylsiloxane) surfaces affect adhesion of Caco-2 cells. J. Biomed. Mater. Res. A *9999A*, NA-NA.

196. Watson, H. (2015). Biological membranes. Essays Biochem. *59*, 43–69.

197. Wells, R.G. (2008). The role of matrix stiffness in regulating cell behavior. Hepatology *47*, 1394–1400.

198. Westein, E., van der Meer, A.D., Kuijpers, M.J., Frimat, J.-P., van den Berg, A., and Heemskerk, J.W. (2013). Atherosclerotic geometries exacerbate pathological thrombus formation poststenosis in a von Willebrand factor-dependent manner. Proc. Natl. Acad. Sci. *110*, 1357–1362.

199. Whiteley, M.S., Dos Santos, S.J., Fernandez-Hart, T.J., Lee, C.T.D., and Li, J.M. (2016). Media Damage Following Detergent Sclerotherapy Appears to be Secondary to the Induction of Inflammation and Apoptosis: An Immunohistochemical Study Elucidating Previous Histological Observations. Eur. J. Vasc. Endovasc. Surg. *51*, 421–428.

200. Whiteley, M.S., Dos Santos, S.J., Lee, C.T., and Li, J.-M. (2017). Mechanochemical ablation causes endothelial and medial damage to the vein wall resulting in deeper penetration of sclerosant compared with sclerotherapy alone in extrafascial great saphenous vein using an ex vivo model. J. Vasc. Surg. Venous Lymphat. Disord. *5*, 370–377.

201. Wollmann, J. (2010). Sclerosant foams. Phlebologie *39*, 208–17.

202. Wong, K., Chen, T., Connor, D.E., Behnia, M., and Parsi, K. (2015). Basic physiochemical and rheological properties of detergent sclerosants. Phlebol. J. Venous Dis. *30*, 339–349.

203. Worthington-Kirsch, R.L. (2005). Injection sclerotherapy. Semin. Interv. Radiol. *22*, 209–217.

204. Xiong, J.-Y., Narayanan, J., Liu, X.-Y., Chong, T.K., Chen, S.B., and Chung, T.-S. (2005). Topology Evolution and Gelation Mechanism of Agarose Gel. J. Phys. Chem. B *109*, 5638–5643.

205. Yamaki, T., Nozaki, M., and Iwasaka, S. (2004). Comparative Study of Duplex-Guided Foam Sclerotherapy and Duplex-Guided Liquid Sclerotherapy for the Treatment of Superficial Venous Insufficiency. Dermatol. Surg. *30*, 718–722.

206. Yang, L., Shridhar, S.V., Gerwitz, M., and Soman, P. (2016). An *in vitro* vascular chip using 3D printing-enabled hydrogel casting. Biofabrication *8*, 35015.

207. Yiannakopoulou, E. (2016). Safety Concerns for Sclerotherapy of Telangiectases, Reticular and Varicose Veins. Pharmacology *98*, 62–69.

208. Zanotelli, M.R., Ardalani, H., Zhang, J., Hou, Z., Nguyen, E.H., Swanson, S.,

Nguyen, B.K., Bolin, J., Elwell, A., Bischel, L.L., et al. (2016). Stable engineered vascular networks from human induced pluripotent stem cell-derived endothelial cells cultured in synthetic hydrogels. Acta Biomater. *35*, 32–41.

209. Zarrintaj, P., Manouchehri, S., Ahmadi, Z., Saeb, M.R., Urbanska, A.M., Kaplan, D.L., and Mozafari, M. (2018). Agarose-based biomaterials for tissue engineering. Carbohydr. Polym. *187*, 66–84.

210. Zheng, Y., Chen, J., Craven, M., Choi, N.W., Totorica, S., Diaz-Santana, A., Kermani, P., Hempstead, B., Fischbach-Teschl, C., Lopez, J.A., et al. (2012). In vitro microvessels for the study of angiogenesis and thrombosis. Proc. Natl. Acad. Sci. *109*, 9342–9347.

211. Zhu, W., Qu, X., Zhu, J., Ma, X., Patel, S., Liu, J., Wang, P., Lai, C.S.E., Gou, M., Xu, Y., et al. (2017). Direct 3D bioprinting of prevascularized tissue constructs with complex microarchitecture. Biomaterials *124*, 106–115.

Website reference.

1. https://opentextbc.ca/anatomyandphysiology/chapter/20-5-circulatory-pathways/).
2. https://en.wikipedia.org/wiki/Varicose_veins.
3. https://en.wikipedia.org/wiki/Skeletalmuscle_pump#/media/File:2114_Skeletal_Muscle_Vein_Pump.jpg
4. https://en.wikipedia.org/wiki/Agarose#/media/File:Agarose_polymere.svg).

Appendix I

1. Python script for foam drainage analysis.

```
mport cv2
import numpy as np
import math

# FILENAME = "xx.mp4"
FILENAME = "xx.MOV"
DELTA = 3
def black_and_white(image):
    height, width, _ = image.shape
    # Grayscale
    image = cv2.cvtColor(image, cv2.COLOR_BGR2GRAY)

    for x in range(0, width):
        for y in range(0, height):
            if image[y, x] > 127:
                image[y, x] = 255
            else:
                image[y, x] = 0
    return image

def get_crop_coordinates(frame):
    print("1) Click on the top left corner of the crop rectangle")
    print("2) Click on the bottom right corner")
    print("3) Press any key to continue")
    tmp_image = frame.copy()
    pt = []
    num_clicks = 0

    def getxy(event, x, y, flags, param):
        nonlocal pt, num_clicks
```

```
        if event == cv2.EVENT_LBUTTONDOWN:
            cv2.circle(tmp_image, (x, y), 2, (0, 0, 255), 3)
            cv2.imshow("image", tmp_image)
            pt.append((x, y))
            num_clicks += 1
            if num_clicks == 2:
                cv2.rectangle(tmp_image, pt[0], pt[1], (0, 255, 0), 2)
                cv2.imshow("image", tmp_image)

    cv2.namedWindow('image')
    cv2.setMouseCallback('image', getxy)
    cv2.imshow('image', tmp_image)
    cv2.waitKey(0)
    cv2.destroyAllWindows()
    return pt

def measure_foam_length(image):
    height, width = image.shape
    foam_crop = image[:, (width // 2 - DELTA):(width // 2 + DELTA)]
    ll = []
    for x in range(0, 2 * DELTA):
        ll.append(sum(1 for p in foam_crop[:, x] if p == 255))
    return np.mean(ll)

def measure_liquid_lenght(image):
    height, width = image.shape
    bot_crop = image[(height // 2):height, (width // 2 - DELTA):(width // 2 + DELTA)]
    ll = []
    for x in range(0, 2 * DELTA):
        ll.append(sum(1 for p in bot_crop[:, x] if p == 0))
    return np.mean(ll)

def save_on_file(filename, lst):
```

```
    with open(filename, 'w') as f:
        for item in lst:
            f.write(f"{item}\n")


def get_calibration_line_length(frame):
    # frame = cv2.imread(f"data/{FILENAME}_0.jpg")
    print("Calibration")
    print("1) Click on start point of the calibration line")
    print("2) Click on end point of the calibration line")
    print("3) Press any key to continue")
    pt = []
    num_clicks = 0

    def getxy(event, x, y, flags, param):
        nonlocal pt, num_clicks
        if event == cv2.EVENT_LBUTTONDOWN:
            cv2.circle(frame, (x, y), 2, (0, 0, 255), 3)
            cv2.imshow("image", frame)
            pt.append((x, y))
            num_clicks += 1
            if num_clicks == 2:
                cv2.line(frame, pt[0], pt[1], (0, 255, 0), 2)
                cv2.imshow("image", frame)

    cv2.namedWindow('image')
    cv2.setMouseCallback('image', getxy)
    cv2.imshow('image', frame)
    cv2.waitKey(0)
    cv2.destroyAllWindows()

    x1, y1, x2, y2 = pt[0][0], pt[0][1], pt[1][0], pt[1][1]
    pixel_distance = math.sqrt(((y2 - y1) ** 2) + ((x2 - x1) ** 2))
    real_distance = float(input("How many mm is that line? "))
```

```
    print()
    print("Calibration")
    print(f'{pixel_distance:.2f} pixel')
    print(f'{real_distance:.1f} mm')

    return pixel_distance, real_distance


if __name__ == '__main__':
cap = cv2.VideoCapture("data/" + FILENAME)
    if not cap.isOpened():
        print("Error opening video stream or file")
        exit(1)

foam_length = []
    liquid_length = []
    pixel_height = 0
    mm = 0
    delay = 0

    cur_frame = 0
    while True:
ret, frame = cap.read()

if not ret:
            break

# pt = []
        if cur_frame == 0:
            # cv2.imwrite(f"data/{FILENAME}_0.jpg", frame)
            pt = get_crop_coordinates(frame)
            pixel_height, mm = get_calibration_line_length(frame)
```

```
            print()
            delay = int(input("How many seconds delay before video started? "))

        image = frame[pt[0][1]:pt[1][1], pt[0][0]:pt[1][0]]

        # Trasform in Black and White
        image = black_and_white(image)

        foam_length.append(measure_foam_length(image))
        liquid_length.append(measure_liquid_lenght(image))
        cur_frame += 1
        if cur_frame % 50 == 0:
            print(f"Analyzed {cur_frame}/{len(foam_length)} frames so far")
    cap.release()

    foam_length = [x * mm / pixel_height for x in foam_length]
    liquid_length = [x * mm / pixel_height for x in liquid_length]

    video_end_approx = len(foam_length) // 30 + delay + 1

    xs = np.arange(delay, video_end_approx, 1.0 / 30.0)
    xs = xs[:len(foam_length)]

    save_on_file(f'data/{FILENAME}_foam', foam_length)
    save_on_file(f'data/{FILENAME}_liquid', liquid_length)
    save_on_file(f'data/{FILENAME}_xs', xs)

import matplotlib.pyplot as plt

FILENAME = "x.mp4"
# FILENAME = "x.mp4"

if __name__ == '__main__':
```

```
    foam = []
    with open(f'data/{FILENAME}_foam', 'r') as f:
        for line in f:
            foam.append(float(line))
liquid = []
    with open(f'data/{FILENAME}_liquid', 'r') as f:
        for line in f:
            liquid.append(float(line))

xs = []
    with open(f'data/{FILENAME}_xs', 'r') as f:
        for line in f:
            xs.append(float(line))

    plt.plot(xs, foam, "r", label="foam".upper())
    plt.plot(xs, liquid, "b", label="liquid".upper())
    plt.xlabel("time (s)".upper())
    plt.ylabel("length (mm)".upper())
    plt.title("foam analysis".upper())
    plt.grid()
    plt.legend(loc="center right")

    plt.show()
```

Appendix II

1. Python script for analyzing spectral videos.

```
import sys
from PIL import Image, TiffImagePlugin
with Image.open("0.0625percent.tif") as ti:
    for i in range(ti.n_frames // 23):
        for idx in range(i * 23, (i + 1) * 23):
            ti.seek(idx)
            with TiffImagePlugin.AppendingTiffWriter("frame_%d.tif" % i) as tf:
                ti.save(tf)
```

Appendix III

1. MATLAB® script fro storing pressure data.

```
%%pressure test for harvard pressure transducer running through DAQ board
clear all
close all
clc
s = daq.createSession('ni')
s.addAnalogInputChannel('Dev2','ai0','Voltage')
s.DurationInSeconds = 100
s.Rate=100
data = s.startForeground();
mean(data)
x=0:0.01:99.99;
data=data*100;
plot (x,data)
xlabel('Time (secs)')
ylabel('Pressure (mmHg)')
title('Pressure plot')
x2=x';
save('contrast1ml.xls', 'x2','data','-ASCII');
```